Th. Kahn, F. A. Jolesz, J. S. Lewin

10th Interventional MRI Symposium

Book of Abstracts

October 10–11, 2014
Leipzig, Germany

Department of Diagnostic and Interventional Radiology,
University of Leipzig, Germany

Department of Radiology,
Brigham and Women's Hospital,
Harvard Medical School, Boston, USA

Department of Radiology and Radiological Science,
Johns Hopkins University, School of Medicine, Baltimore, USA

Editors Thomas Kahn, MD
Ferenc A. Jolesz, MD
Jonathan S. Lewin, MD

ISBN 978-3-00-046995-4

Welcome to the 10th Interventional MRI Symposium

Two years have passed since the city of Boston has welcomed the interventional MRI community to the last iMRI Symposium in 2012 boasting a record number of scientific abstracts. The 2014 meeting, the 10th of its kind, is about to kick off in Leipzig and we are very thankful for having received so many excellent abstracts once again reflecting the enormous activity in our field.

This year's two-day program (Fr., Oct. 10 – Sa., Oct. 11) is divided into eight topical sessions and comprises 29 short overview talks by invited speakers and 28 selected oral presentations. On Friday afternoon, 75 minutes will be exclusively reserved for the discussion of 63 scientific posters. Both days have two morning and two afternoon sessions with intermediate coffee breaks.

For the first time in our event history, 2014 will feature three one-hour symposia over lunch and dinner which are hosted by our gold and silver sponsors. Our technical exhibition is open all day on Friday and Saturday showcasing solutions and products of more than 20 industrial partners whose financial support is also greatly acknowledged. The meeting is endorsed by the European Society for Magnetic Resonance in Medicine and Biology (ESMRMB) and the International Society for Magnetic Resonance in Medicine (ISMRM).

Whether this is your first time to Leipzig or whether you're a returning visitor, the official website <english.leipzig.de> may be a good starting point to explore some of the facts and myths. On the eve of iMRI 2014, for example, Leipzig happens to celebrate the 25th Anniversary of the so-called Peaceful Revolution in Germany – a short but important period in view of the city's 999 years since its first documentation.

On behalf of our Program Committee, we wish you all the best for a successful meeting and memorable time in Leipzig.

Thomas Kahn   Harald Busse

Program at a Glance

	Thursday, Oct. 9	Friday, Oct. 10	Saturday, Oct. 11
08:00 am 09:00 am		**Scientific Session I** Prostate	**Scientific Session V** Brain Musculoskeletal
10:00 am 11:00 am		**Scientific Session II** Pelvis Technology General Issues	**Scientific Session VI** Cardiovascular I
12:30 pm		**Lunch Symposium Philips: State-of-the-art MR-guided Interventions**	**Lunch Symposium Siemens: From Diagnosis to Therapy: Innovations for better outcomes**
01:45 pm		**Scientific Session III** Poster Discussion	**Scientific Session VII** Cardiovascular II Chest
03:30 pm 04.00 pm 05:00 pm	**Registration**	**Scientific Session IV** Focused Ultrasound Breast Technology	**Scientific Session VIII** Abdomen Technology
05:30 pm		**Dinner Symposium General Electric: MR-guided Focused Ultrasound: New developments**	
07:30 pm	**Welcome Reception**		

Symposium Chair

Thomas Kahn, Leipzig, Germany

Co-Chairs

Ferenc A. Jolesz, Boston, USA
Jonathan S. Lewin, Baltimore, USA

Faculty

Nathalie Agar, Boston, USA
Roberto Blanco Sequeiros, Turku, Finland
Paul Bottomley, Baltimore, USA
Harald Busse, Leipzig, Germany
Keyvan Farahani, Rockville, USA
Frank Fischbach, Magdeburg, Germany
Jan Fritz, Baltimore, USA
Jürgen Fütterer, Nijmegen, Netherlands
Afshin Gangi, Strasbourg, France
Wladyslaw Gedroyc, London, UK
Alexandra Golby, Boston, USA
Matthias Gutberlet, Leipzig, Germany
Julian Hägele, Lübeck, Germany
Jagadeesan Jayender, Boston, USA
Dara L. Kraitchman, Baltimore, USA
Gabriele Krombach, Marburg, Germany
Christiane Kuhl, Aachen, Germany
Michael Laniado, Dresden, Germany
Joachim Lotz, Göttingen, Germany
Nathan McDannold, Boston, USA
Michael Moche, Leipzig, Germany
Chrit Moonen, Utrecht, Netherlands
Christopher Nimsky, Marburg, Germany
Reza Razavi, London, UK
Maximilian Reiser, München, Germany
Christian Rosenberg, Greifswald, Germany
Ehud Schmidt, Boston, USA
Clare Tempany, Boston, USA
Frank Wacker, Hannover, Germany
Clifford Weiss, Baltimore, USA
Shuo Zhang, Göttingen, Germany

Topics

Friday, October 10

SESSION I	08:00 am – 10:05 am Prostate
SESSION II	10:35 am – 12:25 pm Pelvis, Technology, General Issues
	12:30 pm – 01:30 pm Lunch Symposium Philips State-of-the-art MR-guided Interventions
SESSION III	01:45 pm – 03:00 pm Poster Discussion Session
SESSION IV	03:30 pm – 05:20 pm Focused Ultrasound, Breast, Technology
	05:30 pm – 06:30 pm Dinner Symposium General Electric MR-guided Focused Ultrasound: New Developments

Saturday, October 11

SESSION V	08:15 am – 10:20 am Brain, Musculoskeletal
SESSION VI	10:50 am – 12:30 pm Cardiovascular I
	12:30 pm – 01:30 pm Lunch Symposium Siemens From Diagnosis to Therapy: Innovations for better outcomes
SESSION VII	01:45 pm – 03:05 pm Cardiovascular II Chest
SESSION VIII	03:35 pm – 05:10 pm Abdomen Technology

Scientific Program Objectives

Friday, October 10 – Saturday, October 11, 2014

Upon completion of the Scientific Meeting, participants should be able to:

- Identify new findings in interventional and intraoperative magnetic resonance imaging most relevant to their own fields;
- Explain the impact of newly developed methods in interventional MRI;
- Describe possible future trends and developments in interventional MRI and evaluate the possible impact of these trends and developments on their own clinical and scientific work in the future;
- Assess the state-of-the-art in interventional MR.

Session I

Friday, October 10, 08:00 am – 10:05 am

Prostate

Moderators:		F. A. Jolesz (Boston, MA, USA) J. S. Lewin (Baltimore, MD, USA) Th. Kahn (Leipzig, Germany)
08:00		Welcoming address Th. Kahn, F. A. Jolesz, J. S. Lewin
08:15	V-01	MR-guided prostate interventions C. Tempany Boston, MA, USA
08:30	V-02	MRI-guided prostate biopsy: Correlation of pathology results with pre-biopsy multiparametric prostate MRI findings in 153 lesions A. D. Nicholson, V. Master, T. E. Powell, J. Kang, A. O. Osunkoya, M. G. Sanda, S. G. Nour Atlanta, GA, USA
08:40	V-03	Clinical experience with a virtual real-time MRI navigation option for prostate biopsies at 3 T A. Schaudinn, J. Otto, N. Linder, N. Garnov, G. Thörmer, M. Do, J.-U. Stolzenburg, L.-C. Horn, T. Kahn, M. Moche, H. Busse Leipzig, Germany
08:50	V-04	Prostate interventions: the Nijmegen experience J. J. Fütterer Nijmegen, The Netherlands
09:05	V-05	Interim results of phase II clinical trial for evaluation of MRI-guided laser-induced interstitial thermal therapy (LITT) for low-to-inter mediate risk prostate cancer A. Oto, A. Yousuf, S. Wang, T. Antic, G. S. Karczmar, S. Eggener Chicago, IL, USA
09:15	V-06	MRI-guided "Male Lumpectomy": Technical aspects and outcome data of focal laser ablation for localized prostate cancer S. G. Nour, T. E. Powell, P. J. Rossi Atlanta, GA, USA
09:25	V-07	MR-guided focal laser ablation for prostate cancer followed by radical prostatectomy: Validation of MR predicted ablation volume J. G. R. Bomers, E. B. Cornel, S. F. M. Jenniskens, C. A. Hulsbergen - van de Kaa, J. A. Witjes, J. P. M. Sedelaar, J. J. Fütterer Nijmegen, The Netherlands

09:35 V-08 Magnetic Resonance imaging-guided cryoablation of whole gland prostate cancer:
An initial institutional experience
M. L. White, L. A. Mynderse, A. Kawashima, K. Rampton, K. R. Gorny, T. D. Atwell, J. P. Felmlee, M. R. Callstrom, D. A. Woodrum
Rochester, MN, USA

09:45 V-09 MR-guided focal cryoablation of prostate cancer recurrence following radiotherapy: short term follow-up
J. G. R. Bomers, S. F. M Jenniskens, C. G. Overduin, H. Vergunst, E. N. J. T. van Lin, F. de Lange, E. B. Cornel, J. O. Barentsz, J. P. M. Sedelaar, J. J. Fütterer
Nijmegen, Hengelo, Enschede, The Netherlands; Essen, Germany

09:55 V-10 Perirectal saline infusion facilitates better treatment margins for MR guided cryoablation of recurrent prostate cancer
D. A. Woodrum, K. R. Gorny, J. P. Felmlee, M. R. Callstrom, A. Kawashima, L. A. Mynderse
Rochester, MN, USA

10:05–10:35 **Coffee Break**

Session II

Friday, October 10, 10:35 am – 12:25 pm

Pelvis / Technology / General Issues

Moderators: J. Lotz (Göttingen, Germany)
P. Bottomley (Baltimore, MD, USA)

10:35 V-11 3 Tesla MR-guided interventions in chronic pelvic pain syndromes: Initial clinical experience
J. Morelli, E. Williams, A. L. Dellon, A. Belzberg, J. Carrino, J. Lewin, J. Fritz
Baltimore, MD, USA

10:45 V-12 MR-guided active catheter tracking for gynecologic brachytherapy interventions
E. Schmidt, W. Wang, Z. T. H. Tse, W. Loew, C. L. Dumoulin, R. T. Seethamraju, T. Kapur, R. A. Cormack, A. N. Viswanathan
Boston, MA, USA

11:00 V-13 MRI endoscopy: a path to high resolution parametric imaging and intervention
P. A. Bottomley, Y. Zhang, G, Wang, M. A. Erturk, S. S. Hegde
Baltimore, MD, USA

11:15 V-14 In vivo MR imaging of porcine gastric ulcer model using intra-cavitary RF coil for MR-endoscope system
Y. Matsuoka, Y. Morita, E. Kumamoto, H. Kutsumi, T. Azuma, K. Kuroda
Kobe, Japan

11:25 V-15 A hydrostatically actuated robotic system for real-time MRI-guided interventions
R. Yasin, S. Mikaiel, K. Sung, D. Lu, H. H. Wu, T.-C. Tsao
Los Angeles, CA, USA

11:35 V-16 Design, development, and control of a 3-axis-MRI-compatible robot for remote catheter navigation
M. A. Tavallaei, M. K. Lavdas, M. Drangova
London, ON, Canada

11:45 V-17 Magnetic resonance electrical impedance tomography for assessment of electric field distribution during tissue electroporation
M. Kranjc, B. Markelc, F. Bajd, M. Cemazar, I. Sersa, T. Blagus, D. Miklavcic
Ljubljana, Slovenia

11:55 V-18 The challenges of healthcare transformation on iMRI
J. S. Lewin
Baltimore, MD, USA

12:10 V-19 Global paradigms for open science assessment of technologies in image-guided interventions
K. Farahani
Rockville, MD, USA

12:25–01:45 **Lunch Break**

12:30–01:30 **Lunch Symposium**

Philips Healthcare

State-of-the-art MR-guided Interventions

MR-HIFU in Oncology – From Hyperthermia to Ablation
T. Andreae, Philips Healthcare

Non-invasive treatment of breast cancer – MR-HIFU Feasibility Study
F. M. Knuttel, Department of Radiology, University Medical Center Utrecht
The Netherlands

MRI-guided interventions using the Interventional MRI Suite (iSuite)
S. Weiss, B. Schnackenburg, Philips Healthcare

Session III

Friday, October 10, 01:45 pm – 03:00 pm

01:45–03:00	**Poster Discussion Session**
03:00–03:30	**Coffee Break**

Session IV

Friday, October 10, 03:30 pm – 05:20 pm
Focused Ultrasound / Breast / Technology

Moderators:		W. Gedroyc (London, UK) C. Kuhl, (Aachen, Germany)
03:30	V-20	Focused ultrasound – Update on clinical applications W. Gedroyc London, UK
03:45	V-21	MR-guided focused ultrasound in drug delivery C. T. W. Moonen Utrecht, The Netherlands
04:00	V-22	MR-guided breast interventions C. Kuhl Aachen, Germany
04:15	V-23	Initial clinical experience with a dedicated MR-guided high-intensity focused ultrasound system for treatment of breast cancer F. M. Knuttel, L. G. Merckel, R. H. R. Deckers, C. T. W. Moonen, L. W. Bartels, M. A. A. J. van den Bosch Utrecht, The Netherlands
04:25	V-24	Real-time imaging for MR-guided interventions – Where is the current limitation? S. Zhang Göttingen, Germany
04:40	V-25	Interventions in a standard MR environment M. Moche Leipzig, Germany
04:55	V-26	Visualization and navigation techniques H. Busse, N. Garnov, T. Kahn, M. Moche Leipzig, Germany
05:10	V-27	Building and operating a comprehensive clinical interventional MRI program: Logistics, cost-effectiveness, and lessions learned B. Burrow, H. D. Kitajima, K. Doan, L. Cooper, R. Pierson, G. Pennington, S. G. Nour Atlanta, GA, USA

Session IV

05:30–06.30 **Dinner Symposium**

General Electric Healthcare

MR-guided Focused Ultrasound: new developments

Focused ultrasound neurosurgery – clinical experience treating Parkinson and neuropathic pain
R. Bauer
Department of Neurosurgery
Kantonsspital St.Gallen, Switzerland

MR-guided focused ultrasound, the best kept medical secret?
R. Sigal
President and CCO InSightec

Session V

Saturday, October 11, 08:15 am – 10:20 am

Brain / Musculoskeletal

Moderators: C. Nimsky (Marburg, Germany)
R. Blanco Sequeiros (Turku, Finland)

08:15 V-28 MR-guided neurosurgery and brain tumor laser ablation
A. Golby, O. Olubiyi, R. Torcuator, L. Rigolo, I. Norton
Boston, MA, USA

08:30 V-29 MR-guided neurosurgery and fiber tracking
C. Nimsky
Marburg, Germany

08:45 V-30 Stereotactic laser amygdalo-hippocampotomy for mesial temporal lobe epilepsy: single-center, prospective, investigator-initiated study
R. E. Gross, J. T. Willie, S. Helmers, S. G. Nour
Atlanta, GA, USA

08:55 V-31 Real-time MRI for predicting stem cell distribution and subsequent monitoring of cell infusion to the central nervous system
M. Janowski, J. Wojtkiewicz, A. Nowakowski, M. Chehade, A. Habich, P. Holak, J. Xu, Z. Adamiak, M. Pearl, P. Gailloud, B. Lukomska, W. Maksymowicz, J. W. M. Bulte, P. Walczak
Baltimore, MD, USA

09:05 V-32 Guiding focal blood brain barrier disruption and targeted delivery of chemotherapy with interventional MRI
M. Pearl, M. Janowski, E. Wyse, E. Ngen, A. Bar-Shir, A. Gilad, P. Walczak
Baltimore, MD, USA

09:15	V-33	Transcranial MR-guided focused ultrasound surgery N. McDannold Boston, MA, USA
09:30	V-34	Recent advances in MRI guided musculoskeletal therapy R. Blanco Sequeiros Turku, Finland
09:45	V-35	MR-guided pain management J. Fritz Baltimore, MD, USA
10:00	V-36	3 Tesla MR-guided injections in patients with neurogenic thoracic outlet syndrome: Initial Clinical Experience J. Morelli, Y. Lum, J. Carrino, J. Lewin, J. Fritz Baltimore, MD, USA
10:10	V-37	Real time MR-guided freehand direct shoulder arthrography employing an open 1.0 Tesla MR-scanner C. Wybranski, O. Kosiek, F.-W. Röhl, A. Gazis, M. Pech, J. Ricke, K. Fischbach, F. Fischbach Magdeburg, Germany
10:20–10:50		**Coffee Break**

Session VI

Saturday, October 11, 10:50 am – 12:30 pm

Cardiovascular I

Moderators:		M. Reiser (München, Germany) G. Krombach (Giessen, Germany)
10:50	V-38	Devices for MR-guided cardiovascular interventions – What is still missing? G. Krombach Giessen, Germany
11:05	V-39	New generation laser lithographed dual axis magnetically assisted remote controlled endovascular catheter for interventional MR imaging: In vitro navigation at 1.5 T and 3T versus X-ray fluoroscopy S. W. Hetts, P. Moftakhar, P. Lillaney, A. Losey, B. Thorne, A. Martin, M. Saeed, M. W. Wilson San Francisco, CA, USA

11:15	V-40	MR-guided treatment of low-flow vascular malformations C. R. Weiss, P. A. DiCamillo, W. D. Gilson, J. S. Lewin Baltimore, MD, USA
11:30	V-41	Percutaneous ablation for treatment of symptomatic vascular anomalies using CT and MRI guidance S. Thompson, M. R. Callstrom, K. R. Gorny, J. P. Felmlee, A. Kawashima, M. McKusick, D. A. Woodrum Rochester, MN, USA
11:40	V-42	MRI-guided sclerotherapy for intraorbital vascular malformations: Early experience A. D. Nicholson, T. E. Powell, J. A. Saunders, B. Hayek, T. H. Wojno, S. G. Nour San Francisco, CA, Atlanta, GA, USA
11:50	V-43	MR-guided sclerotherapy of low-flow vascular malformations using T2-weighted interrupted bSSFP (T2W-iSSFP): Comparison of pulse sequences for visualization and needle guidance D. Xu, D. A. Herzka, W. D. Gilson, E. R. McVeigh, J. S. Lewin, C. R. Weiss Baltimore, MD, USA
12:00	V-44	MR-guided interventions in patients with congenital heart disease R. Razavi London, UK
12:15	V-45	MR-guided EP procedures – limitations and challenges M. Gutberlet, M. Grothoff, G. Hindricks Leipzig, Germany
12:30–01:45		**Lunch Break**
12:30–01:30		**Lunch Symposium** **Siemens Healthcare** **From Diagnosis to Therapy: Innovations for better outcomes** C. F. Staehler CTO Siemens Healthcare

Session VII

Saturday, October 11, 01:45 pm – 03:05 pm

Cardiovascular II / Chest

Moderators: D. Kraitchman (Baltimore, MD, USA)
M. Gutberlet (Leipzig, Germany)

01:45 V-46 Image fusion for cardiovascular interventions
D. L. Kraitchman, S. S. Hedge, Y. Fu, G. Wang, T. Ehtiati, W. Gilson
Baltimore, MD, USA

02:00 V-47 First in man: Real-time magnetic resonance-guided ablation of typical right atrial flutter using active catheter tracking
H. Chubb, J. Harrison, S. Williams, S. Weiss, S. Krueger, J. Weisz, G. Stenzel, J. Stroup, S. Wedan, K. Rhode, M. O'Neill, T. Schaeffter, R. Razavi
London, UK; Hamburg, Germany; Burnsville, MN, USA

02:10 V-48 MRI-guided cardiac cryo-ablation
E. G. Kholmovski, R. Ranjan, N. Coulombe, J. Silvernagel, N. F. Marrouche
Salt Lake City, UT, USA; Montreal, Canada

02:20 V-49 Magnetic particle imaging – Potential for MR-guided vascular interventions?
J. Hägele
Lübeck, Germany

02:35 V-50 MR-guided parathyroidectomy and intraoperative recurrent laryngeal nerve identification
J. Jayender, M. A. Nehs, T. C. Lee, F. Jolesz, D. T. Ruan
Boston, MA, USA

02:50 V-51 MR-guided cryotherapy – Rationale, technique and clinical applications
A. Gangi
Strasbourg, France

03:05–03:35 **Coffee Break**

Session VIII

Saturday, October 11, 03:35 pm – 05:10 pm

Abdomen / Technology

Moderators: M. Laniado (Dresden, Germany)
F. Wacker (Hannover, Germany)

03:35 V-52 MR-guided laser therapy of liver tumors
C. Rosenberg
Greifswald, Germany

03:50 V-53 MR-guided RFA of the liver
F. Fischbach
Magdeburg, Germany

04:05 V-54 Liver lesion conspicuity in interactive MR fluoroscopic sequences: dependency on lesion histology, size and image weighting
H. Rempp, R. Hoffmann, E. Rothgang, P. Li, H. Loh, P. L. Pereira, K. Nikolaou, S. Clasen
Tübingen, Heilbronn, Germany

04:15 V-55 Technique and long-term efficacy results of in-bore MRI-directed laser ablation for malignant renal neoplasms
S. G. Nour, A. D. Nicholson, T. E. Powell, M. M. Lewis, V. Master
Atlanta, GA, USA

04:25 V-56 MR-guided tumor sampling using mass spectrometry
N. Agar
Boston, MA, USA

04:40 V-57 Hybrid interventions – indirect MR assistance or direct MR guidance?
F. Wacker
Hannover, Germany

04:55 **Poster Awards and Conclusions**
F. A. Jolesz, J.S. Lewin, Th. Kahn

05:10 **Adjourn**

Poster Presentations

Prostate

P-01 Localization of the puncture spots of index lesions (PSIL) and detection rate of prostate carcinomas (PCa) in MR guided biopsies (MRGB) after negative TRUS [Transrectal Ultrasound] guided biopsies (TRGB)
S. Rödel, S. Blaut, E. Dürig, M. Burke, R. Paulick, G. Haroske, F. Steinbach, T. Kittner
Dresden, Germany

P-02 Application of multiparametric MRI PI-RADS scores and a novel system for MRI/TRUS-fusion guided biopsy for the detection of prostate cancer
S. Tewes, H. Katja, D. Hartung, F. Imkamp, T. Herrmann, J. Weidemann, M. A. Kuczyk, F. Wacker, I. Peters
Hannover, Germany

P-03 MRI-guided prostate biopsy in the treatment planning of tumor-boosted radiotherapy
P. Chung, J. Abed, A. Simeonov, W. Foltz, T. Craig, C. Menard
Toronto, ON, Canada

P-04 Feasibility of a pneumatically actuated MR-compatible 2nd-generation robot for transrectal prostate biopsy guidance
J. G. R. Bomers, D. G. H. Bosboom, G. H. Tigelaar, D. Yakar and J. J. Fütterer
Nijmegen, Arnheim, Enschede, The Netherlands

P-05 Catheter reconstruction and displacement during MRI guided focal HDR prostate brachytherapy
M. Maenhout, M. A. Moerland, J. R. N. van der Voort van Zyp, M. van Vulpen
Utrecht, The Netherlands

P-06 Outcomes of MRI-guided local salvage after radiotherapy for prostate cancer: implications for a focal strategy
C. Menard, T. Pulvirenti, N. Samavati, J. Lee, J. Abed, A. Simenov, W. Foltz, A. Rink, M. Haider, K. Brock, M. Jewett, P. Chung
Toronto, ON, Canada

P-07 Design considerations for a flexible RF coil design for an endorectal HIFU device
J. M. Pavlina, T. Dadakova, M. Hoogenboom, M. van Amerongen, J. Futterer, M. Bock
Freiburg, Germany; Nijmegen, The Netherlands

P-08 Accuracy, precision and safety of needle tapping using a MR compatible robotic device for prostate interventions
M. Maenhout, M. A. Moerland, L. J. van Schelven, J. J. van Veldhuijzen, E. Boskovic, H. Kroeze, J. R. N. van der Voort van Zyp, M. van Vulpen, J. J. W. Lagendijk
Utrecht, The Netherlands

P-09 Pushing X-ray CT out of the equation: In vivo RASOR MRI-based seed detection for post-implant dosimetry in LDR prostate brachytherapy
P. R. Seevinck, C. A. van den Berg, F. Zijlstra, M. E. Philippens, S. J. Hoogcarspel, J. J. Lagendijk, M. A. Viergever, M. A. Moerland
Utrecht, The Netherlands

HIFU

P-10 The animal test of a portable MRI guided HIFU system
I. Kuo, V. Hsieh, C.-J. Wang, S.-C. Hwang, H. Chang
Zhunan, Taiwan

P-11 Respiratory-induced deformation analysis of liver using branching structure of portal vein for MR images for HIFU
T. Matsumoto, E. Kumamoto, D. Kokuryo, K. Kuroda
Kobe, Chiba, Hiratsuka, Japan

P-12 Real time MR guided HIFU treatment of mice melanoma tumors: a feasibility study
M. Hoogenboom, M. den Brok, D. Eikelenboom, E. Dumont, G.J. Adema, A. Heerschap, J. Fütterer
Nijmegen, Twente, The Netherlands; Pessac, France

P-13 Non-invasive magnetic resonance-guided high intensity focused ultrasound ablation of a vascular malformation in the lower extremity
J. M. M. van Breugel, R. J. Nijenhuis, M. G. Ries, R. J. Toorop, E. P. A. Vonken, J. W. Wijlemans, M. A. A. J. van den Bosch
Utrecht, The Netherlands

P-14 Spatio-temporal quantitative thermography of pre-focal interactions between high intensity focused ultrasound and rib cage
L. Petrusca, S. Terraz, C. D. Becker, R. Salomir
Geneva, Switzerland

Breast

P-15 Wireless phased array coils for MR guided breast interventions
M. Fallah-Rad, H. Zhu, L. Petropoulos
Minnetonka, MN, USA

Brain

P-16 Novel percutaneous skull mounted guidance frame base facilitates minimally invasive MR-guided functional neurosurgical procedures
J. T. Willie, R. E. Gross, D. Lozada, S. Nour
Atlanta, GA, USA

P-17 An MR safe radiolucent horseshoe headrest system integrated with a sterile wireless RF coil system for neurosurgical and interventional applications
G. Vanney, E. Heinz, H. Zhu, B. Burkholder,
L. Petropoulos
Minnetonka, MN, USA

Musculoskeletal

P-18 Body-mounted MRI-compatible robot for shoulder arthrography
R. Monfaredi, R. Seifabadi, I. Iordachita, R. Sze, N. Safdar, K. Sharma,
S. Fricke, A. Krieger, C. Dumoulin, K. Cleary
Washington, DC, USA; Baltimore, MD, USA;
Cincinnati, OH, USA

P-19 MRI-guided percutaneous core decompression of osteonecrosis of the femoral head
P. Kerimaa, M. Väänänen, P. Hyvönen, R. Ojala, P. Lehenkari,
R. Blanco Sequeiros
Turku, Oulu, Finland

P-20 Development of a pneumatic x-ray transparent and MR-safe bone drilling system for interventional MRI
F. Güttler, K. Winterwerber, A. Heinrich, U. Teichgräber
Jena, Berlin, Germany

P-21 Technical feasibility of MR-guided vertebral cryoablation: Assessment in a porcine model
J. Morelli, D. Kraitchman, C. Weiss, J. Carrino, J. Lewin, J. Fritz
Baltimore, MD, USA

P-22 MR-guided periradicular therapy (PRT) in patients with chronic lumbar pain: an optimized approach in an open 1.0 Tesla MRI-system
F. Fischbach, A. Gazis, C. Wybranski, M. Pech, J. Ricke, K. Fischbach
Magdeburg, Germany

P-23 MRI compatible hammer for MR-guided bone interventions such as biopsies and ablations
S. Nair, E. Kaye, G. Seimathveeravalli, M. Maybody
New York , NY, USA

Cardiovascular

P-24 Determining the location of the tip of an active transceive guidewire
J. Lockwood, G. H. Griffin, G. Wright, K. Anderson
Toronto, ON, Canada

P-25 Dynamic MR imaging with motion prediction aided by catheter tip tracking
P. Wang, O. Unal
Madison, WI, USA

P-26 Cardiac electrophyiology intervention with intrapro-cedure magnetic resonance imaging
H. Halperin, M. Zviman, M. Guttman, A. Kolandaivelu,
R. Berger, S. Nazarian
Baltimore, MD, USA

P-27 Magnetically assisted remote-controlled endovascular catheter for interventional MR imaging: In vitro navigation at 1.5 T versus X-ray fluoroscopy
A. D. Losey, P. Lillaney, A. J. Martin, D. L. Cooke, M. W. Wilson,
B. R. H. Thorne, R. S. Sincic, R. L. Arenson, M. Saeed, S. W. Hetts
San Francisco, CA, USA

P-28 Micro resonant marker for endovascular catheter tracking in interventional MRI: In vitro imaging at 3T
B. R. H. Thorne, P. Lillaney, A. Losey, X. Zhang, D. Vinson, Y. Pang, S. Hetts
San Francisco, CA, USA

P-29 Evaluating RF safety of a magnetically assisted remote controlled (MARC) catheter during MRI
P. Lillaney, M. Etezadi-Amoli, A. Losey, B. R. H. Thorne, A. J. Martin,
L. B. Evans, G. C. Scott, S. W. Hetts
San Francisco, Palo Alto, CA, USA

P-30 Novel MR safe guidewires for MRI-guided interventions
K. Düring
Hannover, Germany

P-31 Development of a passive-trackable catheter system to perform MR-guided minimal invasive intramyocardial injections – in vivo and consecutive ex vivo study
S. Bock, S. Dahl, S. Tacke, M. Schneider, A. Hartmann, M. Kramer,
H.-W. Henke, M. Friebe, G. A. Krombach
Giessen, Bochum, Germany

Chest / Abdomen

P-32 Pain assessment and prediction following MRI-guided laser ablation of hepatic metastases
T. E. Powell, R. Shi, N. Gallagher, J. Kang, M. A. Bowen, S. G. Nour
Atlanta, GA, USA

P-33 MRI-guided mediastinal biopsies: retrospective evaluation on 15 cases
J. Garnon, G. Tsoumakidou, E. Rothgang, M. de Mathelin, E. Breton, A. Gangi
Strasbourg, France; Baltimore, MD, USA

Thermometry

P-34 Reference-less PRF thermometry for MR-guided focused ultrasound (MRgFUS) liver treatment in a pre-clinical Thiel-embalmed human cadaver model
I. Karakitsios, N. Le, X. Xiao, A. Melzer
Dundee, UK

P-35 MR thermometry for clinical hyperthermia: In vivo comparison of FLASH and EPI double-echo sequences
T. Dadakova, J. Gellermann, O. Voigt, J. Korvink, J. M. Pavlina, J. Hennig, M. Bock
Freiburg, Tübingen, Germany

P-36 Temperature distribution inside a cryoablation iceball studied using UTE MR signal intensity at 11.7T
C. G. Overduin, Y. Sun, J. J. Fütterer, T. W. J. Scheenen
Nijmegen, Enschede, The Netherlands

P-37 Signal processing for noninvasive temperature imaging of fat and aqueous tissues using methylene T1 and water proton resonance frequency
S. Morita, M. Obara, M. Honda, Y. Imai, K. Kuroda
Kanagawa, Japan

P-38 Feasibility of MR thermometry of the knee joint cartilage under thermal therapy
A. Shiina, K. Takahashi, J. Nakano, K. Kuroda
Kanagawa, Japan

Technology

P-39 Multinuclear (19F + 1H) intravascular MRI at 3T
S. S. Hegde, L. Pan, G. Wang, Y. Fu, D. L. Kraitchman
Baltimore, MD, USA

P-40 Incorporation of ultrasound instrumentation and imaging into an interventional MRI suite
C. Lewis, J. P. Felmlee, K. R. Gorny, M. R. Callstrom, D. A. Woodrum
Rochester, MN, USA

P-41 Instrument calibration for an accurate needle guidance using the optical Moiré Phase Tracking System on a 3T wide-bore system
U. Kaegebein, O. Speck
Magdeburg, Germany

P-42 Operation of a RFID based navigation during MRI
F. Güttler, A. Heinrich, M. Sonnabend, U. Teichgräber
Jena, Germany

P-43 Intermittent pneumatic compression for venous thromboembolism prophylaxis during magnetic resonance imaging-guided interventions
B. Taslakian, M. Maybody, E. Kaye, S. Govindarjan, J. P. Erinjeri, J. C. Durack, S. Solomon
Beirut, Lebanon; New York, NY, USA

P-44 Generation of distinct artifacts along conductive structures in Spin-Echo phase images by application of sequence-triggered direct currents
F. Eibofner, H. Wojtczyk, H. Graf, S. Clasen
Tübingen, Germany

P-45 A combined high-resolution internal imaging and RF ablation probe at 3T
A. Erturk, S. S. Hegde, P. A. Bottomley
Minneapolis, MN, Baltimore, MD, USA

P-46 MRI compatible linear motion stage
M. A. Tavallaei, J. Liu, P. Johnson, M. Drangova
London, ON, Canada

P-47 Utilization of a sterilizable interventional MRI coil for procedures in the magnet
D. A. Woodrum, K. R. Gorny, R. Hashoian, J. P. Felmlee
Rochester, MN, Brookfield, WI, USA

P-48 Simultaneous contact-free monitoring of the cardiac and respiratory cycle in real-time during MRI using an optical tracking system
F. Lüsebrink, O. Speck
Magdeburg, Germany

P-49 A 40 channel wireless torso-pelvic array coil for parallel MR imaging interventional applications at 3.0 T
S. Ha, S. Rzeszowski, H. Zhu, L. Petropoulos
Minnetonka, MN, USA

P-50 RTHawk: A development and control system for real-time interventional MRI
R. R. Ingle, B. S. Hu, K. O. Johnson, M. M. Nystrom, W. R. Overall, G. D. Reed, J. M. Santos
Menlo Park, CA, USA

P-51 Advances in tracking multiple markers within a MR scanner
D. Brujic, F. Galassi, M. Ristic
London, Oxford, UK

P-52 Miniaturizing floating traps for suppression of induced RF currents on linear conductors
G. H. Griffin, K. J. T. Anderson, G. A. Wright
Toronto, ON, Canada

P-53 MR monitoring of thermochemical ablation injections
F. Maier, C. J. MacLellan, D. Fuentes, E. N. K. Cressman, K. Hwang, J. P. Yung, J. D. Hazle, J. J. Stafford
Houston, TX, Waukesha, WI, USA

P-54 Wireless hybrid passive and active tracking for automatic image plane alignment
M. Neumann, E. Breton, L. Cuvillon, L. Pan, E. Rothgang, A. Hengerer, M. de Mathelin
Strasbourg, France; Baltimore, MD, USA

P-55 A comparative method to evaluate the performance of different resonant MR marker designs
E. Pannicke, M. Kaiser, G. Rose, R. Vick
Magdeburg, Germany

P-56 Feasibility study of a single-layered resonant MR marker fabricated by thin film technology
M. Kaiser, E. Pannicke, M. Deckert, B. Schmidt, R. Vick, G. Rose
Magdeburg, Germany

P-57 Improved RF transmit coil and methods for MRI
J. T. Vaughan, J. Tian
Minneapolis, MN, USA

P-58 Numerical and experimental test configuration for evaluating MRI induced RF heating of interventional devices
E. Lucano, G. Mendoza, T. Lloyd, M. I. Iacono, S. Wedan, W. Kainz, L. M. Angelone
Burnsville, MN, USA

P-59 Gradient-induced voltages on 12-lead ECG traces during high-duty-cycle MRI sequences and a theoretically-based method for their removal
S. H. L. Zhang, Z. T. H. Tse, C. L. Dumoulin, R. Watkins, W. Wang, J. Ward, R. Y. Kwong, W. G. Stevenson, E. J. Schmidt
Boston, MA, USA

P-60 RF safety in MRI: gauging body-average SAR and local heating of interventional coils
A. Erturk, A.-M. El Sharkawy, P. A. Bottomley
Minneapolis, MN, Baltimore, MD, USA

P-61 Understanding RF safety for MRI
J. T. Vaughan, J. Tian, D. Shrivastava
Minneapolis, MN, USA

P-62 Device powering using inductively coupled coils with transmit MR excitation
M. Venkateswaran, D. Van der Weide, K. Kurpad
Madison, WI, USA

P-63 Electro/magneto/thermal acoustic ultrasound generation in iMRI devices
G. Scott, M. Etezadi-Amoli, H. Nan, M. Aliroteh, A. Arbabian, P. Stang, J. Pauly
Stanford, CA, USA

Oral Presentations

Magnetic resonance (MR)-guided prostate interventions

Clare Tempany, MD

Abstract

Introduction: Magnetic resonance (MR) guided prostate interventions are well-established, with an almost 20 year history. We established the first MR guided brachytherapy program in the MRT Signa SP 0.5T device at Brigham and Women's Hospital (BWH) in the late 1990s. Since that time, there has been a dramatic increase in prostate MR imaging and interventions. This is primarily due to the fact that multi-parametric MRI (mpMRI) examinations have been established and are very well validated for prostate cancer detection and tumor volume imaging. MpMRI examinations of the prostate have now become widely accepted as the optimal imaging technique for men suspected of having prostate cancer, staging known prostate cancer, planning therapy and following men after treatment. Today, as when we began the program in 1997, the baseline pre-procedure imaging remains the defining step. This protocol has been optimized (1) and standardized through ESUR PIRADS in 2012 (2) and US PIRADS in development. New prostate intra-glandular maps with 36 sectors have been defined to allow for careful pre-interventional planning. The interventions are either diagnostic biopsy, or whole-gland or focal therapies.

MR-guided prostate biopsy: The role of MR in prostate biopsy has been a major advance for patients. Now it is possible with a small number of core samples to target a focal suspicious lesion and obtain pathology confirmation of cancer, and more importantly, sample the clinically relevant disease. In other words, we have moved from transrectal ultrasound blind biopsy involving many cores (12-80) to a small number of cores (average: four per gland) to detect significant cancers, defined as adenocarcinoma with Gleason pattern 4 or higher. There are several approaches: 1) MR cognitively used during TRUS; 2) in-bore MR guided and targeted biopsy (either transperineal or transrectal); and, 3) so-called "fusion" biopsies. The latter uses pre-obtained MR images in real-time TRUS guidance. Each of these will be discussed and compared to the in-bore transperineal 3T MR guided prostate biopsy program at BWH. Our experience will be reviewed in detail.

MR guided therapies for localized prostate cancer: As with diagnosis, the treatment options for men with prostate cancer are changing. There is a trend away from whole-gland therapies, and their associated morbidities, towards focal or less than total treatments. A consensus is lacking regarding which patients are best-suited to which focal therapy. But clearly, image-guided therapy requires clear and accurate imaging of the 3D volume of cancer and the adjacent normal structures. The goal, as in all image-guided therapy (IGT), is maximal therapy to target with minimal side effects or damage to adjacent normal tissues. MR guided ablations have also been successfully applied to men who have failed primary treatment and require so-called "salvage" therapy. There are several ablative techniques which utilize MR guidance and monitoring. These include cryotherapy, laser, FUS/HIFU, and interstitial electroporation (IRE). Again, as with biopsy these can be done using MR either in or out of bore. The in bore techniques will be the primary focus of this presentation. MR guided cryotherapy and MR guided focused ultrasound will be presented and comparisons to other methods introduced.

1. Hegde JV, Mulkern RV, Panych LP, Fennessy FM, Fedorov A, Maier SE, Tempany CM. Multiparametric MRI of prostate cancer: an update on state-of-the-art techniques and their performance in detecting and localizing prostate cancer. J Magn Reson Imaging. 2013 May;37(5):1035-54. Review. PMID: 23606141; PMCID: PMC3741996.
2. Barentsz JO, Richenberg J, Clements R, et al.; European Society of Urogenital Radiology. ESUR prostate MR guidelines 2012. Eur Radiol. 2012 Apr;22(4):746-57. PMID: 22322308; PMCID: PMC3297750.

MRI-Guided Prostate Biopsy: Correlation of Pathology Results with Pre-biopsy Multiparametric Prostate MRI Findings in 153 Lesions.

Andrew D. Nicholson[1,2,6], Viraj Master[3,6], Tracy E. Powell[1,2], Jian Kang[1,4], Adeboye O. Osunkoya[5,6], Martin G. Sanda[3,6], and Sherif G. Nour[1,2,6]. [1]Department of Radiology and Imaging Science, Emory University Hospital, Atlanta, GA, United States [2] Interventional MRI Program, Emory University Hospital, Atlanta, GA, United States [3]Department of Urology, Emory University Hospital, Atlanta, GA, United States [4]Department of Biostatistics and Bioinformatics, Emory University, Atlanta, GA, United States [5]Department of Pathology and Laboratory Medicine, Emory University Hospital, Atlanta, GA, United States [6]School of Medicine, Emory University, Atlanta, GA, United States

PURPOSE The diagnosis of CaP is often made in through serial serum prostate-specific antigen (PSA) measurements, with trans-rectal ultrasound-guided (TRUS) biopsy for those patients with rising PSA. TRUS biopsy is limited by the nature of the procedure being performed "blinded" to the location of the cancer, which can result in false negative biopsies, or sampling of less aggressive regions of tumor, both of which can delay the necessary therapy. Prostate MRI allows physicians to assess the entirety of the gland in a non-invasive manner. Our study is designed to correlate MRI-guided biopsy histopathology with pre-biopsy MRI parameters. With this data, we present a method that is reliable and easily implemented in clinical practice for evaluating lesions detected on mpMRI of the prostate.

METHODS Following IRB approval, a retrospective review was conducted of patients undergoing MRI-guided prostate biopsy at our institution. All included patients had a multiparametric MRI exam of the prostate prior to the biopsy. This pre-procedure scan included the following sequences: high-resolution tri-plane T2, axial DWI / ADC (b-values=0-2000), 3D multi-voxel spectroscopy and axial dynamic contrast-enhanced (DCE) T1 perfusion. Pre-biopsy MRI was reviewed by two radiologists with experience reading prostate MRI. Both reviewers graded each lesion as a 0 (negative) or 1 (positive) based on the following parameters: elevated intrinsic T2 signal, diffusion restriction (high DWI and low ADC recorded separately), elevated choline spectroscopy peak (relative to the citrate peak), elevated perfusion on DCE perfusion imaging, and malignant contrast washout on DCE perfusion imaging (defined as greater than 20% washout from the peak). Statistical analysis was performed using JMP software. Data was analyzed for the sensitivity, specificity, positive predictive value, negative predictive value, and accuracy of each individual parameters. The parameters were then analyzed as a whole using logistic regression analysis.

RESULTS Our dataset includes 35 patients with a total of 153 MRI-guided biopsied lesions. Average patient age = 63.2 years (range 52-79). Average serum PSA value prior to biopsy = 9.00 ng/mL (range: 1.31-44.47 ng/mL). Of the 29 patients, 23 (79.31%) had positive MRI-guided biopsies; of the 114 biopsies, 29 (25.4%) were positive. We computed true positive (TP), true negative (TN),

Table 1: Prediction Accuracy For The Individual Parameters

Method	TP	TN	FP	FN	Sn	Sp	PPV	NPV	Accuracy
DWI	7	30	1	10	0.41	0.97	0.88	0.75	0.77
ADC	17	22	9	0	1.00	0.71	0.65	1.00	0.81
Spectroscopy	8	21	10	9	0.47	0.68	0.44	0.70	0.60
Incr Perf	14	18	13	3	0.82	0.58	0.52	0.86	0.67
Malig Wash	6	29	2	11	0.35	0.94	0.75	0.72	0.73

False negative and false positive (FP) along with the sensitivity, specificity, positive prediction value (PPV), negative predictive value (NPV) and overall accuracy (Table 1). We then considered a logistic regression model to combine the outcome from the different parameters. This model is defined by the equation: $\mathrm{Probability(CaP)} = \frac{1}{1+e^{55.14-36.3[DWI]+19.54[ADC]+18.07[Cho]+17.94[Perf]+18.07[Wash]}}$, where each *[Parameter]* is given a value of 1 if positive, and 0 if negative . This model was analyzed separately, with results in Table 2. Our analysis shows this model is superior to the ADC alone.

Table 2: Prediction Accuracy For The Logistic Regression Model

Method	TP	TN	FP	FN	Sn	Sp	PPV	NPV	Accuracy
Model	17	24	7	0	1.00	0.77	0.71	1.00	0.85

CONCLUSIONS Standardization of how mpMRI is interpreted is important as the technique becomes more widely available. The scoring system presented herein is both simplistic and robust in its utility for evaluating lesions detected on prostate MRI. With the logistic regression model in mind, a scoring system for the parameters can be derived wherein a 1 is assigned for the ADC, Elevated Choline Peaks on Spectroscopy, Increased Perfusion, and Malignant Washout, and a 2 is assigned for a positive DWI. Any given lesion will therefore receive a score between 0-6. Using the model equation, we can see that a lesion with a score of 3 has a probability of being CaP of 22.6%, whereas a lesion with a score of 4 has a probability of being CaP of >99%. This technique will allow for improved sensitivity and specificity in the detection of CaP. Patients with lesions scoring no higher than a 2 can be triaged into a low probability of cancer category, whereas those patients with a lesion scoring 3 or greater can be offered a directed biopsy, knowing the probability of cancer becomes significant with a score of 3 and very high with a score of 4 or more.

Clinical experience with a virtual real-time MRI navigation option for prostate biopsies at 3 T

A. Schaudinn [1], J. Otto [1], N. Linder [1], N. Garnov [2], G. Thörmer [1], M. Do [2], J.U. Stolzenburg [2], L.C. Horn [3], T. Kahn [1], M. Moche [1], H. Busse [1]

[1] Diagnostic and Interventional Radiology Department, [2] Urology Department, Leipzig University Hospital, [3] Institute of Pathology, University of Leipzig, Leipzig, Germany

Purpose

To report on our clinical experience with a virtual real-time navigation option for transrectal MRI-guided prostate biopsies in patients with suspicion of prostate cancer.

Materials and Methods

Under IRB approval and with written informed consent, 34 patients between 52 and 78 years old (mean 64) with mean PSA level 12.7 (3.6–42) ng/mL and after 1 to 9 (mean 1.9) negative transrectal ultrasound-guided biopsies underwent MRI biopsy of the prostate. Interventional guidance was provided by a passive device (DynaTRIM, Invivo, Gainesville, FL) with a transrectal, MRI-visible needle guide, two translational and two rotational degrees of freedom. Tracking and referencing elements were added to this device and combined with proper in-room tracking, procedural planning and visualization components (Localite GmbH, St. Augustin, Germany) in a 3-T MRI (Magnetom Tim Trio, Siemens) environment (Fig. 1). Histopathological biopsy results, intervention times and complications were documented.

Results

MR image quality and patient comfort were not impaired by the additional hardware components. The interventional radiologist considered the real-time feedback on the virtual needle direction to be helpful for procedural guidance, in particular for less accessible regions like the apex, lateral mid gland and basis of the prostate. Median intervention time for 34 patients was 70 minutes (34-110 minutes) including 10 patients where two suspicious lesions were targeted. No major complications were observed, one minor complication (fever) was resolved within 24 hours. The obtained specimens were diagnostic in all cases. In 17 patients (50%), histopathology revealed prostate cancer with Gleason Scores 6 (GS 3+3, n=10) and 7 (GS 3+4, n=7).

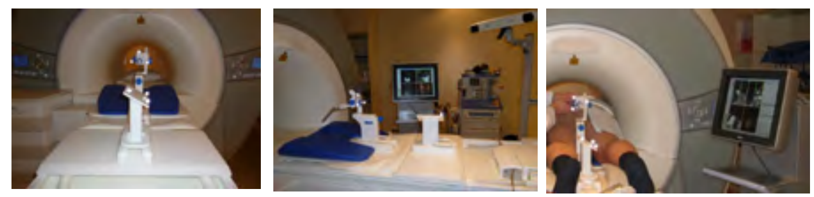

Figure 1. Transrectal 3-T MRI biopsy with navigation option. **left:** Modified interventional device (Invivo) and table-mounted element (front) for constant patient registration. **middle**: Setup with in-room monitor and tracking camera. **right:** Clinical navigation scene

Conclusion

The presented navigation option for MRI-guided prostate interventions was technically feasible and accurate. Procedures were rather time consuming but also revealed a relatively high number of prostate cancers. The virtual real-time navigation scene was found to improve orientation and guidance, in particular for less accessible locations in the prostate.

Prostate interventions: the Nijmegen experience

Jurgen Fütterer
Department of Radiology, Radboud University Nijmegen

Due to widespread use of the prostate-specific antigen (PSA) test and the lowered PSA threshold for biopsy, the number of newly diagnosed prostate cancers (PCa) has strongly increased. Consensus exists that it is essential to treat aggressive PCa. However, whole gland treatment (i.e. surgical or any form of radiotherapy) can lead to significant morbidities, such as incontinence and impotence and can have substantial impact on quality of life.

Focal therapy of prostate cancer has the potential to reduce treatment-related complications such as incontinence and impotence, without making concessions to cancer-specific outcome. About 13 – 33% of the patients has a unifocal prostate cancer lesion and would be eligible for focal therapy. Consistent with the "index lesion theory" even more patients would be suitable.

On one hand ample discussion exists how to select the appropriate patient for focal therapy. However, on the other hand there is almost no discussion about the optimal focal therapy method. The latter has to meet numerous requirements: first, to be able to treat a specific area or one lobe of the prostate. Second, to accurately shape the ablation zone, with no significant effect on the surrounding tissue. Third, to be minimally invasive with a low per- and post-operative complication rate and fourth to be reproducible.

Consequently, ablation techniques such as cryosurgery, high intensity focused ultrasound (HIFU), and laser-induced thermal therapy (LITT) have emerged as feasible minimal invasive therapy for treatment of prostate cancer. Although most of these techniques are still considered experimental. In this presentation, these techniques will be highlighted and discussed.

TITLE: Interim Results of Phase II Clinical Trial for Evaluation of MRI-guided Laser-induced Interstitial Thermal Therapy (LITT) for Low-to-Intermediate Risk Prostate Cancer

AUTHORS AND AFFILIATIONS: Aytekin Oto[1], Ambereen Yousuf[1], Shiyang Wang[1], Tatjana Antic[2], Gregory S. Karczmar[1], Scott Eggener[3]
Departments of Radiology[1], Pathology[2] and Urology[3], University of Chicago, Chicago, IL

PURPOSE: To assess the oncologic efficacy and safety of MRI-guided laser-induced interstitial thermal therapy of biopsy confirmed and MR-visible prostate cancer.

MATERIAL AND METHODS: 17 patients with biopsy proven low-to-intermediate risk prostate cancer underwent MRI guided laser ablation of the cancer using Visualase laser ablation device. All patients had a pre-procedure endorectal MRI which showed suspicious foci concomitant with the positive sextant on TRUS guided biopsy. The area of interest was targeted transperineally using 1.5 T Philips MRI scanner and Visualase ablation device. Ablation was monitored by real time MR thermometry using Visualase MRI thermometry software. Perioperative, early and late complications and adverse events were recorded. Follow-up was performed with 3- month MRI examination and MR-guided biopsy and validated quality of life questionnaires to assess urinary and sexual function.

RESULTS: MRI guided laser ablation of prostate cancer was successfully performed in all 17 patients without significant peri-procedural complications. All patients were discharged home the same day. Average duration of the procedure was 3 hours 39 minutes and average duration of a single laser ablation was 1 minute 21 seconds. Total number of ablations per patient ranged from 2-7, with a median of 4. The treatment created an identifiable hypovascular defect in all cases. Post procedure complications were minor and included urinary symptoms, perineal bruising and erectile dysfunction, all of which self- resolved. MR-guided biopsy of the ablation zone performed at the 3-month time point showed no cancer in all patients. Validated quality of life urinary and sexual questionnaires obtained before and 3 months after the procedure did not reveal any significant differences ($p \geq 0.05$).

CONCLUSION: Very early results of MRI-guided focal laser ablation for treatment of clinically localized, low-to-intermediate risk prostate cancer appear promising. It may offer a minimally invasive procedure for selected patients that does not appreciably alter sexual or urinary function.

MRI-Guided "Male Lumpectomy": Technical Aspects and Outcome Data of Focal Laser Ablation for Localized Prostate Cancer

Sherif G. Nour[1,2,3], Tracy E. Powell[1,2], Peter J. Rossi[3,4]

[1]Department of Radiology and Imaging Sciences, Emory University Hospital, Atlanta, GA, USA
[2]Interventional MRI Program, Emory University Hospital, Atlanta, GA, USA
[3]Emory University School of Medicine, Atlanta, GA, USA
[4]Department of Radiation Oncology, Emory University Hospital, Atlanta, GA, USA

Purpose: Current options for patients with prostate cancer include whole gland treatments, hormonal therapy, or active surveillance. These options represent a dilemma for patients with localized low-grade cancer who are offered a choice of either observation or disproportionately aggressive therapy resulting in significant complications including urinary incontinence and erectile dysfunction. We report the technical aspects and outcome results of a minimally-invasive focal treatment using laser ablation under MRI guidance and monitoring to treat localized low-grade cancer while preserving the rest of the prostate gland.

Methods: 6 male patients (age=51-67y, mean=59) with localized low-risk prostate cancer underwent MRI-guided focal laser ablations. Procedures were performed within a 3T MRI suite (Magnetom Trio, Siemens, Germany) under conscious sedation (*n=4*) or general anesthesia (*n=2*). Patients were laid in the prone position and a transrectal MR-compatible needle guide was inserted. It was attached to a trans-rectal interventional MR positioning device (DynaTRIM®, Invivo, FL, USA) and imaged with a fast sagittal T2-weighted sequence (TR/TE/FA°/NSA=6340/96/150°/1). A midline image was used to calibrate the needle guide position to the localization software (DynaLOC, Invivo, FL, USA). Axial and sagittal sequences were used to target the lesion. A 1.0-cm (n=4) or 1.5-cm (n=2) active-tip diode laser fiber (Visualase, TX, USA) was introduced within an internally cooled catheter through a 14-gauge introducing sheath. The catheter tip location was confirmed on TSE-T2WIs (TR/TE/FA= TR/TE/FA°/NSA=4320/101/150°/3). A test laser dose of 5 watts was applied for 20s. Definitive ablation was then conducted utilizing 12 (n=2), 15 (n=1), or 21 (n=3) watts. Simultaneous temperature maps and cumulative damage maps were obtained, co-registered and overlaid on anatomical imaging to obtain real-time monitoring of extent of ablation zones (Fig.1). Fiber repositioning for additional ablation was conducted as needed. The procedures were concluded when the cumulative damage maps were noted to encompass the entire tumors. Final ablations were evaluated on TSE-T2 and pre- and post-contrast VIBE and TSE-T1 scans.

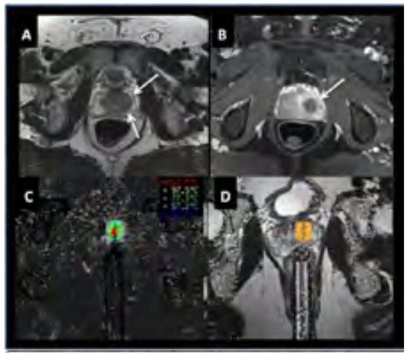

Figure 1: (a) Pre-treatment TSE-T2 scan showing a 1.7-cm left central midgland localized prostate cancer (Gleason 3+3=6) (arrow). (b) Post-treatment gadolinium-enhanced TSE-T1 scan showing the generated laser ablation zone replacing the target tumor. (c) and (d) Intra-procedural real-time temperature (c) cumulative damage (d) maps allowing interactive online assessment of the extent of ablation and determination of treatment endpoint.

Results: All targeted tumors treatment-naïve were Gleason 3+3=6 prostate adenocarcinomas. Target tumor sizes were 1.3 - 2.5 cm (mean = 1.9 cm). 3 tumors were right-sided and 3 were left-sided. 2 tumors were in the peripheral zone and 4 were in the central gland. All tumors were at the mid-gland level. One tumor extended into the gland base and one extended into the gland apex. Access to the desired part of the prostate gland was feasible in all cases. The applied laser energy was 3708- 8820J (mean = 6235J) per treated tumor, with dosage calibrated based on real time feedback of tumor response to ablation. Treatments required 2-4 ablation cycles/laser fiber positionings and resulted in complete tumor necrosis in a single session in all cases as shown on intraprocedural Gadolinium-enhanced MRI. Laser ablation zones demonstrated central iso-to-hypointense signal surrounded by hyperintense/enhancing rim on T2&T1, respectively (Fig.1). The patients tolerated the procedures well and were discharged 4-6 hours after procedure. No immediate or delayed complications were encountered. Follow-up durations ranged between 3-24 months. Significant drop of pretreatment PSA level occurred in all cases (Fig.2). One of the 6 patients had a 5mm focal recurrence at the edge of the ablation zone at his 24-month follow-up time point. No recurrence was noted in the other cases at their 3-month (n=3) and 12-month (n=2) follow-up time points.

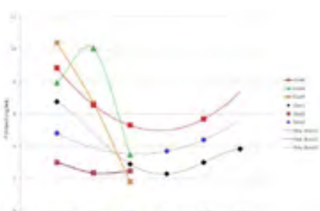

Figure 2: Timeline of PSA response to focal laser ablation in all cases

Conclusion: This report describes a technique for MRI-guided and monitored transrectal focal laser ablation for minimally-invasive targeting of localized low-grade prostate cancer. The technique is feasible and well tolerated as an outpatient procedure. This small series indicates a promising efficacy for up to 24-month follow-up durations. Prospective assessment of safety and efficacy awaits further evaluation on a larger cohort of subjects.

MR-guided focal laser ablation for prostate cancer followed by radical prostatectomy: Validation of MR predicted ablation volume

JGR Bomers[1], E Cornel[2], SFM Jenniskens[1], CA Hulsbergen – van de Kaa[3], JA Witjes[4], JPM Sedelaar[4], JJ Fütterer[1,5] [1]Department of Radiology, [3]Pathology, [4]Urology, Radboud University Medical Center Nijmegen, the Netherlands, [2]Department of Urology, Ziekenhuisgroep Twente, Hengelo, the Netherlands, [5]MIRA, University of Twente, Enschede, the Netherlands

Purpose Focal therapy is a promising treatment option for low- and intermediate grade prostate cancer (PCa). Laser-induced interstitial thermal therapy, also known as focal laser ablation (FLA) is a relatively new technique. To date, only a few studies have been performed on MR guided FLA in PCa patients (1-4). The goal of our study was to validate MR-guided FLA: Before radical prostatectomy, patients with PCa were treated with transrectal MR-guided FLA. Hereafter, laser software, MR images and histopathologic specimens were used to assess the expected and actual size of the ablated region.

Methods The study was approved by the Institutional Review Board. Six patients with newly diagnosed and histopathologically proven low or intermediate grade PCa were included. For all patients transrectal MR-guided FLA was intended as extra treatment and for this reason only one ablation per patient was performed. Their main treatment was radical prostatectomy. All MR-guided FLA procedures were performed on a 3T MR scanner under local anaesthesia. The ablation procedure was continuously monitored with real-time MR temperature mapping. Based on the temperature maps, a damage estimation map (figure 1A) of the final ablation zone was computed by the laser software using the Arrhenius model. Directly after the ablation T1-weighted contrast enhanced (CE) images (figure 1B) were acquired. Three weeks later patients underwent radical prostatectomy. The resected prostate specimens underwent normal pathology workup with hematoxylin-eosin staining and additional immunostaining to verify tissue necrosis. Ablation volumes were contoured and measured on the histopathologic specimens, on the T1-weighted CE images and on the damage estimation maps.

Results MR-guided FLA was feasible to perform in 5/6 patients and no intraoperative complications were encountered. In one patient MR-guided FLA was not possible since the tumor lesion was too close to the bladder wall. All patients were discharged 1 hour after treatment. All radical prostatectomies were uncomplicated. The median ablation volumes estimated by the laser software and measured on T1-weighted CE images were respectively 6.7x (range 1.6 – 29.2) and 0.9x (range 0.5 – 2.4) larger than the necrotic volume measured on the histopathology specimen. On histopathology, in all cases the homogeneous necrotic area was surrounded by a reactive transition zone of variable thickness (1 – 5 mm), showing neovascularisation and an increased mitotic index, indicating an increased tumor activity.

Conclusions The laser software overestimates the final necrotic area. T1-weighted CE images give a better indication of the necrotic volume. Histopathology results indicate a margin of 5 mm around the tumor should be ablated and the total tumor must be ablated because of increased tumor activity in the transition zone between necrotic and viable tissue.

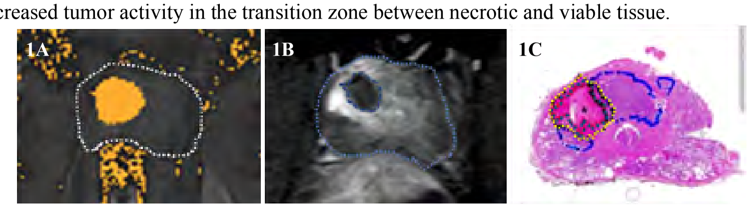

Figure 1A: Damage estimation map**.** The orange spot indicates the ablation zone. **1B:** T1-weighted CE image. The dark blue line indicates the non enhancing ablation zone **1C:** Histopathology specimen. The blue dotted line indicates the necrotic zone. The area between the blue and yellow line indicates the transition zone between necrotic and viable tissue.

Magnetic Resonance Imaging-guided Cryoablation of Whole Gland Prostate Cancer: An Initial Institutional Experience.

Mariah L. White, MD, Lance A. Mynderse, MD, Akira Kawashima, MD/PhD, Karen Rampton, MD, Krzysztof R Gorny, PhD, Thomas D. Atwell, MD, Joel P. Felmlee, PhD, Matthew R. Callstrom, MD, PhD, David A. Woodrum, MD/PhD
Mayo Clinic, Rochester, MN

Purpose: To establish the short-term efficacy and safety of whole gland prostate cryoablation under MRI-guidance.

Material and Methods: Five patients (mean age 66, range 63-69 years) were treated with MRI-guided cryoablation for prostate adenocarcinoma. Average prostate volume prior to ablation was 20 cc (range 17-25 cc). Four of five patients had a history of abdominal perineal resection, with chemotherapy alone (1 of 5 patients) or in conjunction with radiotherapy (3 of 5 patients) for colorectal cancer and one patient had received only external beam radiation for prior prostate adenocarcinoma with no prior prostate surgery. Each had hyperenhancing nodules on MRI with positive confirmation biopsy under imaging guidance showing Gleason score ranging from 7-9. Each procedure was performed under general anesthesia with MRI guidance (Siemens, Espree 1.5 T MRI) for needle placement and iceball monitoring. Before initiation of freezing, there was placement of a transurethral warming catheter to protect the urethra and urinary sphincter from iceball encroachment. For each gland, 7-9 cryoneedles (Galil, Inc.) were placed approximately 0.5 cm apart in the prostate gland by a transperineal approach with 2-3 freeze-thaw cycles performed. PSA values and voiding function before and after procedure were reviewed to assess a short term PSA efficacy and safety.

Results: Average pre-procedure prostate specific antigen (PSA) was 5.91 ±1.78 ng/mL and average 1-3 months post-procedure PSA was 0.15 ± 0.1ng/mL (P<0.01). All patients had independent voiding at 1-week post ablation. No perioperative complications were observed.

Conclusion: MRI guided cryoablation of the whole prostate gland for prostate cancer in the setting previous pelvic surgery and/or pelvic radiation for prior pelvic malignancy is both safe and feasible with initial follow-up PSA values nearly undetectable. The short-term morbidity on this small cohort of patients appears good with no degradation from baseline.

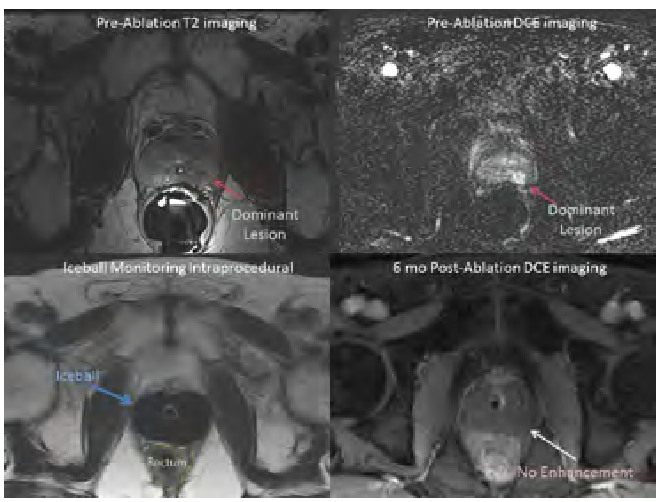

MR-guided focal cryoablation of prostate cancer recurrence following radiotherapy: short term follow-up

JGR Bomers[1], SFM Jenniskens[1], CG Overduin[1], H Vergunst[2], ENJT van Lin[3], F de Lange[1], EB Cornel[4], JO Barentsz[1], JPM Sedelaar[5], JJ Fütterer[1,6]
[1]Department of Radiology, [5]Urology, Radboud University Medical Center, Nijmegen, the Netherlands. [2]Department of Urology, Canisius Wilhelmina Ziekenhuis, Nijmegen, the Netherlands. [3]Westdeutsches Protonentherapiezentrum, Essen, Germany. [4]Department of Urology, Ziekenhuisgroep Twente, Hengelo, the Netherlands. [6]MIRA, University of Twente, Enschede, the Netherlands

Purpose: Cryoablation of prostate cancer (PCa) under transrectal ultrasound (TRUS) guidance has been performed for several years for salvage treatment purposes after radical prostatectomy or radiotherapy. However, high complication rates are not uncommon, due to poor visibility.

Magnetic resonance (MR) imaging guided cryoablation of the prostate may reduce these high complication rates, because of the excellent soft tissue contrast. Furthermore, MR image guidance enables both accurate lesion targeting as well as three-dimensional monitoring of iceball growth.

Purpose of our study was to assess short-term clinical outcome of MR-guided focal cryoablation in patients with prostate cancer (PCa) recurrence after previous radiotherapy.

Methods: Since May 2011, 37 patients with histopathologically proven local PCa recurrence after radiotherapy without evidence for local or distant metastases underwent MR-guided focal cryoablation. In June 2014, 31 of these patients had a follow-up of at least 12 months and were included in our study.

Follow-up after MR-guided cryoablation consisted of a visit to the urologist, PSA-level measurement and a multi-parametric MRI after 3, 6 and 12 months. In the last 9 patients the multi-parametric MRI at 12 months was followed by 2-3 targeted MRI-guided biopsy samples of the edge of the ablated region to confirm treatment success with histopathology.

Results: One patient died 5 months after treatment for reasons unrelated to PCa and was therefore excluded. As a result, 30 men were included in analyses. Median follow-up was 25 months (range 12 – 37). In one patient the procedure was cancelled because the urethral-warmer could not be inserted. Two months later he was treated successfully. All other procedures were technically feasible.

In 7/30 of the patients stress incontinence was seen. One patient developed total urinary incontinence. Temporary urinary retention was experienced by 4/30 of the patients, 2/30 suffered from continuing urinary retention, needing clean-intermittent catheterization. One of them needed surgery to remove an urethral stricture. Another patient underwent surgery to remove a bladder neck stenosis after 24 months. Fistulas were not recorded.

After 12 months, 5/30 (16.7%) patients developed node and/or bone metastases. They probably had micrometastases at the time of their MR-guided cryoablation, which were not detected during pre-treatment imaging. Eleven patients (36.7%) were diagnosed with remnant or recurrent disease. Five of them were retreated with MR-guided cryoablation. In 9 patients MR-guided biopsy was performed of the edge of the ablation zone. Vital tumor cells were found in 4/9 (44.4%) patients.

Conclusion: Transperineal focal MR-guided cryoablation of recurrent PCa after radiotherapy was technically feasible and safe. Initial results are promising, however longer follow-up is needed and more patients have to be studied.

Perirectal saline infusion facilitates better treatment margins for MR guided cryoablation of recurrent prostate cancer.

David A. Woodrum, MD/PhD, Krzysztof R Gorny, PhD, Joel P. Felmlee, PhD, Matthew R. Callstrom, MD, PhD, Akira Kawashima, MD/PhD, Lance A. Mynderse, MD
Mayo Clinic, Rochester, MN

Purpose: To quantitate the marginal separation between the prostate cancer recurrence and the rectum before and after MR guided transperineal saline displacement.
Materials and Methods: Under IRB approval, we retrospectively reviewed 15 patients with prostate cancer recurrence treated with MR guided cryoablation where saline displacement was used to facilitate better treatment margins. In these cases, the separation between the prostate cancer recurrence and rectal wall was measured before and after saline displacement to determine whether significant changes were made. The average age was 64 years old with size of recurrence ranging from 2.3-0.6 cm. Seven patients had prior surgery but no radiation. Six patients had prior surgery and radiation. One patient had no surgery or radiation and one patient had only prior radiation. Clinical followup was made regarding rectal injuries.
Results: Analysis of the 15 patients demonstrated a starting average distance between the cancer recurrence and rectum of 0.2cm with average saline displacement of 1.1cm (t-test, $p<0.05$). In the group with prior surgery but no radiation (7), starting separation distance was 0.2cm with saline displacement averaging a separation of 1.1cm(0.7-1.4cm) ($p<0.05$). In the group with prior surgery and radiation (6), there was a starting separation of 0.3cm with saline displacement average distance of 1.1cm(0.4-2.1cm)($p<0.05$). There was no significant difference between the starting distance between the recurrence and the rectum in any group. Saline displacement averages were similar in all groups as well.
Conclusion: Saline displacement is a valuable tool in the perirectal space for creating greater separation between the prostate cancer recurrence and the rectum allowing for a better potential treatment margin.

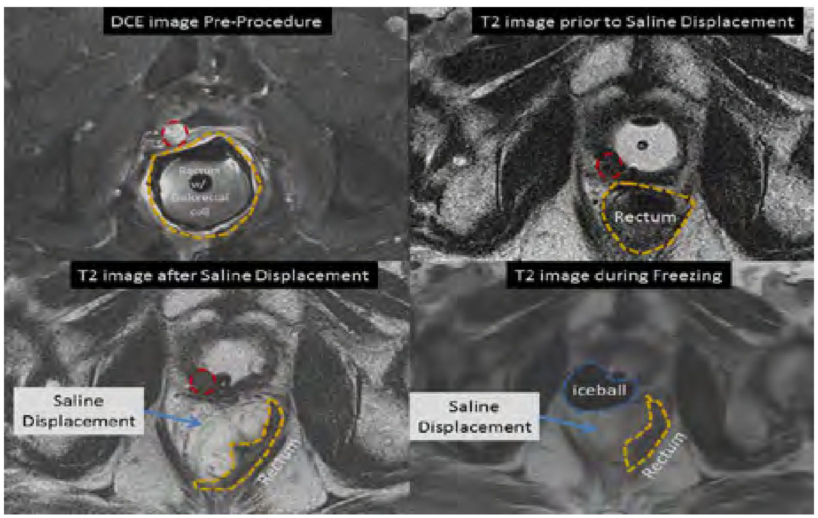

3 Tesla MR-guided Interventions in Chronic Pelvic Pain Syndromes: Initial Clinical Experience

John Morelli[1], Eric Williams[2], A. Lee Dellon[2], Allan Belzberg[3], John Carrino[1], Jonathan Lewin[1], Jan Fritz[1]

[1]The Russell H. Morgan Department of Radiology and Radiological Science, [2]Department of Plastic and Reconstructive Surgery, [3]Department of Neurosurgery, Johns Hopkins University School of Medicine

Purpose: To assess the feasibility of 3 Tesla MR-guided diagnostic and therapeutic injections for the management of chronic pelvic pain syndromes.

Materials & Methods: 28 consecutive neuropathic pelvic pain interventional MRI procedures performed on a 70 cm wide-bore 3 Tesla MRI system (Magnetom Skyra, Siemens Healthcare) were retrospectively assessed. Peripheral nerve blocks were performed with steroid and local anesthetic for diagnostic purposes (3 ml total volume) and injections of the piriformis muscle for diagnosis or treatment. Technical success of nerve blocks was defined as demonstration of the injectant surrounding the targeted nerve on post-procedural MR images. Anesthetic response was defined as the occurrence of anesthesia in the respective nerve distribution within 1 hour. For muscle injections, technical success was defined as intra-muscular accumulation of the injectant without extra-muscular spread. Pain response was assessed on a standard 1-10 visual analog scale before and after the procedure. Clinical and procedural records were examined for evidence of complications.

Results: A total of 21 diagnostic perineural injections with local anesthetic were performed including sciatic (n=7), pudendal (n=5), posterior (PFCN, n=4) and lateral (LFCN, n=3) femoral cutaneous, obturator (n=1), and genitofemoral (n=1) nerve blocks. All (21/21, 100%) were technically successful; however, 1 PFCN and 1 pudendal nerve block lacked anesthetic response (2/21, 10%). Concomitant anesthesia in the sciatic distribution was noted in 1 of the 4 PFCN blocks, and motor weakness was observed following 1 of 7 sciatic nerve blocks. 6 therapeutic injections of the piriformis were performed with botulinum toxin or steroids, whereas 1 diagnostic piriformis injection was performed with local anesthetic. All piriformis injections were technically successful. No complications occurred.

Conclusion: 3 Tesla MRI is technically feasible for guidance of pelvic perineural and intramuscular injections with a high technical success rate. High resolution MRI enables accurate and reliable identification of pelvic peripheral nerves and is advantageous due to a lack of ionizing radiation and direct visualization of the injectant.

Clinical Significance: High resolution 3 Tesla interventional MRI enables successful diagnostic and therapeutic perineural and intramuscular injections for the management of chronic pelvic pain syndromes.

MR-guided active catheter tracking for gynecologic brachytherapy interventions

Ehud J. Schmidt[1], Wei Wang[1,2], Zion T. H. Tse[3], Wolfgang Loew[4], Charles L. Dumoulin[4], Ravi T. Seethamraju[5], Tina Kapur[1], Robert A. Cormack[2] and Akila N. Viswanathan[2]. [1]Radiology & [2] Radiation Oncology, Brigham & Women's Hospital, [3]Engineering, Univ. of Georgia, [4]Radiology, Cincinnati Children's Med. Ctr., [5]Siemens Healthcare

Background: MRI is increasingly used for radiation therapy, due to the improved visualization of the tumor and its surroundings. In MRI-guided interstitial radiation therapy (brachytherapy), treatment outcomes may improve via placement of catheters (the radioactive source holder) into selected regions in or around the tumor and precise identification of the catheter trajectories after placement (fig.1A), with maximum dose provided to the tumor, and minimum irradiation of surrounding tissues . The catheters (fig.1B), which are filled with MR-compatible metallic needles, can be passively tracked, but this process is time-consuming (~1 minute/frame) and relatively inaccurate (~3x3x5mm^3 resolution). Active MR-Tracking [1,2] is challenging because a) the metallic needles in the catheter lead to static (B_0) and RF (B_1) magnetic field in-homogeneities which are exacerbated by the close proximity of 10-30 needles; b) RF currents induced on metal surfaces can distort imaging and cause heating. Our purpose was to enable accurate real-time tracking of the metallic needle, improving the accuracy and speed of MRI-guided clinical interventions.

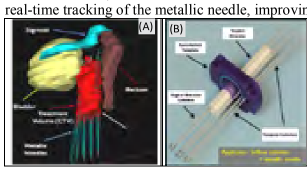

Fig.1: Cervical cancer brachytherapy. (A) The goal of brachytherapy, which is administered after patients have already received external beam radiation, is to deliver a large dose of radiation to the treatment volume, so as to kill residual tumor, while not irradiating surrounding critical structures, such as the sigmoid or rectum. This requires well-controlled catheter placement; (B). Radiation is delivered in hollow plastic tubes (catheters), which are driven through tissue using stiff metallic needles (stylets). Complications for active MRI guidance result from 20-30 closely placed metallic structures. In addition, tracking based on the position and orientation of the proximal end of the catheter is in-accurate due to catheter bending as they are pushed through stiff muscle tissue.

Fig 2: (A) Groves were carved into the surface of the needle for mounting tracking coils (yellow arrows); (B) Each coil was built on a double-layered flexible printed circuit sheet, consisting of four rectangular conductive loops; (C) The modified needle fits into the original hollow plastic brachytherapy catheter.

Method: Three micro-coils were built onto flexible printed circuits and mounted on the surface of a machined brachytherapy needle (Fig. 2). The microcoils were connected to an 8-channel receiver. The coil design was optimized by modeling the receive sensitivity (B_1^-) of different coil configurations placed on metal. 3D tracking coil positions were measured by an MR-tracking sequence, implemented on a Siemens 3T scanner. Phase-field dithering (PFD) was integrated to suppress the effects of B_1 and background inhomogeneities[2]. The tracked coil positions (resolution: 0.6 × 0.6 × 0.6 mm^3; 40 updates/sec) were continuously transferred to an external workstation for real-time visualization. The system was tested in a phantom and then used in three clinical procedures.

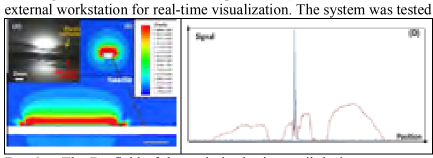

Fig. 3: (A) A sagittal MR image of the tracking coil mounted on the metallic needle, showing that a strong signal can be obtained 3-4mm away from the needle surface; (B) Axial view and (C) sagittal views of the B_1^- field simulation carried out with the coil immersed in a saline solution at 123 MHz (3T) using a finite element method. (D)Comparison of tracking signals before (red) and after (blue) phase field dithering (PFD) was applied. PFD allowed for high SNR peak localization.

Results: The B_1^- field of the optimized micro-coil design was perpendicular to the needle surface, with its profile extending beyond the region where the susceptibility-induced B_0 gradient was larger than the gradient applied by the tracking sequence (~ 2 mm from the surface[3]) (Fig. 3A-C). This field profile was still adequately spatially localized (3mm), which is essential for accurate tracking. PFD provided a sharp signal peak by eliminating the broad signal arising from coupling to neighboring metallic needles (Fig. 3D)

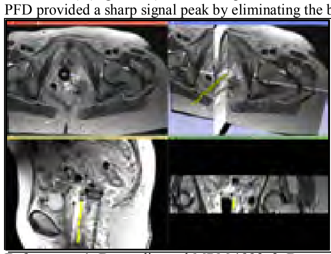

Fig. 4: 3D rendering and three orthogonal views of one needle trajectory (in yellow) overlaid on the 3D turbo spin echo images of the patient pelvis. The trajectory was reconstructed by tracking the positions of the tip coil during needle pull-out.

Patient Study: Active MR-tracking was conducted for catheter placement in an adeno-carcinoma patient during insertion and pull-out of two needles. The catheter tip position/ orientation was displayed on pre-acquired 3D images, which was used as a guide for the physician to place needles into the patient during the procedure. After catheter placement, needle trajectories were reconstructed by continuously tracking the distal micro-coil position during pull-out (Fig. 4).

Conclusion: For the first time[4], a metallic needle was actively MR -tracked in a clinical case. This method facilitates accurate and fast catheter insertion and enables improved targeting in radiation therapy. This approach can be used in interventions requiring metallic devices (guide-wires, cannulas, trocars).

References: 1. Dumoulin et al.MRM 1993. 2. Dumoulin et al. MRM 2010. 3. Müller-Bierl et al. Med Phys. 2004. 4. Wang et al. MRM 2014 (in press)

MRI endoscopy: a path to high resolution parametric imaging and intervention

Paul A Bottomley, Yi Zhang, Guan Wang, M Arcan Erturk, and Shashank S. Hegde
Division of MR Research, Dept. of Radiology & Radiological Sciences, Johns Hopkins University, Baltimore, MD, USA.

The ability to visualize anatomy with MRI at a spatial resolution of <100µm is currently unachievable in human-compatible scan-times with non-invasive external detectors, in any body-sized scanner at any field strength. Only with invasive internal detector coils can such resolution be realized[1-3]. However, the sacrifice of non-invasiveness raises the bar on requiring that the technology provide a unique or added value to justify the incursion.

Fig. 1: 50µm IVMRI of a human iliac lesion at 7T.

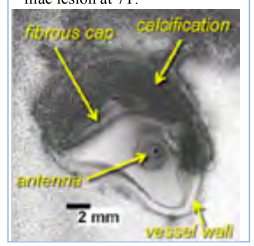

Like optical endoscopy, MRI endoscopy provides images from a frame-of-reference intrinsically locked–or at least transposed to, the MRI probe, except that it can see through vessel walls and adjacent tissues[2]. At 3T, a nitinol guidewire-based intra-vascular (IV) MRI endoscope can identify atherosclerotic lesions at 300µm resolution and 2 frame/s as the device is advanced, and provide follow-up 80µm IVMRI of suspected vascular pathologies[2]. Our goals are to develop: (i) a novel, safe, minimally-invasive, fast, high-resolution, transluminal cardio-vascular imaging modality, with lesion-specific contrast for assessing and monitoring disease status and progression; and (ii) provide a means of precision targeted therapy delivery.

Atherosclerosis is a prevalent factor in cardiovascular disease with consequences that include cerebral and myocardial infarction. It presents an obvious potential application for IVMRI, not only for identifying possibly dangerous lesions, but also for evaluating the efficacy of experimental therapies, diets etc. Existing catheter or guidewire-based imaging modalities have only limited capabilities for measuring factors relevant to disease classification, identifying a plaque's content and assessing its stability. Working at 7T, we have recently achieved spatial resolution of 50µm and less[1] (Fig. 1), which could enable measurement of the thickness of a plaque's fibrous cap as a predictor of its vulnerability to rupture and cause events[4]. The detection of mobile lipid contents with chemical-selective MRI of fat and water components (Fig. 2)[5] could also provide a biomarker for what happens when a lesion does rupture.

Fig. 2: (a) Water & (b) fat 3T endoscopic images from a diseased human iliac specimen obtained by the Dixon method.

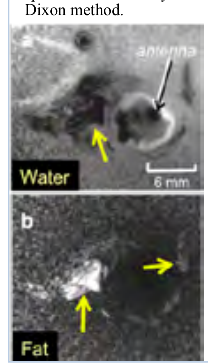

Fig. 3: (a) 80µm *in vivo* 3T endoscopic MRI from rabbit aorta, (b) reconstructed after 2.5-fold under-sampling.

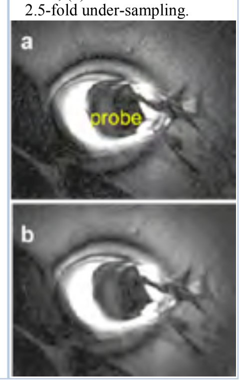

We are developing both delivery catheter and thermal ablation systems to investigate the potential for IVMRI-guided, precision-targeted therapy delivery for intra- and extra-vascular applications. Key to IVMRI's practical utility and success will be its speed and specificity, for which we are adapting new sparse sampling and reconstruction methods[6]. These reduce the number of spatial encoding steps, accelerating acquisition by the same factor, provided that the reconstruction can keep up (Fig. 3).

References: (1) Erturk MA et al, Magn Reson Med 2012; 68: 980. (2) Sathyanarayana S et al, JACC Card Im. 2010; 3:1158-1165. (3) El-Sharkawy AM et al. Med Phys 2008; 35:1995. (4) Burke AP et al, N Engl J Med 1997; 336:1276. (5) Dixon WT, Radiol 1984 153: 189. (6)Lustig et. al, Magn Reson Med, 2007; 58:1182.
Supported by NIH grant R01 EB007829.

In vivo MR imaging of porcine gastric ulcer model using intra-cavitary RF coil for MR-endoscope system

Yuichiro Matsuoka [1,2], Yoshinori Morita [3], Etsuko Kumamoto [4], Hiromu Kutsumi [2], Takeshi Azuma [2], Kagayaki Kuroda [5]
1 Center for Information and Neural Networks (CiNet), National Institute of Information and Communications Technology (NICT)
2 Department of Internal Medicine, Kobe University Graduate School of Medicine
3 Department of Gastroenterology, Kobe University School of Medicine
4 Information Science and Technology Center, Kobe University
5 School of Information Science and Technology, Tokai University

Purpose

To improve the accuracy of endoscopy and endoscopic surgeries, we have developed a magnetic resonance- (MR) endoscope system by integrating the endoscope into magnetic resonance imaging (MRI). For high-resolution MR imaging of a cross-sectional structure of the gastrointestinal (GI) tract, an intra-cavitary RF coil[1] has been developed to be inserted into the GI tract through the mouth. In addition, a navigation software[2] has been also developed to show both the MR images and an endoscopic view. We examined the feasibility of MR imaging of a gastric ulcer model in a pig in vivo using this coil and the navigation software for the MR-endoscope system.

Materials and Methods

We used a 1.5-T MRI (GE Healthcare) and a receive-only intra-cavitary RF coil (2-turn flexible surface coil with about 40×50 mm). The gastric ulcer models in pig (34 kg), which were formed by endoscopic surgeries just before MRI examination, were observed by an MR-compatible endoscope. In addition, their coordinates in the MRI system were measured using a tracking device[3] (EndoScout, Robin Medical, Inc.) with the navigation. The intra-cavitary RF coil was inserted into the stomach through the mouth and placed near the ulcer regions. The ulcer model's coordinates were applied to the setting of the MR scan plane and region, and then MR images were obtained by T1- and T2-weighted FSE with FOV; 8×8 cm, slice thickness; 3 mm, acquisition matrix; 256×256 for T1FSE and 256×160 for T2FSE.

Results

The MRI scan range was derived from the ulcer model's coordinates using the navigation software. The gastric ulcers were visualized with both T1- and T2-weighted images as a defect of mucosa to submucosa. A 3D-rendered image created by multi-slice MR images showed the relative position of the ulcer models, and it was comparable to the endoscopic view.

Conclusion

The feasibility of visualizing gastric ulcers through the MR-endoscope system was demonstrated. A quick and precise adjustment of the tuning and matching of the intra-cavitary RF coil placed in the GI tract should be established.

References

[1] H. Yoshinaka, et al., J Gastroenterol 2010;45:600-607
[2] A. Takahashi, et al., Proc. 22nd ISMRM 2014; 2324
[3] Y. Matsuoka, et al., Proc. 20th ISMRM 2012; 1590

A Hydrostatically Actuated Robotic System for Real-time MRI-guided Interventions

Rashid Yasin[1], Samantha Mikaiel[2], Kyung Sung[2], David Lu[2], Holden H. Wu[2], Tsu-Chin Tsao[1]
[1]*Mechanical Engineering and* [2]*Radiology, University of California, Los Angeles, CA, USA*

Purpose: MRI can provide extraordinary image contrast for real-time visualization and guidance of minimally invasive interventions. However, the closed bore of state-of-the-art MRI scanners limits continuous interventional access to the patient. In this work, we propose and evaluate a new robotic system based on hydrostatic actuation that enables remote control of interventional devices inside the scanner bore under real-time MRI guidance.

Figure 1. (a) Operator manipulates master controls at end of table with slave actuators and devices inside the MRI scanner bore. (b) 2-DOF prototype for angular positioning and (c) 1-DOF prototype for linear translation of interventional devices. (d) Real-time MRI along one axis of motion for 2-DOF angular positioning and (e) Real-time MRI during 1-DOF insertion of a biopsy needle in phantoms.

Material and Methods: [*System Design*] We developed an MR-compatible master-slave robotic system using low-pressure water-based hydrostatic actuators. In contrast to other pneumatic or hydraulic solutions that require complicated and expensive high-pressure valves, our system uses pairs of pistons connected to closed fluid channels to transmit force and displacement into and out of the scanner bore. Polypropylene was used to reduce construction cost and avoid adverse effects on imaging. While the system can be actuated by motors using long connections that run outside of the scanner room, it has the additional benefit of being able to be actuated completely by hand. This allows a physician to manipulate devices inside the bore from the end of the patient table with short fluid lines of only three to four feet, which can provide haptic feedback with minimal loss (Fig. 1a). Two prototypes were constructed to separately evaluate 2-degree-of-freedom (DOF) control of angular positioning (Fig. 1b) and 1-DOF control of linear translation (Fig. 1c). [*System Characterization*] A trapezoidal displacement profile was used to emulate device translation. The system tested comprised two plastic syringes connected by 5.3 m tubing, where each was measured by a 0.0006 mm resolution laser displacement sensor and the input end driven by a position feedback controlled voice coil actuator. [*Experiments*] Phantom experiments were performed on a 3 T MRI scanner (TIM Trio, Siemens). Gradient echo (GRE) and fast spin echo scans were obtained to assess image artifacts and signal-to-noise ratio (SNR). Real-time GRE scans guided manual control of 2-DOF positioning and 1-DOF insertion of an MR-compatible biopsy needle (Cook) in phantoms (Fig. 1).

Results: [*System Characterization*] The voice coil actuator under proportional integral feedback control achieved steady state error less than 0.025 mm on the input side while the end effector on the output side of fluid transmission line created error less than 1.27 mm. This confirms our low-pressure system's ability in achieving a tight accuracy inside the scanner bore via a long tube and external control. [*Experiments*] No image artifacts were observed and SNR differences were negligible with the robotic system inside the scanner bore. Both prototypes could be easily manipulated by an operator at the end of the table to position and insert a biopsy needle in phantoms (Fig. 1).

Conclusion: The proposed hydrostatic robotic system is able to transmit force and displacement repeatedly into the scanner bore without image degradation. Our system is inherently MR-compatible and is simple and cheap to develop and implement. This can potentially provide physicians continuous access to patients during real-time MRI-guided interventions with improved visualization and accuracy.

DESIGN, DEVELOPMENT, AND CONTROL OF A 3-AXIS-MRI-COMPATIBLE ROBOT FOR REMOTE CATHETER NAVIGATION

Mohammad Ali Tavallaei,[1,2] Mike Konstantine Lavdas[1] and Maria Drangova[1,2,3]
[1]Robarts Research Institute, [2]Biomedical Engineering Graduate Program, [3]Dept. of Medical Biophysics, Western University, London Ontario, Canada.

PURPOSE: MRI guided minimally invasive therapy in conventional closed bore scanners is hindered by limited patient access, requirement of MRI compatible viewing and control panels, and acoustic noise. To overcome these impediments we have developed an MRI compatible robot that allows remote catheter navigation inside the magnet bore with 3 degrees of freedom (DOF) in catheter motion.

METHODS: The master-slave robotic system (Fig. 1) measures the motions imparted on a conventional catheter by the user (master) and relays them to a slave within the scanner room, replicating this motion on a patient catheter inside the magnet bore. The slave comprises a catheter manipulator (CM) and a knob actuator (KA). A versatile mount allows the CM to be positioned and orientated arbitrarily at the catheter point of entry. The CM incorporates a differential gear mechanism and a set of rollers that grip the patient catheter. This mechanism enables radial and axial catheter manipulation while the actuators remain fixed. Components of the CM that come in contact with the catheter can be easily disconnected for replacement/sterilization. The KA comprises a rotating gantry that holds the catheter handle and uses a spring/string combination to push/pull the catheter knob/plunger. Two actuators are used in the KA – one pulls the string and another rotates the gantry in synchrony with catheter rotation to prevent catheter twisting. Non-magnetic Ultrasonic motors (USM) were used as the slave-robot actuators. A challenge specific to USMs is that they are highly time-variant, temperature dependent and nonlinear. To design a controller, first a dynamic model of the USM-driver combination was identified, linearized and validated. Using this model a robust controller was designed based on the Lyapunov function redesign method and implemented in real-time on custom designed electronic hardware. To evaluate the controller's performance in positioning control, the step response was analyzed. To evaluate the controller's performance for dynamic motion control, sinusoidal motion profiles with amplitudes of 1 rad at frequencies of 0.25 Hz, 0.33 Hz, 0.5 Hz, and 1 Hz under a load of 5 Ncm were prescribed. Each profile was executed continuously over 5 minutes. The delay between the reference and encoder position was also characterized.

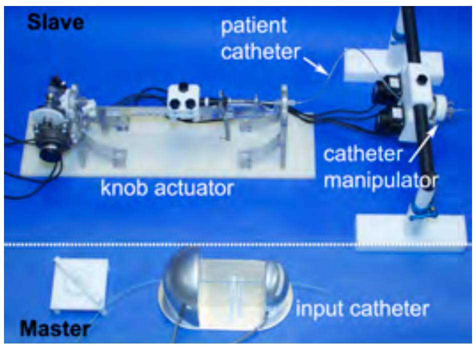

Fig. 1. Master and slave components of the system.

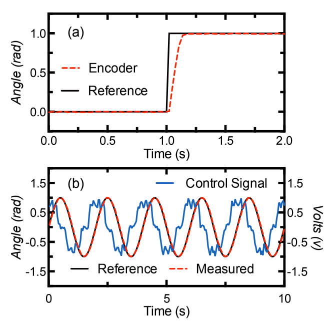

Fig. 2. a) Step response, b) Dynamic response.

RESULTS: The step response (Fig. 2a) showed no overshoot nor any offset, proving that the controller is capable of accurate position control. The dynamic response evaluation showed excellent agreement between reference and motor position (Fig. 2b), with the worst-case normalized root mean square error smaller than 5%. The controller was capable of maintaining this performance for at least 5 minutes of continuous operation. The delay between the reference and the encoder position was measured to be 25 ms.

CONCLUSIONS: We have developed a robot that allows for remote manipulation of a catheter with 3 DOF inside the magnet bore. The novel control system allows for accurate, robust and dynamic control of the USM motors that actuate the robot. Further evaluation is needed to demonstrate the robot's efficacy and safety. While specifically developed for catheter manipulation, the robust control system and differential gear manipulator have applications in all areas of MR guided intervention that require precise dynamic positioning.

Magnetic resonance electrical impedance tomography for assessment of electric field distribution during tissue electroporation

Kranjc M.[1], Markelc B.[2], Bajd F.[3], Cemazar M.[2], Sersa I.[3], Blagus T.[2], Miklavcic D[1].
[1]University of Ljubljana, Faculty of Electrical Engineering, Slovenia
[2]Institute of Oncology Ljubljana, Slovenia
[3]Institut "Jozef Stefan", Ljubljana, Slovenia

The purpose of this study was to investigate the feasibility of MREIT technique [1] for *in situ* monitoring of electric field distribution during *in vivo* electroporation of mouse tumors in order to predict reversibly electroporated tumor areas.

All experiments received institutional animal care and use committee approval. Group 1 consisted of eight tumors which were used for determination of predicted area of reversibly electroporated tumor cells by means of MREIT using a 2.35 MRI scanner. In addition, T1-weighted images of tumors were acquired to determine entrapment of contrast agent within the reversibly electroporated area. A correlation between predicted reversible electroporated tumor areas as obtained by MREIT and areas of entrapped MR contrast agent was evaluated to verify the accuracy of the prediction. Group 2 consisted of seven tumors that were used for validation of radiologic imaging with histopathological staining. Histological analysis results were then compared with predicted reversible electroporated tumor areas from group 1.

Coverage of tumors with reversibly electroporated tumor cells obtained by MREIT (Fig. 1a) and fraction of tumors with entrapped MR contrast agent were correlated (Pearson, r = 0.956, p = 0.005) as shown on Fig. 1b. Obtained coverages and fractions were statistically similar to fraction of tumors with entrapped fluorescent dye (ANOVA, p = 0.11).

Our *in vivo* study showed that MREIT can be used for the assessment of electric field distribution *in situ* during tissue electroporation. As accurate coverage of treated tissue with a sufficiently large electric field represents one of the most important conditions for successful electroporation [2], electric field distribution determined by means of MREIT could be used as predictive factor of electrochemotherapy and ireversible electroporation tissue ablation outcome.

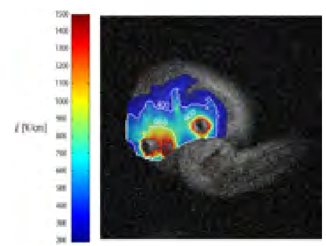
a

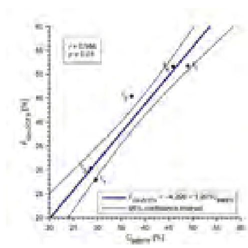
b

Fig 1a: The electric field distribution in the tumor obtained by MREIT superimposed to the T1-wighted image acquired before the application of electric pulses. Fig 1b: Scatterplot of the coverage of tumors (t_{1-5}) with the electric field of reversible electroporation (C_{MREIT}) and Gd-DOTA cell entrapment ($F_{Gd\text{-}DOTA}$).

[1] Kranjc *et al.*, Magnetic resonance electrical impedance tomography for monitoring electric field distribution during tissue electroporation, IEEE T. Med. Imaging 30: 1771-1778, 2011.
[2] Miklavcic *et al*., Importance of tumour coverage by sufficiently high local electric field for effective electrochemotherapy, Eur J Cancer Suppl, 2006;4(11):45–51.

The Challenges of Healthcare Transformation on iMRI

Jonathan S. Lewin, MD, FACR, FISMRM
Johns Hopkins Medicine
Baltimore, Maryland, USA

The funding of healthcare has become a significant issue in many countries around the world. In the US, there are ongoing economic forces that create both opportunities and challenges for interventional MRI. These forces have come to a head in the US in the current environment of "healthcare transformation", manifested through the Affordable Care Act (sometimes known as "Obamacare"), along with a number of other insurance and healthcare delivery changes. The underlying reason for these changes is based on trends in total US spending on healthcare, which is projected to nearly double by the year 2020, rising from $2.6 trillion to $4.8 trillion dollars. In 2020 it is estimated that it will consume almost 20% of GDP, twice the average of European countries. The economic pressure that this presents to US healthcare will demand payment reform, and will require "bending the curve" in the trend-line of current healthcare spending. In an attempted solution to this challenge, the Affordable Care Act is primarily structured as a vehicle for insurance reform – guaranteeing coverage for a broader range of the US population – built on the premise that approaching universal coverage and encouraging competition will result in lower costs and improved quality. In addition to changes on the payment side, the Affordable Care Act also attempts to promote reform of the healthcare delivery system, intended to foster innovation in how healthcare is delivered while increasing provider accountability.

For expensive advanced technology, this increased emphasis on cost reduction will present several challenges. Historically, many medical institutions in the US competed for patients by having the most advanced technology available. The increased emphasis on cost, along with efforts to decrease utilization of more expensive tests and procedures, has already created a downward pressure on the acquisition of high-tech devices. For an expensive and "cutting edge" field such as iMRI, the ease with which institutions will be able to purchase and install iMRI suites will be challenged. It will become an imperative for the iMRI research community to show the actual value of these procedures, and to demonstrate that the advantages of guiding procedures with MRI justifies any incremental costs over guidance with other imaging modalities.

Several aspects of healthcare transformation will present opportunities for iMRI techniques, as well. With increased emphasis on health of entire populations and the development of payment methods that more accurately reflect the cost of care across the entire continuum, there will be increased opportunity for minimally-invasive procedures to flourish. Healthcare institutions will increasingly value the diminished need for lengthy hospitalizations associated with open alternatives. The ability to limit the number of treatments, as seen with MRI monitoring of thermal ablation to cancer and other disorders, for example, provides an opportunity for the research community to demonstrate the cost savings that can be attained by providing the right care at the right time in the right healthcare setting. In the evolving healthcare environment, the need for repeated or additional procedures will be seen as additional expense, and not as a revenue opportunity. The healthcare delivery system will be better aligned with the needs of patients.

In summary, financial pressures on healthcare delivery, already present in the United Kingdom, Europe, and many other countries, have been increasingly seen in US healthcare and have resulted in a number of shifts in payment and delivery systems. While impact on the purchase of expensive technology may result in challenges for iMRI, the opportunities provided by shifting from inpatient to outpatient procedures, replacing open surgery with minimally invasive interventions, and shortening the post-treatment recovery period, provide tremendous opportunities for iMRI in this new environment. It is the responsibility of the iMRI research community to demonstrate the value of our techniques, both in the improvement in the care of our patients and in the economic benefit that is brought to bear through these technologies.

Global Paradigms for Open Science Assessment of Technologies in Image-Guided Interventions

Keyvan Farahani

Division of Cancer Treatment and Diagnosis, National Cancer Institute, Bethesda, MD, USA

Image-guided interventions (IGI) and Image Guided Drug Delivery (IGDD) in oncology represent areas of convergence in biomedical science where physical scientists and engineers partner with cancer biologists and oncologists to develop minimally invasive methods for diagnosis and treatment of cancer. The IGI research community, is however, very diverse and technology-driven. While these characteristics are advantageous for growth of the field, ironically they decelerate development of good practices and standards and translation of the most promising technologies to the clinic. This presentation outlines a number of global community-based approaches taken to help assess technologies in IGI, useful in development of standards toward their clinical translation. Examples are drawn from MR image segmentation and MR-guided focused ultrasound.

Focused ultrasound – Update on clinical applications

Wladyslaw M. Gedroyc

St Mary's Hospital, Imperial College London, London, UK

This lecture is an introduction to the areas of clinical work that are happening using MR guided focused ultrasound around the world. The larger details of these aspect s will not be provided in this lecture because the lectures that will follow will fill in these gaps in many of these applications. I will aim to provide details of the use of MR guided focused ultrasound and the overall description of which patients are suitable for this therapy in the following body areas. Brief descriptions will be provided of MR guided focused ultrasound utilisation in fibroids, bony tumours including secondaries, treatment of facet joints, liver applications, prostate cancer, brain applications, soft tissue applications and drug activation programs. The time provided for this lecture is insufficient to provide substantial detail in all of these areas but hopefully the information provided will act as a stimulus to further investigation of this field.

MR-guided focused ultrasound in drug delivery

Chrit Moonen

UMC Utrecht, the Netherlands

OBJECTIVES

The primary goal of image guided drug delivery is to increase the therapeutic index of potent, often toxic treatments through personalized image-guided treatment, ultimately decreasing adverse effects of drugs by better controlling the pharmacokinetics (PK) and pharmacodynamics (PD) of therapy. This can be achieved by locally triggering the deposition or activation of drugs via image guided ultrasound.

INTRODUCTION

Ultrasound can be focused within a region with a diameter of about 1 mm. The bio-effects of ultrasound can lead to local tissue heating, cavitation, and radiation force, which can be used for 1) local drug release from nanocarriers circulating in the blood, 2) increased extravasation of drugs and/or carriers, and 3) enhanced diffusivity of drugs. When using nanocarriers sensitive to mechanical forces or to temperature, their content can be released locally. Thermo-sensitive liposomes have been suggested for local drug release in combination with local hyperthermia more than 30 years ago. Microbubbles may be designed specifically to enhance cavitation effects. Real-time imaging methods, such as magnetic resonance, optical and ultrasound imaging have led to novel insights and methods for ultrasound triggered drug delivery. Image guidance of ultrasound can be used for: 1) target identification and characterization; 2) spatio-temporal guidance of actions to release or activate the drugs and/or permeabilize membranes; 3) evaluation of biodistribution, pharmacokinetics and pharmacodynamics; 4) Physiological read-outs to evaluate the therapeutic efficacy.

METHODS

Thermosensitive liposomes have been suggested for local drug release in combination with local hyperthermia more than 30 years ago. Liposomes may carry both hydrophilic and hydrophobic drugs in their aqueous interior and lipid bilayer membrane, respectively. Nanoparticles may be designed specifically to enhance cavitation effects. Most microbubbles consist of air- or perfluorocarbon-filled microsphere stabilized by an albumin or lipid shell with a size in the range of 1-10 µm.

RESULTS

Several recent publications have shown that ultrasound triggered delivery is feasible (reviewed by 1,2). Real-time imaging methods, such as Magnetic Resonance, optical and ultrasound imaging have lead to novel insights and methods for ultrasound triggered drug delivery. Image guidance of ultrasound has been used to locally release or activate the drugs and/or permeabilize barriers such as the Blood-Brain-Barrier, the endothelial cell layer, cell membranes, and to evaluate the therapeutic efficacy.

CONCLUSION

The bio-effects of (Focused) Ultrasound can be used for various aspects of local drug delivery and cellular uptake from circulating nanocarriers. MRI guided FUS is particularly useful in case of thermo-sensitive drug nanocarriers. Real-time ultrasound and optical imaging are leading to new insights with respect to the uptake mechanisms and ultrasound parameters to increase the therapeutic window.

REFERENCES

1) Deckers et al. JCR 2010, Lentacker et al. ADDR 2014
2) Frenkel et al. Adv Drug Del Rev 2008

Initial Clinical Experience with a Dedicated MR-guided High-Intensity Focused Ultrasound System for Treatment of Breast Cancer

F.M. Knuttel[1], L.G. Merckel[1], R.H.R. Deckers[2], C.T.W. Moonen[2], L.W Bartels[2], M.A.A.J. van den Bosch[1]

[1] *Department of Radiology, University Medical Center Utrecht, Utrecht, The Netherlands*
[2] *Image Sciences Institute, University Medical Center Utrecht, Utrecht, The Netherlands*

Purpose
To assess the safety and treatment accuracy of Magnetic Resonance-guided High Intensity Focused Ultrasound (MR-HIFU) ablation in breast cancer patients, using a novel dedicated breast system.

Material and methods
Patients with invasive breast cancer of ≥ 1 cm in diameter underwent partial tumor ablation, 48 hours to one week prior to surgery. Treatments were performed using a dedicated breast platform (Sonalleve, Philips Healthcare, Vantaa, Finland). The system contains eight circumferentially positioned ultrasound modules with 32 elements each, embedded in a water-filled table top (figure 1 and 2). The system is integrated in a clinical 1.5 T MRI scanner. Proton resonance frequency shift (PRFS) with multi-baseline correction of respiration-induced field disturbances during sonications was used for thermometry. Patients received procedural sedation during treatments. Treatment accuracy was determined by assessing the location of the actual focus as compared to the planned focus, based on thermal maps. The size and location of the area that reached a temperature of > 56 degrees Celsius was determined. Furthermore, the size of thermal damage was assessed at histopathology. Safety was assessed by monitoring adverse events until patients underwent surgical resection.

Results
Ten female patients with histopathologically proven invasive breast cancer underwent MR-HIFU ablation. Three minor adverse events were observed, no major adverse events occurred. On average, the actual focal point was within one voxel (1.7 mm) of the planned focal point. In 5 patients, clear thermal damage, with a size comparable to the number and extent of applied sonications was found. In one patient, sonications were erroneously aborted and did not lead to clear thermal damage. One patient refused to undergo surgery. In one patient, the tumor was unexpectedly not in reach of the HIFU beams, sonications were located in the adjacent adipose tissue. In one patient, no thermal damage was observed in the surgical specimen, retrospectively this was due to deviation of the ablation focus. The results of the last patient are not analyzed yet. No non-perfused volumes were visible on contract-enhanced MRI after treatments.

Conclusion
MR-HIFU ablation with the dedicated breast system is safe and accurate, this feasibility study let to technical improvements after every treated patient. MR-HIFU is a promising technique for non-invasive tumor ablation.

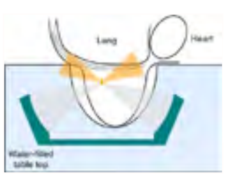

Figure 1 Schematic overview of the dedicated breast system, providing lateral sonications.

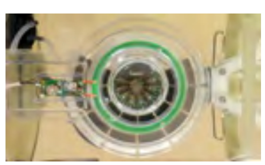
Figure 2 Breast cup of the dedicated breast system, with eight circumferentially positioned transducers.

Real-time imaging for MR-guided interventions – where is the current limitation?

Shuo Zhang, PhD

Biomedizinische NMR Forschungs GmbH at the Max-Planck-Institute for Biophysical Chemistry, Göttingen, Germany

Minimally invasive surgical and therapeutic treatment is targeting increasingly complex processes. By providing both morphological and functional information of organs and tissues without ionizing radiation exposure, magnetic resonance imaging (MRI) facilitates traditional procedures while enabling new approaches. Currently, preliminary clinical and preclinical demonstrations of interventional MRI show great promise [1].

Due to their intrinsic dynamic properties, real-time MR-guided approaches may represent the key for almost all interventional applications, including surgical interventions (e.g., biopsy needle, guide-wire, cannula, trocar), drug distribution, tissue characterization and temperature changes. A recent advantageous development for real-time MRI is the advent of regularized nonlinear inverse (NLINV) reconstruction with its use of multiple receiver coils for parallel imaging. Furthermore, the technique efficiently exploits the temporal continuity of a dynamic process (e.g., movement, contrast changes) using highly undersampled radial gradient-echo MRI sequences at millisecond temporal resolution [2-4].

Although the principle imaging capabilities for real-time MR guidance have already been described for clinical MRI systems [5], the challenge remains how to bring the technology into clinical practice. In addition to the obvious tradeoffs between imaging parameters (e.g., temporal vs spatial resolution), this presentation will cover a range of limitations and challenges, from imaging speed to reconstruction delay, from motion monitoring to feedback steering, and from operational simplicity to hardware- and software accessibility.

It is foreseeable that with adequate spatial resolution, good image contrast and SNR, real-time imaging may boost MR-guided interventions to become faster and less invasive which in turn will improve treatment accuracy and enhance safety by providing continuous guidance, feedback, and assessment during the entire procedure.

[1] Kahn T, Busse H. Interventional Magnetic Resonance Imaging (Medical Radiology / Diagnostic Imaging, Reiser MF, Hricak H, Knauth M). Springer 27 Aug, 2012.

[2] Uecker M, Zhang S, Voit D, Karaus A, Merboldt KD, et al. Real-time MRI at a resolution of 20 ms. NMR Biomed 2010; 23:986-994.

[3] Zhang S, Uecker M, Voit D, Merboldt KD, and Frahm J. Real-time cardiovascular magnetic resonance at high temporal resolution: radial FLASH with nonlinear inverse reconstruction. J Cardiovasc Magn Reson 2010; 12:39-46.

[4] Uecker M, Zhang S, Voit D, Merboldt KD, Frahm J. Real-time MRI – Recent advances using radial FLASH. Imaging Med 2012; 4:461-476.

[5] Merboldt KD, Uecker M, Voit D, Frahm J. Spatially encoded phase-contrast MRI-3D MRI movies of 1D and 2D structures at millisecond resolution. Magn Reson Med 2011; 66:950-956.

Interventions in a standard MR environment

M. Moche, N. Garnov, J. Fuchs, T. O. Petersen T. Kahn, H. Busse
Diagnostic and Interventional Radiology Department, Leipzig University Hospital, Leipzig, Germany

The aim of this presentation is to highlight state-of-the-art techniques, instruments, and add-on tools for performing various MR-guided interventions in a standard diagnostic MR-scanner.

Excellent soft-tissue contrast, prolonged enhancement of MR contrast agents and absence of ionizing radiation make MRI a superior modality for image-guided minimally invasive interventions. MRI interventions are still not very common when compared to CT or US procedures. The major limiting factor of using closed-bore MRI scanners for that purpose is the reduced access when the patient is in the magnet. The use of dynamic MR sequences for instrument guidance is not feasible in most cases. Even wide-bore scanners with a bore size of 70 cm often do not allow for comfortable MR fluoroscopy and scanners with magnet lengths as low as 125 cm have been discontinued. While dedicated interventional MRI systems have been installed, their distribution is limited–often to larger, specialized or academic institutions–and operating costs are high.

On the other hand, diagnostic high-field MRI systems with powerful imaging capabilities are widely available. It is much easier to transfer diagnostic information to the interventional setting when both imaging sessions are performed in the same system. A good selection of MR-compatible instruments has become available over the years. There is also a variety of strategies, from simple to sophisticated ones, that are aiming to overcome some of the limitations of closed-bore scanners. For the breast and prostate, for example, dedicated imaging coils and targeting devices are commonly used in diagnostic MR scanners. Specific solutions for other body regions, however, are relatively rare. This presentation therefore aims to present some techniques that work in other parts of the body as well.

In its simplest form, the interventionalist defines cutaneous access point and needle orientation and then approaches the lesion by iteratively controlling and readjusting the needle position inside and outside the magnet, respectively. An alternative option would be a robotic assistance system which fits into the bore. After patient, device and MRI coordinates have been registered, entry and target can be directly defined in the MR images. The system then automatically moves and orients the needle at the entry point. The needle insertion itself is still performed by the radiologist.

Another solution is an add-on navigation system outside the magnet. A fast automatic registration helps to provide a smooth workflow and accurate targeting. The combination of diagnostic image quality and high frame rates resulted in a good hand-eye coordination to navigate and insert the instrument outside the bore. At any time, the patient can be moved into the scanner for control imaging. A sterilizable flexible instrument holder prevents dislocation of the instrument but still tolerates some patient movement such as that occurring under free breathing.

In conclusion, simpler MR-guided procedures can be performed in a conventional diagnostic MR environment by using some basic instruments and techniques. More complex procedures are safely possible after implementing more advanced assistance devices.

Visualization and Navigation Techniques

H. Busse, N. Garnov, T. Kahn, M. Moche
Diagnostic and Interventional Radiology Department, Leipzig University Hospital, Leipzig, Germany

Purpose

This presentation provides an overview of clinically emerging techniques and underlying tools for the visualization and navigation of various MRI-guided procedures.

Methods and Results

MRI is widely known for its soft tissue contrast and absence of ionizing radiation but also has additional advantages for procedural guidance such as arbitrary scan geometries, relatively long contrast enhancement and therapeutic monitoring options (e. g., MR thermometry). Unlike ultrasound or CT imaging, however, MRI is generally limited by spatial confinement, need for special materials, longer acquisition times and resulting workflow issues. Therefore, proper visualization and navigation techniques are in great demand ultimately serving to improve the user's orientation, safely reach the target or apply the desired treatment.

Specific methods and materials largely depend on the type of procedure (e. g., aspiration, biopsy, drilling or ablation) as well as organ region (e. g., brain, breast, liver, prostate, musculoskeletal or cardiovascular), and range from optimized pulse sequences and user interfaces via convenient positioning and targeting devices to fully fledged tracking and navigation solutions. Special challenges are created whenever well-established technologies can simply not be used in an MRI environment, for example, instrument tracking by electromagnetic fields.

The selection of techniques and applications presented here was taken from recent reports in the literature as well as scientific contributions to this symposium.

Conclusion

Visualization and navigation techniques are at the heart of MRI guidance and contribute to the overall accuracy, safety and ease of such procedures. Developments often start as ideas and concepts from individual groups but also seem to take a concerted effort by technicians, scientists and clinicians alike to progress. The ongoing commercial involvement may help to promote the clinical translation of some promising tools and applications.

Building and Operating a Comprehensive Clinical Interventional MRI Program: Logistics, Cost-Effectiveness, and Lessons Learned

Bobbie Burrow [1,2], Hiroumi D. Kitajima [1-3], Kenny Doan [1,2], Lynn Cooper [1,2], Robin Pierson [1,2], Greg Pennington [1], Sherif G. Nour [1-3]

[1]Department of Radiology and Imaging Sciences, Emory University Hospital, Atlanta, GA, USA
[2]Interventional MRI Program, Emory University Hospital, Atlanta, GA, USA
[3]Emory University School of Medicine, Atlanta, GA, USA

Purpose: The interventional MRI community has significantly grown over the past two decades from sporadic attempts of using MRI to guide simple procedures to multiple sites performing cutting-edge research and introducing new exciting soft and hard ware developments. One of the serious challenges to this developing field is the obvious mismatch between the fast scientific developments and the relatively sluggish environment of clinical applications. The goal of this report is to share our institutional experience in building and operating a high volume comprehensive clinical interventional MRI service.

Materials and Methods: The interventional MRI program at our institution has been in place for 3 years. We evaluated the logistics of building and operating a model site for clinical MRI-guided interventions. Evaluation of the logistics of building the program included assessment of the interventional MRI suite location and capabilities, use of available space, room amenities, infection control compliance, and suite safety. Evaluation of service operations included assessment of clinical case volume, scheduling, physician time use, referral pattern evolution, mix of staff needed to support the program activities, resource sharing, and cost assessments.

Results: The interventional MRI Program at our institution utilizes 3 MRI scanners used as shared resources with the diagnostic MRI service, with one suite being the main fully-equipped interventional MRI suite. The latter utilizes a 1.5T short, wide bore system (Magnetom Espree, Siemens, Germany) and is located in the main hospital at the in-patient side next to the interventional CT and ultrasound services. The feature that we find most facilitating to the iMRI work flow is the main suite's proximity to main hospital hallways, proximity to the pre-procedure care area (PPCA), and the presence of dedicated cytopathology, drug dispensing, and nursing stations within the same area. The other 2 iMRI suites include a 3T system (Magnetom Trio, Siemens, Germany) used for prostate interventions and located next to the main iMRI suite along with another 1.5T wide bore system (Magnetom Aera, Siemens, Germany) located at the children's hospital to serve the pediatric intervention needs. We made a better use of suite space by aligning the magnet obliquely in the room to maximize the usable space behind the gantry for the interventionist and adjacent to the table for the anesthesia team. We had the lay out approved by the anesthesia team prior to construction. All pipes, gas lines, suction, power outlets, and waveguides for existing use and for potential future needs were accounted for. We consulted our infection control department to assure the capabilities to perform procedures that require a sterile environment similar to an operating room suite. Air flow into the room did have to be adjusted to meet the requirement. We set up our room with equipment that could easily be moved in and out of the suite as needed to do a terminal clean when necessary. Metal detectors were placed and individual stuff MR safety certifications were enforced for all involved personnel.

We performed a total of 453 MRI-guided interventions over 3 years of iMRI service operation. The clinical case load grew exponentially and we currently perform 3-7 MRI-guided interventions per week. There are 3 dedicated days per week for MRI guided interventions with a dedicated interventionist and a general anesthesia team. We find that scheduling 2 successive general anesthesia cases adversely affects the usage of the scanner for diagnostic imaging due to long room turn-in time. We therefore try to combine general anesthesia with conscious sedation cases on the same day to minimize scanner downtime. Referral base naturally starts with institutional referrals. We find that the implementation of the "iMRI Clinic" model significantly boosts and diversifies the referral base which has grown at our site to include regional, national, and international referrals. Patient care is supported by a clinical team, including an interventional radiologist, neurosurgeons, nurse practitioner, MR technologists, nurse anesthetist, registered nurse, medical assistant and an administrative assistant. We trained our existing MRI staff and MRI nurses to perform their duties during an IMRI procedure keeping MRI safety the most important step. We created our chargeable CPT codes to perform the exams using the existing codes. Our reimbursement rate for MRI guided interventions is approximately 25%, which surpasses our institutional reimbursement rates for other Interventional Radiology procedures. The downstream revenue generated from follow up examinations is an additional factor adding favorably to the cost effectiveness of the program.

Conclusion: The application of interventional MRI technology in a clinical environment is a reality. We have shown a model for a comprehensive, high volume, clinical interventional MRI program. Building the program requires a plan for possibly needed interventions, a clear vision for future expansion, and a careful assessment of the planned iMRI suite location. The logistics of operating a cost-effective service for MRI-guided interventions utilizing institutional shared resources are workable. Finally, creating an institutional culture of utilizing MRI for indicated interventions is fundamental to the success of iMRI programs and for the future dissemination of this technology.

MR-guided neurosurgery and brain tumor laser ablation

Alexandra J. Golby, MD, Olutayo Olubiyi, MB.ChB, MPH, Roy Torcuator MD, Laura Rigolo MS, Isaiah Norton BS.

Department of Neurosurgery Brigham and Women's Hospital
75 Francis Street Boston, MA 02115

Technological advances over the last few decades have made neurosurgical resection of brain tumors much safer and more effective. Improvements in imaging and visualization including functional imaging, advanced structural imaging such as diffusion tensor imaging (DTI), and intra-operative treatment monitoring with intra-operative MRI allow the surgeon to have a much better understanding of the anatomy and pathology as well as of the progress of the intervention. To decide whether surgery is safe for a patient with a given lesion, the surgeon requires a complete and accurate map of the complex and critical functional and structural anatomy of that individual's brain. Our group has used fMRI to perform pre-operative individual patient brain mapping in over 750 patients since 2003. Of these, 455 had language mapping, 427 motor mapping, 73 visual cortex mapping and 6 had somatosensory mapping. Over 450 patients have had DTI with tractography to define white matter tracts. Integration into clinical navigation systems for multi-modality functional navigation has been performed in the majority of cases. The volume of clinical requests for functional imaging has risen dramatically each year. The indication for awake craniotomy has been narrowed to the small subset of patients requiring this. Moreover, we have found that pre-operative fMRI/DTI can be very useful even in cases in which awake surgery is pursued; in approximately 25% of awake surgeries, mapping is either aborted, inconclusive or incomplete and having the non-invasive functional maps can allow the surgeon to proceed with more confidence.
Another challenge in brain tumor surgery results from the progressive deformation of anatomy that takes place during the surgical intervention (brain shift), making preoperative images and associated neuronavigation increasingly inaccurate. We have recently developed the Advanced Multi-Modality Image-Guided Operating (AMIGO) suite at BWH. This suite allows intraoperative image using all contemporary imaging modalities. We have built on our history of over 1000 craniotomies in the original first intra-operative MRT (double donut) with active clinical programs in brain tumor resection and biopsy, laser hyperthermia ablation, transphenoidal pituitary resection, and functional neurosurgery. Laser hyperthermia provides an example of true image guided neurosurgery in which imaging forms the basis of treatment targeting and monitoring. Further advance in minimally invasive neurosurgery will depend critically on multi-modal pre-operative and intra-operative imaging. Together these methods allow the evaluation of surgical risks, selection of the best method of intervention, and planning of the safest surgical approach.

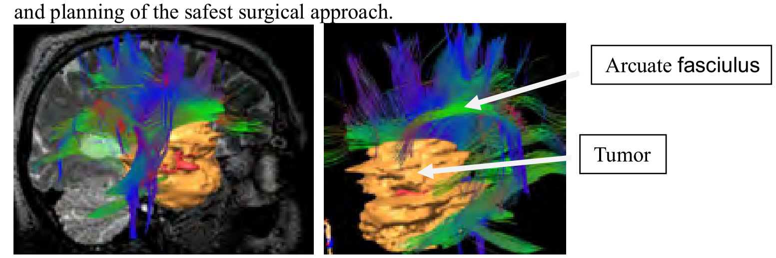

MR-guided neurosurgery and fiber tracking

Christopher Nimsky

Department of Neurosurgery, Philipps-University Marburg, Marburg, Germany

Meanwhile diffusion tensor imaging (DTI) is established in the clinical routine in neurosurgery. Fiber tracking is probably the most clinically appealing and understandable technique for representing major white matter tracts. Due to multiple free software packages, as well as the integration of fiber tracking modules in the major commercial navigation software systems, DTI-based fiber tracking has a broad application in Neurosurgery.

However, the DTI approach to model the complex anatomical information has some distinct limitations. Diffusion weighted imaging is inherently a noise-sensitive and artefact-prone MRI technique. To obtain a reliable representation of major white matter tracts the following three steps are required in the process of diffusion MRI fiber tracking: the acquisition of appropriate diffusion weighted image data, the correct estimations of fiber orientations, and finally the appropriate tracking algorithm.

Despite of its fundamental limitations DTI-based tractography is still the most widely applied tractography method in neurosurgical settings to delineate major white matter tracts. Correct identification of areas of fiber crossings is not possible by standard DTI because of its inability to resolve more than a single axon direction within each imaging voxel. Techniques, that can resolve multiple axon directions within a single voxel, may solve the problem of white matter fiber crossings, as well as the problem to reconstruct the correct white matter insertions into the cortex. Further challenges in the clinical setting relate to the effects of edema surrounding a tumor where fiber tracking is performed. Effects of the edema and the tumor itself impede the correct tracking so that either existing fibers are not visualized at all or even an erroneous tracking may result.

There are various technical attempts to approach the limitations of DTI-based tractography, an agreed standard, or ideal solution is not yet defined. It will be important to compare the different approaches especially in respect to their reliability and also clinical applicability.

At the moment however, most neurosurgeons use the DTI-tractography method, because it is easily available, e.g. as software package in navigation systems. It is mandatory that either these commercial systems become more open to facilitate integration of better solutions or the technical advantages are directly implemented in the commercial systems, so that they are available for the whole neurosurgical community.

Stereotactic Laser Amygdalo-Hippocampotomy for Mesial Temporal Lobe Epilepsy: Single-Center, Prospective, Investigator-Initiated Study

Robert E. Gross, MD, PhD[1], Jon T. Willie, MD, PhD[1], Sandra Helmers, MD[2], Sherif Nour, MD[3]
Department of Neurosurgery[1], Neurology[2], and Radiology[3], Interventional MRI Program, Emory University, Atlanta, GA

Objectives

To evaluate effectiveness, safety, and related findings following stereotactic laser amygdalohippocampotomy (SLAH), a minimally invasive option to open anterior temporal lobectomy and selective amygdalohippocampectomy for mesial temporal lobe epilepsy (MTLE).

Methods

Twenty-one subjects from a single center with medication-resistant MTLE underwent SLAH (Visualase, Houston, TX) 6 – 30 months prior, and data was collected prospectively via validated case report forms (CRFs). Demographic, medical history, and medical/surgical care data were also gathered, along with seizure outcome. Seizure diary, quality-of-life scales, neurocognitive testing at 6 and 12 months and post op MRI at 6 months were acquired.

Results

Mean age at surgery was 35±14.7 (20 – 65); age at onset was 1 – 36 years-old, and duration of epilepsy was 3 – 59 years. Thirteen of 21 patients (62%) had MRI findings consistent with mesial temporal sclerosis (MTS: hippocampal atrophy and increased signal on T2-weighted and/or FLAIR-imaging). The most common pre-ablation seizure type was complex partial, with some exhibiting simple partial and secondarily generalized seizures as well. At 6-month follow-up of all available subjects since the beginning of SLAH being performed (August, 2011), 57% of subjects were Engel I (free of disabling seizures). Five of ten patients were seizure-free at 12 months follow-up, with recurrent seizures, when present, occurring by 6 months in all patients. However, one of these 5 patients had a cluster of recurrent seizures at 14 months. Of 13 subjects with MTS, 10 (77%) were seizure-free at 6-months, whereas only 2 of 8 (25%) of subjects without MTS (MRI normal, or only T2 signal change or hippocampal atrophy) were seizure-free. Two hemorrhages occurred: 1 subdural hematoma which, although small, was evacuated with no transient or permanent neurological deficit; 1 temporal lobe hematoma with visual field deficit that recovered. Median length of hospital stay was 1 day.

Conclusions

SLAH achieved Engel 1 outcome in the majority of subjects at 6- and 12-month follow-up, with acceptable safety. Further prospective study, with greater numbers of subjects, will help elucidate and/or strengthen these findings.

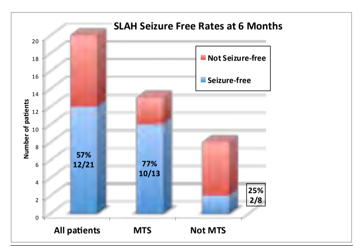

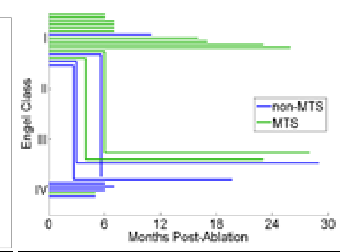

Real-time MRI for predicting stem cell distribution and subsequent monitoring of cell infusion to the central nervous system

Miroslaw Janowski *‡**††, Joanna Wojtkiewicz‡‡, Adam Nowakowski**, Moussa Chehade‡§, Aleksandra Habich‡‡, Piotr Holak¶¶, Jiadi Xu***, Zbigniew Adamiak¶¶, Monica Pearl†, Philippe Gailloud†, Barbara Lukomska**, Wojciech Maksymowicz‡‡, Jeff W.M. Bulte *‡,§,¶,||, and Piotr Walczak *‡§§
*Division of MR Research, † Division of Interventional Neuroradiology, Russell H. Morgan Dept. of Radiology and Radiological Science, ‡Cellular Imaging Section and Vascular Biology Program, Institute for Cell Engineering, §Dept. of Biomedical Engineering, ¶Dept. of Chemical & Biomolecular Engineering, || Dept. of Oncology, The Johns Hopkins University School of Medicine, Baltimore, MD, 21205, USA **NeuroRepair Dept., ††Dept. of Neurosurgery, Mossakowski Medical Research Centre, Polish Academy of Sciences, Warsaw 01-809, Poland, ‡‡Dept. of Neurology and Neurosurgery, §§Dept. of Radiology, Faculty of Medical Sciences, ¶¶Dept. of Surgery and Radiology, Faculty of Veterinary Medicine, University of Warmia and Mazury, Olsztyn, (10-082) Poland, ***F.M. Kirby Research Centre, Kennedy Krieger Institute, Baltimore, MD, 21205 USA

Purpose Up until now, MRI stem cell tracking has only enabled detection of cells after the transplantation was completed. Real-time monitoring allows unprecedented precision of cell delivery by interactive procedure.

Materials and Methods: Stem cells were labeled with SPIO for detection in MRI. Intra-arterial, intraventricular and intrathecal routes of stem cell delivery were investigated. GE-EPI sequence has been employed for real-time MRI. For rats, a Bruker 7T horizontal bore magnet and 15 mm planar surface coil were used with TE=17 ms, TR=2000 ms, FOV=260x260mm, matrix=96x96, and acquisition time=2 s. For dogs and pigs, a 3T Siemens Trio was employed with TE=36 ms, TR=3000 ms, FOV=1080, matrix=128, and acquisition time=3 s. For assessment of cerebral perfusion, the cell injection in the dog brain was preceded by infusion of the USPIO (Feraheme®).

Results: Real-time EPI was able to demonstrate that cells rapidly engrafted within the stroke periphery, with a delayed inflow into the core of the infarct (**Fig. 1A**, infarcted area outlined in yellow). We detected and quantified the speed and magnitude of cell inflow to the different segments of spinal cord (**Fig. 1B)** showing more robust engraftment in proximal to Adamkiewicz artery ROI1 and 2, compared to distal ROI3 and 4. Cell inflow was also observed in real-time after intraventricular and intrathecal delivery. Perfusion imaging using USPIO (Feraheme®) (three bolus injections of 3mg/ml, 300µl each completed in interval between 0 and 170s) was performed to predict the cell inflow area and preservation of cerebral blood flow (CBF) following cell delivery **(Fig. 1C)**. Cell injection completed in an interval between 170-400s resulted in a gradual signal decrease in the region previously highlighted by USPIO (Feraheme®) injection. To confirm that the CBF was not altered by transplanted cells, USPIO (Feraheme®) was injected a second time after cell delivery (three boluses), demonstrating a similar perfusion in the area containing injected cells (**Fig. 1C**, interval between 400-600 sec.).

Conclusions: We have shown that intraarterial cell delivery to the CNS can be monitored in real-time by MRI and that perfusion imaging with USPIO (Feraheme®) can be used as a predictor of cell distribution.

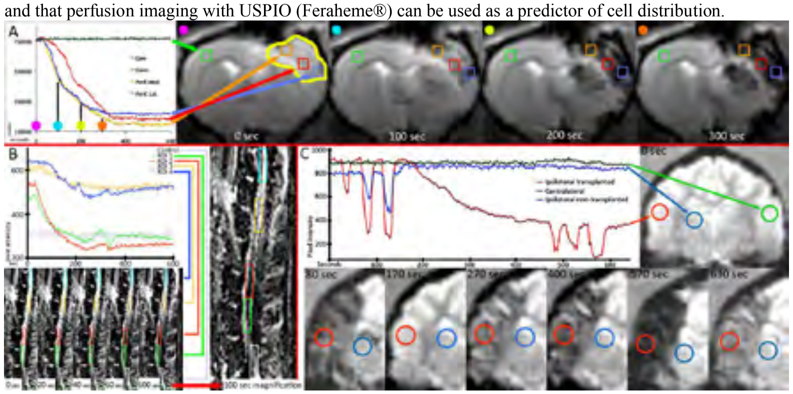

Guiding Focal Blood Brain Barrier Disruption and Targeted Delivery of Chemotherapy with Interventional MRI

Monica Pearl, Miroslaw Janowski, Emily Wyse, Ethel Ngen, Amnon Bar-Shir, Assaf Gilad and Piotr Walczak
Russell H. Morgan Dept. of Radiology and Radiological Science, Johns Hopkins University, Baltimore MD

Purpose: Inadequate penetration of chemotherapeutic agents across an intact blood brain barrier (BBB) and lack of methodology for precise drug delivery represents a major therapeutic challenge in the treatment of pontine gliomas. The purpose of this study is to demonstrate that intra-arterial (IA) chemotherapy administration can be performed with high precision after focal blood brain barrier disruption (BBBD) and that parenchymal penetration can be validated with fluorescent microscopy using drug-sized surrogate markers.

Materials & Methods: Our IACUC approved this protocol. Using a hybrid MRI angiography suite (Miyabi, Siemens), the left vertebral arteries of 4-kg New Zealand white rabbits were catheterized with a 4-French catheter. A 1.7-French microcatheter was then advanced into the basilar artery. The rabbits were transported to a 3T MRI (Magnetom Trio, Siemens) for anatomical reference images (horizontal and sagittal T2-weighted (TR/TE=1500/105)). Real-time assessment of trans-catheter contrast enhanced perfusion territory using GE-EPI sequence (TR/TE=3000/30) was performed during infusion of iron oxide nanoparticle solution (Feraheme) (rates of 0.001-0.1ul/s).

IA mannitol (20% over 5 minutes at the pre-determined optimized infusion rate) was administered for focal BBBD. Intravenous gadolinium (Magnevist, 0.5 mM, 0.125 mmol/kg) was administered followed by T1-weighted (TR/TE=300/9.1) images. IA melphalan-conjugated fluorescein isothiocyanate (FITC; 19 µmol) was then infused. The brains were immediately harvested and snap frozen on crushed dry ice. Cryo-sectioned tissue slices were counterstained with DAPI for fluorescent microscopy.

Results: Feraheme-enhanced real-time MRI demonstrated that the perfusion territory is variable and for a desired coverage, the injection parameters need to be adjusted on a case-by-case basis. Infusion rates resulting in selective perfusion of the pons were used for IA mannitol injection and resulted in specific pontine BBBD as visualized by gadolinium enhanced T1-weighted images. Injection of FITC-melphalan at the same rate resulted in its extravasation with the distribution correlating well with T1 enhancement.

Conclusion: MRI-guided targeted IA mannitol-induced BBBD facilitates highly selective and reproducible delivery of chemotherapeutic agents to the pons.

Figure 1.

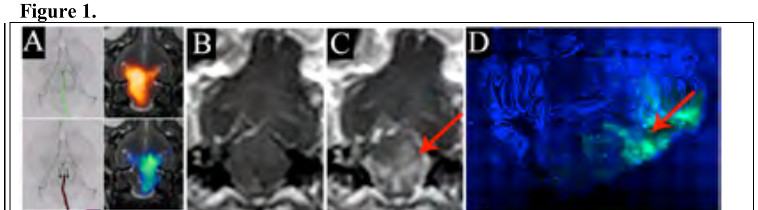

(A) Basilar artery catheterization by digital subtraction angiography and contrast-enhanced perfusion MRI showing completely different perfusion territory (shown with color-coding) after minimal repositioning of the catheter tip (arrows). T1-w gad MRI before (B) and after (C) mannitol injection shows enhancement in the region previously pinpointed by feraheme perfusion (C, red arrow). Coronal section through rabbit brain showing area of FITC-Melphalan conjugate (green) in the brain parenchyma with distribution correlating well to MRI.

Transcranial MR-guided focused ultrasound surgery

Nathan McDannold

Department of Radiology, Brigham and Women's Hospital, Boston, MA

In the last two decades, technological developments have enabled focused ultrasound (FUS) methods and devices that can safely focus high intensity ultrasound beams through the intact human skull. The fine balance between tolerable skull heating and focal thermal doses capable of inducing coagulate necrosis, along with the integration with high-field MRI, have made noninvasive FUS ablation in the brain a reality. In addition to thermal effects, the mechanical effects associated with ultrasonically driven microbubbles in the brain vessels can provide a number of new therapies, including targeted drug delivery via focal opening of the blood brain barrier. This talk will review transcranial focused ultrasound technology and the current state of this noninvasive method.

Recent advances in MRI guided musculoskeletal therapy

Roberto Blanco Sequeiros

Magnetic resonance imaging (MRI) presents as an intriguing tool to direct diagnostic and therapeutic procedures performed in the musculoskeletal region and to steer patient management. Studies have demonstrated that MRI-guided procedures involving bone, soft tissue, joints and intervertebral discs are safe and in selected indications preferred action to manage clinical situation. Often these procedures are technically similar to other modalities for bone and soft tissue lesions. However, the procedural perception to the operator can be very different to other modalities due to the vastly increased data.

Teamwork is essential, and the role of the clinicians is of paramount importance. Instrumentation and procedural techniques are unique and require thorough training and perception of relevant anatomy. In principle there are three categories for MRI-guided MSK interventions: biopsy, percutaneous minimally invasive therapy and intraoperative use. All have multitude of common and indication specific factors to be assessed when performing these procedures. Consistent with "one-stop" approach, MR imaging can be used to plan, guide, monitor and control the procedure.

MRI guidance is particularly advantageous should the lesion not be visible by other modalities, for selective targeting, intra-articular locations, cyst aspiration and locations adjacent to surgical hardware. Spine injections and pain management such as sacroiliac joint injections, selective nerve blocks and palliative ablation are a subset of procedures frequently performed.

In this presentation I will describe in detail the technical aspects of performing MRI guided MSK procedures as well as the most frequent clinical indications for diagnostic procedures. Novel clinical therapeutic procedures described and will also touch the new emerging methods for MRI guided MSK procedures.

MR-guided pain management

J. Fritz

Baltimore, MD, USA

Magnetic resonance (MR)-guided pain management procedures comprise selective injections around nerves, into muscles and vascular anomalies, as well as ablation and augmentation techniques. MR imaging and MR neurography techniques are used to visualize fine and deep anatomic targets, track needle placement, monitor injectants and ablation zones, and detect spread of injectants to potentially confounding nearby structures.

Magnetic resonance imaging guidance provides unparalleled soft-tissue detail for identification and targeting of neural structures, small muscles, joints and osseous targets; and avoids radiation exposure of patients, operators and staff.

The introduction of clinical high-field wide-bore MR imaging systems has increased the practicability and availability of MR- guided pain management procedures. Specifically, the recent introduction of wide-bore 3-Tesla MR imaging systems now enables percutaneous, high-field MR-guided pain management procedures. Modern coils and parallel imaging technology facilitate fast temporal image acquisition, higher spatial image resolution, and high image contrast, or combinations thereof.

Passive needle visualization is an easily achievable and reliable method. The resulting needle artifact is influenced by several factors such as the alloy of the needle, the strength of the static magnetic field, the sequence type, the spatial orientation of the therapy needle as well as the echo time and may further be optimized during the intervention by alteration of the last three factors. Injectants can be visualized based on their native T2 properties or based on the T1-shortening effects of added Gadolinium-based contrast agents. Fast acquisition techniques and image processing allow for continuous, near real-time MR fluoroscopic imaging and interactive needle navigation.

MR-guided pain management procedures include perineural injections of the brachial plexus, such as suprascapular nerve blocks; spine such as facet joint injections, sacroiliac joint injections, spinal nerve perineural injections, and drug delivery to the lumbar sympathetic chain; and lumbosacral plexus such as perineural injections of the obturator nerve, lateral femoral cutaneous nerve, pudendal nerve, posterior femoral cutaneous nerve, sciatic nerve, ganglion impar, and sacral spinal nerve. Intramuscular injections of the anterior scalene and piriformis muscles can be used to diagnose and treat neurogenic thoracic outlet and piriformis syndromes, respectively. Percutaneous sclerotherapy techniques can be used to successfully treat vascular anomalies, such as lymphatic and venous malformations. Painful vertebral body conditions can be treated with osseous cryoablation and subsequent cement augmentation.

3 Tesla MR-guided Injections in Patients with Neurogenic Thoracic Outlet Syndrome: Initial Clinical Experience

John Morelli[1], Ying Lum[2], John Carrino[1], Jonathan Lewin[1], Jan Fritz[1]

[1]The Russell H. Morgan Department of Radiology and Radiological Science,
[2]Department of Vascular Surgery, Johns Hopkins University School of Medicine

Purpose: To assess the feasibility and technical outcome of 3 Tesla MR-guided diagnostic and therapeutic injections in patients with clinical signs of neurogenic thoracic outlet syndrome.

Materials and Methods: We retrospectively assessed 27 consecutive interventional MRI procedures performed in patients with neurogenic thoracic outlet syndrome on a 3 Tesla, wide bore MR imaging system (Magnetom Skyra). Optimized TSE and HASTE sequences were used for needle guidance and visualization of the injectant. 22G MR-conditional needles were used. Procedures included diagnostic injections of the anterior scalene and pectoralis minor muscles with a local anesthetic agent (3 ml of ropivacaine) as well as therapeutic injections with botulinum toxin A (100 units) or glucocorticoids (40 mg Triamcinolone acetonide). Technical succ ess was defined as intra-muscular delivery of the injectant. Post-procedural fluid sensitive MR images were assessed for the presence of extra-muscular spread and clinical and procedural records were examined for evidence of brachial plexus anesthesia and symptoms of arm weakness.

Results: A total of 26/27 (96%) injections were completed including diagnostic intramuscular injections of the anterior scalene muscle (20/27, 74%) and pectoralis minor muscle (1/27, 4%) as well as therapeutic intra-muscular injections with steroid or botulinum toxin (6/27, 22%). 1/27 (4%) patient terminated the procedure prematurely due to claustrophobia. The targeted muscle was successfully injected in all completed cases (26/26, 100%). Extramuscular spread occurred in 4/26 (15%) cases of diagnostic scalene injections with transient ipsilateral motor weakness (3/26, 11%) and ptosis (1/26, 4%). No extramuscular spread occurred with therapeutic injections.

Conclusion: 3 Tesla MRI is feasible with a high technical accuracy of intramuscular injections of the anterior scalene and pectoralis minor muscle. MR is advantageous due to a lack of ionizing radiation and, in distinction to ultrasound, enables direct visualization of the injection for the detection of extramuscular spread and extension to the brachial plexus, which may lead to false positive results.

Clinical Significance: High-resolution 3 Tesla interventional MRI can achieve high technical accuracy of targeted intramuscular drug delivery in the setting of neurogenic thoracic outlet syndrome.

Real time MR-guided freehand direct shoulder arthrography employing an open 1.0 Tesla MR-scanner

Authors

Christian Wybranski [1], Ortrud Kosiek [1], Friedrich-Wilhelm Röhl [2], Maciej Pech [1], Jens Ricke [1], Katharina Fischbach [1], Frank Fischbach [1]

1 Department of Radiology and Nuclear Medicine, Otto-von-Guericke University Medical School, Magdeburg, Germany
2 Institute of Biometry and Medical Informatics, Otto-von-Guericke University Medical School, Magdeburg, Germany

Purpose

To assess the feasibility and efficacy of MR-guided, freehand direct shoulder arthrography (FDSA) in an open 1.0Tesla (T) MR-scanner, and to compare the image quality (IQ) achieved with the interventional MR platform with a standard MR shoulder protocol at 3.0T.

Materials and Methods

Technical success rate of MR-guided FDSA employing an open 1.0T MR-scanner, puncture-needle positioning rate (PNPR), and overall puncture times (PT) of a trained and less-experienced interventional radiologist were evaluated in 80 patients. Diagnostic imaging comprising T1, T2 and fat-saturated proton density weighted (T1w, T2w, fs-PDw TSE) sequences was performed consecutively in the open 1.0T and a closed-bore 3.0T MR-scanner in 5 healthy volunteers. Signal- and contrast-to-noise ratio (SNR, CNR) as well as IQ based on a 5-point-grading-scale (5: excellent – 1: poor/insufficient) of humerus, deltoid muscle (DM), anterior and superior glenoid labrum (aGL and sGL) and supraspinatus muscle tendon (SSM) were assessed.

Results

Technical success of FDSA was 96.3%. PNPR (25.4% vs. 86.2%, $p<0.001$) and PT were lower for the trained radiologist (5.6±2.7 min vs. 7.9±4.8 min, $p<0.001$). SNR of humerus and DM were significantly higher at 3.0T in T1w and T2w ($p\leq0{,}027$) but comparable to 1.0T in fs-PDw sequences ($p\geq0{,}057$). Only CNR of the aGL was higher in T1w and fs-PDw sequences at 3.0T ($p\leq0{,}035$). Visualization of aGL, sGL, and SSM was comparable at 1.0T and 3.0T in the T1w (2.0±1.1 vs. 2.2±1.1, $p=0.16$) and slightly better at 3.0T in the fs-PDw sequence (3.8±0.9 vs. 4.1±0.8, $p=0.09$).

Conclusions

Freehand direct shoulder arthrography employing an open 1.0T MR-scanner is effective and yields high-quality diagnostic images comparable to a closed-bore 3.0T MR-scanner.

Devices for MR-guided cardiovascular interventions – What is still missing?

Gabriele A. Krombach
Department of Radiology, University Hospital Giessen, Germany

The potential benefits of MR-guided cardiovascular interventions comprise the excellent soft tissue contrast, inherent to the method, the resulting possibility of delineating target structures such as vessel walls, myocardium and valves, tissue characterization combining established sequences and tissue mapping, which has recently entered the clinical arena and measurement of physiologic parameters, including cardiac function and flow velocity. The lack of any radiation renders the technique attractive especially for young patients, patients with chronic diseases and staff members. In recent years refined studies conducted in animals or phantoms have been published. Transfer to the clinical arena still remains limited to a small number of centers worldwide. Up to now self-made devices are usually employed for animal studies while dedicated prototypes, which are not commercially available, are used for interventions in human. Commercially available devices for endovascular interventional MRI are still sparse. Development of such devices is expensive and can only be pursued, if the expected revenue will exceed the development costs. This requires broad acceptance of the method in the clinical arena. Broad acceptance can only be expected for interventions that provide paramount advantages compared to the competing x-ray guidance. Identification and development of interventions with high clinical impact that are not possible using other imaging platforms are indispensable. Currently, the most promising fields are: 1. treatment of congenital heart diseases, 2. EP interventions, 3. local delivery of drugs or cells targeted at the recovery of damaged tissue.

MR-safe guide wires need to provide torque, stiffness and diameters, similar to those used for x-ray guided endovascular interventions. At the same time the material needs to be irrefrangable in order to avoid breaking of the guide wire with the sequel of losing parts in the body during the intervention. In contrast to conventional guide wires, which obtain their stiffness and torque either from a stainless steel core or nitinol, MR-safe guide wires cannot be manufactured using metal, since it carries the risk of tissue heating in the MR environment. MR-safe catheters also need to provide the properties of their counterparts, used under x-ray guided interventions, namely torque, diameter, flexibility and artefact free visibility.

Ideally, catheters and guide wires should be visible over their whole length, with the tip clearly distinguishable. This is either possible with a huge scan volume or by obtaining a multiple bended slice, that is adapted to the course of the device. The device as well as the surrounding anatomical structures should be delineated in real time. Currently either passive visualization or active tracking are applied. For passive visualization the inherent imaging features of the devices are used and the devices are depicted as signal voids on bright blood imaging. Tracking such devices can be difficult, if the vessels are tortuous.

Active visualization becomes possible after integrating small radiofrequency coils into the devices and connecting them to the scanner. It allows for adjustment of the slice to the tip of the device. Also with this concept selection of the appropriate imaging strategy and scan volume and is of critical importance for safety and success of the intervention.

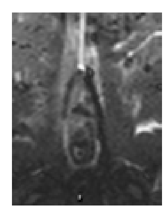

Passive tracking

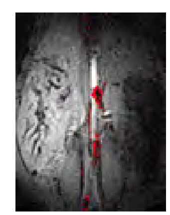

Active tracking

New Generation Laser Lithographed Dual Axis Magnetically Assisted Remote Controlled Endovascular Catheter for Interventional MR Imaging: In Vitro Navigation at 1.5 T and 3T versus X-ray Fluoroscopy

Steven W. Hetts, MD, Parham Moftakhar, MD, Prasheel Lillaney, PhD, Aaron Losey, MD, Bradford Thorne, Alastair Martin, PhD, Maythem Saeed, DVM, PhD, Mark W. Wilson, MD
Department of Radiology and Biomedical Imaging, University of California, San Francisco

Purpose:
To compare in vitro navigation in a vascular phantom using a 3rd generation magnetically assisted remote controlled (MARC) catheter under real-time MR imaging versus x-ray guidance in endovascular catheterization procedures.

Materials and Methods:
A custom 2.7 French clinical grade microcatheter prototype with a double saddle coil manufactured with custom 3D laser lithography at the distal tip was deflected with a foot pedal actuator used to deliver ± 300 mA. Inexperienced and experienced operators navigated the catheter into branch vessels in a custom cryogel abdominal aortic phantom. This was repeated under conventional x-ray fluoroscopy guidance. MR imaging experiments were performed at 1.5 T and 3T using steady state free precession real-time sequences. The mean procedure times and percent success of selecting a vessel within 90 seconds were determined and analyzed with a linear mixed effects regression analysis.

Results:
The catheter tip was clearly visible under real-time MRI at 1.5T and 3T. Among inexperienced operators, magnetically assisted MR guidance was equivalent to x-ray guidance at 1.5T (67/100 (67%) successful vessel-selection turns with 1.5T MRI vs 76/100 (76%) with x-ray $p=0.157$) and at 3T (75% turns with 3T MRI vs. 76% with x-ray $p=0.869$). Among experienced operators, x-ray guidance was more frequently successful at catheterizing a branch vessel within 90 seconds than MRI at 1.5T (98/100 [98%] successful turns with x-ray vs 65/100 [65%] with MRI, $p<0.001$). However, at 3T, MRI guidance among experienced operators improved (75% successful turns), but was less frequently successful than x-ray guidance. Among inexperienced operators, overall mean procedure time was equivalent between magnetically guided assistance (31 seconds) and x-ray guidance (34 seconds) ($p=0.436$). Among experienced operators, overall mean catheterization time was faster with x-ray (20 seconds) compared to MRI at 1.5T (42 seconds) ($p<0.001$), but magnetically assisted guidance improved at 3T (31 seconds). When stratified by branch vessels, magnetic assisted MR guidance was equivalent to x-ray guidance for the celiac artery, superior mesenteric artery (SMA) and (IMA). Only the renal arteries (small diameter, 60 degree angle) were easier to navigate with x-ray for experienced operators.

Conclusions:
We have developed and tested a 3rd generation MARC catheter for endovascular navigation in multiple planes under real-time MRI guidance. Magnetic-assisted navigation is feasible at 1.5T, improves at 3T, and is comparable to x-ray guidance for a variety of vessels. Furthermore, this technology is easily used by inexperienced operators. This work further strengthens the foundation for endovascular catheter navigation under MRI guidance, enabling further exploration of simulated interventions for the treatment of stroke, vascular malformations, and tumors - all of which may benefit from the physiologic information available through real-time MRI but not x-ray fluoroscopic guidance.

References:
1. Wilson MW, Martin AB, Lillaney P, Losey AD, Yee EJ, Bernhardt A, Malba V, Evans L, Sincic R, Saeed M, Arenson RL, Hetts SW. Magnetic Catheter Manipulation in the Interventional MR Imaging Environment. J Vasc Interv Radiol. 2013 Jun; 24(6):885-91.
2. Hetts SW, Saeed M, Martin A, Lillaney P, Losey A, Yee EJ, Sincic R, Do L, Evans L, Malba V, Bernhardt AF, Wilson MW, Patel A, Arenson RL, Caton C, Cooke DL. Magnetically-Assisted Remote Controlled Microcatheter Tip Deflection under Magnetic Resonance Imaging. J Vis Exp. 2013; (74).

MR-Guided Treatment of Low-Flow Vascular Malformations

Clifford R. Weiss[1], Paul A. DiCamillo[2], Wesley D. Gilson[3], Jonathan S. Lewin[2]

[1] Vascular and Interventional Radiology, The Johns Hopkins University, Baltimore, MD
[2]Department of Radiology, The Johns Hopkins University School of Medicine, Baltimore, MD
[3] Center for Applied Medical Imaging, Siemens Corporation, Baltimore, MD

Background: Venous (VM) and lymphatic malformations (LM) are typically treated using ultrasound and X-ray fluoroscopic guided percutaneous sclerotherapy. However, certain lesions are particularly difficult to visualize and/or treat using these modalities. Real-time MR-guided intervention may serve as a safer alternative, with better visualization of surrounding critical soft tissue structures and without patient exposure to ionizing radiation. We present here our experiences with this technique using a short bore 1.5T MRI/X-Ray "Miyabi" suite.

Materials and Methods: Patients with VM or LM previously treated using ultrasound and fluoroscopic guided sclerotherapy were enrolled into this IRB approved study between 9/2010 and 4/2014. Each was referred for MR guidance for actual or predicted inability to find the lesion using ultrasound. **Intervention:** Imaging was conducted with a MAGNETOM Espree 1.5T MR scanner (Siemens Healthcare, Erlangen, Germany) and an AXIOM Artis dFA (Siemens Healthcare, Forchheim, Germany) “Miyabi” suite. After planning MR (3mm T2 TSE SPAIR), all lesions were punctured under real time MR guidance with Interactive Real-Time TrueFISP imaging (BEAT_IRTTT, Siemens Corporate Research & Technology, slice thickness 4mm, 465 ms per slice), HASTE acquisition (slice thickness 4mm, ~750 ms per slice) or a custom-made T2-Weighted Steady State Free Procession (CP-SSFP) sequence using 20-22 gauge MR-compatible needles (Cook, InVivo, MReye) ranging from 5-20 cm in length. Once access was confirmed by fluid return, confirmatory T2 TSE sequences were acquired. When indicated, patients were transferred to the in-room Artis where a direct injection of ioxilan 350 (Guerbet) was used to confirm MR findings. Patients with VM were treated with anhydrous (100%) ethanol (ETOH), gad-doped 5% ethanolamine oleate (EO), or gad-doped 3% sodium tetradecyl sulfate (STS). Patients with LMs were treated with doxycyclene (10mg/cc). After treatment, confirmatory imaging was conducted (3mm T2 TSE SPAIR or 3mm 3D VIBE).

Results: 23 patients have been enrolled in this study with an age range of 8 - 56 years old. 21 patients had VM and two had LM. Of the 33 embolization sessions 29 were technical successes (the target lesion was accessed and treated). The two patients with LM were treated with doxycylene. Of the remaining 27 VM embolizations two were treated with EO, six were treated with ETOH alone, 18 were treated with STS alone, and one was treated with a combination of ETOH and STS. There were no minor or major immediate or delayed complications. All of the treated patients reported reduced symptoms.

Conclusions: VMs and LMs can be safely and effectively accessed and treated using a short bore 1.5 T MR system, and the MR/angiographic hybrid system provides an additional margin of safety when administering a highly caustic but most effective therapeutic (100% ETOH).

Percutaneous ablation for treatment of symptomatic vascular anomalies using CT and MRI guidance.

Scott Thompson, Matthew R. Callstrom, MD, PhD, Krzysztof R Gorny, PhD, Joel P. Felmlee, PhD, Akira Kawashima, MD/PhD, Michael McKusick, MD, David A. Woodrum, MD/PhD
Mayo Clinic, Rochester, MN

Purpose: To determine the feasibility and safety of image-guided percutaneous ablation for treatment of symptomatic vascular anomalies.

Materials and Methods: An IRB-approved retrospective review was undertaken of all patients who underwent image-guided percutaneous ablation of symptomatic vascular anomalies (VA) that failed percutaneous Sotradecol or ethanol sclerotherapy. Ablations were performed under general anesthesia with US/CT or MRI-guided cryoablation or MRI-guided laser ablation. Cryoprobes or laser fibers were placed under intermittent CT or MR imaging. Intraprocedural monitoring was performed with intermittent CT or MRI during cryoablation to monitor ice-ball formation or with proton-resonance frequency MR thermometry every seven seconds during laser ablation to monitor thermal changes. Post-ablation monitoring varied between observation or hospital admission. Clinical follow-up began at one month post-ablation.

Results: Eight patients (ages 10 to 48; 4 female) with nine VA (N=8 intramuscular; N=1 subcutaneous) were treated with US/CT (N=3) or MRI-guided (N=2) cryoablation or MRI-guided laser ablation (N=4) for pain (N=7) or diffuse bleeding secondary to hemangioma-thrombocytopenia syndrome (N=1) The VA volume [median, range] was 158.2 cm3 (12.8 to 220.6 cm3) for those undergoing cryoablation and 5.5 cm3 (3.0 to 10.3 cm3) for undergoing laser ablation. Eight VA were ablated in one session and one in a planned two-stage session. Two laser fibers and 3 to 10 cryoprobes were used per ablation session. The number of hospital days ranged from 1 to 3 for cryoablation and 0 to 1 for laser ablation. Minor complications included a small hematoma, which did not require further intervention (laser) and numbness of the dorsal aspect of first toe (cryoablation) which resolved without further intervention. There were no major complications. There was no recurrence of bleeding at four years post ablation in the patient with hemangioma-thrombocytopenia syndrome and 5 of 6 patients with painful VMs reported symptomatic pain relief beginning as early as one month post ablation.

Conclusion: Image-guided percutaneous ablation of symptomatic vascular anomalies is feasible and safe in patients who have failed percutaneous sclerotherapy and provides symptomatic relief for the majority of patients at short-term follow-up.

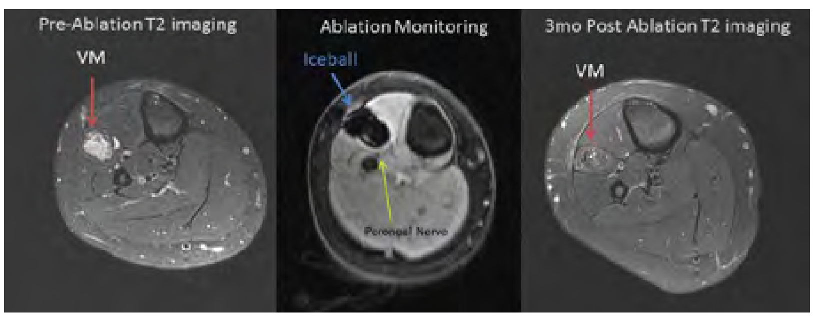

MRI-Guided Sclerotherapy for Intraorbital Vascular Malformations: Early Experience

Andrew D. Nicholson[1,2,3], Tracy E. Powell[1,2], Justin A. Saunders[3,4], Brent Hayek[3,4], Ted H. Wojno[3,4], Sherif G. Nour[1,2,3]
[1]Department of Radiology and Imaging Sciences, Emory University Hospital, Atlanta, GA, USA, [2]Interventional MRI Program, Emory University Hospital, Atlanta, GA, USA. [3] Emory University School of Medicine, Atlanta, GA, USA. [4]Section of Oculoplastics, Orbital & Cosmetic Surgery, Department of Ophthalmology, Emory University, Atlanta, GA,USA

Purpose: Despite their benign histology, many congenital intra-orbital lesions are prognostically aggressive owing to the limited anatomical space and the intimate optic nerve association, resulting in pain, disfigurement, and vision loss. Complete surgical excision while preserving function may not be possible [1]. The use of conventional fluoroscopically-guided interventions has been limited due to inability to visualize soft tissue anatomy. This work aims at evaluating the feasibility of applying interventional MRI technology to access and treat these challenging intraorbital lesions.

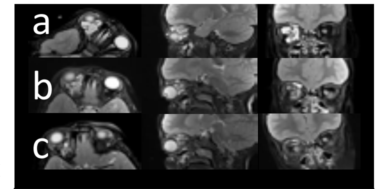

Fig. 1: 3-year-old male with a complex right-sided retrobulbar veno-lymphatic malformation encasing the optic nerve. The patient presented with proptosis, ecchyemosis, squint, and visual impairment. He was subjected to 2 prior unsuccessful surgical interventions. (a:1-3) are axial, sagittal, and coronal T2-WIs demonstrating the extent of malformation prior to MRI-guided sclerotherapy. (b:1-3) are the corresponding scans obtained 6 weeks after the first sclerotherapy session. (c:1-3) are the same scans obtained 12 weeks after the first, and 6 weeks after the second session of sclerotherapy. There has been significant shrinkage of the overall dimensions of the malformation and noticeable reduction of proptosis.

Methods: 10 MRI-guided sclerotherapy procedures were performed on 4 patients (4M,0F,age=3-30y) with retrobulbar(n=2), and orbital margin(n=1) veno-lymphatic malformations, and retrobulbar cystic teratoma(n=1). Patients presented with proptosis (n=3), visual impairment (n=2), diplopia (n=1), ecchymosis (n=2), and/or pain (n=1). 2 lesions were treatment-naïve and the other 2 lesions were post-surgical recurrences. All procedures were exclusively performed within an interventional MRI suite with an in-room monitor used for real-time needle guidance, injection monitoring and bedside scanner operation. A 22g MR-compatible needle was inserted into the targeted lesions under "MR-fluoroscopy" using triorthogonal image plane guidance[2] to interactively monitor the needle on continuously updated sets of true-FISP images (TR/TE, 4.35/2.18; FA, 60°;NSA, 3;TA, 3.11 s/slice). 0.6% gadolinium was mixed with 5% Ethanolamine Oleate (Ethamolin®) (0.15ml:1.0ml vol.) and injected under real-time monitoring using a triorthogonal FLASH sequence (TR/TE,2484/5.4).

Results: Initial intra-orbital needle insertion and subsequent repositioning were feasible in all cases. The flexibility of triorthogonal guidance was most helpful in accessing the retrobulbar intraconal space. Adequate monitoring of sclerosing agent was persistently achieved on 3 planes. Targeted lesions ranged between 1.5 and 4cm. 3 lesions encircled/abutted the optic nerve. 1-5.5 mls of sclerosing material were injected per procedure. The smallest lesion was completely filled with sclerosing material during each of 2 treatment sessions. The remaining 3 lesions were partially filled to avoid excessive intraorbital pressure. Procedures were tolerated by all patients. Noticeable local edema and bruising were a standard finding for 1-2weeks following procedures. In one patient an additional complication of corneal dryness occurred. Complete resolution of one lymphatic malformation occurred. The 3 other lesions has undergone significant shrinkage without delayed complications.

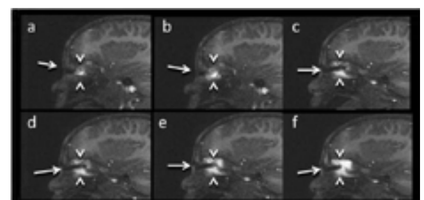

Conclusions: This initial report highlights the feasibility of utilizing interventional MRI technology in treating intraorbital congenital lesions. This potential role for interventional MRI may open a new avenue for those patients who are typically deprived of surgical and other conventional interventional options. The initial safety and efficacy reported herein are to be further evaluated on a larger number of procedures and compared to existing surgical data.

References:
[1] Chung EM, et al. Radiographics. 2007;(27):1777-799.
[2] Derakhshan JJ, et al. Proc ISMRM 15: 487 (2007).

MR-guided Sclerotherapy of Low-Flow Vascular Malformations Using T_2-weighted Interrupted bSSFP (T_2W-iSSFP): Comparison of Pulse Sequences for Visualization and Needle Guidance

Di Xu[1], Daniel A. Herzka[1], Wesley D. Gilson[3], Elliot R. McVeigh[1], Jonathan S. Lewin[2], and Clifford R. Weiss[2]
1. Biomedical Engineering, The Johns Hopkins School of Medicine, Baltimore, MD, United States, 2.Radiology, The Johns Hopkins School of Medicine, Baltimore, MD, United States, 3.Imaging & Computer Vision, Corporate Technology, Siemens Corporation, Baltimore, MD, United States

PURPOSE
To evaluate a new technique, T_2-weighted interrupted bSSFP (T_2W-iSSFP), specifically designed to improve real-time visualization of venous (VM) and lymphatic (LM) malformations during image guided interventions.

MATERIAL & METHODS
Sequence design: T_2W-iSSFP is a variable flip angle interrupted bSSFP sequence. Simultaneous T_2 contrast and fat suppression are needed for VM visualization and are achieved using a prolonged TR in combination with T_2-TIDE[1] and FS-TIDE[2,3] T_2 weighting and fat suppression are increased or decreased by using either higher or lower flip angles (HFA/LFA) in the bSSFP train, respectively.
Pre-procedural Imaging: To compare the VM visualization, patients (N=8) were scanned prior to intervention using HASTE, bSSFP, T_2W-iSSFP and TSE. To evaluate the sequence performance, CNR efficiency (CNR of VMs vs. muscle divided by the square root of acquisition time) and image sharpness (the reciprocal of mean edge width of needles in the images of swine)[4] were used.
Interventional Imaging: MR-guided percutaneous needle placement procedures were performed on swine (N=3) and on VM patients (N=8) using T_2W-iSSFP. All patients had undergone prior percutaneous sclerotherapy procedures with an actual or predicted inability to access their malformations using ultrasound.

Table 1. Evaluation of image contrast, sharpness, speed, and SAR.

Metrics	HASTE	bSSFP	T_2W-iSSFP
CNR efficiency (a.u.)	797±66	281±44	860±29
Image sharpness (mm^{-1})	0.21±0.06	0.48±0.02	0.49±0.03
Time per slice (sec)	1-2	0.3-0.6	0.3-0.7
SAR (W/kg)	1.6±0.1	1.1±0.3	1.3±0.1

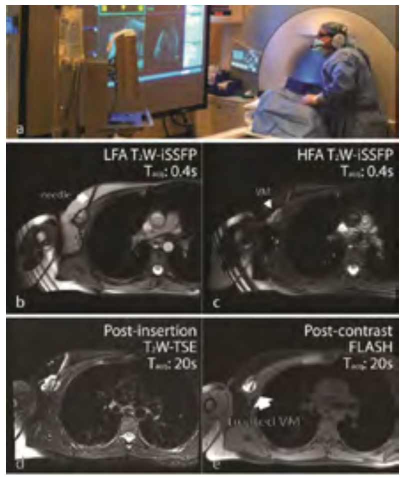

RESULTS
Using TSE as the reference sequence for lesion detection, 14 VMs were detected. The lesion detection rates were 14/14 (HASTE), 7/14 (bSSFP) and 14/14 (T_2W-iSSFP). A summary of the sequence performance is shown in Table 1. All MR guided sclerotherapy procedures using T_2W-iSSFP were successful. Specifically, all needles (14 punctures) were placed in the targeted lesions and were confirmed by post-insertion T_2W-TSE and post-contrast FLASH. A successful MR guided VM embolization is presented in Fig 1.

CONCLUSION
T_2W-iSSFP provides effective lesion identification and needle visualization, and was used successfully in 8 MR-guided sclerotherapy cases. It may be useful for other MR-guided procedures where heavily T_2-weighted real-time images are needed.

REFERENCES
1. Paul et al, MRM 2006; 2. Paul et al, MRM 2006; 3. Xu et al, ISMRM 2012; 4. Lai et al, MRM 2008.

MR-guided EP procedures – limitations and challenges

Matthias Gutberlet [1], Matthias Grothoff [1], Gerhard Hindricks [2]

[1] Department of Diagnostic and Interventional Radiology and
[2] Department of Electrophysiology

University Leipzig – Heart Center

Magnetic resonance imaging (MRI) combines the advantages of excellent soft-tissue characterization in a true 3D anatomical and functional model with the possibility of lesion and gap visualization without the need of any radiation. Therefore, real-time MRI presents a particularly attractive imaging technology to guide electrophysiology studies and catheter ablation procedures. Benefits relate to (1) the fluoroscopy-free environment, (2) substrate analysis, (3) combination of 3D anatomical and functional information, as well as (4) real-time visualization of introduced catheters (**Fig. 1A**) and ablation lesions (**Fig. 1B,C**) – [1,2]. This lecture should give an overview on current routine clinical applications of MRI in the setting of interventional electrophysiology. Furthermore, development of real-time MRI guided electrophysiology studies and first experiences with MRI guided catheter ablation procedures are depicted [2,3]. In this context advantages, challenges and limitations of real-time MRI guided catheter ablation as well as future perspectives and first results of active EP-catheter tracking (**Fig. 2**) are discussed.

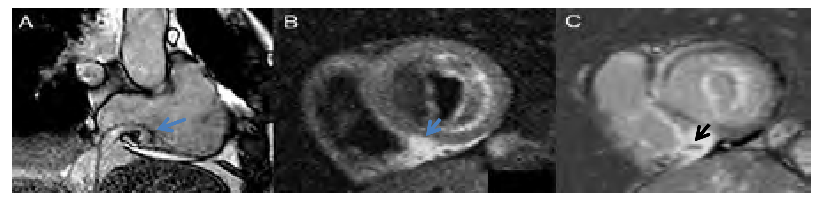

Fig. 1: Sixty-one yo male 6 hrs after inferior isthmus ablation of typical atrial flutter (EHRA I-II). Hx DCM (LV-EF=26%) exclusion of CAD. (**A**) Passively tracked IMRICOR ablation catheter (arrow) at the site of the inferior tricuspid isthmus. (**B**) SA T2-w STIR image with an edema (arrow) and (**C**) scar tissue with MOV (black arrow) in the PSIR image post contrast and „midwall" enhancement.

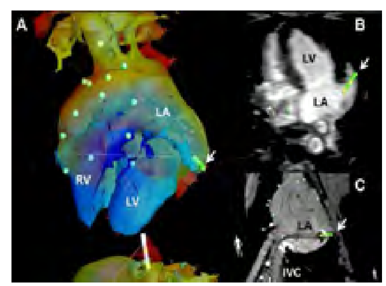

Fig. 2: Images from an animal study: (**A**) 3D-shell of the advanced navigation platform iSuite (Philips) in anterior-posterior orientation used for active tracking (green catheter tip – white arrow) of the IMRICOR (Vision) ablation catheter. The tip is located in the left atrial appendage (**B** – white arrow) after successful transseptal puncture. **C**: Active tracking overlay (green tip – white arrow) on the passively visualized catheter in the IVC and LA.

References:
1. Eitel C et al. (2014) Curr Cardiol Rep.
2. Grothoff M. et al. (2014) Radiology
3. Sommer P et al. (2013) Europace

Image Fusion for Cardiovascular Interventions

Dara L Kraitchman[1,2], Shashank S. Hedge[1] , Yingli Fu[1], Guan Wang[1,3],Tina Ehtiati[4],Wesley Gilson[4]

[1]Russell H. Morgan Dept. of Radiology & Radiological Sciences, [2]Dept of Molecular and Comparative Pathobiology, [3]Dept. of Electrical & Computer Engineering, Johns Hopkins University, Baltimore, MD, [4]Center for Applied Medical Imaging, Siemens Corporation, Corporate Technology, Baltimore, MD

Background: Because cardiovascular interventions demand high temporal and spatial resolution imaging in addition to extensive physiological monitoring, interventional MRI techniques are exceptionally challenging. However, the soft tissue detail, ability to distinguish ischemic, infarcted tissue from at risk myocardium, and the lack of ionizing radiation offer several advantages over X-ray-based interventions. Multimodality imaging or image fusion offers the ability to utilize the advantages of each imaging modality to potentially enhance the safety in existing procedures or drive new image-guided procedures.

Methods and Results: Cardiac MRI was performed using a variety of 2D and 3D techniques to obtain multiphase systolic and diastolic images of cardiac function and myocardial boundaries, late gadolinium enhancement of cardiac viability, and the coronary vasculature at 1.5T and 3T (Espree and Trio, Siemens). Segmentation of the cardiac MRI was registered to cone beam computed tomographic (CBCT) images (cardiac-gated DynaCT, Axiom Artis, Siemens) using semi-automated registration tools. Real-time fluoroscopic images were overlaid on the 3D rendering of the previous acquired segmented MRI and used to guide injections to stem cell injections to the pericardial space in swine without evidence of pericardial effusion.[1] Stem cells were labeled with X-ray visible contrast agents to enable tracking of cell fate over one week. In another study, magnetic resonance imaging of fluorinated stem cells was compared to CBCT to determine the persistence of stem cells after administration in the hindlimb of rabbits.

X-ray fused with MRI (XFM) for guiding intrapericardial injections resulted in successful stem cell administration in ten animals. X-ray guidance without the MRI overlay resulted in perforation of the ventricle in three animals and the development of pericardial adhesions and diminished cell survival. Perfluorinated stem cells can be successful visualized using ^{19}F MRI and CBCT.[2] Preliminary data suggests that both X-ray and MRI can quantify fluorine concentrations, but stem cells can often not be uniquely distinguished from other in radiopaque structures, such as bone and metallic devices.

Conclusions: XFM offers the ability to perform interventions under image guidance with a higher temporal resolution using existing devices and enables extensive physiological monitoring. XFM offers the potential to decrease radiation dose and enhance the safety profile of new techniques,such as intrapericardial stem cell administration in the face of normal pericardial anatomy. In addition, using non-proton moieties the ability to have a high sensitivity to track stem cells may be enhanced using MRI.

1 Fu, Y. *et al.* Fused X-ray and MR Imaging Guidance of Intrapericardial Delivery of Microencapsulated Human Mesenchymal Stem Cells in Immunocompetent Swine. *Radiology*, 131424, doi:10.1148/radiol.14131424 (2014).

2 Kedziorek, D. A. *et al.* Using C-arm x-ray imaging to guide local reporter probe delivery for tracking stem cell engraftment. *Theranostics* **3**, 916-926, doi:10.7150/thno.6943 (2013).

First in Man: Real-time magnetic resonance-guided ablation of typical right atrial flutter using active catheter tracking

Henry Chubb[1], James Harrison[1], Steven Williams[1], Steffen Weiss[2], Sascha Krueger[2], Jennifer Weisz[3], Gregg Stenzel[3], Jason Stroup[3], Steven Wedan[3], Kawal Rhode[1], Mark O'Neill[1], Tobias Schaeffter[1], Reza Razavi[1].
[1]Division of Imaging Sciences and Biomedical Engineering, King's College London, London, United Kingdom.[2] Philips Technologie GmbH, Hamburg, Germany. [3]Imricor, Burnsville, MN, USA.

Introduction
MR-guided electrophysiology (MR-EP) has the potential to improve catheter navigation, to visualize ablation injury and to avoid ionizing radiation. This study investigated the feasibility of an actively-tracked, fully MR-guided, electroanatomical mapping and ablation system. This represents first such system used in humans.

Methods
Three patients with typical right atrial flutter underwent cavotricuspid isthmus (CTI) ablation under MR guidance. The MR-EP suite integrated a Philips 1.5T Achieva scanner (Philips, Best, The Netherlands), an EP recording system (Horizon System, Imricor, Burnsville, MN, USA), an RF generator (St Jude Medical, St Paul, MN, USA), and a real-time image guidance platform (iSuite, Philips).
Under anesthesia, a baseline MRI was performed. 3D right atrial shells were created by automated segmentation of a whole-heart MR scan (3D BTFE) and CTI anatomy delineated. Using the shell for guidance, deflectable MR-EP RF Vision catheters (Imricor) were placed in the CS and RA using MR-guided active tracking alone. Isochronal activation maps were created prior to ablation. RF ablation of the CTI was performed under active MR-guidance, with brief cine sequences for catheter position confirmation (35-45W for 40-60sec). Post ablation, activation maps were repeated and native-T1 weighted, T2 weighted and LGE imaging of the lesions was performed prior to removal from the scanner.

Results
All patients underwent ablation of the CTI without use of fluoroscopy, with no complications. High fidelity electrograms were recorded with minimal MR interference. Active tracking of the catheter tip was accurate, with tracking position corroborated by conventional imaging sequences. Mean total procedure time was 304minutes (range 290 to 315min). Septal to lateral transisthmus conduction interval was lengthened to mean 153msec (range 134ms to 182ms), and atrial flutter was uninducible post-ablation. One patient had confirmed bidirectional block (figure 1). Imaging confirmed both T2 weighted and late gadolinium enhancement of the CTI with no gaps identified. The patients remain free of atrial flutter post ablation (maximum follow-up 64days).

Conclusions
This study confirms feasibility in man of active-tracked MR-guided ablation of typical atrial flutter in man.

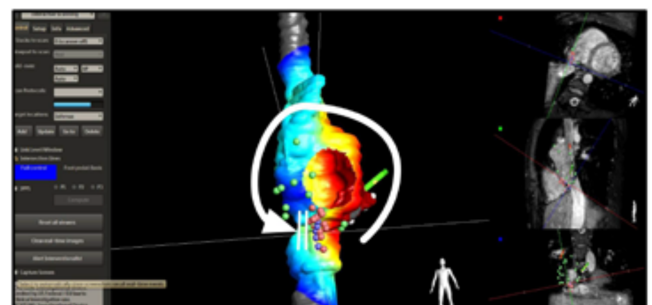

Figure 1. MR-generated post ablation activation map of the right atrium on coronary sinus pacing, demonstrating cavotricuspid isthmus conduction block at the site of ablation (red dots). White arrow indicates direction of activation, and multi planar reconstruction is shown on the right of the image.

MRI-guided Cardiac Cryo-ablation

Eugene G. Kholmovski[1,2], Ravi Ranjan[2], Nicolas Coulombe[3], Joshua Silvernagel[2], Nassir F. Marrouche[2]
[1]*UCAIR, University of Utah, Salt Lake City, USA;* [2]*CARMA Center, University of Utah, Salt Lake City, USA;* [3]*Medtronic CryoCath, Montreal, Canada*

Introduction: Cryo-ablation is being increasingly used for treatment of atrial fibrillation and ventricular tachycardia. However, reported success rate of the procedures is moderate. The main causes of failure are tissue recovery and gaps in desired ablation patterns. MRI can be used to assess extent of ablation and confirm tissue destruction. In this study, we have validated feasibility of MRI based cardiac cryo-ablation system.

Methods: Three MRI-guided cryo-ablation studies were performed in canines (n=3) according to protocols approved by the local IACUC. Cryo lesions were created using two MR-compatible cryo-ablation devices built for animal use: cryo-catheter with 8 mm catheter tip and 28 mm diameter cryo-balloon (Medtronic CryoCath, Montreal, Canada). MR imaging was performed at 3T Verio scanner (Siemens Healthcare, Erlangen, Germany).

Cryo-catheter was advanced into the right ventricle (RV) via the femoral vein assess under MRI guidance. The catheter was positioned on RV septal wall and catheter tip–tissue contact was validated. Cryo-ablation was performed for 4 minutes with simultaneous MRI monitoring of freeze zone formation.

MRI compatible cryo-balloon was advanced into the right atrium (RA) under MRI guidance. The balloon was positioned at superior vena cava (SVC) – right atrium (RA) junction and inflated. 10 ml of 10% diluted solution of gadolinium based contrast (MultiHance (Bracco Diagnostic Inc., Ponceton, NJ)) was injected to confirm SVC-RA junction occlusion. In the case of partial occlusion, balloon was deflated, re-positioned, inflated, and occlusion was re-validated. In the case of complete occlusion, cryo-ablation was initiated and the junction was frozen for 3 minutes with simultaneous MRI monitoring of freeze zone formation. High-resolution T1-weighted imaging and LGE-MRI were performed to assess the ablations and possible complications. Heart was excised to confirm the tissue changes.

Results: Figure 1 illustrates focal 4-minute cryo-ablation of RV wall. Diameter of freeze zone increases during the first minute of freeze (Figs. 1a and 1b) and stay about the same later during freeze (Figs. 1c and 1d). Dimension of freeze zones is well correlated with LGE-MRI (Fig. 1e) and tissue pathology. Figure 2 illustrates the main steps of cryo-ablation of SVC-RA junction using MRI based balloon cryo-ablation system.

Discussion and Conclusion: MRI based cryo-ablation system was implemented and validated in animal studies. It allows real time catheter navigation, confirmation of catheter tip–tissue contact and vessel occlusion by balloon, real-time visualization of a freeze zone, and assessment of lesion formation and collateral damage.

Acknowledgments: This study was supported in part by Medtronic.

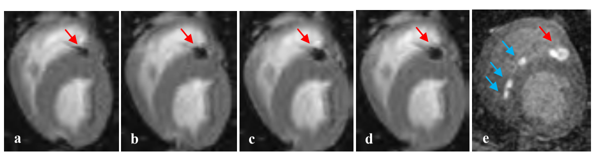

Figure 1. Cryo ablation of RV septal wall: (**a**) pre, (**b**) 1 minute freeze, (**c**) 2-minute freeze, (**d**) 4-minute freeze, (**e**) LGE-MRI demonstrating acute lesions created using MRI-compatible cryo (red arrow) and RF (blue arrow) catheters.

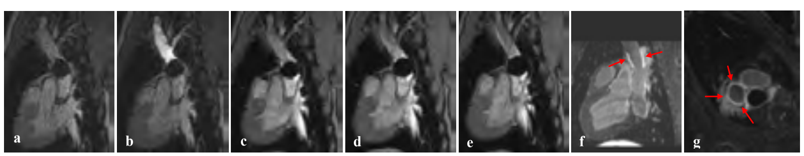

Figure 2. Cryo ablation of SVC-RA junction using MRI-compatible cryo balloon. (**a-b**) Navigation and validation of SVC occlusion by the balloon (a) pre contrast, (b) after contrast injection; (**c-e**) Real-time visualization of cryo ablation: (**c**) pre, (**d**) 1 minute freeze, (**e**) 3 minute freeze. (**f-g**) Assessment of the ablation by LGE-MRI: (**f**) sagittal and (**g**) axial views. Red arrows indicate circumferential ablation with no gaps at SVC-RA junction.

Magnetic particle imaging – potential for MR-guided vascular interventions?

Julian Haegele

Clinic for Radiology and Nuclear Medicine, University Hospital Schleswig Holstein, Lübeck, Germany

Magnetic Particle Imaging (MPI) is a new imaging modality using magnetic fields to visualize the spatial distribution of Superparamagnetic Iron Oxide Nanoparticles (SPIOs). In difference to Magnetic Resonance Imaging (MRI), in MPI SPIOs are used as a tracer, i.e. are visualized directly by their change of magnetization when exposed to an oscillating magnetic field. Because of the SPIOs high magnetic moment, sensitivity in MPI is considerably higher in comparison to MRI, i.e. 13 nmol(Fe)/l (for a voxel size of 1 mm^3) opposite to about 50 µmol(Fe)/l (independently of the voxel size). Another advantage in comparison to MRI is the very high temporal resolution in the order of milliseconds for sampling of a whole three-dimensional imaging volume. This is based on the fact that the SPIOs signal can be measured directly without delay due to e.g. an echo time. Furthermore, the signal to noise ratio (SNR) is high because the SPIOs are imaged directly as a tracer and missing MPI-signal generation by the body does not contribute to noise. Spatial resolution of 1 mm^3 and less can be achieved.

Due to these characteristics we consider MPI as a promising tool for cardiovascular imaging and perhaps even for guidance of interventions. Similar to MRI, interventional devices like guide wires and catheters have to be modified to be discernible in MPI and, especially in stainless steel instruments, heating and artifact generation has to be kept in mind. Further safety issues are, also like in MRI, peripheral nerve stimulation and tissue heating.

In this talk, a short introduction to MPI shall be given. The potential for cardiovascular imaging and interventions will be highlighted with emphasis on the differences and similarities to MRI and how both methods could be combined to a sensible hybrid concept.

3D MRI-Guided Parathyroidectomy and Intraoperative Recurrent Laryngeal Nerve Identification

Jagadeesan Jayender, PhD [1], Matthew A. Nehs, MD[2], Thomas C. Lee, MD[3], Ferenc Jolesz, MD[1], and Daniel T. Ruan, MD[2]
Depart of Radiology[1], Surgery[2], Neuroradiology[3]
Brigham and Women's Hospital,
Harvard Medical School
Boston, MA 02115

Background: Although parathyroid localization by ultrasound and sestamibi are useful to guide parathyroidectomy, intraoperative localization of parathyroid adenomas (PA) can still be challenging, particularly in the reoperative setting. MRI has proven to be very useful in identifying the PA and Recurrent Laryngeal Nerve (RLN) preoperatively. We sought to map patients' PA and RLN pre-procedurally by MRI and localize them intraoperatively during parathyroidectomy using a novel image-guided navigation system.

Methods: Five patients with primary hyperparathyroidism underwent pre-procedural MRI in the surgical position to localize their PA and RLNs and subsequent parathyroidectomy in the state-of-the-art Advanced Multimodality Image-guided Operating (AMIGO) suite. The MR imaging consisted of T1 VIBE, T2 BLADE and T2 TSE sequences. Using semi-automatic segmentation techniques, three-dimensional patient-specific models of the skin, trachea, carotid artery, thyroid, RLN, and PA were created. A modified Bovi pencil instrumented with an electromagnetic position sensor was used as a localization probe to assess each structure's position in 3D space. We calculated the target registration error (TRE) for the navigation system, which was defined as the position difference in 3D space between the seven distinct points on the patient mapped to the image space and their corresponding position on the pre-procedural MRI. The RLNs were identified and confirmed by electromyography (EMG) nerve monitoring. The thyroid edge, trachea and PA were localized using the probe and their position was mapped to the image space.

Results: All parathyroid adenomas were identified by preoperative MRI and were concordant with ultrasound and intra-operative findings. The average TRE was 3.1 mm +/- 0.3mm. The RLN was mapped by MRI and then visually identified and confirmed by EMG signal using the intraoperative nerve monitor. We identified both true positive EMG signals and true negative EMG signals along the course of the RLN. The minimum distance of the probe to: a) thyroid edge = 1.26 mm, b) trachea = 0.64 mm, c) PA = 0.31 mm. All parathyroid adenomas were successfully resected, and there were no RLN palsies or postoperative neck hematomas.

Conclusions: In this proof-of-concept study, we were able to map the parathyroid adenomas in the three-dimensional virtual space with a high degree of accuracy and were able to identify the recurrent laryngeal nerve by MRI pre-procedurally. This technology can be useful for the intraoperative localization of parathyroid adenomas, and to the best of our knowledge, it is the first report of the identification of the recurrent laryngeal nerve by MRI.

MR-guided laser therapy of liver tumors

Christian Rosenberg
Department of Diagnostic Radiology and Neuroradiology, University Hospital Greifswald
Greifswald, Germany

Laser-induced thermal ablation in combination with MR guidance may be seen as the most efficient technical setting for online therapy monitoring within the hepatic target zone. Artifact-free high-resolution thermometry of fiber and target tumor, as well as fiber placement in the liver, benefit from MR-specific imaging qualities. MRI performance is superior to CT in displaying non-enhanced focal lesions, which is important, as the procedure – just as any other image-guided liver intervention – is lasting too long to maintain a solitary extracellular intravenous contrasting of the target lesion. Catheter placement in general benefits from multiplane reconstructive imaging. The importance of modern liver-specific intracellular contrast media, such as Gd-EOB-DTPA, is widely respected and has made MRI the imaging gold standard in staging focal hepatic disease. With a broader availability, these contrast agents qualify for periinterventional liver imaging, especially in metastatic disease. Gadolinium-based lasting signal enhancement in hepatic tissue at late-phase is a substance- and MR-specific property. With a given metallic catheter mandrin and a non-enhancing target tumor contrast-induced elevation of the parenchymal signal is anticipated to promote the feasibility of catheter placement. Particularly when performing therapeutic laser ablation with modality-specific parallel placement of multiple applicators per procedure, beneficial effects are equally expected to multiply. The procedural setting in a closed bore 1.5 T system is primarily determined by the need of high spatial resolution, for the intended laser ablation is being controlled through real-time MR thermometry within the target zone.

MR guided Radiofrequency Ablation (RFA) of the Liver

Frank Fischbach

Primary and secondary malignant hepatic tumors are some of the most common tumors worldwide. In inoperable cases local ablation techniques as RFA are the method of choice for palliative treatment due to its minimally invasive character. Ablation is performed by continuous heating under temperature control. The device consists of a needle electrode and an electrical generator to produce an alternating electric current to induce thermal injury to the tissue.
For the adequate destruction of tumor tissue the entire volume of the lesion must be subjected to cytotoxic temperatures. Ideal tumors for RFA are smaller than 3 cm in diameter, completely surrounded by hepatic parenchyma, and with distance from large hepatic or portal veins to avoid cooling effects of the blood flow limiting the extent of the ablation. Additonally, the treatment is limited to patients with three or fewer lesions in order to minimise the interventional period.

considerations for magnetic resonance MR guidance

Due to the inherent soft tissue contrast MR imaging offers a higher sensitivity for liver lesions than CT, which can be further increased by hepatocyte-specific contrast agents. As a result of hepatocyte uptake, normal liver parenchyma exhibits T1 shortening leading to an increase in signal intensity on T1w images, whereas malignant focal liver lesions do not exhibit T1 shortening. This increases image contrast and thus lesion conspicuity compared with unenhanced scans. Peak liver signal intensity remains for approximately 2 h providing ample time for minimally invasive liver interventions.
Several studies have already demonstrated the feasibility of MR-guided RF ablation in the treatment of hepatic malignancies. Up to now open architecture MR systems or closed-bore MR systems operating at higher field strength were used. The open configuration allows access to the patient from the side and hence allows for a freehand approach.
For MR guidance MR compatibility must be considered. Most commercially available devices are not suitable as they produce giant susceptibility artefacts which may mask the target lesion or structures at risk. In addition the radiofrequency output of the generator precludes imaging. To prevent the interaction between the RF generator and the MR scanner RF-filtering using a low pass filter has to be implemented.
After the RFA cycle is finished dynamic contrast media application proves complete ablation of the tumor. In addition or alternatively T1- and T2-weighted sequences are used for therapy control. The zone of coagulation is characterized by decreased signal intensity on T2w images and increased signal intensity on T1w images. Furthermore, T2w imaging adds information regarding post-interventional complications such as perihepatic hematomas and biliomas.

drawbacks and future perspectives

At present only dedicated systems can be used for MR guidance. Further drawbacks are constraints in communication between the control and magnet room. Headphones and microphone sets with noise cancellation would improve communication. In theory temperature mapping is an excellent tool for therapy monitoring. However, up to now all proposed techniques (e.g. proton resonance frequency (PRF) shift method) do not work reliably when performed during free breathing as is necessary for liver interventions.

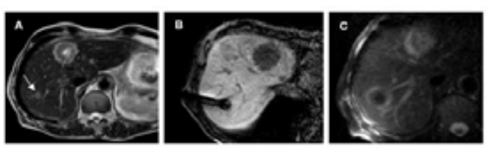

A • RFA of a metastasis in segment 7 of the right liver lobe illustrated in T2w imaging (arrow)
B • T1w imaging demonstrates intralesional location of the RFA-probe
C • complete tumor ablation proven by loss of signal intensity due to carbonisation in T2w images

Liver lesion conspicuity in interactive MR fluoroscopic sequences: dependency on lesion histology, size and image weighting

Rempp H[1], Hoffmann R[1], Rothgang E[2], Li P[3], Loh H[1], Pereira PL[4], Nikolaou K[1], Clasen S[1]

1 Diagnostic and Interventional Radiology, Eberhard Karls University, Tübingen, Germany
2 Siemens Healthcare, Erlangen, Germany
3 Siemens Corporate Technology, Center for Applied Medical Imaging, Baltimore, USA
4 Diagnostic and Interventional Radiology, SLK Clinics, Heilbronn, Germany

PURPOSE

To evaluate the conspicuity of primary and secondary liver lesions at fluoroscopic MR sequences used for applicator placement at MR-guided radiofrequency ablation.

METHOD AND MATERIALS

MR-guided radiofrequency ablation was performed in 103 patients using a wide-bore 1.5 T MR scanner. Interactive fluoroscopic MR sequences were applied for applicator placement using a T1 weighted multislice spoiled gradient echo sequence and a T2/T1 weighted balanced steady-state free precession sequence. Three image planes containing the lesion and the applicator were consecutively updated. Only non-enhanced examinations were selected for this study. The lesion conspicuity of 41 hepatocellular carcinomas (size 22 ± 8 mm) and 67 liver metastases of different primary tumors (size 21 ± 10 mm) was assessed retrospectively (easily detectable/difficult to detect/ not detectable). The contrast-to-noise ratio (CNR) of all lesions was calculated.

RESULTS

HCC could better be visualized in the SSFP sequence. The majority of HCC were hypointense in the GRE sequence (mean CNR 9.1, range 0 – 30) and hyperintense in the SSFP sequence (mean CNR 16.4, range 0 - 89). Size of the lesions and lesion conspicuity (CNR) did not correlate. HCC was easily detectable in 33/52% (GRE/SSFP), difficult to detect in 30/18%, and not detectable in 37/30% of the cases. 8/41 HCC lesions were neither detectable in GRE and nor in SSPF-fluoroscopy. The mean size of the lesions classed “not detectable” was 20.1 mm/21.1 mm (GRE/SSFP). Targeting was performed in these cases step-by-step or by using anatomic landmarks.
Liver metastases were hypointense in the GRE sequence in 65/67 cases (mean CNR 11.5, range 0 – 41) and hyperintense in T2 to a variable extent (mean CNR 12.7, range 0 – 63). Size of the lesions and lesion conspicuity (CNR) did not correlate. Liver metastases were easily detectable in 58/41% (GRE/SSFP), difficult to detect in 14/21%, and not detectable in 28/38% of the cases. 13/67 metastases were neither detectable in GRE and nor in SSPF-fluoroscopy. The mean size of the lesions classed “not detectable” was 15.1 mm/17.6 mm (GRE/SSFP).

CONCLUSION

The majority of liver lesions can be visualized in MR fluoroscopy without using contrast agent. Lesion conspicuity seems to depend more on lesion histology than on lesion size. Metastases tend to be better visualized in spoiled GRE imaging, and HCC in balanced SSFP imaging. Both weightings should be used complementary.

Technique and Long-Term Efficacy Results of In-Bore MRI-Directed Laser Ablation for Malignant Renal Neoplasms

Sherif G. Nour [1-3], Andrew D. Nicholson[1-3], Tracy E. Powell[1,2], Melinda M. Lewis[3,4], Viraj Master[3,5]

[1] Department of Radiology and Imaging Sciences, Emory University Hospital, Atlanta, GA, USA
[2] Interventional MRI Program, Emory University Hospital, Atlanta, GA, USA
[3] School of Medicine, Emory University, Atlanta, GA, USA
[4] Department of Pathology, Emory University Hospital, Atlanta, GA, USA
[5] Department of Urology, Emory University Hospital, Atlanta, GA, USA

Introduction & Purpose: Percutaneous ablative treatment has become a viable treatment option for selected patients with localized malignant renal neoplasms. The primary ablative technologies used are cryoablation and radiofrequency ablation (RFA), commonly performed under CT or ultrasound guidance. The use of MRI guidance has shown an added value for intraprocedural confirmation of a tumor-free ablation zone, thereby reducing the incidence of residual /recurrent neoplasms [1, 2]. MRI guidance of these procedures has, in our experience as in others', been hampered by the cumbersome handling of cryoprobes and RFA probes and their cablings within the already limited room available within the MRI gantry, particularly when utilizing superconducting magnet designs. The aims of this investigation are to a) describe the technical aspects of using laser fibers to deliver ablative energy to renal tumors, circumventing the space constraints within the MRI environment; b) describe patient tolerance and complication rates; and c) report the long term efficacy of laser ablation of renal malignancies.

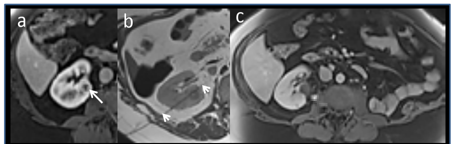

Fig 1: 48-year-old male with history of left radical nephrectomy for RCC and a new 1.7-cm enhancing lesion on gadolinium-enhanced VIBE in the interpolar segment of the right kidney (arrow, a). MRI-guided biopsy performed in the same ablation session confirmed a clear cell RCC. The laser fiber placement is confirmed on TSE-T2 prior to ablation (arrowheads, b). Venous phase post contrast VIBE scan obtained 3 weeks following ablation demonstrate a circumscribed non-enhancing ablation zone (arrow, c) without residual tumor or delayed complications.

Patients & Methods: 12 patients (5M, 7F, age=28-83y) with 21 renal masses underwent MRI-guided biopsies followed by laser ablations in the same session. Procedures were performed within an interventional MRI suite equipped with 1.5T wide bore scanner. Interventions were performed under general anesthesia, entirely within the scanner bore while viewing real-time image updates on an in-room monitor. Interactive visualization on a tri-orthogonal plane True-FISP sequence (TR/TE/FA=2700/84/170°) was used to guide a 14.5-cm-long, 14G MRI-compatible introducing needle into the targeted lesion. 20G FNA and, if inconclusive, 18G core samples were obtained. A laser fiber with 15mm diffusing tip encased in 5.5 F cooling catheter (Visualase, Texas, USA) was then introduced into the target lesion through the pre-existing short 14G introducing needle (Figs 1&2). The optic fiber and cooling tubing were extended through a waveguide to a laser generator located outside the MRI room. A test dose of diode laser energy (980nm,30sec,9W) was applied to verify the location of ablation nidus on real-time temperature and cumulative damage estimate mapping(TE/TE=24/10). Subsequently, ablative energy dose was delivered (27W for cycles of 90-271sec) with treatment endpoint based on on-line thermal monitoring of growing ablation. Fiber repositioning for additional ablation was conducted as needed. Final ablations were evaluated on a repeat set of pre-ablation scans consisting of TSE-T2 and pre- and post-contrast VIBE scans.

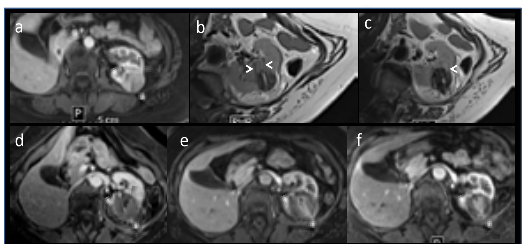

Fig 2: 83-year-old female with history of right radical nephrectomy for RCC. A 3.8-cm mildly enhancing left kidney lesion is noted on gadolinium-enhanced VIBE (arrows, a). MRI-guided biopsy performed in the same ablation session confirmed a oncocytic RCC. Multiple laser fiber placements were necessary based on initial size and on actual thermal damage maps obtained during ablation. The laser fiber placements are confirmed on intraprocedural TSE-T2 (arrowheads, b&c). Post contrast VIBE scans obtained immediately following ablation (d), after 5 weeks (e), and after 5 months (f) demonstrate a circumscribed non-enhancing ablation zone (arrows, d-f) without residual tumor or delayed complications.

Results: 3 biopsies revealed benign masses. One lesion was not biopsied. This analysis therefore includes 17 laser ablations of renal tumors. Biopsy results showed 16 RCCs (10 clear cell, 2 chromophobe, 1 oncocytic, 1 papillary, 2 not specified) and one renal metastasis from lung cancer. Target tumor sizes were 0.7-3.8 cm (10 right-, 7 left-sided). 5 patients had a single kidney, 2 patients had prior ipsilateral partial nephrectomy, 2 patients had prior contralateral ablations, and 2 lesions were recurrent masses at prior cryoablation margins. Access to the desired part of the kidney using the 14.5-cm-long introducing needle was feasible in all cases, including one morbidly obese patient, with no space constraints encountered within the 70-cm magnet bore. The flexible nature of optic laser fibers eliminated the complexity of handling bulky ablation probes, and the traction exerted by their cablings and fitted the MRI environment. The short ablation cycle facilitated accurate temperature mapping during controlled suspended ventilation without the need to implement motion correction algorithms. Applied laser energy was 4050- 79380J per lesion, with dosage calibrated based on real time feedback of tumor response to ablation. One patient had a moderate self-limited perinephric hematoma related to the biopsy part of the procedure. Otherwise, no early or delayed complications were encountered. Follow-up durations ranged between 0.6 - 28.6 months (mean = 11.9 months). No residual or recurrent neoplasm was identified in any patient.

Discussion & Conclusion: This investigation reports the improved access for interactive guidance and real time monitoring of renal ablation procedures performed entirely within an interventional MRI suite via the use of a short introducing needle and a flexible laser fiber. The technique represents a considerable departure from the complex handling of cryo- and RFA probes within the MRI environment and may facilitate a better future dissemination of MRI-guided renal ablation as a mainstream technology. The procedure is well tolerated with a high safety profile. Long-term follow up results for up to >28 months also point to a promising, efficacious ablative technique with no residual or recurrent neoplasms in our series. Further assessment of long-term efficacy in a larger cohort of subjects is underway.

References:

[1] Lewin JS, Nour SG, Connell CF, et al. Radiology. 2004; 232(3):835-45.
[2] Silverman SG, Tuncali K, vanSonnenberg E, et al. Radiology. 2005; 236(2):716-24.

MR-guided tumor sampling using mass spectrometry

Nathalie Y.R. Agar
Departments of Neurosurgery and Radiology, Brigham and Women's Hospital, and Department of Cancer Biology, Harvard Medical School and Dana-Farber Cancer Institute, Boston, MA, USA

Mass spectrometry provides a new tool for the direct molecular analysis of tissue during surgery, and can also provide significant insight in the development of drugs targeting tumors of the central nervous system.

Using ambient ionization mass spectrometry, we rapidly detect tumor metabolites from tissue sections of surgically-resected tumors without time-consuming preparation. The method is validated by correlating 2D mass spectrometry imaging of tissue specimens with histopathology, and used to characterize the molecular composition of tissue within seconds to minutes. Imaging tissue sections with mass spectrometry shows that diagnostic molecular signatures overlap with areas of tumor, thereby indicating tumor margins. We have installed a mass spectrometer in our Advanced Multimodality Image Guided Operating (AMIGO) suite at BWH and demonstrate the molecular analysis of surgical tissue during brain surgery. Imaging tissue sections with DESI MS shows that the onco-metabolite 2-hydroxyglutarate (2-HG) signal overlaps with areas of tumor and that 2-HG levels correlate with tumor content, thereby indicating tumor margins. Mapping the 2-HG signal onto 3D MRI reconstructions of tumors allows the integration of molecular and radiologic information to potentially inform clinical decision making.

Drug transit through the blood-brain barrier (BBB) is essential for therapeutic responses in brain tumors. Using matrix assisted laser desorption ionization mass spectrometry imaging (MALDI MSI) in pre-clinical animal models, we visualize drug and metabolites penetration in brain tissue without molecular labeling. We validated heme as a simple and robust MALDI MSI marker of the vasculature and go on to provide examples of how MALDI MSI can provide chemical and biological insights into BBB penetrance and metabolism of small molecule signal transduction inhibitors in the brain.

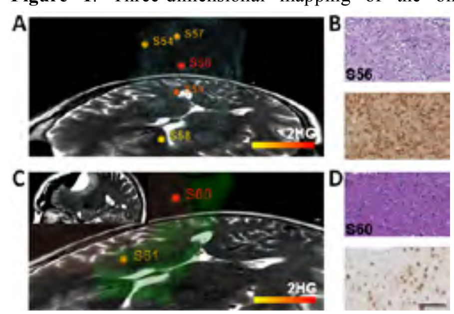

Figure 1. Three-dimensional mapping of the onco-metabolite 2-HG over MRI volume reconstruction for an oligoastrocytoma grade II surgical case. (**A**) Normalized 2-HG signal is represented with a warm color scale as indicated by the scale bar, set from the lowest to highest levels detected from this individual case. (**B**) High magnification microscopy images of an H&E-stained section of FFPE tissue from sample S56 showing high tumor cell concentration (**Upper**) and of IHC for IDH1 R132H mutant (**Lower**). (**C**) 2-HG over tumor volume reconstruction from the T2-weighted intraoperative MRI. (**Inset**) The residual lesion. (**D**) Microscopy images of H&E-stained sections of FFPE tissue from sample S60 showing the presence of residual tumor cells (**Upper**) and of IHC for IDH1 R132H mutant (**Lower**). (Scale bar, 100 μm.)

Hybrid interventions – indirect MR assistance or direct MR guidance

F. K. Wacker

Department of Radiology, Hannover Medical School, Germany

Abstract: With the increasing diagnostic use of MRI over the last decades a growing interest for MR guidance of interventional procedures became evident. This stems from the unique advantages of MRI which include excellent soft tissue contrast, functional as well as structural information, flexible image plane adjustments and lack of ionizing radiation exposure. Technical improvements such as short magnet bores, stronger and more homogeneous magnets, improved gradient performance as well as new data sampling and reconstruction techniques have fueled the growth of MR-guided procedures. However, workflow issues, poor access to the patient in the magnet and lack of devices make MR guided procedures somewhat challenging.

At the same time, established interventional imaging techniques such as x-ray fluoroscopy for vascular procedures and CT and ultrasound for percutaneous needle based interventions show a remarkable progress as well. Systems specifically tailored for interventions, interventional modes in diagnostic scanners and interactive device guides are examples for hardware improvements. Progress in image fusion, online registration and overlay techniques help to augment 2D techniques such as fluoroscopy or ultrasound with information from MRI. In combination with device tracking techniques fusion technologies offer a tailored workflow in a procedure friendly environment.

A few institutions use combined X-ray fluoroscopy/MR imaging systems in one or two connected rooms. Such hybrid systems offer the strengths of two modalities. However, the patient has to be moved between the two separate gantries, which is somewhat time consuming. In addition, rooms and equipment of such setups constitute a high capital investment. Therefore, the use of MRI images independently acquired prior to the procedure is a valuable alternative to both, hybrid rooms as well as true MRI guidance

We will present clinical and preclinical examples for hybrid interventions, MRI guided procedures and interventions based on previously acquired MR images. Techniques such as cone beam C-arm CT including 2D-3D and 3D-3D registration methods, ultrasound MRI fusion based guidance and augmented reality will be discussed.

Poster Presentations

Localization of the puncture spots of index lesions (PSIL) and detection rate of prostate carcinomas (PCa) in MR guided biopsies (MRGB) after negative TRUS [Transrectal Ultrasound] guided biopsies (TRGB)

Dr. med. Stefan Rödel (1), Sebastian Blaut (2), Dr. med. Eberhard Dürig (3), Dr. rer. nat. Michael Burke (4), Dipl.-Ing. Ronny Paulick (5), Prof. Dr. med. habil. Gunter Haroske (3), Prof. Dr. med. habil. Frank Steinbach (2), Prof. Dr. med. habil. Thomas Kittner (1)

(1) Radiologische Klinik, Krankenhaus Dresden-Friedrichstadt, Dresden, Germany
(2) Urologische Klinik, Krankenhaus Dresden-Friedrichstadt, Dresden, Germany
(3) Pathologisches Institut, Krankenhaus Dresden-Friedrichstadt, Dresden, Germany
(4) GE Healthcare, Solingen, Germany
(5) Saegeling Medizintechnik Service- und Vertriebs GmbH, Heidenau, Germany

Purpose: Retrospective analysis of the localization of puncture spots of index lesions and the detection rate of prostate carcinoma using MRGB after systemic negative TRGB.

Material and Methods: 76 patients (pat), median age 68 years, after at least one (median 2) negative TRGB with suspicious PSA (median 8.6 ng/ml) and with "punctureable lesions" defined by mpMRI (multiparametric MRI) [1.5 T, ER-coil, T2/DWI/DCE] underwent a MRGB (T2/DWI, TRIM, 18 G - biopsy gun). For patients with histological confirmed PCa, a retrospective classification of the PSIL was conducted according to a standardized 27 (36)-MR graphic prostate reporting scheme and the measurement of the distance of the dorsal and caudal prostate border and lateral to the sagittal midplane. Mann-Whitney Rank Sum Test was used to assess statistical significance.

Results: Detecion rate for prostate carcinomas by MR guided biopsy after negative TRUS guided biopsy was 35%. In these patients the preoperative distribution of Gleason Score (Gl) was: Gl 6 in 48.1%, Gl 7a in 33.3%, Gl. 7b in 14.8%, Gl. 8 in 3.75%.
41% of PSIL were solely located more than 17 mm away from the dorsal prostate border and are thus difficult to access with a common systemic TRGB. 59% of PSIL were located at a distance less than 17 mm from the dorsal prostate border and therefore should be accessible by TRGB. Posterior PSIL were significantly (p=0.02) further caudal than anterior PSIL (median: 19 mm vs. 28 mm to the apex level). 82% of anterior PSIL and 94% of posterior PSIL were located in the peripheral zone (PZ). 75% of posterior PSIL are located laterally.

Conclusion: Detection rate for prostate carcinomas by MR guided biopsy after negative TRUS guided biopsy in our clinic is comparable to results given in the literature.
Unexpectedly striking was the high number of puncture spots on index lesions posterior lateral caudal. These dorsal puncture sites actually should be accessible via systemic TRGB; however are they not detected within the scope of the systemic unsighted TRGB.

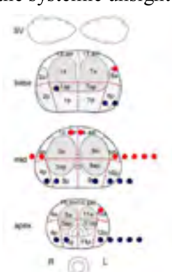

Fig.: Prostate regions of localization of puncture spots of index lesions (MRGB after negative TRGB).

Application of multiparametric MRI PI-RADS scores and a novel system for MRI/TRUS-fusion guided biopsy for the detection of prostate cancer

Susanne Tewes[1*], Katja Hueper[1*], Dagmar Hartung[1], Florian Imkamp[2], Thomas Herrmann[2], Juergen Weidemann[1], Markus A Kuczyk[2], Frank Wacker[1], Inga Peters[2]
*contributed equally
[1]*Institute for Diagnostic and Interventional Radiology, Hannover Medical School*
[2]*Department of Urology, Hannover Medical School*

Purpose - To evaluate multiparametric MRI PI-RADS scores as proposed by the ESUR and a novel system for MRI/TRUS-fusion guided biopsy for detection of prostate cancer (PCa) in patients with previous negative biopsy (91%), no previous biopsy (6%) and on active surveillance (3%).

Material and Methods – Thirty-tree men with clinical suspicion of PCa underwent multiparametric MRI (T2, DWI, DCE) on a 3T MRI. 65 lesions were evaluated in consensus of two radiologists who were blinded to clinical findings and histology. PI-RADS scores for each MRI sequence, the sum of the PI-RADS scores (PI-RADS sum) and a global PI-RADS were determined (figure 1). MRI/TRUS-fusion guided biopsy was performed after manual contouring of the prostate and the target lesions using BioJet® software (D&K Technologies, Germany, figure 2a) combined with a transrectal ultrasound system (BK Medical). Fusion of MRI- and TRUS-images is based on rigid registration (figure 2b). PI-RADS scores of the dominant lesion were compared with pathological evaluation. Diagnostic accuracy was determined on a per-patient basis using ROC-curve analysis.

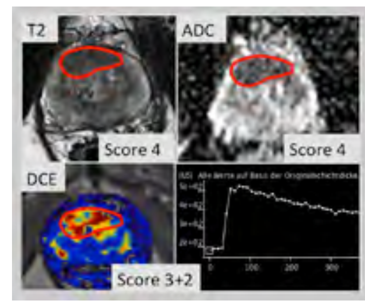

Figure 1: 70-year-old patient. After two negative TRUS- biopsies, PSA-levels rose to 6.5 µg/l. Multiparametric MRI was performed. A PIRADS-Sum of 13 was determined, giving an overall PIRADS of 5, most probably malignant. Fusion-guided biopsy revealed a Gleason 4+5=9 tumour in 5/5 biopsy cores.

Results - MRI/TRUS-fusion guided biopsy was reliable and successful for 64/65 lesions and revealed PCa in 25% of patients. One anterior lesion was not reached by transrectal biopsy; this patient was excluded from the analysis. No difference of PSA-levels between patients detected with and without PCa was found (11.4±8.4 vs 8.4±3.8 µg/L, p=0.36). Lesion size was comparable (12.4±6.7 vs 12.7±4.8 mm, p=0.87), whereas global PI-RADS and PI-RADS sum scores were higher in patients with PCa (global PI-RADS: 4.0±1.3 vs 2.6±0.9, p<0.01; PI-RADS sum: 10.6±3.5 vs 6.9±2.7, p<0.01). Best diagnostic accuracy with sensitivity and specificity of 88% and 83%, respectively, was achieved by using global PI-RADS with a cut-off ≥4 (AUC = 0.82) or PI-RADS sum scores with a cut-off of ≥10 (AUC = 0.79). The negative predictive value was 95%. Each sequence alone had a lower diagnostic accuracy. Sensitivities/ specificities were 88/71% for T2 (cut-off ≥3), 88/71% for DWI (cut-off ≥3) and 75/82% for DCE (cut-off ≥4).

Conclusion - Multiparametric MRI PI-RADS scores allow diagnosis of PCa with high sensitivity and specificity and were superior to scores of each sequence alone. The novel system is reliable for MRI/TRUS-fusion guided biopsy.

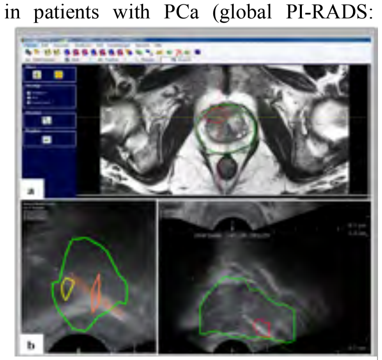

Figure 2: a) BioJet® software for contouring of the prostate and the target lesion.
b) MRI/TRUS-fusion and –biopsy.

MRI-guided Prostate Biopsy in the Treatment Planning of Tumor-Boosted Radiotherapy

Ménard C[1,2], Abed J[2], Simeonov A[1,2], Foltz W[1,2], Craig T[1,2], Chung P[1,2]. University of Toronto[1] and Princess Margaret Cancer Centre[2]

Purpose: To determine the role and need of biopsy confirmation in the treatment planning process of tumor-boosted radiotherapy.

Materials and Methods: 22 patients with localized prostate cancer and a visible nodule on MRI corresponding to histopathology on TRUS-guided biopsy were prospectively enrolled between 2012 and 2014. In the treatment planning process for tumor-boosted radiotherapy, patients underwent a confirmation MRI-guided tumor biopsy at the time of fiducial marker (FM) insertion. Integrated treatment planning MRI and biopsy procedures were performed in a 3T scanner (Verio, Siemens) using a endorectal coil system (Hologic Inc) and transperineal template under online nagivation (Aegis, Hologic). Images were acquired with needs *in situ* to document tumor targeting accuracy. MRI included axial T2w TSE, DWI, and DCE acquisitions. Tumor bearing regions were scored according to PI-RADS classification. All PI-RADS=3-5 lesions were targeted for 1-2 core biopsy prior to insertion of FMs. Tumors were segmented based on MRI and biopsy findings. 11 patients received an integrated boost to external beam radiotherapy to 95Gy, and 11 patients received and HDR brachytherapy boost of 11Gy.

Results: Thirty six biopsy targets were identified, of which 28 were confirmed malignant. All (12/12) PI-RADS=5 lesions were confirmed malignant, while 88% (14/16) PI-RADS=4 lesions and 25% (2/8) PI-RADS=3 lesions were found malignant. Importantly, six targets were missed marginally at the time of biopsy, primarily due to needle deflection by tumors.

Conclusions: Biopsy confirmation of PI-RADS 4,5 lesions may not be necessary in the treatment planning process for tumor-boosted radiotherapy, while PI-RADS=3 lesions should be confirmed prior to dose-escalation. Our observation of needle deflection by tumors highlights the difficulties inherent in limited sampling, and potential challenges if using alternate guidance strategies.

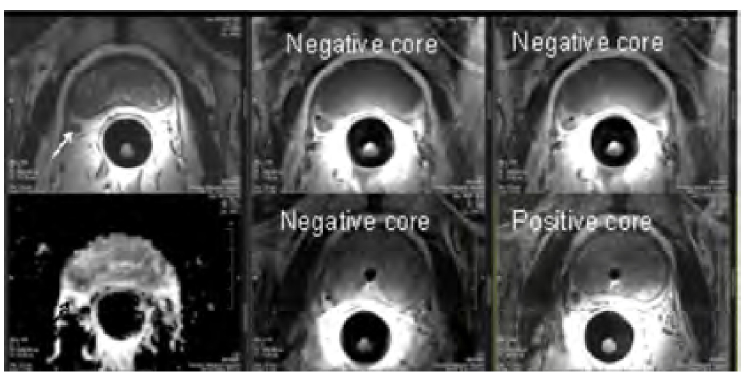

Feasibility of a pneumatically actuated MR-compatible 2nd-generation robot for transrectal prostate biopsy guidance

JGR Bomers[1], DGH Bosboom[1], G. Tigelaar[2], D Yakar[1], JJ Fütterer[1,3]
[1]Department of Radiology, Radboud University Medical Center, Nijmegen, the Netherlands.
[2]Soteria Medical, Arnhem, the Netherlands
[3]MIRA, University of Twente, Enschede, the Netherlands

Purpose:
The purpose of this study was to assess the feasibility of an MR-compatible, robotic device as an aid to perform transrectal prostate biopsy in males with rising PSA and previous negative biopsies.

Materials and Methods:
This prospective study was approved by the institutional review board and written informed consent was obtained from all patients. Permission was given for inclusion of 20 patients. Inclusion criteria for prostate biopsy were; a history of at least one negative transrectal ultrasound-guided biopsy, no prior treatment of the prostate, and at least one suspicious prostate lesion with a PIRADS score of 3 or higher detected on the diagnostic multi-parametric MRI. The multi-parametric MRI comprised T2-weighted, diffusion-weighted, and dynamic contrast-enhanced sequences. All procedures were performed in a 3T MR scanner with an MR-compatible, remote controlled, second generation robotic biopsy device (Soteria Medical, the Netherlands).

Results:
Thus far 9 patients were included in this ongoing study. A total of 9 prostate lesions with a PIRADS score of 3 or higher were detected in 9 patients. Median patient age, PSA, previous negative TRUS sessions was 69 years, 11 ng/mL, and 2 sessions respectively. All lesions were reachable for biopsy. No complications occurred. A median of 2 biopsies per lesion were taken. Six out of 9 lesions (67%) were proven to be prostate cancer (1x Gleason Score (GS) 9, 1xGS8, 3xGS7, 1x GS6). Two biopsies contained prostatitis, and one contained no abnormality. The median procedure time was 37 minutes. Median manipulation time for needle guide movement was 7.8 minutes.

Conclusion:
It is feasible to perform transrectal prostate biopsy using a remote controlled, MR-compatible, robotic device as an aid. It is a safe, fast, and efficient way to biopsy suspicious prostate lesions with a minimum number of biopsies per patient.

Catheter reconstruction and displacement during MRI guided focal HDR prostate brachytherapy

M. Maenhout[1], M.A. Moerland[1], J.R.N. van der Voort van Zyp[1], M. van Vulpen[1]

[1]Department of Radiation Oncology, University Medical Centre Utrecht, The Netherlands

Purpose/Background

Localized prostate cancer is common in men. Many of these localized tumours are biologically indolent. However, nowadays, whole gland treatments, such as radical prostatectomy or low dose rate brachytherapy, are often implemented. These whole gland treatments can lead to overtreatment and severe toxicity. Therefore, strategies to reduce toxicity, such as focal treatment, are warranted. With the use of multiparametric MRI, the focal tumour region can be localized (Figure 1). After insertion of the catheters for the high-dose-rate (HDR) brachytherapy procedure, reconstruction of these catheters is required to obtain a brachytherapy treatment plan. In case of whole gland low-dose-rate brachytherapy procedure, needles are often reconstructed on ultrasound images. In focal HDR brachytherapy treatment, exact irradiation of the tumour focus is of great importance. With the help of MRI guidance, precise catheter placement within the tumour in the prosate is possible. Therefore, reconstruction of the catheters on MR imaging is required to generate a focal high-dose-rate (HDR) brachytherapy treatment plan. Furthermore, it is possible to determine whether catheter tips are in the desired position within the tumour prior to irradiation and if migration of the catheter has occurred during HDR brachytherapy treatment. In this abstract, reconstruction and displacement of the brachytherapy catheters on MR images are described.

Material and Methods

In the UMC Utrecht, 18 patients underwent MRI guided focal high dose rate brachytherapy. For this treatment, self-anchoring umbrella catheters were used, developed by Pieters *et al.* (2006)(1). Before treatment, a 3 T multiparametric MRI was performed to assess tumour localization (Figure 1). During the MRI guided brachytherapy procedure, a 1.5 T MRI was made directly after catheter placement. 3D images were acquired with balanced steady state free precession sequence. In sagital direction SPIR (spectral presaturation with inversion recovery) and in transverse direction SPAIR (spectral attenuated inversion recovery) fat suppression was applied. These scans were used for catheter reconstruction and generation of the intra-operative HDR brachytherapy plan. After treatment, a few hours later, a second MRI was made and matched with the previous MRI, to determine if the irradiation catheters migrated.

Results

For all 18 patients, irradiation catheters were clearly visible on MRI (see Figure 2), so catheter reconstruction for treatment planning was easily performed.

In 5 patients, catheter migration was assessed by comparing the coordinates of the needle tip on the planning MRI with the coordinates of the needle tip on the MR imaging after treatment. A maximum displacement of 4 mm was seen in only 1 catheter. A displacement of 2-3 mm was seen in 3 catheters and a displacement of 1-2 mm in 8 catheters. In all other 58 catheters, a maximum catheter migration of only 0-1 mm was measured.

Conclusion

Catheter reconstruction on MRI during MRI guided treatment can be performed easily. There is hardly any displacement of catheters during MRI guided treatment.

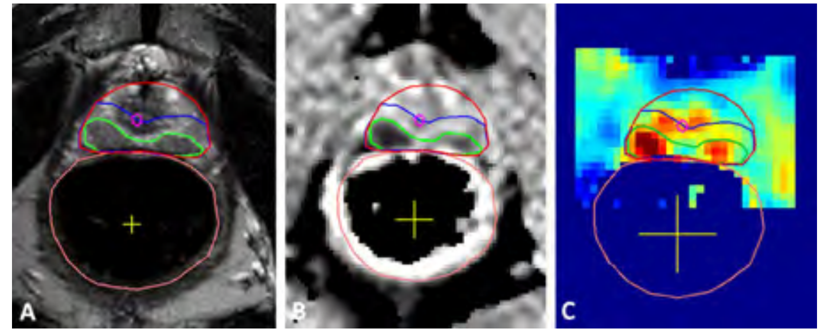

Figure 1: Assessment of tumour localization on multiparametric MRI. A. transversal T2 weighted image, B. transversal ADC, C. transversal K-trans

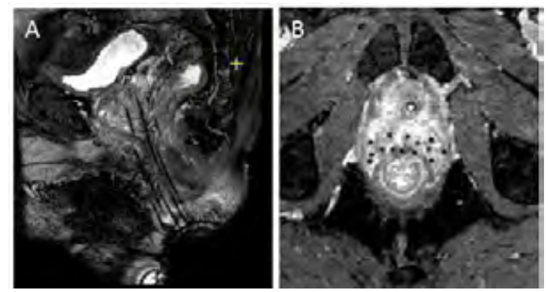

Figure 2: catheter visualization on MRI. A. sagital view, B. transversal view.

References

1. Pieters BR, van der Grient JN, Blank LE, Koedooder K, Hulshof MC, de Reijke TM. Minimal displacement of novel self-anchoring catheters suitable for temporary prostate implants. Radiother Oncol. 2006 Jul;80(1):69-72.

Outcomes of MRI-Guided Local Salvage after Radiotherapy for Prostate Cancer: Implications for a Focal Strategy

Ménard C[1,2], Pulvirenti T[1,2], Samavati N[1], Lee J[2], Abed J[2], Simeonov A[1,2], Foltz W[1,2], Rink A[2], Haider M[1], Brock K[1], Jewett M[1,2], Chung P[1,2]. University of Toronto[1] and Princess Margaret Cancer Centre[2]

Purpose: To determine if early results using MRI-guidance supports a focal salvage brachytherapy strategy to improve patient outcomes.

Materials and Methods: 21 patients with focal recurrence of prostate cancer after radiotherapy were prospectively enrolled between 2009 and 2013. Recurrent tumors were segmented using multiparametric MRI-guided biopsy. 6 patients underwent radical prostatectomy (RP), and whole-mount histopathology was registered to MRI. 15 patients were treated with HDR salvage brachytherapy using a dose-painting approach. 2 patients did not complete therapy and were excluded from analysis. Median follow-up was 36 and 42 months for the RP and HDR cohorts, respectively. Brachytherapy was delivered in two implants a mean 10 days apart (7-14). For each implant, a dose of 11Gy to the tumor (8Gy to the prostate gland) was administered. Rates of biochemical control, local control, and distant failure were measured at last follow-up. Local control was determined using MRI-guided biopsy 2-3.5 years after HDR. Late adverse events were graded according to CTCAEv4.0, and compared using a 2-tailed Z test.

Results: Local failure was found in 3 of 11 patients with repeat biopsy, all within the high-dose region. Biochemical failure was prevalent (n=7/13) due to systemic progression. Outcomes were similar between HDR and RP cohorts, except for higher grade 3 toxicity with RP (8 vs. 67%, p=0.007) due to bladder neck contractures. RP histology corresponded with all sites of MRI-defined tumors, but segmentation underestimated disease extent in all cases, and distant microfoci were found in 4/6 cases.

Conclusions: Dose-painted salvage HDR brachytherapy achieved favorable toxicity and local control. Patterns of failure indicate a need for better selection of patients with local-only disease and further dose-escalation to the tumor. A focal salvage strategy must consider uncertainties in tumor segmentation despite MRI-guided biopsy.

Figure: TOP – recurrence within GTV. BOTTOM: successful salvage.

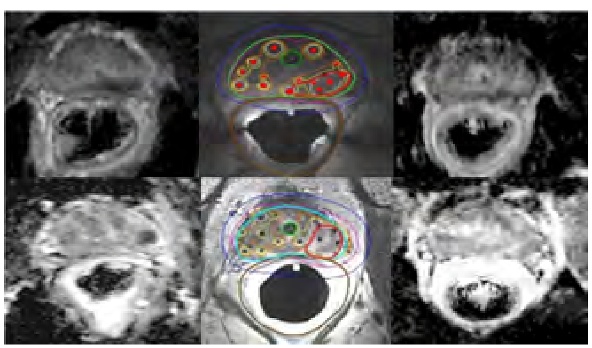

Design Considerations for a Flexible RF Coil Design for an Endorectal HIFU Device

John Matthew Pavlina[1], Tetiana Dadakova[1], Martijn Hoogenboom[2], Martin van Amerongen[2], Jurgen Futterer[2], Michael Bock[1]
[1]Medical Physics, Department of Diagnostic Radiology, University Medical Center Freiburg, Germany.
[2]Department of Radiology, Radboud University Nijmegen Medical Centre, Nijmegen, Netherlands.

Introduction

MR imaging of the human prostate is commonly performed with endorectal coils to increase the local SNR in the prostate gland. At present, two prostate coil types are commercially available: single-channel flexible loop coils (Medrad) at 1.5T and 3T, and two channel rigid coils (Hologic, Inc).The purpose of this work was to evaluate whether flexible endorectal coils can be combined with an endorectal high intensity focused ultrasound (HIFU) device. The endorectal coil is designed to increase the MR sensitivity in the HIFU treatment area which reduces the temperature error during HIFU ablation. As the coil is in close proximity to the US transducer and is loaded by the US coupling medium, it requires tuning within the magnet bore under tissue loading conditions. Tuning is impracticable for clinical applications, and thus this research aims at defining design considerations for an endorectal coil so that it can be pre-tuned and matched for endorectal HIFU applications.

Materials and Methods

Coupling between RF coil and US transducer can be minimized by increasing the distance between coil and transducer, and thus a coil design was chosen that can be etched on a flexible substrate. For feasibility analysis a flexible coil was made using copper on a Kapton® polyimide substrate (Fig. 3). The dielectric loading of the coil by the proximity of a dielectric medium (here: water) induces losses that can be described [1] by a parasitic capacitance and a series resistance between the coil and the dielectric (cf. equivalent circuit in Fig. 1). Using this simplified coil model an analytical solution has been derived for the circuit.

For comparison with this theoretical solution, a numerical coil model was implemented and simulated using the FEM software package (HFSS, ANSYS, Inc.). The coil (length: 8 cm, width: 4 cm, copper thickness: 0.035 cm) was placed in proximity to a US transducer (modeled as a copper sheet on a substrate) and water, and the conductivity of the water was varied. To assess the coil performance the field profile as well as, the change in reflected power was calculated, and the coil quality factor Q and the resonance frequency were evaluated.

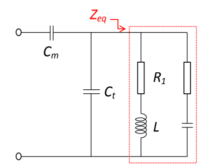

Fig. 1: Coil model with parasitic capacitance.

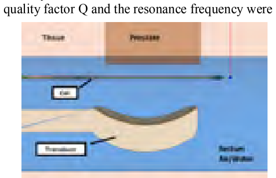

Fig. 2: FEM model with coil, US device, and surrounding medium.

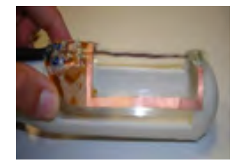

Fig. 3: Sample coil made on a flexible substrate

Results

As expected, when the coil was simulated with the US transducer the effect on the field profile was less than 1% in the area of interest. While when the conductivity of the water was varied between distilled water (0.00001 S/m) and tap water (0.1 S/m) some change is observed. Figure 4a shows a comparison between the *Q* changes calculated with simulation and the simplistic model. Both calculations predict a reduction of Q with increasing conductivity. The change in resonance frequency with respect to conductivity is shown in Figure 4b. At a conductivity of greater than approx. 10^{-3} the two models start to deviate. When the Q is no longer considered "high" (~Q<10) new parameters must be taken into account for which the simplistic model cannot accommodate. Since an RF coil in a HIFU system is directly exposed to the surrounding material, tuning and matching can become impractical, if the influences of loading conditions are not taken into account. Automatic tuning of coils has been proposed to compensate for different loading conditions; however, this requires additional tuning hardware which complicates the coil design. Since limited space inside the rectum (<4cm diameter) and size relative to all the other HIFU components must be considered as well, the use of a limited number of devices on the coil is preferable. Based on these calculations it is possible to characterize the change in resonance frequency based on prior conductivity assessments, which would greatly simplify the design and optimization of endorectal coils in HIFU treatment devices. A HIFU test was performed using a sample coil for evaluation purposes. The coil was placed in water and wrapped around a store bought chicken breast. Thermal ablation was performed and the temperature information was extracted during post processing. The coil worked as expected providing significant signal to backround of above 30dB in most areas of interest.

Acknowledgements

This work was supported by the BMBF, Eurostars Project E!6620 PROFUS.

References[1] J. Mispelter, et al. NMR Probeheads for Biophysical and Biomedical Experiments, 2006

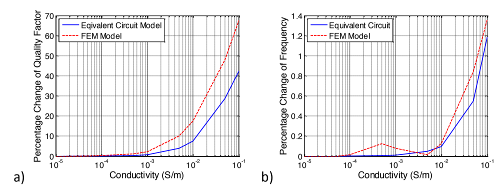

Fig. 4: The effect of conductivity on the quality factor (left) and resonance frequency (right) of the coil using the FEM model and an equivalent circuit model.

Fig. 5: 3T image of the meat with surrounding water bath.

Accuracy, precision and safety of needle tapping using a MR compatible robotic device for prostate interventions.

M. Maenhout[1], M.A. Moerland[1], L.J. van Schelven[2], J.J. van Veldhuijzen[2], E. Boskovic[2], H.Kroeze [2], J.R.N. van der Voort van Zyp[1], M. van Vulpen[1], J.J.W. Lagendijk[1]

[1]Department of Radiation Oncology, University Medical Centre Utrecht, The Netherlands
[2]Medical Technology & Clinical Physics, University Medical Centre Utrecht, The Netherlands

Purpose

In diagnostic and treatment procedures such as biopsies and brachytherapy for prostate cancer, magnetic resonance imaging (MRI) offers superior soft tissue contrast and therefore, improved visualization of the tumour and organs at risk. MR guidance during treatment can lead to more precise irradiation of the tumour location. Due to space restrictions inside the closed-bore MR scanner, the development of a MR-compatible robotic interventional system is required. A robot dedicated to MRI-guided interventions (Figure 1) in prostate cancer patients is being developed at the University Medical Center Utrecht (UMCU). This robotic device allows on-line MRI-guided needle placement. The needle is inserted stepwise using a hammering mechanism, this to prevent prostate deformation.

The aim of this work is to investigate accuracy, precision and safety of the unique needle system (Figure 2) and tapping mechanism of the robotic device. The robotic device will only target the focal tumour lesion within the prostate through a focal HDR brachytherapy technique. Therefore, accuracy, precision and safety are of great importance to reach the exact tumour focus.

Material and Methods

Hammering experiments were performed on a foam phantom with a body equivalent insertion force (30-40 N), to determine safety of the needle system. Safety of the needle system was defined as no damage to the needle and no excessive needle bending.

Different size steps and pressures were used to insert the needle into a phantom. Step sizes varied from 2-5 mm, the hammer was launched using air pressures varied from 2-4.5 bar. The needle was inserted several times. After each needle insertion, bending of the needle was measured and the needle was inspected for macroscopic damage.

To assess precision, the needle was inserted 5 times through an agar gel phantom to a predefined target point on a 1 mm grid paper (Figure 3).

Tests in the MR scanner were performed to assess accuracy of targeting. A marker attached on the robot near the needle exit point was used as a reference. This was at 9 cm from the target point in the phantom.

Results

Bending of the needle depends on step size and the pressure of the hammering system. A step size of 2 mm with a pressure of 2 bar showed no damage to the needle and an acceptable bending of $\leq$1.5 mm for all insertions. After the agar gel phantom was perforated 5 times, a needle deviation of 1.2 mm was observed (needle diameter of 1.9 mm, Figure 3). Moving the robotic device 2 cm in left-right direction and 9 cm in cranio-caudal direction, targeting a phantom in the MR coordinate system, with the marker on the robot as a reference, was accurate within 1mm.

Conclusion

The preclinical tests of the needle system and tapping mechanism show that the needle is safe and that the robotic MR guided targeting is accurate.

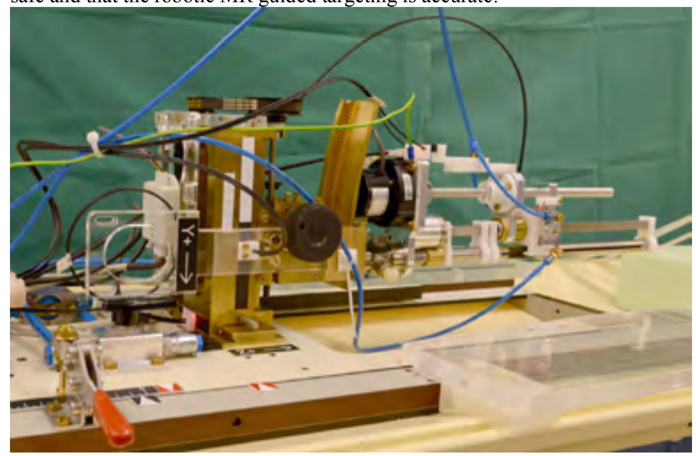

Figure 1. MR compatible robotic device


Figure 2. Needle

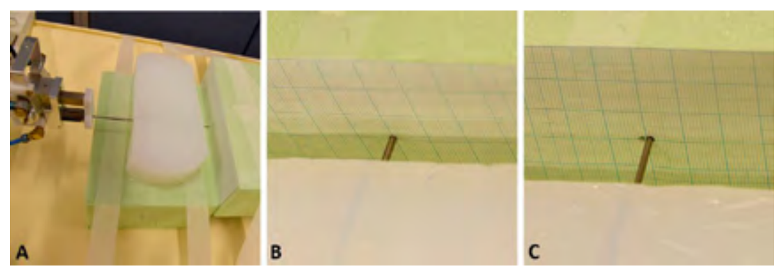

Figure 3. Precision of needle insertions by hammering mechanism. A. Set up. B. First insertion. C. 5 insertions within a circle of 1.2 mm radius (needle diameter of 1.9 mm).

Title: Pushing X-ray CT out of the equation: In vivo RASOR MRI-based seed detection for post-implant dosimetry in LDR prostate brachytherapy.

Seevinck PR[1], van den Berg CA[2], Zijlstra F[1], Philippens ME[2], Hoogcarspel SJ[2], Lagendijk JJ[2], Viergever MA[1], Moerland MA[2]
[1]*Image Sciences Institute, Imaging Division, University Medical Center Utrecht, Netherlands,* [2]*Department of Radiotherapy, Imaging Division, University Medical Center Utrecht, Netherlands*

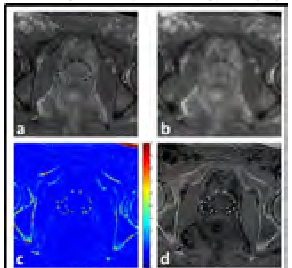

Fig. 1.a) Onresonance, b) off-resonance, c) relative signal increase (scale 0-10) and d) background-suppressed RASOR image of the prostate after permanent seed brachytherapy.

Introduction: Postimplant dosimetry is a crucial quality assurance measure for permanent seed low dose rate (LDR) prostate brachytherapy[1]. In recent years, X-ray CT has been the modality of choice for the visualization of seeds for postimplant dosimetry. However, CT faces difficulties in accurate contouring of the prostate due to poor soft tissue contrast, whereas MRI exhibits superior soft tissue contrast[2]. Therefore, it would be favorable if MRI could be used to both accurately depict the seeds and delineate the prostate, enabling fully MRI-based postimplant dosimetry. Here, the feasibility to depict brachytherapy seeds *in vivo* using an optimized version of the method called center-out radial sampling with off-resonance reconstruction (RASOR), eventually aiming at fully MRI-based postimplant dosimetry, will be investigated and qualitatively compared to conventional X-ray CT.

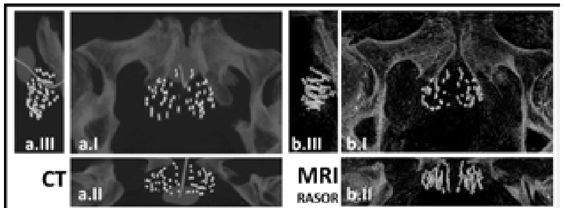

Fig. 2. a I,II,III) Orthogonal MIP's of a 3D CT dataset, depicting seeds, bone and a urinary catheter. b I,II,III) Orthogonal MIP's of a 3D background-suppressed RASOR dataset rigidly registered to the CT data using the bone structures, also depicting both the seeds and the bone in a fluoroscopic representation.

Methods: *Imaging parameters:* A 3D Stack-of-Stars balanced Turbo Field Echo (bTFE) with SPAIR fat-suppression (220Hz offset) and full profile sampling was developed; TFE factor = 30; TR/TE =3.3/1.6ms; BW = 1085 Hz; NSA = 2; density of angles = 90%; total scan time = 3min24sec. Other imaging parameters included a field strength of 3T (Philips Achieva TX), FOV = 250x250x90 mm, scan matrix 250x250x45; recon. matrix = 512x512x90; flip = 25. *Processing:* Off-resonance reconstructions were obtained retrospectively using Δf_0=2KHz[3,4]. The relative signal increase (Fig. 1c) was calculated by dividing the RASOR image (Fig. 1b) by the onresonance image (Fig. 1a). The final background-suppressed (bs) RASOR image (Fig. 1d) was obtained by subtraction of the onresonance image. Orthogonal maximum intensity projections (MIP's) were made from the bs-RASOR data after rigid registration to the CT data, as depicted in Fig. 2b I, II, III. *Patients:* Four patient who underwent permanent seed prostate brachytherapy and standard dosimetry (CT and MRI based) at 1 month postimplant received an additional MRI scan according to the methods just described.

Results: The proposed RASOR imaging sequence enabled accurate depiction of the brachytherapy seeds with high positive contrast and high specificity. The background suppression enabled seed visualisation in a fluoroscopic way (Fig. 2.b). Interestingly, the bs-RASOR technique depicted bone structures with relatively high values, enabling 3D rigid registration of MRI (fig. 2b) to CT (Fig. 2a). When aiming at fully MRI-based postimplant dosimetry, the fact that a seed is depicted as a 'dumbell-shaped' hyperintensity, as thoroughly described and demonstrated in previous work[3,4], should be taken into account.

Conclusions: This study demonstrates the feasibility of *in vivo* MRI-based localisation of implanted brachytherapy seeds with positive contrast and high specificity, using a robust, clinically available imaging sequence with RASOR reconstruction and straightforward post-processing.Other applications of this technique may be bone and fiducial imaging for MRI-based treatment planning in external beam radiotherapy, bone imaging for dose calculation and attenuation correction in PET-MRI.

References: [1]Henry AM et al. Int.J.Rad.Oncol.Biol.Phys.2010;76,1,50–56., [2]Brown AP et al. Brachytherapy. 2013;12(5):401-7., [3]Seevinck PR et al. Magn Reson Med. 2011;65(1):146-56., [4]de Leeuw H et al. Magn Reson Med. 2013;69(6):1611-22.

The animal test of a portable MRI guided HIFU system

Ihyuan Kuo[1], Vivi Hsieh[2], Chin-Jung Wang[3], San-Chao Hwang[2], Hsu Chang[2]

[1] EpiSonica Corporation, [2] National Health Research Institute, [3] Chang Gung Memorial Hospital, Taiwan

The prototype of a portable MRI guided High Intensity Focused Ultrasound (HIFU) system for abdominal applications had been developed in the National Health Research Institute in Taiwan. The system configures with an arc positioning structure, which is detachable from the patient table and which fits inside the gantry of an MRI system. The system is equipped with a home-made annular array HIFU probe, attached to the arc structure for treatment. Four degrees of freedom, three mechanical and one electronic, are allowed for automatic control of the position of the focal lesions. In order to prepare for the first-in-human clinical trial, three live porcine animals have been tested to produce thermal lesions on the inner side of the thigh muscle area using a 3T MRI system in Chang Gung Memorial Hospital at Linkou, Taiwan. The animals were 6 to 8 months old and weighed between 50 to 70 kg. When 300W electrical power was applied to the HIFU probe for 30 and 45 seconds, there showed successful thermal lesion generation on the targeted spots. MR Thermometry was used to monitor the temperature rise on the treatment spots every 2 seconds throughout the treatment procedures. Post procedure MR T2 images also showed clearly lesion contrast on the treatment spots.

Respiratory-induced Deformation Analysis of Liver using Branching Structure of Portal Vein for MR Images for HIFU

Tatsuhiko Matsumoto[1], Etsuko Kumamoto[2], Daisuke Kokuryo[3] and Kagayaki Kuroda[4,5]
[1] *Graduate School of System Informatics, Kobe University, Kobe, Japan,*
[2] *Information Science and Technology Center, Kobe University, Kobe, Japan,*
[3] *Molecular Imaging Center, National Institute of Radiological Sciences, Chiba, Japan,*
[4] *Graduate School of Engineering, Tokai University, Hiratsuka, Japan,*
[5] *Kobe International Frontier Medical Center, Kobe, Japan.*

Purpose: The target tracking technique to “lock-on” the focal spot is required for High intensity focused ultrasound (HIFU) treatment of the liver[1)]. In order to maintain sufficient tracking accuracy, both translation and deformation of the tissue need to be detected. In this study, we analyzed the three-dimensional deformation of the liver under slow breathing based on the morphological changes of the branching structures of the portal vein obtained by MR imaging.

Method: Multi-slice MR images were acquired in a healthy volunteer liver with Fast Imaging Employing Steady state Acquisition (FIESTA) with 3.0T MRI (Signa EXCITE HDxt ver.16, GE Healthcare UK Ltd.). Imaging conditions were as follows: TR/TE, 4.85/1.98 ms; slice thickness, 5mm; inter-slice spacing, 0 mm; field of view, 35 x 35 cm^2; acquisition matrix, 256 x 192; flip angle, 90 degrees. Six slices covering a sagittal slab of 3-cm thickness were continuously acquired during slow breathing. The images in a slab were then linearly interpolated to have isotropic voxel data. The slabs at different time points were re-ordered according to the diaphragm position extract from each image using a three-dimensional template-matching method. Nine regions of interest including branching vessels in the volume were also tracked using the three-dimensional template-matching method. Search areas of tracking branching points were set in order to height of diaphragm. Distance between the center of the reference ROI and other eight ROIs’ center were calculated for each image sets. Expansion and contraction of each ROI pair were calculated.

Result: As shown in Figure 1, distance between the reference and the other ROIs were not flat. The expansion and contraction were 5mm, 60mm and 20mm in AP, SI and LR direction. The gradient of the each line expresses the degree of the expansion. The expansion in the anterior region was 5 to 6 mm larger than the posterior region, suggesting that the organ motion was more restricted in the posterior region by the surrounding tissues.

Conclusion: The results demonstrated that the three-dimensional motion tracking of the liver was feasible by observing the vessel branches with rapid MR imaging and the pattern matching techniques.

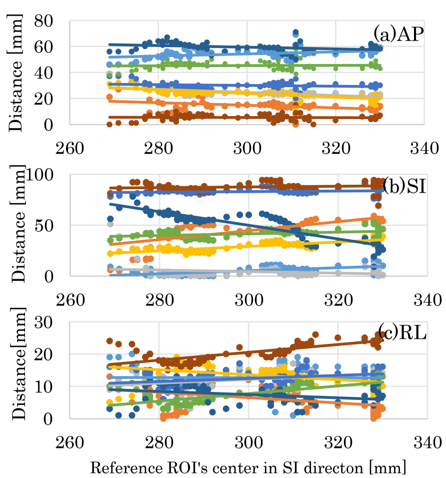

Figure1: Distance between the reference ROI and the other ROIs at the position of the reference ROI in SI direction.

References: 1) Kokuryo D, Kumamoto E, Takao E, Fuji S, Kaihara T, Kuroda K: Evaluation of a vessel-tracking-based technique for dynamic targeting in human liver, Magn Reson Med, 67(1), pp156-163, 2012

Real time MR guided HIFU treatment of mice melanoma tumors: a feasibility study

Martijn Hoogenboom[1], Martijn den Brok[2], Dylan Eikelenboom[2], Erik Dumont[4], Gosse J. Adema[2], Arend Heerschap[1], Jurgen J. Fütterer[1,3]
Department of Radiology[1] and Tumor Immunology[2] Radboud University Medical Center, Nijmegen, The Netherlands, [3]MIRA Institute for Biomedical Technology and Technical Medicine, University of Twente, The Netherlands. [4]Image Guided Therapy, Pessac, France

Purpose: There are different high intensity focused ultrasound (HIFU) ablation techniques for the treatment of tumors such as hyperthermia or thermal ablation. However, the pathologic and immunologic effects of these techniques are often uncertain. Large mice studies could help to get a better understanding of these responses. Here for a stable and safe high field (7T) MR guided HIFU for small animals is developed and tested, which can be used for real time visualization and follow up with high resolution.

Methods: Six C57Bl/6n wild type mice were injected subcutaneously with B16OVA tumor cells at the right femur. After 10-12 days tumor sizes between 7 and 11 mm in diameter were reached. A 3MHz, 48W acoustic output power HIFU system is placed in a 7T wide bore animal MR scanner. The mice were carefully positioned in a cavity of an in-house made gel pad, filled with degassed water for acoustic coupling, on top of the HIFU system in line with the transducer (Fig 1). An 2x2 array receive surface coil was positioned on top of the mouse. T1-weighted MR images are acquired to localize the transducer and to check the ultrasound beam path. T2-weighted (T2W) images are made before and after treatment for therapy planning and treatment evaluation. These images are sent to the HIFU trajectory planner software to determine the transducer position on the MR images. A test pulse is created within an phantom cube positioned next to the tumor to check the accuracy of the focus spot. The ablation process is visualized using real-time MR thermometry (GRE-EPI sequence, proton resonance frequency shift method, 4 slices, voxel size 1x1x1.5mm) with a temporal resolution of 1.9s/dynamic. The thermometry stability was measured within one mouse for 3 minutes without heating. A total of 6 mice were treated with continuous wave HIFU ablation of 4 seconds per focus spot. 3-5 focus spots were positioned within the tumor to distinguish between different focal spots. The mice were sacrificed 1 and 3 days after treatment (3 mice per group). The tumor was removed for pathologic evaluation, using H&E-staining.

Fig 1: Set up: green: gel pad, blue: water, black: transducer, yellow: ultrasound beam

Results: The standard deviation from baseline temperature (after phase drift correction) was +/-0.35ºC. With the use of the gel pad the mouse could easily be positioned with good acoustic coupling between the transducer and the mouse. The heated focus spots were accurately correlated with the preset focus spot. The focal maximum temperature within the focus spots varied between 57 and 70ºC. No skin burns were noted directly after treatment, however 2 mice showed a necrotic point at the skin 1 day after treatment. One mouse showed difficulties using the leg 1 day after treatment. In 4 of the mice a high intensity spot was shown at the preset focus spot on the T2W images after treatment (Fig. 2). H&E-stained sections showed large necrotic areas within all tumors, which correlated with the temperature rise shown at the MR thermometry maps. One day after treatment still some dying cells were found within the ablated region, which was not seen three days after treatment. Separate focus spots as shown at the T2W images could not be distinguished on pathology slices.

Conclusion: A stable and safe HIFU set up is implemented on a 7T animal MR system with real-time thermometry to treat mice with melanoma. It includes remote positioning of the focus within the tumor. Further research is now possible to optimize the treatment settings and follow up by MRI after HIFU treatment.

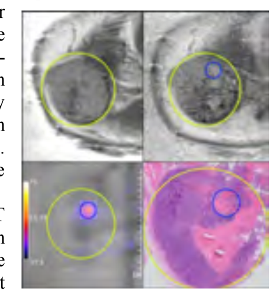

Fig 2: Yellow circle is the tumor. Top: T2W images before (left) and immediately after (right) 3 ablation spots. Bottom left: Temperature map of one focal spot corresponding with blue circle at pathology and T2W image after treatment. Bottom right: HE slice of the tumor, 3 days after treatment.

Non-invasive Magnetic Resonance-guided High Intensity Focused Ultrasound ablation of a vascular malformation in the lower extremity

J.M.M. van Breugel, MSc[1]; R.J. Nijenhuis, MD PhD[1]; M.G. Ries PhD[1]; R.J. Toorop, MD PhD[2]; E.P.A. Vonken, MD PhD[1]; J.W. Wijlemans, MD[1]; M.A.A.J. van den Bosch, MD PhD[1]

[1] Department of Radiology, University Medical Center Utrecht, Utrecht, The Netherlands [2] Department of Vascular Surgery, University Medical Center Utrecht, Utrecht, The Netherlands

Purpose: To report for the first time the magnetic resonance guided high intensity focused ultrasound (MRgHIFU) ablation of a vascular malformation in the lower extremity in a clinical patient leading to interruption of the local perfusion and the associated debulking of the malformation.

Material and Methods: An 18-year old male without prior medical history suffered from chronic pain in the medial side of his left lower limb for over ten years. Diagnostic MR evidenced a lesion of ±1.9 mL that was diagnosed as a vascular malformation with a feeding vessel branching off from the arteria tibialis posterior. The position of the ultrasound transducer was chosen such that the tibial nerve, the fascia, and the tibial vessels did not lie in the acoustic near or far field. Therapeutic ablation consisted of five volumetric ablations (4 x 4 x 8 mm, 200 W), which were planned to cover as much volume as possible while keeping a safety margin of 2-3 mm from the adjacent nerve and vessels. During ablation, MR thermometry provided near real-time temperature mapping of the target area and adjacent tissues.

Results: Temperatures of 62.1-80.8 °C were reached during the ablation procedure. A contrast enhanced MR scan did not show enhancement after treatment of the targeted region within the vascular malformation, indicating a successful interruption of the local perfusion. At three-month follow-up a contrast-enhanced scan was performed, which showed a decrease in volume of the lesion of around 30% (rest volume of ±1.3 mL). The part of the vascular malformation that was targeted with HIFU showed a large decrease in size, whilst the part adjacent to the nerves and main vessels, which was not targeted, was still intact. Furthermore, the patient reported qualitatively sustained pain reduction after three months and normal motoric function and sensibility.

Conclusion: In conclusion, we have reported a successful treatment of a vascular malformation with MRgHIFU, a completely non-invasive treatment modality.

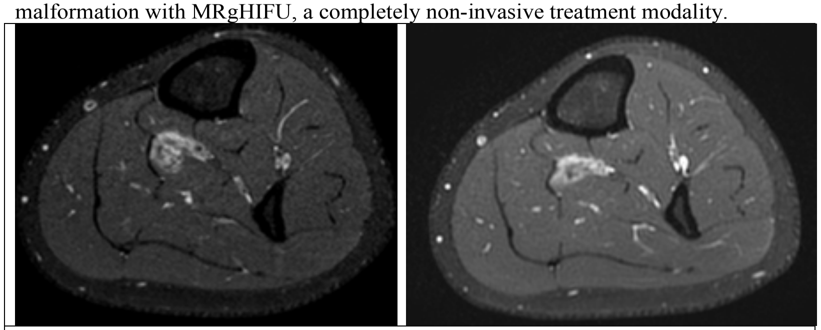

Figure 1: contrast enhanced T1 weighted MR scan. Left: before treatment. Right: 3 month follow-up, a volume reduction of the vascular malformation can be seen.

Spatio-Temporal Quantitative Thermography of Pre-Focal Interactions between High Intensity Focused Ultrasound and Rib Cage

Lorena Petrusca[1], Sylvain Terraz[1,2], Christoph D. Becker[1,2] and and Rares Salomir[1,2]

[1]Faculty of Medicine, University of Geneva, 1211 Geneva, Switzerland

[2]Department of Radiology, University Hospitals of Geneva, 1211 Geneva, Switzerland

Purpose. The aim of the current study was to quantitatively investigate the prefocal thermal effects generated by the HIFU beam's interaction with the rib cage during trans-costal focusing. The study is motivated by preliminary findings reported by ourselves (1) and other groups (2) in the context of minimally invasive ablation for the treatment of patients with unresectable liver metastases and hepatocellular carcinoma using extracorporeal HIFU.

Material and Methods. HIFU sonications were produced by a phased array MR compatible transducer (256 elements, f1.031 MHz, F-number 1.07) on degassed Turkey muscle placed on a specimen of freshly excised thoracic cage specimen from sheep. The *ex vivo* thoracic wall was positioned in the pre-focal zone 3.5 to 6.5 cm below the focus. Thermal monitoring was simultaneously performed using high resolution MR thermometry (PRFS method, voxel: 1x1x5 mm^3, 4 multi-planar slices positioned to monitor interleaved both the focal point and the peri-costal soft tissues) and fluoroptic temperature sensors inserted in the medullar cavity of ribs.

Results. MR thermometry data indicated a nearly isotropic distribution of the thermal energy at ribs surface in the perpendicular section. The temperature elevation at the focal point was comparable with the peri-costal temperature elevation around unprotected ribs, while being systematically inferior to the measured values intra-medullar inside the rib. The ratio between the true intra-medullar temperature elevation and the nearest peri-costal MR thermometry estimation, determined from 18 independent experiments with varying values for acoustic power and duration, was found to be 4.16 ± (SD) 2.84, with a minimum – maximum range of [1.4 - 9.9]. One dimensional spatial profiles of thermal build-up through the ribs were connecting as a Gaussian functions between peri-costal and intra-medullar measurements. Dynamics of thermal relaxation post-sonication were demonstrated to be theoretically coherent with the experimental observations.

Conclusion. As a measure of the thermal risk of the rib itself, when comparing the peri-costal thermometry in soft tissue adjacent to the rib with the true intra-medullar temperature provided by the "gold standard" sensors, large miscorrelation is noticed, greater than a multiplicative factor of 4 in average.

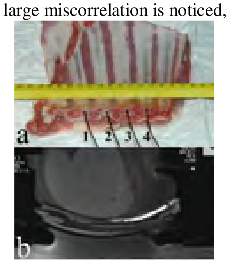

Fig. 1 a) *Ex vivo* setup using "gold standard" fluoroptic temperature sensors (1 to 4) inserted into the medullar cavity "tunnel"; **b)** Transverse oblique section in the T1w 3D MR data visualizing a tagged "tunnel" guiding the fiber intramedular.

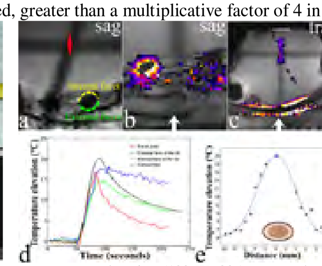

Fig. 2. a) Magnitude GRE-segEPI image illustrating the definition of the external and internal rib facets and the focal point (red spot). **b),c)** Temperature elevation maps illustrating the end point of the HIFU sonication in 2 different experiments (b: 92W, 30s; c: 150W, 60s). Frame **b** and **c** demonstrates the symmetry of the thermal buildup around the left rib (one rib is shielded) and the symmetry of the internal/external facet heating, respectively. White arrow indicates the direction of the HIFU cone. **d)** Plot of the temperature elevation (192 W, 30s) measured at the focal point (red), at the external (blue) and internal (green) facets of the rib using MRT, and inside the medullar cavity of the rib using the fluoroptic sensor (black). **e)** 1D profiles of the thermal build-up through unshielded rib along a direction perpendicular to the HIFU beam and corresponding to the sonication end point. The perpendicular section of the rib is qualitatively illustrated. Peri-costal temperature elevation data ("*" symbols) are obtained from PRFS thermometry in the axial plane. The highest point of the Gaussian fit was constrained according to the intra-medullar fluoroptic sensor data, ("o" top symbols).

References: 1.Salomir et al, *Invest Radiol*, 48(6):366-80,2013; 1.Jung et al, *Abdom Imaging*, 36(2):185-95,2011;

Wireless Phased Array Coils for MR Guided Breast Interventions

M. Fallah-Rad, H. Zhu, L. Petropoulos
IMRIS Inc., Minnetonka, MN, USA

Introduction: Breast cancer is one of the most common forms of cancer among women. It is well known that early cancer detection and diagnosis can improve patient survival rates [1]. Amongst all the diagnostic modalities, MRI offers many benefits such as superior soft tissue contrast, multi-plane imaging capabilities, ability to detect small size lesions, and dynamic contrast enhanced imaging [2,3]. Additionally, compared with traditional mammography MRI has the ability to identify and detect the extent of cancer or lesions to other areas of the body. A key element in MRI image quality is the use of appropriate radio frequency (RF) coil. For breast imaging applications, MRI coils providing optimum SNR and image uniformity for unilateral and bilateral imaging, as well as peripheral lymph-node imaging are imperative. Furthermore, RF coil designs yielding increased patient comfort in prone positions are preferred. The traditional trend of RF coil design was towards higher number of elements to provide improved image quality assisting in better detection and identification of tumors and lesions. However, the introduction of clustered multichannel arrays restricts the comfort of the patient and inhibits the ability of a physician to perform interventional procedures on the breast. This restriction requires the use of two sets of RF coils, one for diagnostic imaging and one for biopsy applications. Furthermore traditional RF coils designs include active components and cables with cable traps to prevent RF heating. This leads to bulky, heavy weight and complicated coil designs with increased patient setup time and imaging restrictions.
In this paper, a novel 4 channel wireless phased array breast coil for diagnostic/interventional MRI imaging adaptable to any OEM MR system with similar field strength is presented. Due to the absence of cables and active components, the coil is extremely light, flexible and patient friendly. Furthermore, the absence of the cables and traps allows for the coils to be worn by the patient similar to a traditional bra accommodating to different patient sizes and imaging in the supine position. Volunteer imaging with the wireless breast coil yields similar imaging performance compared with the standard OEM phased array coils. The open concept design of the elements in the wireless breast coil accommodates biopsy procedures while the lack of active components allows for wearable sterile disposable coil design.

Methods: Two alternative wireless phased array coil designs for breast imaging at 1.5T are presented in Figures 1(a) and 1(b) respectively. Fig. 1(a) shows a 4 channel phased array wireless breast coil while Fig. 1(b) displays an alternative 6 channel wireless breast coil better suited for interventional imaging applications. For the first coil, two loops with geometrically decoupled butterflies were implemented. The desired isolation between the right and left elements was achieved using a combination of capacitive decoupling and copper shielding. For feasibility studies, elements were wrapped around a cone shaped plastic funnel to create a conformal shape. Coils were tuned to 63.6 MHz and were passively detuned from the RF body coil during transmit. Additional RF fuses were incorporated to create secondary protection. The second coil configuration shown in Fig. 1(b) consists of a total of 6 elements (3 on each side). Each side of the coil is made up of three geometrically decoupled channels consisting of an end ring and two parallel partially overlapped half rings. There are a total of six tuner capacitors (one for each loop) on this coil.

(a) (b)

Fig. 1 Geometry of the fabricated wireless coils (a) 4-CH coil (b) 6-CH coil

Results and discussion: Bench tests on the fabricated coils showed an unloaded to loaded quality factor (Q_u/Q_L) of 6.7 for the coil in Fig. 1(a). Similar measurements for coil in Fig. 1(b) showed a ratio of 7.8. Volunteer imaging was conducted with a TIRM sequence (TR/TE = 6190/96 ms, Slice thickness = 3mm, FOV = 182 mm x 192 mm) with the results depicted in figure 2. Figure 3 shows a T2 weighted volunteer image (TR/TE = 6000/93 ms, Slice thickness = 3 mm, FOV = 157 mm x 145 mm).

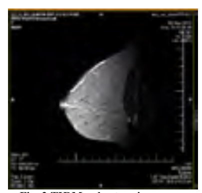

Fig. 2 TIRM volunteer image

Conclusions and Discussion: In this paper, a pair of wireless phased array wearable breast coils was presented. The coil design eliminates the use of cables and active components. This reduces the weight and complexity of the coils. Additionally, patient comfort and setup times are improved significantly. The coils can be designed to work with any OEM system with similar field strengths. Volunteer images showed similar quality as traditional phased array breast coils.

Fig. 3 T2 weighted volunteer image

References:

1. M. R. Smith, X. Zhai, et al. "Excite and Receive Solenoid Radiofrequency Coil for MRI-Guided Breast Interventions. Magnetic Resonance in Medicine", 65:1799-1804 (2011)
2. D. Maillet, A. Ruehle, et al. "An Adaptable MRI Radiofrequency Breast Coil: Evaluation of Size, Coil Diameter, and Uniformity", Concepts in magnetic resonance, Part B, volume 41B, Issue 2, April 2012, Pages: 50–56
3. Yu Li, Feng Liu, et al. "Inverse design of a phased-array coil for breast magnetic resonance imaging", Concepts in Magnetic Resonance Part B, Volume 35B, Issue 4, October 2009, Pages: 221–231

Novel Percutaneous Skull Mounted Guidance Frame Base Facilitates Minimally Invasive MR-Guided Functional Neurosurgical Procedures

Jon T. Willie, MD, PhD[1,2], Robert E. Gross, MD, PhD[1,2], David Lozada, MD[1], Sherif Nour, MD[3]

Departments of Neurosurgery[1], Neurology[2], and Radiology[3], Interventional MRI Program, Emory University, Atlanta, GA

Purpose: An expendable skull bur hole mounted MR guidance miniframe (ClearPoint SmartFrame, MRI Interventions, Inc.) in common practice was optimized for deep brain stimulation (DBS) surgery but requires a disadvantageously large incision unsuitable for minimally invasive applications. A modified frame base (ScalpMount) was designed for percutaneous skull fixation, accommodating minimal incisions and twist drill hole access. We evaluated the accuracy of this device in stereotactic neurosurgical applications.

Methods: We utilized the ScalpMount frame base and SmartFrame tower to perform 32 MR-guided procedures, including 23 stereotactic laser ablations (SLA) for epilepsy and 9 DBS electrode placements for movement disorders; approaches were either prone transoccipital (n=20 all SLA) or supine transfrontal (n= 3 SLA + 9 DBS =12). Targeting was performed and stereotactic accuracy was assessed using the ClearPoint workstation.

Results: The ScalpMount frame facilitated smaller incisions for DBS than that required for previous iteration and minimal stab incisions for SLA. For prone transoccipital versus supine transfrontal approaches, mean 2D radial errors were 1.97+/-1.2 (SEM) mm versus 0.9+/-0.30 mm, respectively. For SLA and DBS indications, 2D radial errors were 1.87+/-1.1 mm and 0.84+/-0.4 mm, respectively.

Conclusions: The ScalpMount modified SmartFrame accommodates minimally invasive MR-guided stereotactic neurosurgical procedures while maintaining accuracy. Prone transoccipital trajectories were found to be slightly less accurate than supine transfrontal trajectories. This discrepancy likely resulted from transoccipital trajectories being less well aligned with the y- or z-axes of the bore, along which MRI distortion lines would be minimized. Recognition of such distortion is critical for optimal patient positioning to maximize stereotactic accuracy.

An MR safe radiolucent horseshoe headrest system integrated with a sterile wireless RF coil system for neurosurgical and interventional applications

Guy Vanney, Eric Heinz, Haoqin Zhu, Brian Burkholder and Labros Petropoulos
IMRIS, Inc.5101 Shady Oak Rd Minnetonka, MN 55343

Introduction:
In general, when craniotomies and brain biopsies are taking place, the patient's skull is rigidly fixated with a clamp device such that ensures no movement can occur during the procedure. Head Fixation Devices , or HFDs, are very common during neurosurgery or head biopsy operations, For the past 10 years, MR safe and radiolucent devices have been introduced to the market incorporating RF coils in order to perform MR guided neurosurgeries and biopsies. The usual force that the HFD device exerts to the skull is ranging between 60 to 80 lbs between the pins[1]. In the majority of cases, such a force exerted to the skull is acceptable, however, there are many instances where any force between the pins will collapse the patient's skull. Neonatal and early childhood patients, as well as, patients that have undergone multiple craniotomies are prime candidates for devices that do not exert any force of the skull. . In this situation an alternative solution is to use a pillow rest that supports the head and has an opening at the center. The most common shape of such a pillow rest is the one of the horseshoe shape, because it does not create any pressure points especially around the eyes and has an opening at the center to allow access of a breathing tube in case that the surgical procedure requires the patient to be in prone position (fig. 1). In general, the horseshoe headrest provides non-pinned head support in prone, lateral, and supine positions during head, neck and cervical spine interventions. It is also desirable the horseshoe device to be MR safe and radiolucent in the case where MR or CT guided interventions are performed.


Fig.1 MR-CT compatible horseshoe headrest with integrated wireless Coil

In this paper, an MR safe and radiolucent horseshoe head support device integrated with a sterile wireless RF coil system that is suitable for MR and CT guided brain and spine interventions[2] is presented. The sterilized wireless coil RF coil system has a 15cmx17cm square opening allowing for positioning it very close to the surgical workspace and is being seamlessly intergraded with the horseshoe head support device. MR Imaging utilizing the sterile RF coil system generated images that are compared favorably to a standard OEM coils. The entire system has been cleared for clinical use and numerous successful MR guided cases, including neurosurgical and interventional procedures, have been performed in various hospitals in US with great success. This horseshoe headrest system may also be useful for other applications not requiring rigid fixation, such as those that access the skull through the nose. This will enhance an already sophisticated technology platform that includes intraoperative MR and the comprehensive team approach we have for pediatric tumor and epilepsy care.


Figure 2. A wireless surface coil fits against the horseshoe headrest base frame and the flex array head coil is located on the top of patient

Methods:
Figure 1, is shown the horseshoe headrest system and the integrated wireless sterile RF coil system that are designed to provide non-pinned head support during surgical procedures when the patient is in prone, supine or lateral patient positions. The entire system comprises of

1. The horseshoe headrest (fig. 1) which is comprised of a base frame, a lower coil support, an accessory mount and adult and neonatal pad supports. The system also includes non-sterile disposable pads for both neonatal and adult patients
2. A wireless sterile coil (figure 2) that is integrated with the lower coil support of the horseshoe system and the Flexible phased array head coil as the upper coil that is also integrated with the horseshoe system
3. The horseshoe headrest is mounted to either the linkage system.

The wireless sterile RF coil system was tuned at 123.2 MHZ and was matched to the head phantom that closely simulates the loading of an average human head. Isolation numbers between individual element of the array were greater than -13dB, unloaded Q values of each element were greater than 225 and the elements were matched to the load of 50Ohm. Active and passive decoupling as well as RF fuses were also incorporated for each element of the wireless RF array system. The method of sterilization that was used was an Ethylene Oxide (EtO) method.

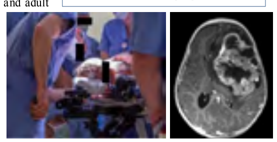
Figure 3. 15 month old diagnosed with AT/RT. Pre-operative MRI using a horseshoe/wireless RF coil system on IMRIS VISIUS theatre

Results:
SNR measurements of the wireless RF coil system were performed at 3.0 T IMRIS VISIUS system using SN gradient echo sequence: (TR/TE/flip/Slice = 300ms/10ms/20deg/3mm, 256x256, FOV = 200mm) and is favorably compared with a standard OEM coil. After the system was cleared for a clinical use, the horseshoe system with the wireless RF coil system was used on a 15 month old with a turning eye where the biopsy indicated an Atypical teratoid rhabdoid tumor (AT/RT). The infant was operated on the IMRIS VISIUS intraoperative suite with a horseshoe/ wireless coil system as shown in Figure 3. Intraoperative MR images, as shown in Figure 4, using the wireless coil system indicated a residual tumor that was further removed during the same operation, After successful resection as identified by postoperative images (fig. 5), the patient was prepared for recovery.

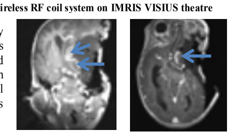
Figure 4. Intra-operative MRI using a horseshoe system shows a residual tumor

Discussion and **Conclusion:**
A new horseshoe headrest that is MR safe and radiolucent and seamlessly integrated with a wireless sterile RF coil system is presented. The horseshoe headrest provides non-pinned head support in prone, lateral, and supine positions during head, neck and cervical spine surgeries where use of a head fixation device (HFD) – a clamp-like device – is not desirable because the skull is too fragile for pinning. The seamless integration of the horseshoe headrest with the RF coil system used with an IMRIS VISIUS theater on a MR guided resection of an Atypical teratoid rhabdoid tumor (AT/RT) with great success. This system will enable surgeons to use interventional MR for even youngest or older patients where pinning patient is not an option.


Figure 5. Post-operation GTR

References:
1. Toshiaki HAYASHI, Takehiko SANADA, Advantages of the DORO® Multi-Purpose Skull Clamp compared to a conventional Horseshoe Headrest System, Neurosurgery Bulletin vol.22 no.7 2012.7
2. Guy Vanney, Eric Heinz, Haoqin Zhu, Brian Burkholder and Labros Petropoulos, US Patent application, November 2011

Body-Mounted MRI-compatible Robot for Shoulder Arthrography

R. Monfaredi[1], R. Seifabadi[1], I. Iordachita[2], R. Sze[1], N. Safdar[1], K. Sharma[1], S. Fricke[1], A. Krieger[1], C. Dumoulin[3], and K. Cleary[1]
[1]Children's National Medical Center, Washington, DC, USA
[2]Johns Hopkins Medical Institutions, Baltimore, MD, USA
[3]Cincinnati Children's Hospital, Cincinnati, Ohio, USA

Purpose. A novel compact and lightweight patient-mounted MRI-compatible robot has been designed for MRI image-guided interventions. This robot is intended to enable MRI-guided needle placement as done in shoulder arthrography. Arthrography is the evaluation of joint condition using imaging modalities such as computed tomography (CT) and magnetic resonance imaging (MRI). Currently, arthrography requires two separate stages, an intra-articular contrast injection guided by fluoroscopy or ultrasound followed by an MRI. While MRI could also be used for guiding the needle placement, patient access in MRI can be difficult, especially for closed bored scanners. Therefore, the development of a small, body-mounted robot to assist in needle placement in the MRI environment could streamline the procedure.

Materials and Methods. The mechanical design was based on several criteria including rigidity, MRI compatibility, compact design, sterilizability, and adjustability. As shown in the CAD model on the right, a four-link parallel mechanism with a spherical joint is used, yielding 2 rotational degrees of freedom (DOF) about the spherical joint, and 2 DOF for needle positioning. The four-link parallel mechanism base, link 4, slides through the robot base to add the third DOF. The mechanism can also rotate to provide the fourth DOF. The robot was fabricated using a rapid prototyping machine (Objet 500) and assembled in our laboratory. A control system was also developed to allow for joystick control of the robot from outside the MRI imaging room. In the envisioned clinical application, the robot will be controlled automatically to position the needle tip at the desired skin entry point and then align the needle orientation to the desired target for the arthrography procedure. The physician will then insert the needle manually once the alignment is verified.

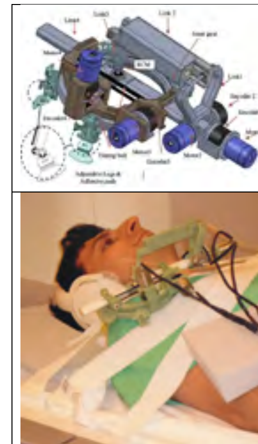
Prototype MRI-compatible robot. Top: CAD model. Bottom: Robot in magnet on shoulder of volunteer. Shoulder images were acquired showing negligible artifacts.

Results. Initial MRI compatibility studies have been done by placing the robot in the MRI scanner on a grating phantom and on the shoulder of a human volunteer (see bottom right image). The grating studies showed that artifacts caused by the piezoelectric motors result in 2.5 cm distortion in the image in all directions. Therefore the robot was redesigned to move the motors at least 2.5 cm from the area of interest. Further studies using a human volunteer showed that the shoulder joint could be imaged satisfactorily for arthrography targeting with the robot strapped to the shoulder.

Conclusion. A newly developed body-mounted robot for use in MRI arthrography is presented. A prototype has been developed and initial MRI compatibility experiments are presented. The results show that artifacts in the region of interest are minimal and that MRI images of the shoulder were not adversely affected by placing the robot on a human volunteer. We have also developed a novel clinical workflow using the robot to enable the entire arthrography procedure to be performed in the MRI suite. Further details will be presented at the conference.

MRI-Guided Percutaneous Core Decompression of Osteonecrosis of the Femoral Head

Pekka Kerimaa[1],Matti Väänänen[1], Petri Lehenkari [2], Pekka Hyvönen[2], Roberto Blanco Sequeiros[3*]. [1]Department of Radiology Oulu University Hospital, [2]Department of Surgery Oulu University Hospital, [3]South Western Finland Imaging Centre Turku University Hospital, *Corresponding author

Introduction Osteonecrosis, or avascular necrosis of the femoral head (ANFH) is an ischemic process of the bone often leading to extensive arthrosis of the joint. Core decompression is a method of treatment where a hole or several holes are drilled into the necrotic cancellous bone. The rationale is to remove necrotic bone and to relieve intraosseous pressure, thus facilitating neovascularization. The treatment is commonly used and has been shown to be efficient and cost-effective at earlier precollapse stages of the disease. Core decompression is most commonly done under fluoroscopic guidance. However, MRI is highly sensitive and specific for detection and classification of ANFH. The purpose of this study was to assess the technical feasibility and, secondly, evaluate the effect of MRI-guided core decompression on patients with ANFH.

Methods The study consisted of eight patients with symptomatic ANFH who went through a total of twelve procedures. Follow up time was 5 years. Mean age was 45.6 years. 3 hips were ARCO stage one, 5 hips were stage two and 4 hips were stage three.

0.23 tesla open bore scanner (Outlook Proview, Philips medical systems, Vantaa, Finland) was used. The most affected area in the femoral head was visualized and chosen as the target. The lateral cortex of the proximal femur was penetrated. A 3mm cylindrical drill was then advanced the target area (Fig1). Two holes were drilled in nine cases, three holes in two cases and only one in a single case. The mean duration of the procedure from skin incision to needle retraction was 54 minutes

Results All MRI-guided core decompressions were technically successful, completion and accuracy 100% and without any reported complications. The average pain on visual analog scale (VAS) declined from 6.5 to 2.2. Edema decreased in 60% (Fig 2a and b). Sustained relief of pain and improved ability to function was reported in five cases, leaving seven cases with a recurrence of symptoms. In these cases, the average duration of relief was 10.6 months. Four hips eventually went through total arthroplasty for recurrence or continuation of symptoms.

Conlusion MRI seems to be a feasible method of guidance for core decompression drilling of avascular necrosis of the femoral head.

Figure 1.

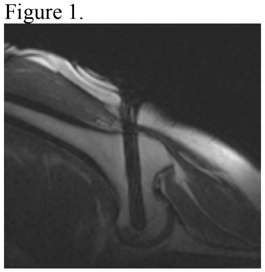

Figure 2a.

Figure 2b.

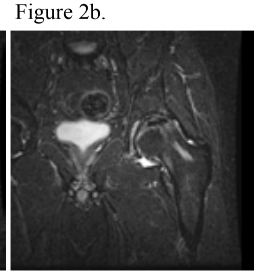

Development of a pneumatic x-ray transparent and MR-safe bone drilling system for interventional MRI

Felix Güttler[1], Kim Winterwerber[2], Andreas Heinrich[1], Ulf Teichgräber[1]
[1]Department of Radiology, University Hospital Jena, Jena, Germany
[2]MGB Endoskopische Geräte GmbH Berlin, Berlin, Germany

Introduction: The precise drilling of bones is a common requirement in orthopaedic surgery. Bone drills are manufactured by metallic components because of their high mechanic load. Image-guided bone bores were usually performed under computed tomography (CT) control. Due to their radiodensity, the metallic components lead to a limited image quality, and thus hinder the control of surgery. Moreover, those devices are not adequate for MRI due to their typically ferromagnetic components. The goal of development was to build a MR-safe prototype, allowing MRI- and CT-interventions and eneables to place Kirschner-wires.

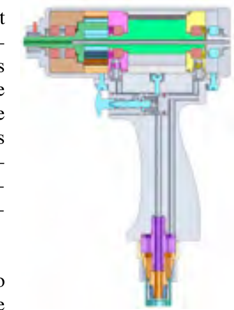

Fig. 1: *CAD drawing of MR-safe bone drilling system.*

Material and methods: The prototype was developed according to common orthopaedic requirements, equal to commercially available drilling machines regarding power and control. An air-driven system made mostly of PEEK and other ferrite-free components was build. After prototype fabrication, the speed, weight, air consumption, operating pressure, perforation and noise level were measured. The evaluation of the engineered prototype occurred under MR-navigation. During a phantom experiment (n=10) the substantia compacta was drilled and a Kirschner wire was laid. The autoclavability, the MR-suitability, the x-ray transparency as well as the practical handling were tested.

Results: The developed bone drilling system, is MR-compatible according to ASTM F2119 and almost completely x-ray transparent. The technical data of the prototype were calculated as follows: rotation speed 0–1000 pro min, weight ca. 800g, air consumption ca. 250 l/min, operating pressure 6–7bar (max. 10bar), perforation 3.2mm, noise level (operator position) ca. 50dB(A). The drilling and placement of the Kirschner-wires could be carried out without any problems. The autoclavability of the bone drilling machine between 134°C and 2 bar showed no interference of the later function.

Conclusion: The manufacturing of a MR-compatible bone drilling machine, comparable to the power of standard non-MR-compatible systems, is possible. Such a machine allows new possibilities in the CT- or MRI-navigated surgery.

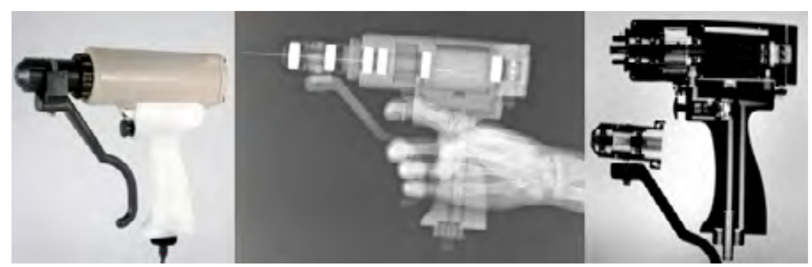

Fig. 2: The prototype of the bone drilling machine (left) as x-ray imaging (middle) and in MRI-imaging in copper sulphate solution (right).

Technical Feasibility of MR-Guided Vertebral Cryoablation: Assessment in a Porcine Model

John Morelli, Dara Kraitchman, Clifford Weiss, John Carrino, Jonathan Lewin, Jan Fritz

The Russell H. Morgan Department of Radiology and Radiological Science, Johns Hopkins University School of Medicine

Purpose: To assess the feasibility of MR guided vertebral cryoablation at 1.5 Tesla with real-time structural monitoring of the ice ball.

Materials/Methods: Thirty-six vertebral cryoablations were performed in the thoracic and lumbar spine of 16 adolescent pigs in this IACUC approved study. A clinical 1.5 Tesla MR system (Magnetom Espree) was utilized for planning, needle navigation, and real-time ice ball visualization. Intermittent proton density TSE sequences were utilized to monitor trans-pedicular placement of an MRI-compatible vertebroplasty needle. Following needle placement within the vertebral body, the inner stylet was removed and an MR compatible cryoablation probe (Ice Seed, Galil Medical) was inserted into the vertebrae co-axially. Utilizing an MR compatible cryotherapy system (SeedNet System, Galil Medical), ice balls of various sizes were created and monitored with a TSE MR fluoroscopy sequence refreshing every 30 seconds during 2 freeze-thaw cycles. The animals were transferred via Miyabi table to a flat panel in-room angiography system (Artis Zee) for gated cone beam CT imaging (dyna CT). The animals were sacrificed immediately (n=8) or allowed to survive for 7-10 days (n=8) under observation of a veterinarian.

Results: All planned procedures (36 of 36, 100%) were successfully performed with no dropouts. Transpedicular needle placement was successfully accomplished in all cases (36 of 36), and MR fluoroscopy accomplished successful real-time ice ball monitoring in all cases (36 of 36). Post-procedural CT demonstrated accurate transpedicular needle placement into the central vertebral body without any inadvertent breaches of the inner vertebral cortex or accidental spinal punctures. In the pigs surviving 7-10 days following the cryoablation, no neurological sequelae were observed.

Conclusion: Needle placement for vertebral cryoablation with real-time fluoroscopic

MR-guided periradicular therapy (PRT) in patients with chronic lumbar pain: an optimized approach in an open 1.0 Tesla MRI-system

Fischbach F, Gazis F, Wybranski C, Pech M, Ricke J, Fischbach K.

Department for Radiology and Nuclear Medicine of the University of Magdeburg

Leipziger Str. 44

39120 Magdeburg

Introduction

Fast dynamic sequences in open high-field MR systems can improve image quality and simplify needle placement. Aim of this study was the optimization of the sequence design for periradicular therapy in open high-field MR systems.

Material and methods

Interventions were performed in an open 1.0 Tesla Scanner (Panorama^{HFO}) employing a MR guided free-hand techniqueMR-guided puncture of the neuroforamen with a MR compatible 22G needle was performed using a dynamic T1 TSE single slice sequence. An external interactive software (iSuite, Philips Medical Systems) allows visualization of needle placement in 2 orthogonal orientations.

Subsequently, 2 ml Bupivacain and 1 ml Triamcinolone were administred. Distribution of the medication was visualized by additional application of 0.5 ml 1:100 diluted contrast media during dynamic imaging and postinterventionally by diagnostic T1-weighted imaging.

Results

20 patients with chronic lumbar pain were treated. Performance of 2 orthogonal orientations allows exact positioning of the needle in the neuroforamen, realtime visualisation of distribution of medication and the online correction of needle placement in case of maldistribution. Hence intraforaminal distribution was achieved in all cases, additional intraspinal/epidural distribution was achieved in 16/20 cases (80%). No complications were observed.

Mean in room time was 23 min (16-47 min) and mean interventional time was 3 min (2-5 min).

Conclusion

MR guided periradicular therapy using a free hand approach is safe and time efficient. The online control of distribution of administered medication may lead to an improved patient outcome.

MRI compatible hammer for MR-guided bone interventions such as biopsies and ablations

Sreejit Nair, Elena Kaye, Govindarajan Srimathveeravalli, Majid Maybody

Cornell University, New York Presbyterian Hospital, Memorial Sloan Kettering Cancer Center, New York, USA

Introduction

In order to overcome the difficulty of penetrating the cortex of the bone in MR-guided bone interventions, a new MR-compatible hammer was designed.

Methods

A total of 90 MRI-guided bone biopsies were performed utilizing the hammer. 5 MR-guided cryoablations of bone lesions were also performed with the hammer.

Results

2 biopsies were non-diagnostic. 26 biopsies were completely negative. 10 biopsies revealed a benign pathology. The remaining 42 biopsies were positive for a malignant lesion. All cryoablations were technically successful.

Conclusion

The new MRI-compatible hammer is an important addition to the toolkit for MRI-guided bone interventions.

Determining the Location of the Tip of an Active Transceive Guidewire

Joshua Lockwood[1], Gregory H. Griffin[2], Graham Wright[1,2], Kevan Anderson[1]
[1]Physical Sciences, Sunnybrook Research Institute, Toronto, ON. [2]Department of Medical Biophysics, University of Toronto, Toronto, ON.

Purpose: The use of guidewires is essential for a variety of cardiovascular interventions as they play a fundamental role in establishing a route through the vasculature. Recent work has demonstrated that a guidewire can be made visible through the use of a toroidal transceiver coupled to the guidewire [1]. One significant advantage of the technique over receive-only coupling techniques [2,3] is that the signal intensity that one would expect along the guidewire is primarily a function of the position along the wire and factors affecting the signal intensity such as flip angle artifacts caused by currents induced from a body coil excitation are not present. As with other techniques, the ability to localize the exact position of the tip of the guidewire is challenging because the signal intensity at the guidewire tip is small and typically below the noise floor of the image. This is especially the case when fully insulated conventional guidewires are used. The purpose of this study is to investigate a technique to determine the location of the tip of a guidewire by fitting a model of the signal characteristics along the guidewire as determined by a method-of-moments simulation to the signal measured along the guidewire proximal to the tip where the signal is of sufficient signal-to-noise ratio.

Methods: The signal intensity expected along a guidewire made visible through the use of a transceive coupling device was simulated using a method-of-moments software package (FEKO, EMSS-SA). In MATLAB (Mathworks, USA) discrete data from the simulation results, was fitted using a piecewise third degree spline function to express the signal intensity profile along the guidewire. The piecewise fit was used to fit the signal intensity profile image of the guidewire to predict the location of the guidewire's distal tip. An experiment was conducted to confirm the validity of this approach. A conventional straight-tip 0.89mm-diameter guidewire (Guidewire #GR3504, Terumo, Japan) was placed in a 65cmx40cmx10cm polyacrilic acid phantom (#436364, Sigma-Aldrich). Using a 1.5T MR scanner (GE Healthcare) projection images of the guidewire in four positions were acquired in a longitudinal plane using the transceive coupling device (SPGR, FOV=16cm, 128x128, NEX=1). Images were processed in MATLAB to obtain the predicted location of the distal tip. Results were compared to locations measured on high-resolution images of the guidewire acquired with a surface coil (SPGR, FOV=, 256x256, NEX=4).

Results: On average, the position of the guidewire tip along the axis of static field as calculated by fitting the signal profile along the guidewire and through identification on a surface coil image varied by 2.3mm among all four positions tested.

Discussion and Conclusion: Images of guidewires are sufficient to visualize the length of the guidewire but the precise location of the tip of the guidewire cannot be identified visually. Results suggest that by utilizing a model of the signal profile along the guidewire one can accurately determine the location of the guidewire tip.

References: **[1]** Etezadi-Amoli et al. MRM 2014; in press; **[2]** Hillenbrand et al. ISMRM 2005:197; **[3]** Anderson et al. ISMRM 2013:474

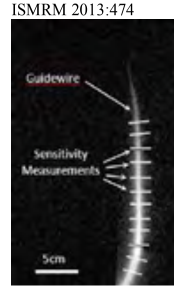

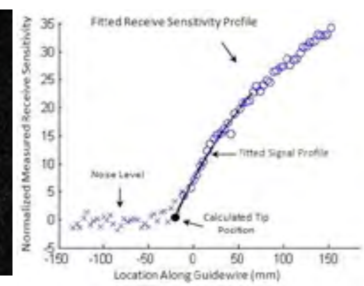

Fig 1. MR image of the guidewire in a homogeneous phantom. The signal intensity profile of the guidewire is measured by integrating the signal over perpendicular linear profiles (shown) to locations along the guidewire.

Fig 2. Measured signal intensity plotted as a function of position along the guidewire. The profile is fitted to model to find the position of the guidewire tip.

Dynamic MR Imaging with Motion Prediction Aided by Catheter Tip Tracking

Peng Wang[1] and Orhan Unal[1,2]
[1]Medical Physics and [2]Radiology University of Wisconsin-Madison

Purpose

MRI-guided radio frequency ablation (RFA) is a promising technique for guiding and conducting thermal therapies such as electrophysiology (EP) procedures. Treatment efficacy, reliability, and patient safety can be greatly improved by performing real-time treatment monitoring using MR thermometry. Temperature mapping is very sensitive to motion and even more difficult when through-motion occurs. In this work, a novel method is presented to dynamically control and update imaging plane location in real-time using information from tip-tracking coils embedded on catheter and a motion prediction algorithm; therefore, making the target appear stationary in the reconstructed images.

Materials and Methods

Multiple solenoid MRI tracking coils were incorporated on the distal end of a 6 F catheter. MRI tip-tracking sequence was implemented on the RTHawk platform [1] using a 4-projection Hadamard method [2]. When the catheter does not move relative to the target tissue, the motion detected by the tip-tracking coils can be regarded as that of the moving organ. A 2D gradient-echo spiral imaging sequence with 6 arms was interleaved with the tip-tracking sequence, resulting in a temporal window of 240 ms. The diagram of imaging plane control is shown in Figure 1. When the catheter moves, its new tip location is detected by the tracking coil, and the imaging location is immediately updated for the subsequent imaging cycles. Since the movement is continuous, the time delay between imaging and catheter tracking causes the information from the catheter tracking to be slightly outdated at the time of imaging. To overcome this, a motion prediction algorithm utilizing Extended Kalman Filter (EKF) was employed.

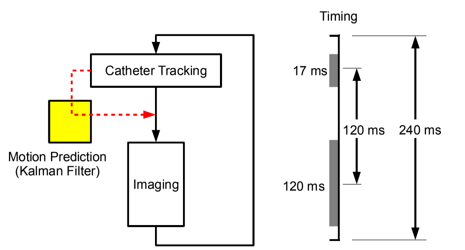

Figure 1: Diagram of imaging location control using catheter tracking and timing.

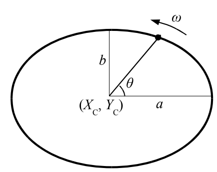

Figure 2: *The elliptical movement model used in EKF for motion prediction.*

In this study, we've established an elliptical movement model (Figure 2) for EKF. The state vector is defined as $x = [\theta, \omega, a, b, X_c, Y_c]^T$ and the location of the tracking coil $[X, Y]^T$ as measurement. Once the EKF state vector converges, the imaging location can be predicted using the current state estimate as:

$$\begin{cases} \hat{X}_{imaging} = \hat{X}_c + \hat{a}\cos\left(\hat{\theta} + \hat{\omega}\Delta t_{imaging}\right) \\ \hat{Y}_{imaging} = \hat{Y}_c + \hat{b}\sin\left(\hat{\theta} + \hat{\omega}\Delta t_{imaging}\right) \end{cases} \quad (1)$$

Real-time imaging and reconstruction was facilitated by the RTHawk engine running on a workstation (Dell Precision T5500, OS: Ubuntu 13.04). The EKF motion prediction algorithm was developed as an RTHawk plugin using the MRPT (mrpt.org) C++ library to control the imaging plane per each 2D acquisition. Experimental setup consisted of a cylindrical phantom doped with CuSO4 solution that contains the catheter with tip tracking coils. Periodic linear motion over a distance of 2 cm was induced by the scanner table rocker capability (HDx, GE Healthcare, Waukesha, WI). Note that this linear motion is a special case of the elliptical motion where a or b = 0. Post-acquisition registration was applied to evaluate the phantom displacement in the image space (Figure 3).

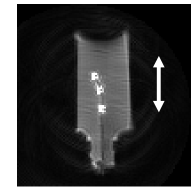

Figure 3: Phantom imaging study. For displacement evaluation.

Results

The detected phantom displacement shown in Figure 4 consists of three segments: (a) displacement with no imaging location control applied, which reflects the induced periodic linear movement of the table, (b) displacement with imaging location controlled by the catheter tip-tracking information without the motion prediction algorithm, and (c) displacement with the motion prediction algorithm applied. The standard deviation of the segment (c), which is half of segment (b), demonstrates the improvement achieved when the EKF motion prediction algorithm is utilized. Note that further improvement can be achieved with higher imaging spatial resolution and optimal noise handling by EKF.

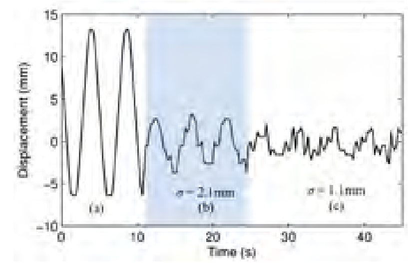

Figure 4: *Phantom displacement detected from image registration.*

Conclusions

The proposed method employing both catheter tip-tracking information and EKF motion prediction algorithm demonstrates the feasibility of real-time imaging location control and therefore allowing images immune to both in-plane and through-plane motions. This method can be utilized to not only improve MR thermometry involving complex organ motion, but also be applied to other scenarios such as characterization of RF ablation lesions using delayed enhancement cardiac magnetic resonance imaging when continuous monitoring of a specific target location is needed.

Acknowledgements
This work was supported in part by NIH grant R01 HL086975.

References

[1] J. M. Santos, et al Proc. 26th Annu Int Conf IEEE Eng Med Biol 2004; 1:1048 –1051.
[2] Dumoulin CL, *et al,* Magn Reson Med 2005; 29:411–415

Cardiac Electrophyiology Intervention with Intraprocedure Magnetic Resonance Imaging

Henry Halperin, Menekhem Zviman, Michael Guttman, Aravindan Kolandaivelu, Ronald Berger, Saman Nazarian

Johns Hopkins University

Purpose: Atrial fibrillation (AF) and ventricular tachycardia (VT) affect millions of patients. These arrhythmias can becured with catheter ablation, but the arrhythmias often recur, and these recurrences are generally due to reversible conduction block from incomplete ablation. The inability to confirm the presence of completely ablated lesions in the desired locations is the major factor in the greater than 40% recurrence of VT after ablation, and the greater than 30 % recurrence of AF after ablation. In addition, it is not possible with current technology to adequately predict the pathways of VT through scar, which are the targets for ablation.

We hypothesize that high resolution Magnetic Resonance Imaging (MRI) with compatible electrode catheters, location sensors, mapping systems, real-time scanner control, and computational modeling, can(1) aid in predicting the locations of arrhythmia circuits (2) aid in predicting the locations of critical ablation targets, (3) provide for accurate catheter navigation to those critical targets, (4) monitor the formation of ablation lesions in real time, and (5) assess the completeness of ablation. Once validated, these enhanced capabilities could dramatically improve the outcomes from complex ablation procedures, become the ablation methodology of the future, and become a platform for improving outcomes from many other interventions.

Materials and Methods and Results: We have already developed MRI-compatible versions of standard ablation equipment, as well as methods for predicting VT ablation targets, for performing ablations in an MRI scanner, and for lesion imaging. We have developed imaging methods that differentiate incompletely ablated (reversibly damaged) tissue from completely ablated (necrotic) tissue. This allows determination of whether there is complete lesion necrosis, or whether additional ablation is needed during the procedure to complete the ablation, and, thereby, reduce recurrences. Our application for regulatory clearance is pending, and we will be starting toapply these innovative technologies to clinical ablation studies, since they already represent a substantial improvement over current methods.

Conclusion: MRI can already distinguish incompletely ablated from completely ablated tissue and can aid dramatically in localizing optimalcath eter ablation targets. We believe that these MRI compatible ablation technologies with intra-procedure imaging will improve the accuracy of ablation and reduce the number of recurrences of arrhythmias after ablation.

Magnetically Assisted Remote-controlled Endovascular Catheter for Interventional MR Imaging: In Vitro Navigation at 1.5 T versus X-ray Fluoroscopy

Aaron D. Losey, MS, Prasheel Lillaney, PhD, Alastair J. Martin, PhD, Daniel L. Cooke, MD, Mark W. Wilson, MD, Bradford R. H. Thorne, Ryan S. Sincic, MS, Ronald L. Arenson, MD, Maythem Saeed, DVM, PhD, Steven W. Hetts, MD
UCSF Department of Radiology

Purpose

To compare in vitro navigation of a magnetically assisted remote-controlled (MARC) catheter under real-time magnetic resonance (MR) imaging with manual navigation under MR imaging and standard x-ray guidance in endovascular catheterization procedures in an abdominal aortic phantom.

Materials and Methods

The 2-mm-diameter custom clinical-grade microcatheter prototype with a solenoid coil at the distal tip was deflected with a foot pedal actuator used to deliver 300 mA of positive or negative current. Investigators navigated the catheter into branch vessels in a custom cryogel abdominal aortic phantom. This was repeated under MR imaging guidance without magnetic assistance and under conventional x-ray fluoroscopy. MR experiments were performed at 1.5 T by using a balanced steady-state free precession sequence. The mean procedure times and percentage success data were determined and analyzed with a linear mixed-effects regression analysis.

Results

The catheter was clearly visible under real-time MR imaging. One hundred ninety-two (80%) of 240 turns were successfully completed with magnetically assisted guidance versus 144 (60%) of 240 turns with nonassisted guidance (P <.001) and 119 (74%) of 160 turns with standard x-ray guidance (P = .028). Overall mean procedure time was shorter with magnetically assisted than with nonassisted guidance under MR imaging (37 seconds ± 6 [standard error of the mean] vs 55 seconds ± 3, P < .001), and time was comparable between magnetically assisted and standard x-ray guidance (37 seconds ± 6 vs 44 seconds ± 3, P = .045). When stratified by angle of branch vessel, magnetic assistance was faster than nonassisted MR guidance at turns of 45°, 60°, and 75°.

Conclusion

In this study, a MARC catheter for endovascular navigation under real-time MR imaging guidance was developed and tested. For catheterization of branch vessels arising at large angles, magnetically assisted catheterization was faster than manual catheterization under MR imaging guidance and was comparable to standard x-ray guidance.

Micro Resonant Marker for Endovascular Catheter Tracking in Interventional MRI: In Vitro Imaging at 3T

Bradford RH Thorne[1]; Prasheel Lillaney[1], PhD; Aaron Losey[1], MD; Xiaoliang Zhang[1], PhD; Drew Vinson[1], BA; Yong Pang[1], PhD; Steven Hetts[1], MD

Interventional Radiology Research Laboratory, Department of Radiology and Biomedical Imaging, University of California San Francisco, San Francisco, California

Purpose: The promise of magnetic resonance (MR) guided endovascular procedures remains largely unrealized, as a safe and appropriately sized method for catheter tracking has yet to be described to date. While markers have been previously described [1,2], size, efficacy and safety shortcomings preclude them from clinical application. The purpose of this study was to create a miniature resonant structure for use as a bright marker on endovascular catheters applied to interventional MR procedures.

Materials and Methods: The resonant marker prototype was initially constructed on a 1.69 mm clinical grade polyethylene ether ketone (PEEK) endovascular catheter. Insulated copper wire with a diameter of 0.160 mm was wound to form a 45° helix around the catheter. This was soldered to a custom flexible capacitor (Fig. 1). A second prototype with an integrated capacitor and inductor was manufactured via flexible circuit technology (Fig. 2). The capacitor is comprised of a 25.4μm thick polyimide film sandwiched between two 17.2μm copper sheets. The markers were fabricated to resonate at a lower frequency than ultimately desired. The capacitor was trimmed until the assembly resonated at the desired frequency. A polyurethane coating was applied to waterproof the assembly and fix coil position (Fig. 2). The protective coating was applied and cured at 110°C. Coils were tuned in water with a network analyzer (Agilent Technologies 300kHz-1.5GHz ENA Series) using an H-field coil probe around the resonant structure (Fig. 3). Experiments were performed at 3T (Discovery MR750w 3.0T, General Electric, Fairfield, CT) using a spoiled gradient echo sequence with a 2° flip angle (TE/TR=1.8/5.6ms, square 32mm FOV, slice thickness 5mm, matrix 256x128). The resonant markers were positioned parallel with B_0 in a water phantom. The contrast-to-noise ratio (CNR) was calculated using OsiriX Viewer (Pixmeo, Switzerland).

Results: The micro resonant marker was clearly visible with a bright and highly localized signal enhancement (Fig. 4). The signal did not contaminate adjacent tissue imaging. The complete resonant structure had a maximum diameter of 1.95 mm (<6 French) and length 8 mm. The coil had a calculated Q of 40.56 (Fig. 3) and CNR of 45.427 (Fig. 4).

Conclusion: We have developed and tested the micro resonant marker for endovascular catheter navigation under MR guidance. The passive structure allows for tracking of sub 6 French endovascular catheters. These findings validate the resonator as a viable marker for MR guided clinical applications by providing an opportunity for safe and accurate catheter tracking and the ability to capitalize on the wealth of physiologic and structural information afforded by the interventional MRI environment. The marker's flexible structure and localized resonance make it an optimal marker for MR guided catheter navigation.

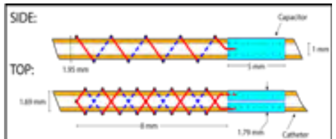

Figure 1: Sagital and coronal views of resonant marker concept. Solid and dashed lines indicate wire in front of catheter and behind catheter, respectively.

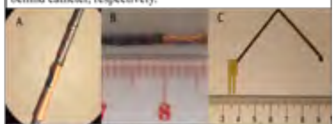

Figure 2: (a) Completed resonant marker viewed through microscope (b)) Resonant marker with scale. (C) Integrated flexible PCB resonator

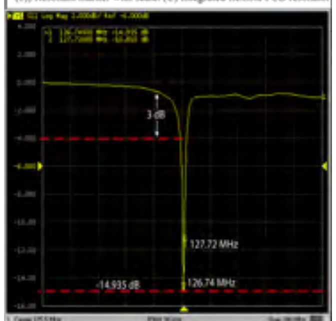

Figure 3: Tuned marker resonating at (1) 126.74 MHz, close to B1 frequency of (2) 127.72MHz (3T magnet). Marker is coupled to custom H-field probe.

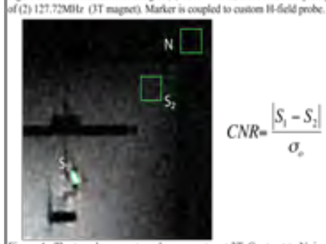

Figure 4: The tuned resonant marker resonates at 3T. Contrast to Noise Ratio (CNR) is calculated from resulting images.

Evaluating RF Safety of a Magnetically Assisted Remote Controlled (MARC) Catheter during MRI

Prasheel Lillaney[1], Maryam Etezadi-Amoli[2], Aaron D. Losey[1], Bradford RH Thorne[1], Alastair J Martin[1], Leland B Evans[1], Greig C Scott[2], and Steven W Hetts[1]

[1]Radiology and Biomedical Imaging, University of California San Francisco, San Francisco, CA, United States, [2]Electrical Engineering, Stanford University, Palo Alto, CA, United States

Target Audience: Interventional MRI community

Purpose: A specialized magnetically assisted remote controlled (MARC) catheter was developed [1] to enhance navigation capabilities in endovascular interventional procedures using MR image guidance. First generation MARC catheter prototypes have a single hand-wound solenoid coil at the tip that is connected to a power supply via two copper wires. When the coil is excited it creates a magnetic moment that aligns with the direction of the main magnetic field (B_0) causing the tip of the catheter to deflect (fig. 1). The MARC catheter poses an RF safety concern because the copper wires couple with the B_1 excitation field leading to undesired heating. The aim of this study is twofold: i) to evaluate the local magnitude of the induced RF current for two different MARC catheter prototypes, and ii) to compare these results to the RF current induced in a nitinol guidewire.

Methods: Two different MARC catheter prototypes were constructed for this study. The first prototype (fig. 2a) was fabricated using a 2.9 Fr custom polyether ether ketone (PEEK) microcatheter with intraluminal copper wires connected to a solenoid coil at the distal tip. The second prototype was also fabricated using a 2.9 Fr PEEK microcatheter, but had copper wires embedded in the catheter wall in a helical manner at a 0.4 mm pitch (fig. 2b). The guidewire (fig. 2c) used in this study (Glidewire GE3501, Terumo, Somerset, NJ) was chosen because it is representative of a typical guidewire used in interventional procedures, and serves as a positive control. The catheters/guidewire were suspended 17 cm from the midline of an acrylic torso phantom (ASTM F2182-02, fig. 3a) in an aqueous solution of 0.35% sodium chloride. An offset position was used to simulate the worst-case scenario where the device is in close proximity to the body coil. To measure the induced RF current an optically powered toroidal current sensor [2, 3] was coupled to the MARC catheter (fig. 3b). The sensor was positioned at 5 cm increments along the catheter starting at the tip and ending at 95 cm distal from the tip. A fast spin echo sequence (echo spacing = 12.8 ms, T_R = 933 ms, ETL = 24, BW = 15.63 kHz, peak SAR = 1.48 W/kg) was used to acquire a single coronal slice (40 x 40 cm) of the phantom using body coil T/R on a 1.5T scanner (Signa, GE, Milwaukee, WI). During RF transmit the signal from the toroidal current sesnor was recorded, and subsequently analyzed using MATLAB scripts (Mathworks, Natick, MA) to find the peak value of the induced RF current for each spin echo excitation.

Results: The mean and standard deviation of the peak RF current was calculated and graphed as a function of position (fig. 4) for each catheter/guidewire. The first MARC catheter prototype had a maximum current value of 0.93 A at 25 cm, the second prototype had a maximum of 0.27 A at 30 cm, while the guidewire had a maximum of 1.01 A at 40 cm.

Discussion/Conclusions: The local maxima in fig. 4 suggest that the induced RF currents create standing waves leading to the concentration of current at distinct locations. The current induced in the first prototype was comparable to the current induced in the guidewire. However, the measured RF current was lower at all distances for the prototype with helical leads suggesting that it offers increased RF safety. The helical geometry could be acting as an RF choke that effectively reduces the coupling to the transmit field. Also, the RF current must travel over a longer effective path length, which may reduce the standing wave resonance. The increased length presents a tradeoff because it increases the total resistance, which causes more heating when the tip is excited with DC current. Future work will correlate the maximum currents to local temperature change along the device during imaging. Mitigating the RF safety risks of the MARC catheter is a critical step towards clinical use of the device for interventional procedures using MR image guidance.

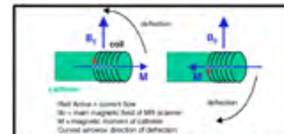

Fig. 1: Schematic of how the B_0 field can be exploited to deflect the catheter.

Fig. 2: a) First MARC prototype with inset of solenoid coil at tip. b) Second MARC prototype with inset of helical wiring in wall. c) Image of the tip of the Nitinol guidewire.

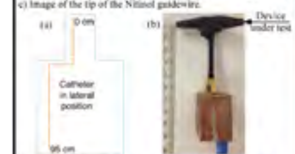

Fig. 3: a) Schematic of acrylic phantom with catheter position shown. b) Image of toroidal current sensor.

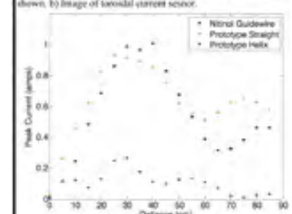

Fig. 4: Induced RF current as a function of distance along device. Tip of catheter is located at 0 cm.

References:

1. Roberts, T.P., et al., *Remote control of catheter tip deflection: an opportunity for interventional MRI.* Magn Reson Med, 2002. **48**(6): p. 1091-5.
2. Zanchi, M.G., et al., *An optically coupled system for quantitative monitoring of MRI-induced RF currents into long conductors.* IEEE Trans Med Imaging, 2010. **29**(1): p. 169-78.
3. Etezadi-Amoli, M., et al. *An Optically Powered Toroidal Current Sensor for RF Safety Monitoring.* in *International Society for Magnetic Resonance in Medicine*. 2012. Salt Lake City, Utah.

Novel MR safe guidewires for MRI-guided interventions

Klaus Düring
MaRVis Medical GmbH, Vahrenwalder Str. 269A, 30179 Hannover

Commercial guidewires consist of a metal core which makes them dangerous in MRI due to inductive heating and electric conductivity.
MaRVis Medical GmbH has developed the first portfolio of MR safe standard and stiff (0.035 inch) and micro (0.014 inch) guidewires. The most critical factors for MR guidewires are excellent mechanical handling quality and visibility in MRI without distortion of the target tissue image. The new guidewire design is based on elongated glass and aramid fiber – epoxy resin compound materials („MaRVis rods"). For standard and stiff guidewires several such MaRVis rods are combined in a defined geometric arrangement in an envelope polymer. Centrically located small metal particles serve as continuous passive-negative MR markers. The guidewires comprise a PTFE shrink tube as the outer surface. A plastically shapeable flexible tip is provided comprising a specifically visible MR tip marker for unambiguous identification of the guidewire tip in the MR image.
The MaRVis MR guidewires provide good mechanical handling properties and precise imaging with minor distortion of the target tissue image in interventional MRI sequences on GE, Philips and Siemens MR scanners. They are universally applicable in 1.5T and 3T MR scanners. Numerous MRI-guided interventions can now be realized by using the MaRVis MR guidewires. CE Mark is expected in the first half of 2015.

Development of a passive-trackable catheter system to perform MR-guided minimal invasive intramyocardial injections – in vivo and consecutive ex vivo study

S. Bock[1], S. Dahl[2], S. Tacke[3], M. Schneider[3], A. Hartmann[3], M. Kramer[3], H.-W. Henke[2], M. Friebe[2], G. A. Krombach[1]

[1] Department of Diagnostic and Interventional Radiology, University Hospital Giessen, Justus-Liebig-University Giessen, Klinikstrasse 33, 35392 Giessen, Germany

[2] Innovative Tomography Products GmbH, Universitätsstrasse 136, 44799 Bochum, Germany

[3] Department for Veterinary Surgery for Small Animals, Veterinary Hospital Giessen, Justus-Liebig-University Giessen, Frankfurter Strasse 108, 35392 Giessen

Purpose: To develop, evaluate and improve a passive-trackable MR-safe catheter system to deliver therapeutic agents to the ischemic heart via minimal invasive percutaneous intramyocardial injections.

Material and Methods: Six domestic pigs (25-44 kg) underwent intramyocardial injections using different iterations of a catheter system prototype (ITP, Bochum, Germany). A mixture of contrast agent and blue dye was injected into the left ventricular myocardium under fluoroscopic guidance. Heart rate and heart rhythm were monitored. Conspicuity of the device and enhancement of contrast agent were verified with MRI (1 T Philips Intera). After the interventions, hearts were excised and examined ex vivo. Subsequently, real time MRI (1.5 T Siemens Magnetom Avanto) in a liquid-filled phantom was performed with the catheter system.

Results: All executions of the catheter system enabled successful and safe injections into the myocardium. A total of 75 injections were placed into the supply areas of the three main recipient vessels (RIVA, RCX and RCA). Occasionally, as long as the needle was entered into the tissue, animals presented isolated ventricular extrasystoles (5 consecutive times maximum). Post interventional MRI and ex vivo examination showed good penetration depth and extensive distribution of the dye-contrast-media mixture. Initially, various scattered hematomas were recognized surrounding the injection sites. Modification of the needle shape lead to the elimination of this effect. Devices were depicted precisely in the MR-Images and phantom MRI allowed real time navigation (12.5 frames per second) with a catheter artifact of 6 mm.

Conclusion: Minimal invasive percutaneous intramyocardial injections can safely be performed using the introduced passive MR-trackable, double-deflectable catheter system. Operability of the device was generally considered comparable to clinically approved devices utilized in angiographic interventions. This catheter system can possibly be introduced in the treatment of humans. By establishing a catheter into the daily clinical practice, patients suffering from cardiac diseases could be provided with a new therapeutic option. Therefore, it may present an improvement of patient care.

Keywords: interventional MRI, passive MR-tracking, intramyocardial injection, coronary heart disease

Figures

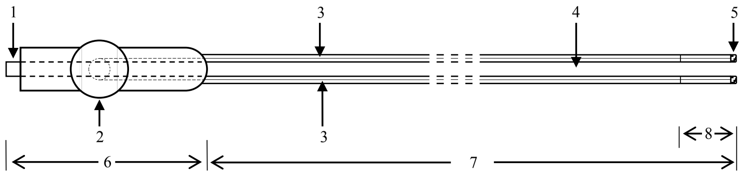

Figure 1: Schematic of the guiding catheter. 1 = screw attachment for syringes, 2 = stepwise adjustable wheel, 3 = pulling strings, 4 = working lumen, 5 = paramagnetic marker, 6 = handle section, 7 = catheter tube, 8 = deflectable distal end.

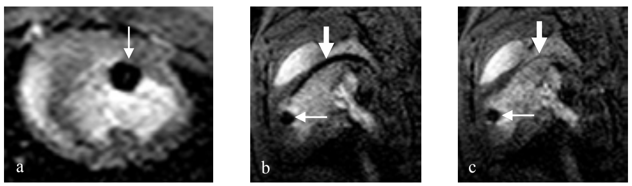

Figure 2: Representative MR-Images (TFE BH). **a** Midventricular short axis slice. **b, c** Left ventricular outflow tract. Circular signal void caused by the paramagnetic marker (thin arrows). Catheter artifact (thick arrows) with (b) and without (c) incorporated injector.

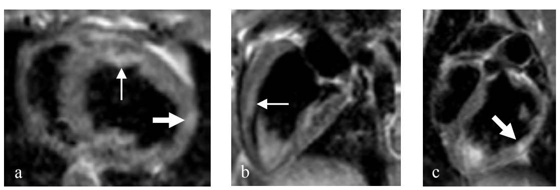

Figure 3: Representative MR-Images (T1 SEEPI). **a** Midventricular short axis slice. **b** Sagittal plane. **c** Coronary plane. Intense signal of the injected contrast agent at the injection sites in anterior (thin arrows) and left lateral (thick arrows) cardiac wall.

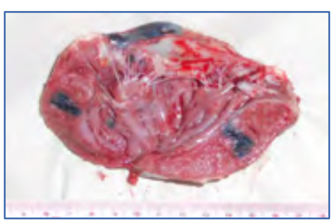

Figure 4: Dissected left ventricle of the heart of animal 4. Dye distribution was already visible on the epicardial surface. Sufficient enhancement and extensive distribution of Evans Blue dye (blue spots).

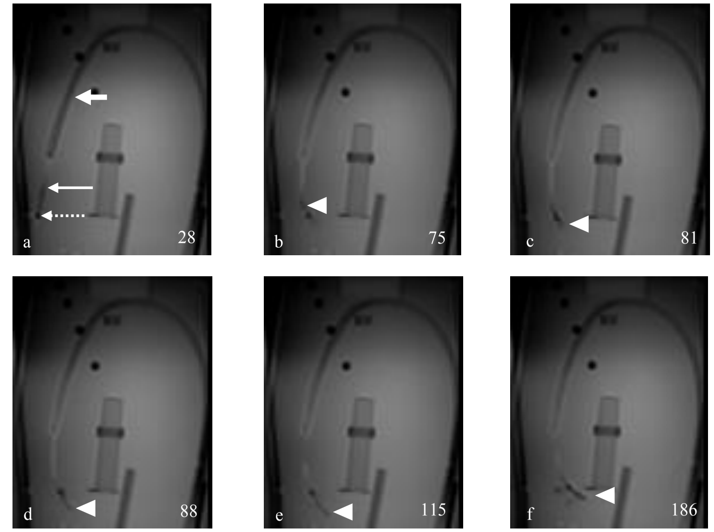

Figure 5: Advancing the injector through the catheter in a liquid filled phantom. Numbers refer to the position in the image series. Thick arrow = plastic tube, thin arrow = guiding catheter, dotted arrow = paramagnetic marker, arrowhead = injection needle

Pain Assessment and Prediction following MRI-Guided Laser Ablation of Hepatic Metastases

Tracy E. Powell[1,2], Ran Shi[3,4], Nicholas Gallagher[1,3], Jian Kang[3,4], Michael A. Bowen[1,2], Sherif G. Nour[1-3]

[1] Department of Radiology and Imaging Sciences, Emory University Hospital, Atlanta, GA, USA
[2] Interventional MRI Program, Emory University Hospital, Atlanta, GA, USA
[3] School of Medicine, Emory University, Atlanta, GA, USA
[4] Department of Statistics, Emory University, Atlanta, GA, USA
[5] Department of Urology, Emory University Hospital, Atlanta, GA, USA

Introduction & Purpose:
Percutaneous ablative treatment has become a viable treatment option for selected patients with metastatic liver disease. The use of MRI to guide and monitor these procedures is associated with better ability to target subtle lesions and lesions at challenging anatomical locations and with a better ability to monitor the progress of ablation and to determine the treatment endpoint. At our institution, we have been using laser fiber optics to ablate tumors under MRI for the past 3 years. Compared to our experience with radiofrequency, microwave, and cryo- ablations, we observed high tolerance of patients to laser ablations and lower needs for post-procedure pain management. The goal of this study is to 1) report numeric pain scores in a large cohort of patients who underwent MRI guided liver laser ablations at our institution; and 2) evaluate potential factors that may predict pain following MRI guided liver laser ablations.

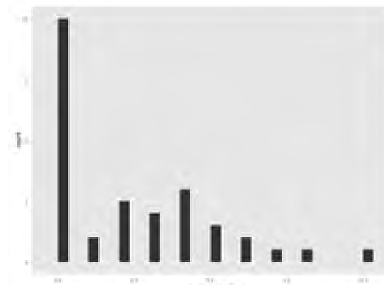

Figure 1. Histogram of numeric pain scores (0-10) on post-ablation day 0 against the number of patients

Patients & Methods:
Following IRB approval, a retrospective chart review was conducted of patients who underwent MRI-guided laser ablation of hepatic metastases between July 2011 and May 2014. Only patients with chart-documented numeric pain scores were included in this study. We identified 45 patients who had 85 laser ablations and fulfilled the inclusion criteria. All procedures were performed exclusively within an interventional MRI suite under general anesthesia. We recorded the number of patients at each pain score level (0-10). We correlated the pain scores with 8 parameters related to the ablation procedures. These parameters are: 1) Ablated liver segment; 2) tumor location in relation to liver capsule and/or diaphragm; 3) number of ablated lesions per treatment session; 4) average largest diameter of tumor; 5) number of used laser fibers/number of fiber repositionings; 6) type of primary neoplasm; 7) whether a biopsy was performed in the same session; and 8) whether a subcapsular hematoma complicated the procedure.
We computed the Pearson correlations between the pain scores and the number of ablated segments, the average largest tumor dimension and the number of used laser fibers/number of fiber repositionings. We used the Pearson test to check whether correlations are significantly different from zero.
We used standard two sample Welch–Satterthwaite t-test to identify differences in pain between single site ablations and multiple site ablations, between patients who had same session biopsies and who did not, and between patients who had subdiaphragmatic ablations, other capsular based ablations, and deep liver ablations. Additionally, the same types of tests were used for comparing subjects who developed subscapsular hematomas and those who did not. The types of primary neoplasms were treated as different factors and standard one-way fixed effect ANOVA were fitted to determine whether there is certain type of neoplasms that contribute significantly to the pain. In addition, a general linear mixed effect model with a random subject-specific intercept was fitted incorporating all the variables with the pain scores treated as outcomes.

Primary tumor	Number of patients
Colon adenocarcinoma	16
Rectal adenocarcinoma	5
Pancreatic neuroendocrine carcinoma	8
Gastric neuroendocrine carcinoma	2
Colonic neuroendocrine carcinoma	1
Melanoma	3
Sarcoma	3
Esophageal adenocarcinoma	2
Clear cell renal cell carcinoma	2
Pancreatic adenocarcinoma	1
Gastrointestinal stromal tumor	1

Table 1: List of primary sources of liver metastases treated with MRI-guided laser ablation

Results:
20 of 45 patients (44.44%) reported no pain at all (pain score = 0) following MRI-guided laser ablation of their liver metastases. Of the remaining patients, 20 (44.44%) reported pain scores between 1-5. Only 5 patients (11.11%) reported pain scores >5 (Fig. 1). Significant correlation was found between pain scores and the average largest diameter of ablated tumors. The Pearson correlations between the largest dimension of the ablated tumors and the pain scores at day 0 and day 1 are 0.4279 and 0.3679 respectively. The p-values for testing whether they are significantly different from zero are 0.0209 and 0.0496. The ANOVA test for the primary neoplasm suggests that there might be significant impact on the feeling of pain exerted by certain neoplasm types (p=0.0778). Table 1 lists the sources of liver metastases treated in this series. The linear mixed effect model fitting results further confirm these two findings: the average largest diameter of ablated tumor is significantly associated with the pain scores (p=0.0239); ablation of metastatic melanoma seems to lead to a stronger pain after procedures (p=0.0398). It is also worthwhile noting that pancreatic neuroendocrine carcinoma might also lead to more pain among patients based on the model fitting results (p=0.088).

Discussion & Conclusion:
MRI-guided laser ablation of hepatic metastases is a well-tolerated procedure with low post-procedure morbidity. 44% of the patient population in this study experienced zero pain following ablations. Additional 44% reported pain scores between 1-5. This investigation shows that the size of ablated tumor is the most significant predictor of post-procedure pain. There might be a correlation between the treated tumor type and post-procedure pain with metastatic melanoma and pancreatic neuroendocrine carcinoma showing a stronger correlation with pain in our series. This finding should, however, be interpreted carefully given the small sample size and warrants further evaluation on a larger cohort of patients. None of the other tested parameters proved to be a significant predictor of post laser ablation pain.

MRI-guided mediastinal biopsies: retrospective evaluation on 15 cases

J Garnon [1], G Tsoumakidou[1], E Rothgang[2], M. de Mathelin[3], E Breton[3], A Gangi[1,3]
[1]*Department of interventional radiology, University Hospital, Strasbourg, France*
[2]*Center for Applied Medical Imaging, Siemens Corporate Research, Baltimore, MD, USA*
[3]*iCube, Strasbourg University, CNRS, IHU Strasbourg, Strasbourg, France*

Purpose

To determine whether MRI allows safe and accurate real-time guidance for biopsies of mediastinal masses.

Material and methods

We retrospectively collected the procedural and histopathological data from all mediastinal biopsies performed under MRI guidance between February 2010 and January 2014. Regarding procedural data, we reviewed the size and location of the lesions, the position of the patient for the biopsy and the duration of the procedure (from the planning MR-scan to the last post-biopsy control). We also evaluated the time necessary to position the biopsy needle (from local anesthesia to the first biopsy). Regarding histological datas, we collected the results of all percutaneous biopsies and also those of surgical specimen when the patient underwent surgery in a second step.

Results

There were 15 patients (7women/8men) included in this retrospective study. Mean age was 74 years old (18-82). Lesions were located in the anterior mediastinum (n=13) and middle mediastinum (n=2). Mean size of the greatest axial diameter of the lesions was 7,1 cm (3,6-11). Biopsies were performed in supine position in 13 cases and in prone position in 2 cases. Total duration of procedure was 42 minutes on average (27-62), with a mean time to position the needle biopsy of 9,4 minutes (3-18). Histological analysis revealed malignancy in 12 cases, with 4 of this 12 lesions being confirmed at surgery. These 12 biopsies were all considered as true positive biopsies. One biopsy was considered as true negative as histology revealed granulomatous inflammation consistent with a sarcoidosis, without any modification of the size of the lesion at 1-year follow-up. One biopsy was considered as false negative as percutaneous biopsy concluded to mesotelial hyperplasia, whereas surgery revealed malignancy. Finally, one biopsy was not diagnostic as there was no clear histological result possible. The lesion turned out to be a thymic hyperplasia on a secondary CT-guided percutaneous biopsy. Given these results, sensitivity, specificity, positive predictive value, negative predictive value and accuracy of MRI-guided biopsies in our study were respectively 92,3%, 100%, 100%, 50% and 86,6%. There was no immediate complication.

Fig.1: biopsy of a mediastinal mass using two orthogonal views. The real-time sequence show good positioning of the needle's tip inside the tumor

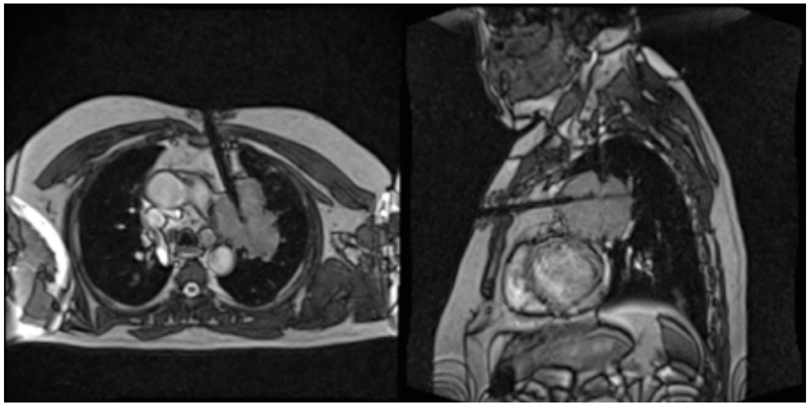

Fig.2: biopsy of a mediastinal mass using a posterior approach. MRI clearly shows the mass, the lung and the great vessels.

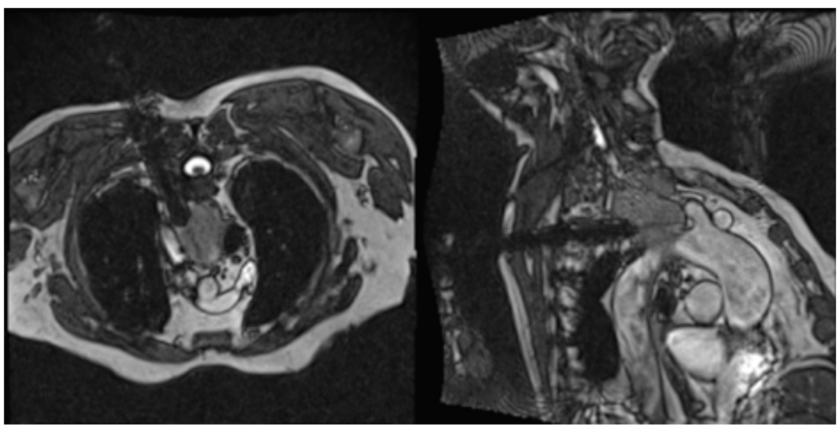

Fig.3: biopsy of a mediastinal mass using an anterior approach. The good contrast resolution of MRI allows to avoid targeting the necrotic parts of the tumor.

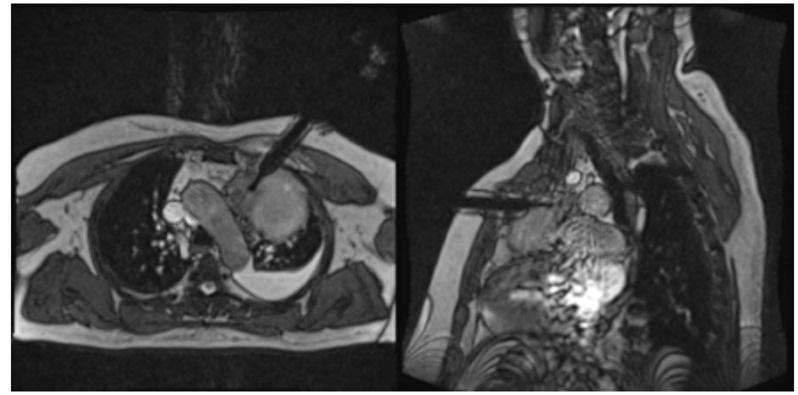

Abstract

Reference-less PRF Thermometry forMR-guided Focused Ultrasound (MRgFUS)liver treatmentin a pre-clinicalThiel-embalmedhuman cadaver model

IoannisKarakitsios*,Nhan Le, Xu Xiao, Andreas Melzer
Institute for Medical Science and Technology (IMSaT), Division of Imaging and Technology, School of Medicine, Dentistry and Nursing, University of Dundee, Dundee, DD2 1FD,United Kingdom

Purpose

MR-guidedFocused Ultrasound (MRgFUS) is a safe, controlled and non-invasive option that utilizes Proton Resonance Frequency (PRF) MR Thermometry forreal-time temperature mapping and control of treatment with Focused Ultrasound. Reference-less Thermometry is more robust to motion and displacement of the tissue than the standard phase-referenced Thermometry. The aim of the present study was to demonstrate reference-less PRF Thermometry on pre-clinical Thiel embalmed human cadaver.

Material and Methods

The liver treatment was conducted onMRgFUS patient table (ExAblate 2100 Conformal Bone System, InSightec Ltd., Tirat Carmel, Israel) embedded in 1.5T MR scanner (SignaHDx, GE Medical Systems, Milwaukee, WI, USA) for the MR imaging. The liver wassonicatedfor 20 sec with acoustic energies 1000, 2000J (Fig.1). Reference-less PRF Thermometry was used for treatment monitoring.

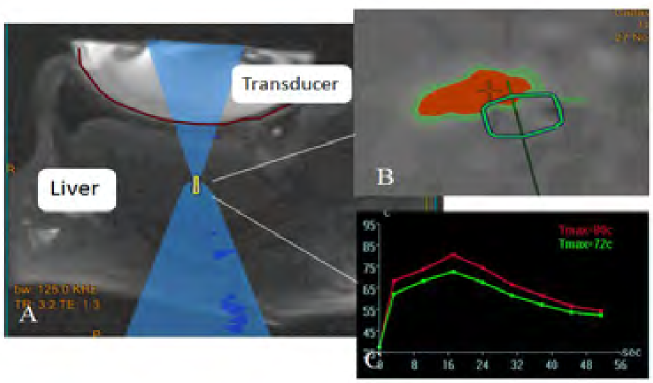

Fig.1: Snapshots of MRgFUS treatment: (A)MR image of the FUS beam path focusing on the liver, (B)post-sonication PRF map showing heated area, (C)post-treatment temperature graph.

Results

A region of interest (ROI) was selected around the heated area,and it was fitted and interpolated using a 2D polynomial (Fig.2). A series of reconstructed temperature maps were generated (Fig.3).

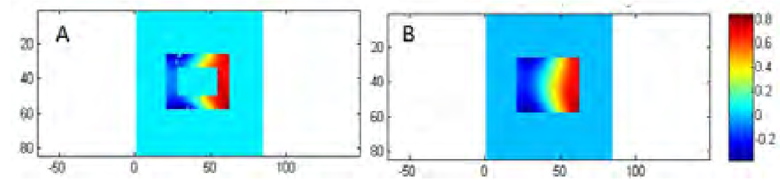

Fig.2: Reconstructed (A)interpolated ROI outside the heated area, (B)fitted in the inside of the heated area.

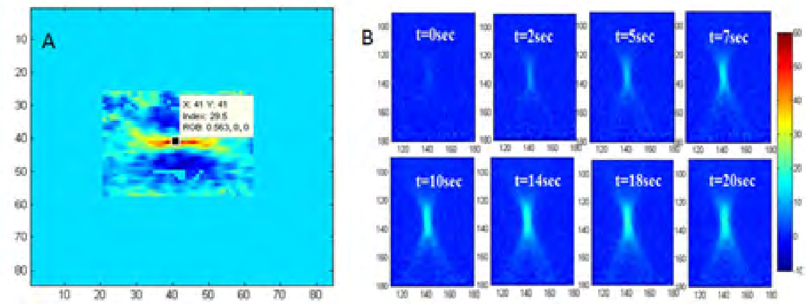

Fig.3: Reconstructed (A)temperature map showing the temperature rise and (B)temperature maps over time duringMRgFUS treatment.

Conclusion

We demonstrated that reference-less PRF Thermometry is suitable on whole Thiel embalmed human cadaver for liver treatment. The quality of the fitting and the interpolation was found satisfactory.

Acknowledgements

The authors are thankful for financial assistance provided by the European Union's Seventh Framework Programme (FP7/2007-2013) under grant agreement nos. 270186 (FUSIMO), 230674 (NANOPORATION) and 238802 (IIIOS). We would also like to thank Dr.RoosEisma from CAHID project and Mrs. Helen McLeod for providing us with Thiel embalmed human cadavers.

MR Thermometry for Clinical Hyperthermia: In Vivo Comparison of FLASH and EPI Double-Echo Sequences

Tetiana Dadakova[1], Johanna Gellermann[2], Otilia Voigt[2], Jan Korvink[3], John Matthew Pavlina[1], Jürgen Hennig[1], Michael Bock[1]

[1]Medical Physics, Department of Diagnostic Radiology, University Medical Center Freiburg, Germany.
[2]Department of Radiation Oncology, University Hospital Tübingen, Germany.
[3]Department of Microsystems Engineering - IMTEK, University of Freiburg, Germany.

Purpose To develop a fast MR thermometry pulse sequence that is not affected by the temperature-related conductivity changes in tissue. For this, a double-echo segmented EPI sequence was developed and compared to conventional spoiled gradient echo sequence in a clinical setting during radiofrequency (RF) regional hyperthermia (HT) treatment.

Materials and Methods A double-echo segmented EPI pulse sequence (DEPI) was developed for a clinical 1.5T MR system (Siemens Symphony). A schematic of the proton resonance frequency shift (PRF) sequence [1, 2] is shown at Fig. 1; here, the first echo is used to remove systematic phase changes due to temperature-related susceptibility changes in the tissue [3].
To test the sequence in a clinical setting, temperature measurements were performed in 3 tumor patients. Each patient received 5-9 HT treatment sessions in an MR-compatible HT unit (BSD 2000 3D MRI, Salt Lake City, UT) with SIGMA-Eye applicator with 24 antennae (100 MHz, P_{max} = 1800W, 75W per antenna). For comparison, a double-echo FLASH sequence was applied in an interleaved manner.
Temperatures were compared using the Passing and Bablok method [4] for the linear regression and Bland-Altman plot [5].

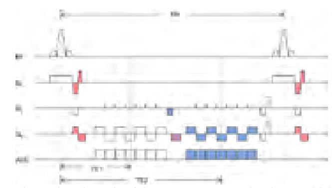

Fig. 1 The schematic of the DEPI sequence. The elements highlighted in blue were added to create the second echo; the elements highlighted in red were added for the flow compensation.

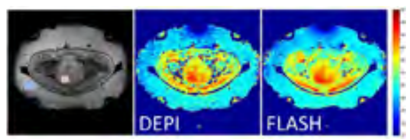

Fig.2 An example from a patient with rectal cancer: anatomical image with ROIs for temperature (red) and field drift correction (blue) and temperature maps from DEPI and FLASH.

Results and Discussion DEPI shows a more inhomogeneous background in the water bolus of the hyperthermia applicator surrounding the patient (Fig. 2) and twofold lower magnitude SNR. In the tissue, however, the heat distribution is clearly seen, and the temperature differences between DEPI and FLASH (averaged over ROIs) never exceeds 1°C. Linear regression (Fig. 3A) shows that DEPI and FLASH temperatures are identical within the measurement errors. Bland-Altman plot (Fig. 3B) shows that the differences between two sequences are between m-2σ = (-1.13 ±0.05)°C and m+2σ = (1.06±0.05)°C and the mean of the differences is m = (-0.035±0.016) °C.

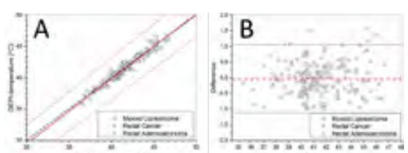

Fig. 3 A. Linear regression. Red solid line is the regression line, thicker dashed black line is an identity line, thinner dashed black lines are the confidence intervals. B. Bland-Altman plot. The red thick dashed line shows the mean m of differences between two techniques and the black thin dashed lines show m±2σ, where σ is a standard deviation of differences between two techniques.

Conclusion The two sequences can be used interchangeably for temperature monitoring during HT treatment. The higher motion sensitivity and lower SNR of the DEPI does not significantly affect the precision of temperature measurements, however, the higher acquisition speed of the DEPI sequence is advantageous for localization of RF hot spots. In addition, high sampling rates allow for a use of DEPI during thermal treatments with fast temperate changes such as HIFU, RF ablation, or LITT.

References [1] Ishihara Y et al. (1995) Magn Reson Med 34:814–823 [2] De Poorter J et al. (1995) Magn Reson Med 33(1):74-81[3] Peters RD et al. (2000) Magn Reson Med 43(1):62-71 [4] Passing H et al. (1983) Clin Chem Clin Bio 21:709-720 [5] Bland JM et al. (1986) Lancet 1(8476):307-310

Acknowlegement This work was supported by the BMBF, Eurostars Project E!6620 PROFUS.

Temperature distribution inside a cryoablation iceball studied using UTE MR signal intensity at 11.7T

Christiaan G. Overduin[1], Yi Sun[1], Jurgen J. Fütterer[1,2], Tom W.J. Scheenen[1]

[1] Radiology and Nuclear Medicine, Radboud University Medical Center, Nijmegen, the Netherlands
[2] MIRA Institute for Biomedical Engineering and Technical Medicine, Enschede, the Netherlands

Purpose: To study the temperature distribution within a cryoablation iceball using ultrashort echo time (UTE) MR signal intensity with applications to cryoablation treatment planning.

Methods: An MR-compatible cryoneedle (IceRod, Galil Medical) was inserted into a porcine muscle specimen at room temperature in a 11.7T pre-clinical MR system (BioSpec, Bruker). Three fiberoptic temperature sensors (T1, Neoptix) were placed at one side parallel to the cryoneedle at lateral distances of respectively 0.5, 1.0 and 1.5cm. Two cycles of 10:3 min. freeze-thaw were applied. Continuous MR monitoring was performed by a single-slice axial UTE sequence (TR/TE = 30ms/286µs, voxel size = 0.47x0.47mm, slice thickness = 1.5mm, acq. time = 12s) positioned around the center of the iceball. For each temperature sensor, signal intensity (SI) values during the experiment were recorded for three different voxels at the same radial distance from the cryoneedle. SI was normalized to its baseline value before cooling and related to temperature. All data points in the subzero temperature range were fitted using an exponential fit. Using the curve fit, normalized SI values could be converted to temperatures to obtain MR temperature maps of the frozen tissue. At each imaging time point, areas of the 0, -20 and -40°C isotherms were extracted (Fig 1).

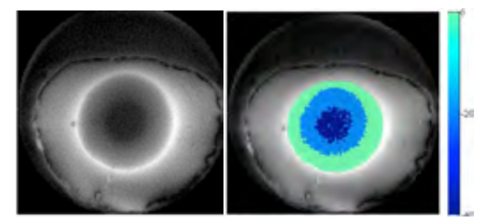

Fig. 1 – UTE MR image at the end of the first freeze cycle (left) and the same image with the 0,-20 and -40°C isotherms calculated using the curve fit overlaid (right).

Results: UTE MR signal intensity decreased exponentially with temperature (T) <0°C. The signal decay was fitted by normalized SI = 1.38e0.05T (R^2=0.95). Maximum area of frozen tissue was 9.32cm^2 and was reached at the end of the second thaw phase. Maximum areas encompassed by the -20 and -40°C isotherms were respectively 5.62 and 1.58cm^2 at 10 and 7.5 minutes into the second freeze cycle. Maximum percentages of the -20 and -40°C isotherms relative to the entire frozen area were respectively 68 and 21% at 7.5 and 6.5 minutes into the second freeze cycle (Fig 2).

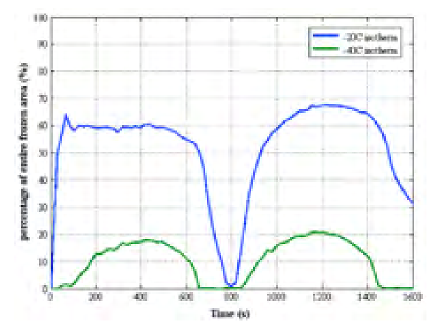

Fig. 2 – Percentages of the -20 and -40°C isotherms relative to the entire frozen area (<0°C).

Conclusion: We have shown the feasibility of imaging the temperature distribution within a cryoablation iceball using UTE MR signal intensity at 11.7T. This information could be useful to validate and improve cryoablation treatment planning models. Limitations of our study were that the ex-vivo tissue was non-perfused and at room temperature and only a small tissue sample could be used due to bore size constraints. Further experiments investigating the reproducibility of our findings under clinically relevant circumstances and using multiple cryoprobes are currently being performed.

Signal Processing for Noninvasive Temperature Imaging of Fat and Aqueous Tissues using Methylene T_1 and Water Proton Resonance Frequency

Shuhei Morita[1], Makoto Obara[2], Masatoshi Honda[2], Yutaka Imai[3], Kagayaki Kuroda[1]

[1]Couse of Information Science and Engineering, Graduate School of Engineering, Tokai University
[2]Philips Electronics Japan Medical Systems
[3]Deptpartment of Radiology, Tokai University School of Medicine

PURPOSE

High intensity focused ultrasound (HIFU) therapy under MR guidance requires temperature distribution images around the target tissue. For tissues with high water content, resonance frequency shift of water proton signal is available. On the other hand, this approach is not applicable to a voxel containing only fat. For solving this issue, we have proposed a novel technique using multiple flip angle and multipoint Dixon methods to use spin lattice relaxation time (T_1) of methylene or terminal methyl proton for fat thermometry [1, 2]. In the present work, we have examined the usefulness of the prior information about the signal intensity and T1's of the fatty acid proton components in reducing the complexity of the signal processing.

MATERIAL AND METHODS

Proton spectra of bovine fat tissues in a glass capillary of 5 mm in diameter were observed with a 11T MR spectrometer at various temperature points to obtain the ratios of signal intensities as well as T_1's between the different chemical shift components of fatty acids. Temperature of the sample was raised from room temperature to 60℃ and lowered to the room temperature again. Signal intensities and T_1's of 8 chemical shift components of the fatty acids were obtained by using inversion recovery for each peak. Then the resultant signal intensity ratio and the chemical shift differences of the fat components were used to simulate the T_1 determination with the multiple flip angle and multiple gradient echo techniques with a numerical phantom with 8 fatty acid components and water The signal to noise ratio (SNR) of the phantom was set to10 for the total signal.

RESULTS

The errors in estimating T_1's of H_2O, CH_2 and CH_3 using a 3-component model with the prior ration information were 1.2%, 1.2% and 0.9%, while those with 9-component model were 0.02%, 0.0% and 0.3%, when TR of 23 ms and 7 echoes with linear TE settings of 1.0 through 7.0 ms were used. Similar results were obtained with different TR, TE settings.

CONCLUSION

The prior knowledge markedly reduced the T_1 estimation error. Between the 3- and 9-component models, the latter yielded better results. The error levels of both models were sufficient for evaluating fat tissue temperature. The use of the prior knowledge seemed to be effective for fat temperature imaging. Experimental verification is under progress.

[1]Kuroda K, Iwabuchi T, Obara M et al. Magn Reson Med Sci 2011;10(3):177-183.
[2]Kuroda K, Morita S, Lam MK et al. Thermal Medicine 2012;28(4):87-96.

Feasibility of MR Thermometry of The Knee Joint Cartilage under Thermal Therapy

Atsushi Shiina[1], Kenji Takahashi[2], Jiro Nakano[3], Kagayaki Kuroda[1,3]
[1]Course of Information Science and Engineering, Graduate School of Engineering, Tokai University
[2]Department of Orthopaedic Surgery, Nippon Medical School
[3]Department of Human and Information Science, School of Information Science and Technology, Tokai University

PURPOSE: The aim of this study was to examine feasibility of MR temperature imaging of knee joint cartilage under thermally induced pain-relief therapy for osteoarthritis.

MATERIALS AND METHODS: Proton spectra of cartilage segment samples collected from an excised a porcine knee joint was observed in 11T NMR spectrometer. The sample was immersed in deuterium oxide (D_2O, 99%, Sigma-Aldrich) in a NMR sample tube of 5 mm in diameter. Trimethylsilyl propanoic acid (TSP) was added as an internal reference. After turning off auto magnetic-field-frequency locking and shimming, the proton spectra were evaluated at various temperature ranging from room temperature and 50 °C. The measurement conditions were TR, 4.09 s; TE, 6.50 μs; FA, 30 degree.

Another porcine knee joint sample was place in lateral position in a 3T clinical scanner and heated in a thermostatic bath. Temperature of the bath was set from 34 to 40 °C. Actual temperature of the sample was monitored by a 4-channel fiber optic thermometer at the suprapatellar bursa (Ch1), meniscus (Ch2), muscle (Ch3) and surrounding water (Ch4). Proton MR imaging with a fast field echo technique was performed in the saggittal slices with the following conditions; TR, 11.3 ms; TE, 8 ms; FA, 15 degree; slice thickness, 5 mm; FOV, 30 cm; and acquisition matrix, 212 x 161. After compensating the static magnetic field drift approximated by a first order plane estimated from the phase change in the complex MR signals in the bone marrow regions or in four olive oil tubes around the sample. Phase change induced by the water proton resonance frequency shift in the aqueous tissues such as articular cartilage and meniscus was converted to temperature elevation using a coefficient of obtained in the spectrometer experiment.

RESULTS: The spectrum of the cartilage sample exhibited only a water signal with a tiny (0.02-0.03%) fractions of other components. The temperature coefficient of the water proton resonance frequency was approximately -0.0108ppm/°C for both heating and cooling period. In the imaging experiment, temperature of the suprapatellar bursa elevated from 33.1 to 38.8 °C. That of the meniscus elevated from 33.7 to 39.2 °C. Signal to noise ratio in the magnitude image was 34 at the articular cartilage or 20 at the meniscus. The resultant temperature images in these tissues agreed fairly well with the actual temperature elevation.

CONCLUSION: The signal to noise ratio in the cartilage and meniscus were sufficient for appreciating the thermal shift of the water proton resonance frequency. The temperature change of the water proton resonance frequency was similar to the other aqueous tissues. Thus feasibility of noninvasive MR thermometry was clearly demonstrated. The magnetic field compensation should be improved in the regions with a complex tissue structure.

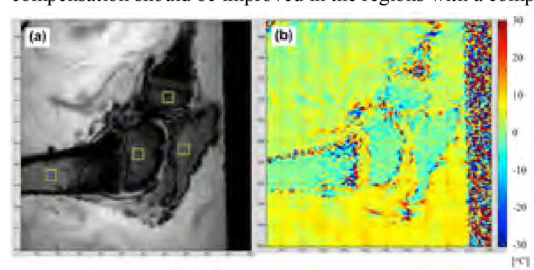

Figure 1 Magnitude (a) and temperature elevation distribution (b) of the porcine knee joint ex vivo at 3T. The yellow squares in (a) delineates the ROI's placed in the bone marrow for field drift correction. The temperature elevation (b) in the cartilage was 5.7°C .

Multinuclear (^{19}F + ^{1}H) intravascular MRI at 3T

Shashank S. Hegde[1], Li Pan[2], Guan Wang[1,3], Yingli Fu[1], Dara L. Kraitchman[1]
[1] Russell H. Morgan Dept. of Radiology & Radiological Sciences, [3] Dept. of Electrical & Computer Engineering, Johns Hopkins University, Baltimore, MD, [2] Center for Applied Medical Imaging, Siemens Corporation, Corporate Technology, Baltimore, MD.

Purpose: One of the challenges in the development of transplanted cellular therapeutic strategies is effective *in vivo* tracking of cells post-delivery. Fluorine (^{19}F) MRI combined with anatomic proton (^{1}H) MRI provides an effective method for tracking labeled cells[1]. Conventionally, surface and/or body radiofrequency coils have been utilized for the MRI component of such multimodal imaging. Recently, using 3T intravascular MRI (IVMRI) probes we have shown high-resolution *in vivo* trans-luminal imaging with local signal-to-noise ratios superior to surface coils[2]. Here, using an IVMRI probe designed for both ^{1}H and ^{19}F MRI, we show high-resolution localization of perfluorooctyl-bromide (PFOB) microcapsules in a porcine heart *ex vivo*. Localization is confirmed by computed tomography (CT) of the microcapsules.

Methods: A 3T IVMRI loopless antenna was designed using either a 2mm outer-diameter (OD) semi-rigid coaxial cable or a 0.8mm OD biocompatible flexible nitinol cable. The same resonant whip length, e.g. 40 mm was used, thereby allowing interchangeable operation at the $^{19}F/^{1}H$ Larmor frequencies (116/123 or 128MHz)[3]. A switchable interface along with its associated 'coilfile' enabled either transmit/receive or receive-only operation[2]. Microcapsules were produced using a modified alginate microencapsulation method with the addition of 12% (v/v) PFOB allowing for multimodality (MRI, CT) detection. Approximately 0.8cc of PFOB capsules was injected into an *ex vivo* porcine heart (Fig. 1a). The IVMRI probe was inserted into the brachiocephalic artery of the porcine heart immersed in saline and used as: (1) a receiver for ^{1}H MRI on a Philips 3T (Achieva) or a Siemens 3T (Tim Trio); and (2) in the transmit/receive mode for ^{19}F MRI on a Siemens 3T (Tim Trio). The proton and fluorine images were co-registered and overlaid to form a composite image. MRI was followed by c-arm CT imaging (Artis Zee, Siemens) to confirm the deposition of the radio-opaque microcapsules.

Results: Real-time tracking of the IVMRI probe insertion in the *ex vivo* heart was readily apparent on ^{1}H MRI (bright line, Fig.1a). PFOB capsules were identified under ^{19}F MRI at 0.8mm in-plane resolution (Fig. 1b, magenta and inset). ^{1}H IVMRI at 0.2mm resolution clearly delineates the vessel wall (around *p*, Fig. 1b. ^{1}H MRI: 3D TSE, TR/TE=298/14ms, FA=90°, voxel $=0.2\times0.2\times4mm^3$, TSE fact. 6; ^{19}F MRI: 3D TruFISP, TR/TE=4/2ms, FA=12°, voxel $=0.8\times0.8\times5mm^3$, 32 avg.). The composite image (Fig. 1b) corresponds well with cone beam CT (CBCT) at the same location (Figs. 1c, 1d. 70kV, 20sDCT).

Conclusions: We show that 3T IV MRI detectors are ideally suited to high-resolution (sub-mm) detection of both fluorine and hydrogen. Multinuclear IVMRI probes provide an effective method to image and potentially monitor ^{19}F-labeled cells in deep structures *in vivo*.

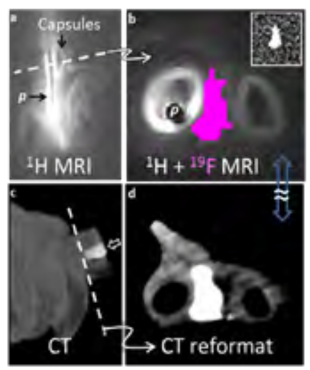

Fig. 1: **(a)** Proton MRI from an intravascular probe *p* inserted into a porcine heart *ex vivo* showing location of PFOB capsules injection. **(b)** ^{19}F IVMRI (inset) overlaid (magenta) on a ^{1}H IVMRI of the vessel at the injection site reveals capsules. **(c)** CBCT of the whole organ confirms location of the radio-opaque capsules (arrow) and **(d)** reformatted CBCT images at the injection location are concordant with (b).

Support: 2011-MSCRFII-0043, Siemens Corp.

Refs: **(1)** Barnett BP, et al. Radiology. 2011;258(1):182-91 **(2)** Sathyanarayana S, et. al., JACC Card Im. 2010; 3:1158-1165. **(3)** El-Sharkawy AM et al. Med Phys 2008; 35:1995-2006.

Incorporation of ultrasound instrumentation and imaging into an interventional MRI suite

Christina Lewis, Joel P. Felmlee, PhD, Krzysztof R Gorny, PhD,
Matthew R. Callstrom, MD, PhD, David A. Woodrum, MD/PhD
Mayo Clinic, Rochester, MN

Purpose: A variety of MRI-guided interventions in the body, including liver, kidney and prostate procedures, would benefit from the complementary strengths of ultrasound (US) imaging for rapid setup, lesion localization, and procedure guidance. However, introduction of US instrumentation into the MRI suite could present a safety hazard due to the risk of attraction to the magnet. Furthermore, proximity to the magnet and motion of the transducer within the magnetic field has the potential to compromise US image quality. The objective of this work was to assess the safety, feasibility, and effect on US image quality of incorporating a solid-state laptop US machine into the interventional MRI (iMRI) suite for US- and MRI-guided interventions.

Methods: A solid-state laptop-based US system, the Samsung UGEO HM70A, was tested in two iMRI suites. One suite was equipped with a 1.5T Siemens Magnetom Espree, the other with a 3.0T GE Discovery MR750w. The US system was tethered to the end of the MRI patient table during use when the table was outside of the bore. To observe the effect of the main magnetic field on US image quality, images were collected with the transducer and subject located both inside the iMRI suite and outside the suite. US images of both an ACR phantom and a human volunteer were acquired. In all settings, a curved transducer was used to acquire structural scans of the phantom and human kidney as well as Doppler and power Doppler with directional flow images. A linear array transducer and phased array transducer were also tested in the human volunteer at 1.5T.

Results: By being tethered to the end of the table and carefully brought into and out of the MR suite, the US system remained outside the 100 Gauss line. Phantom and human volunteer images are shown in Figure 1. When the US system was brought into the scan room, no degradation of image quality or change in Doppler measurements was observed by visual inspection.

Conclusions: The results of this study indicate that the use of a solid-state laptop-based US system inside an iMRI suite is safe and feasible. Of course, it is essential that the US system is confined to a safe distance from the magnet bore. Despite this confinement, we were able to acquire images both at mid-table and at the bore entrance with no visible degradation of image quality.

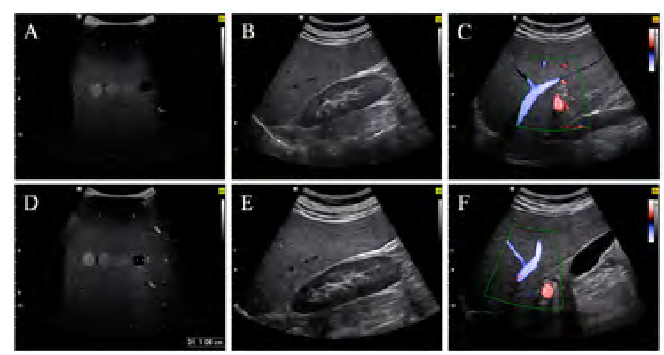

Figure 1: Ultrasound images acquired outside (A-C) and inside (D-F) the 1.5T iMRI suite. No degradation of image quality is observed by visual inspection. Images depict an ACR phantom (A, C), the human kidney (B, D), and power Doppler with directional flow in the human liver (C, F).

Instrument calibration for an accurate needle guidance using the optical Moiré Phase Tracking System on a 3T wide-bore system

Urte Kägebein[1], Oliver Speck[1]
[1]Department Biomedical Magnetic Resonance, Otto von Guericke University Magdeburg, Magdeburg, Germany

Purpose: The freehand technique represents currently the most commonly used procedure to perform MRI-guided biopsy [1]. Combining the advantages of the freehand technique with the accuracy of the stereotactic guidance, the intuitive needle guidance, using the optical high-precision Moiré Phase Tracking System, already demonstrated satisfying results in order to improve and expand the currently available technique [2]. In both procedures, the accuracy and procedure time of needle placement depends strongly on the needle artifact and thereby among other things on the pulse sequence, the needle composition and the needle orientation relative to the main magnetic field [1]. Using the optical tracking system, the accurate position of the needle could be reflected by a single line. Thus, the user would be completely independent of the proposed requirements. The goal of this project is the development of an accurate instrument calibration to precisely reflect the position and orientation of the needle in the MRI image independent of the needle artifact.

Material and Methods: Using a self-constructed calibration board and self-written program in Matlab R2013a, the tip position and orientation of a ceramic needle, relative to its attached Moiré Phase (MP) marker, was determined (see Fig.1). This additional information was added towards a modified gradient echo sequence, capable of aligning the slice along the orientation of the needle with its image centre at the needle tip. For evaluation, a 3D MRI image volume (FOV=128x128x16 mm) was acquired with the modified gradient echo sequence. It was assumed, that the artifact of the ceramic needle is caused through the lack of water protons at this position and is independent of susceptibility. Using the Interactive Front End (Research Prototype by Siemens Healthcare), the displayed needle position and orientation in the resulting 3D MRI volume was evaluated. The calibration experiment was repeated five times.

Fig. 1 *Ceramic needle with attached MP Marker*

Results: The difference of the x, y, and z coordinates between the center of the image and the instrument tip amounted x=1.06±1.08 mm, y=1.59±0.94 mm and z=0.86±1.24 mm, leading to an overall error of $\sqrt{\Delta x^2 + \Delta y^2 + \Delta z^2} = 2.54 \pm 0.99$ mm. The deviation of the orientation of the image plane towards the orientation of the needle tips accounted for φ= 1.27±1°.

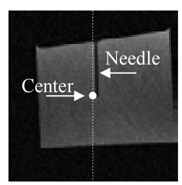

Fig. 2 *Resulting slice*

Conclusion: The overall error of 2.54 ± 0.99 mm represents promising results. However, the calibration board itself needs to be improved for an even higher accuracy. In the next step, these information need to be transformed into a suitable line, reflecting the actual position and orientation of the needle and being thus completely independent of the proposed requirements above. Thereby, the accuracy can be improved and even small lesions are puncturable.

References: [1] Weiss CR, Nour SG, et al.: JMRI 27(2): 311-325, 2008. [2] Kägebein U, Godenschweger F, et al.: ISMRM, 2013.
Acknowledgment: This project was developed within the Saxony-Anhalt funded Forschungscampus STIMULATE (funding code: I 60).

Operation of a RFID based navigation during MRI

F. Güttler, A. Heinrich, M. Sonnabend, U. Teichgräber
University Hospital Jena, Department of Radiology, Jena, Germany

Purpose: MRI-compatible optical tracking solutions are well established i.e. in neurosurgery. Radio-frequency identification (RFID) allows the identification of multiple transponders (tags) in translation and rotation allowing 6 DOF. In contrast to optical tracking solutions, the RFID-based system does not need a permanent line of sight during operation. This is a great advantage and need according to various studies describing problems caused by optical tracking systems. The MR-compatibility of RFID transponders could be proved in several studies, i.e. focusing the use of RFID for patient identification systems[4-5]. The purpose of the study is to evaluate the suitability of a novel RFID-based tracking system (Passive RFID Positioning System, Amedo smart tracking solutions, Germany) for intraoperative MRI. Therefore the spatial accuracy and signal-to-noise ratio (SNR) according to the National Electrical Manufacturers Association (NEMA) standard MS 1-2008 was quantified.

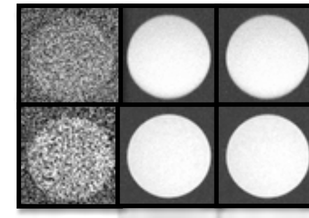

Fig. 1: *SNR before modification (left), after modification (middle) and reference measurement (right) for a HASTE-(upper row) and TrueFISP-sequence (lower row).*

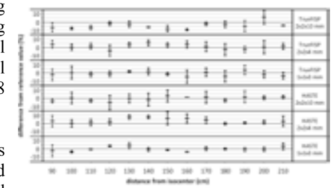

Fig. 2: *The percentage difference (±15%) between RFID system and reference measurement (without RFID system) for varying distances from isocenter of the MRI is shown.*

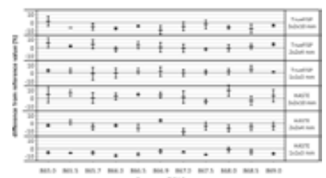

Fig. 3: *The percentage difference (±15%) between RFID system and reference measurement (without RFID system) for varying frequencies of RFID system with 90 cm distance from isocenter of the MRI is shown.*

Material and Methods: The RFID receiver system (reader) was modified to fulfill MRI-compatibility according to ASTM standard F2503, therefor the Power-over-Ethernet component was replaced with an optical fiber for network communication and the voltage source was replaced by a lead-accumulator. All cables and the housing of the reader excepting the antenna were shielded with braided copper foil. The influence of the RFID system on MRI (MAGNETOM Sonata, Siemens, Germany) was analyzed for a phantom of 1kg H2O (dist.) with 1.25g NiSO46H2O and 5g NaCl. The SNR (n=720) was measured with a HASTE- (TR= 3000ms, TE=60-63ms, ETL 256) and a TrueFISP-sequence (TR=12.9ms, TE=2.15ms, flip angle 70°). A voxel size of 1x1x3 mm, 2x2x4 mm and 2x2x10 mm was used. The reader was positioned 90 cm to 210 cm (step 10 cm) from the isocenter of the MRI. During the measurements, the reader continuously sent RF signals at 865.7-867.5 MHz. In a second experiment the RF signal was changed from 865.0-869.0 MHz (step 0.5 MHz) and a distance of 90 cm, 150 cm and 210 cm from the isocenter of the MRI. The specific spatial resolution (n=225) was measured with and without permanent line of sight (LOS) between antenna and RFID tag (ALN-9640 Squiggle Inlay, Alien Technology, Butterfield, USA). An optical tracking system (Polaris Spectra, NDI, Canada) served as reference system.

Results: Compared to the SNR of reference measurement, a SNR of 8-10% could be measured for the unmodified reader (Fig 1). After modification no significant change of the SNR could be observed with increasing distance of the RFID system from the isocenter of the MRI (Fig 2). Also the RF signal of the reader does not significantly influence the SNR of the MRI (Fig 3). The specific spatial resolution deviates on average by 9,0 mm with LOS and 11,6 mm without LOS from the reference system.

Conclusions: The installation of an RFID system including transponders and receivers in the magnet room in close distance to the magnet has low of non-relevant influence on MRI. However the spatial accuracy have to be improved for an application as tracking system in intraoperative MRI.

Title:
Intermittent Pneumatic Compression for Venous Thromboembolism Prophylaxis During Magnetic Resonance Imaging-Guided Interventions

Authors:
Bedros Taslakian[1], Majid Maybody[2]*, Elena A Kaye[3], Srinivasaraghavan Govindarajan[2], Joseph P. Erinjeri[2], Jeremy C. Durack[2], Stephen Solomon[2]

Affiliations:

1. Department of Diagnostic Radiology
   American University of Beirut Medical Center
   Riad-El Sold 1107 2020, Beirut - Lebanon
2. Department of Radiology
   Memorial Sloan Kettering Cancer Center
   1275 York Avenue
   New York, NY 10065, United States
3. Department of Medical Physics
   Memorial Sloan Kettering Cancer Center
   1275 York Avenue
   New York, NY 10065, United States

* Corresponding author

Purpose:
Venous thromboembolism (VTE) is a common cause of morbidity and mortality in hospitalized and surgical patients. Prolonged surgeries and interventions predispose patients to VTE through venous stasis and sometimes venous injury. The risk of VTE is high in patients with active cancer. To reduce risk, perioperative pharmacological and/or mechanical VTE prophylaxis is recommended for cancer patients undergoing surgical or interventional procedures.

Magnetic resonance imaging (MRI) is increasingly used in interventional oncology for diagnostic or therapeutic procedural guidance when alternative imaging modalities do not adequately delineate malignancies **(Figure 1)**. Extended periods of immobilization during MRI guided interventions necessitate MRI compatible devices for intraprocedural mechanical VTE prophylaxis. Such devices are not commercially available. We describe a modification to a standard sequential compression device (SCD) for compatibility in an interventional MRI (iMRI) setting.

Materials:
Kendall SCD™ 700 system, a standard device routinely used at our institution for VTE prophylaxis during non-MR-guided interventions was used. The system consists of the controller labeled "MR-unsafe" and "MR-safe" tubing extensions and single-patient use leg sleeves.

To satisfy MR safety requirements, the controller was installed outside of the MR intervention area and only the compression sleeves were brought into the scanner room. The SCD controller was placed in the MR control room and connected to the compression sleeves in the magnet room through the wave guide using three tubing extensions attached serially **(Figure 2)**. The SCD controller pressure sensor was used to monitor adequate pressure delivery and detect ineffective low or abnormal high pressure delivery, due to air leaks from the system or tube kinking.

The compression sleeves were applied to the patients' lower extremities and VTE prophylaxis was provided using the above mentioned device for all MR-guided ablations performed at our institution.

Thirty eight patients underwent MR-guided cryoablation of malignant lesions under general anesthesia between March 2011 and December 2013 using Galil Medical cryo system. The target lesions included bone (n=6), breast (n=10), kidney (n=5), liver (n=8) and soft tissue (n= 9). As per our institutional guidelines, SCD was indicated for VTE prophylaxis during ablation procedures.

RESULTS:
There was no evidence of device failure during the MR-guided procedures due to loss of pressure in the extension tubing assembly. No interference with the anesthesia or interventional procedures was documented during all 38 ablations.

Conclusion:
Although the controller of a standard SCD is labeled as "MR-unsafe", the SCD can be used in interventional MR settings by placing the device outside the MR scanner room, for example, in the MR control room. Using serial extension tubing assembly did not cause device failure. The described method can be used to provide perioperative mechanical thrombophylaxis for high risk patients undergoing MR-guided procedures.

Figure 1- 82 year old female patient, stage IV bladder cancer and borderline renal function presented with a growing solitary liver metastasis. The liver is the only site of disease progression. (a) Axial T2-weighted fat-saturated MR image of the liver showing a small hyperintense hepatic lesion in segment VII/VIII (arrow). (b) Non-enhanced CT scan at the same level showing difficulty in differentiating the hepatic lesion (curved arrow) from the adjacent vessels rendering CT-guided ablation less desirable.

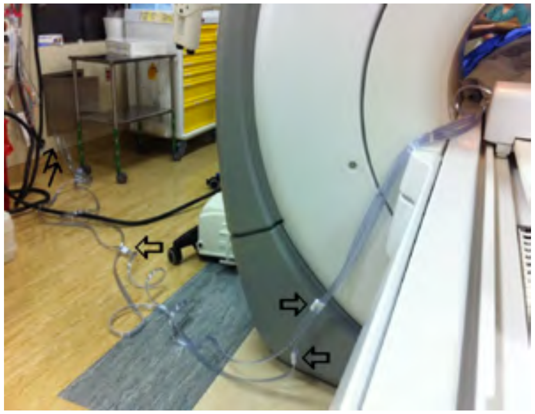

Figure 2- Provision of SCD during an MR-guided renal mass ablation. The patient is in prone position and all IR and anesthesia procedures are performed from the "front side" of the magnet. Photographs of the "back side" of the magnet showing the serial tubing extensions (open arrows) which connect the compression sleeves (applied routinely on the patient's legs inside the magnet) to the controller (not shown) via the wave guide in the wall (double thin arrows). The position and length of extension tubing is checked at the start of each intervention to make sure the patient can easily go in and out of the magnet.

Generation of Distinct Artifacts along Conductive Structures in Spin-Echo Phase Images by Application of Sequence-Triggered Direct Currents

Frank Eibofner, Hanne Wojtczyk, Hansjörg Graf, Stephan Clasen
Diagnostic and Interventional Radiology, University Hospital Tübingen

Purpose: Visualization of metallic devices in interventional MRI is mostly performed by use of susceptibility artifacts. Because device susceptibility is fixed and sequence parameter variability is limited by acquisition time and contrast, artifact sizes are often hardly controllable and differentiation in inhomogeneous tissue is difficult. Applying direct currents (DC) to a metallic device allows generation of artifacts which are controllable by amperage. With triggered DC, distinct dephasing artifacts can be generated in spin-echo (SE) phase images.

Materials and Methods: A current in a straight conductor generates a concentric magnetic field whose z-component is effective in MRI. Application of a triggered DC, e.g., during a time period between RF excitation and refocusing, results in non-static field inhomogeneities. Then, spins acquire a phase offset dependent on the distance to the conductor and on amperage, also in SE imaging. Additionally, false spatial encoding can be avoided if the current is switched only at times when no read-out and slice-encoding gradients are active. A water phantom containing a brass conductor (connected to a DC power supply, triggered by the sequence, water equivalent susceptibility) and a titanium needle (serving as susceptibility source) was used to demonstrate the feasibility of this approach. Gradient-echo (GE) images were acquired for comparison.

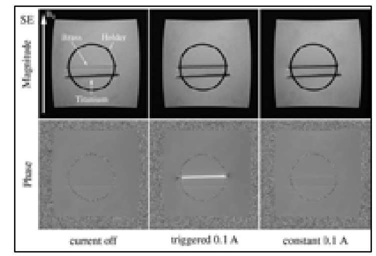

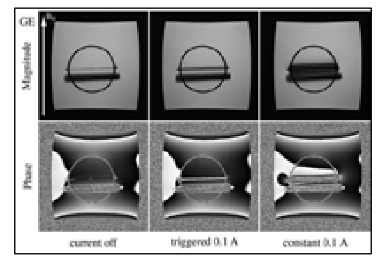

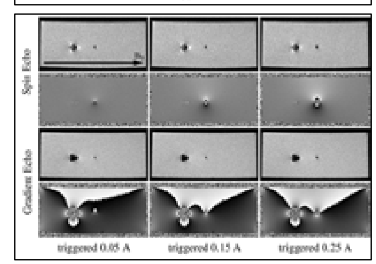

Results: Without DC, the brass conductor is only visible because of smaller proton density. The titanium needle shows typical susceptibility artifacts in SE (Fig.1) and GE images (Fig.2). With triggered DC, the phase offset of the spins near the conductor becomes visible in SE and GE phase images. However, reliable differentiation of susceptibility and DC artifacts is only possible in SE phase images where effects from static field inhomogeneities are not visible due to rephasing. The artifact caused by a constant DC is similar to the titanium needle's susceptibility artifact. The extension of the triggered DC artifact in the phase images is controllable with amperage (Fig.3). In magnitude images, artifact sizes increase slightly due to intravoxel dephasing.

Conclusion: A reliable and distinct localization of a metallic conductor can be achieved by the application of triggered DC in SE imaging. Magnitude and phase images, which display the position of the conductor free from static field inhomogeneities, could be acquired in a single scan and superimposed. This approach might be helpful for accurate tracking of interventional devices, especially if the device is already connected to an external current generator as with radiofrequency ablation.

A combined high-resolution internal imaging and RF ablation probe at 3T

M. Arcan Ertürk[a,b], Shashank S. Hegde[b], Paul A. Bottomley[b]
[a] Center for Magnetic Resonance Research, University of Minnesota Medical School, Minneapolis, MN,
[b] Russell H. Morgan Dept. of Radiology, Johns Hopkins University, Baltimore, MD, USA

Purpose. Conventional MRI-guided radiofrequency (RF) ablation requires a dedicated ablation catheter to deliver RF energy while monitoring treatment efficacy by separate imaging detectors and/or to perform thermometry. Here, we report on the development of a single 3T loopless antenna[1,2] integrating both functions to: (a) deliver RF energy; (b) monitor temperature changes; and (c) provide high-resolution (~300µm) imaging to confirm targeting and localized delivery of thermal therapy.

Methods. Experiments were conducted on a 3T Philips *Achieva*, with a λ/4, 2.2mm diameter loopless antenna[1] inside bovine tissue and pig aorta specimens immersed in a 3.5g/l saline bath. A non-magnetic RF switch was used to connect the loopless antenna to the MR scanner via a detuning/matching box during MRI or an RF power amplifier used for RF heating/ablation. For ablation, RF energy (110MHz, 30-60W) was applied for up to 2-6min. MRI (gradient or turbo spin-echo, TSE; standard T_1/T_2 mapping) and/or MR thermometry (8s temporal resolution; proton resonance frequency-PRF shift method; 2D gradient echo MRI) was performed pre- and post-ablation with the antenna switched to the scanner.

Fig 1. (a-c) MRI of bovine tissue pre-ablation (a), during ablation (b), and (c) post-ablation. Red voxels in (b) indicate a temperature rise greater than 30°C by MR thermometry. The antenna location is annotated in (a); yellow ellipse in (c) depicts tissue changes due to RF heating. (d) Photograph of the tissue post-experiment showing tissue discoloration due to ablation. (MRI sequence in (a) and (c): 4-slice 3D GRE, TR/TE=150/5ms, FA=40°, voxel size: 0.3x0.3x2mm^3, FOV: 50x50x8mm^3, duration: 69s).

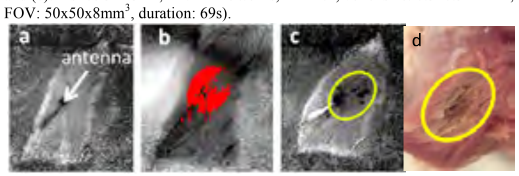

Results. Pre-ablation MRI of bovine tissue (Fig.1a) shows uniform contrast. During RF ablation, tissue heating >30°C is overlaid in red (Fig. 1b). High resolution MRI post-ablation shows hypo-intense signal (Fig. 1c; yellow ellipse) and a ~10% decrease in T_1, consistent with delivery of a thermal lesion, verified by examination post-MRI (Fig. 1d). Fig. 2 shows a 150µm pre-ablation MRI of an aorta specimen (Fig. 2a), and 250µm MR thermometry with delivery of thermal therapy above the antenna (red; Fig. 2b).

Fig 2. (a) High-resolution MRI of a porcine aorta (4-slice 3D TSE; resolution, 0.15x0.15x2mm^3; 170s). (b) Temperature image (PRF shift method; 0.25x0.25x6 mm^3 resolution; 8s) Temperature scale is in °C.

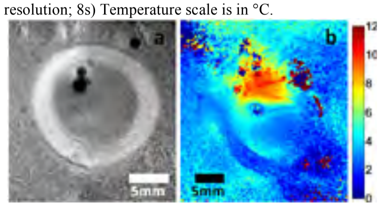

Discussion. The loopless antenna can be configured to receive high-resolution MRI signals at 3T, locally deliver an RF ablation to the specimen, monitor therapy delivery, and then image the outcome post-ablation. MRI excitation could also be done using the probe with adiabatic excitation[3] or spatially-selective B_1-insensitive pulses[4] (with MR thermometry to monitor device safety during procedures). A *single* device deployed in this way avoids size-limitations, device-coupling concerns, and safety issues associated with multiple conductor probes. Basically the device could serve as a complete detection, therapy delivery and monitoring vehicle.

***References*:** (1) Ocali O et al. Magn Reson Med 1997; 37: 112-118. (2) El-Sharkawy AM et al, Med. Phys. 2008; 35:1995-2006. (3) Sathyanarayana S et al, JACC Card Im. 2010; 3:1158-1165. (4) Erturk MA et al. Magn Reson Med 2014; 72: 220-226.
Supported by NIH grant R01 EB007829.

MRI COMPATIBLE LINEAR MOTION STAGE

Mohammad Ali Tavallaei,[1,2] Junmin Liu,[1] Patricia Johnson,[1,3] and Maria Drangova[1,2,3]
[1]Robarts Research Institute, London Ontario Canada, [2]Biomedical Engineering Graduate Program, Western University, [3]Dept. of Medical Biophysics, Western University, London Ontario, Canada

PURPOSE: Controlled dynamic motion of phantoms in MRI may be used for various applications in interventional MRI such as validation and assessment of MRI guided therapy, tracking and navigation techniques, hybrid systems, pulse sequence development, and motion correction. To address this need we have developed an MRI compatible linear motion stage that can deliver highly accurate and reproducible dynamic motion profiles inside the bore during imaging. The completely MRI compatible stage can be placed within the bore at arbitrary orientations, where it can carry conventional phantoms or be used to deform flexible phantoms.

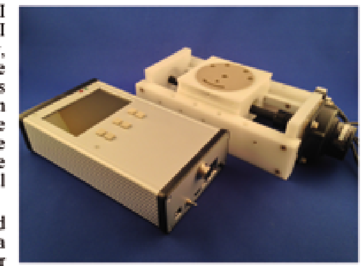

Fig. 1. Photograph of the linear motion stage and the control unit.

METHODS: A compact non-magnetic stage was designed and fabricated (Fig. 1). The stage carriage is driven along a precisely machined lead screw by an ultrasonic motor (USR60-NM, Fukoku-Shinsei). A custom-designed embedded system enables dynamic control of the motor's position. The accuracy of the stage in reaching fixed reference positions was first evaluated in the laboratory using an optical microscope (STM6, Olympus). For all tests the stage was loaded with 1.5 kg. Reference positions of ±1 through ±20 mm were prescribed and repeated 10 times. To evaluate the execution of dynamic motion, an optical tracking tool was attached to the carriage and sinusoidal reference profiles, with amplitudes between 1 and 10 mm at 0.5, 0.33 and 0.25 Hz, were prescribed. The position was tracked using an optical tracker (Vicra, NDI) and logged at 20 Hz for a period of 5 minutes. Simultaneously, the embedded system logged the motor's encoder position at approximately 100 Hz. Stage performance was evaluated within a 3T scanner (MR750, GE). Motion accuracy inside the scanner was evaluated during imaging using a skull-like phantom filled with agar. The phantom was moved to fixed references positions (2,5,10 and 15mm) and sinusoidally (amplitude = 10 mm; freq. = 0.33 Hz). The executed sinusoidal motion was measured using spherical navigator echoes (SNAV) [1] acquired while the phantom was moving with the prescribed motion. Gated FIESTA images were also acquired of a tangerine moving with 5 mm amplitude and frequency of 0.33Hz (TR/TE=8/4 ms, flip 20°, slice thickness 5 mm). The effect of the stage on B_0 variation was quantified using a 3-echo GRE sequence [2] (IDEAL, TR/TE=7/3ms, FOV/ thickness = 32 cm /2 cm, 256x256); images were acquired of a 33x22x13 cm Gd-doped-water phantom placed over the stage. The effect of the stage on image artifact was also evaluated, following standards set by ASTM F2119-07.

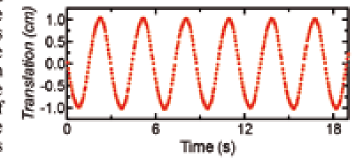

Fig. 2. Translation estimates from SNAV phase shifts of a phantom on the stage moving with sinusoidal motion amplitude of 1 cm.

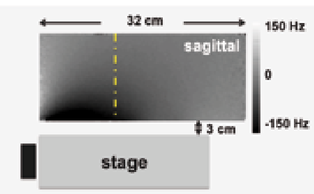

Fig. 3. Effect of stage on B_0 field: Sagittal ΔB_0 map is shown. The dashed yellow line indicates the reference motion position.

RESULTS: The mean absolute error in reaching fixed positions measured with the optical microscope was 0.14±0.06 mm. For dynamic motion, the worst-case RMSE and normalized RMSE measured with the optical tracker were 0.3 mm and 6%, respectively. The translation motion estimates measured with SNAV during imaging matched the results obtained in the laboratory setting (Fig. 2). Also, the gated FIESTA images of the moving tangerine demonstrated the expected motion. The worst case B_0 variation was less than 2 ppm (Fig. 3). The stage did not introduce any image artifacts as is defined in ASTM F2119-07 standard.

CONCLUSION: The MRI compatible linear motion stage can be used to generate reproducible and accurate user-defined motion profiles inside the bore of a scanner. The versatile carriage enables the use of the stage with a variety of custom phantoms for research and quality assurance for MRI-guided interventional procedures.

REFERENCES: [1] J. Liu and M. Drangova, *Magn. Reson. Med.*, vol. 65, no. 2, pp. 506–14, Feb. 2011. [2] J. Liu, D. W. Holdsworth, and M. Drangova, in *Proc. Intl. Soc. Mag. Reson. Med*, p. 1615, May 2014.

Utilization of a Sterilizable Interventional MRI Coil for Procedures in the Magnet

David A. Woodrum, MD/PhD[1], Krzysztof R Gorny, PhD[1], Ralph Hashoian[2], Joel P. Felmlee, PhD[2]
[1]Mayo Clinic, Rochester MN and [2]Clinical MR Solutions, Brookfield WI

Purpose: Evaluate the use of a sterilizable interventional MRI coil for procedures within the bore of the magnet.

Methods and materials: The iCoil (Clinical MR Solutions, Brookfield, WI) is a 3 coil receive only array that is designed for interventional applications. The 3 coil array has an S/I (superior/inferior) dimension of 216mmm (8.5 inches). The central coil has a width of 229 cm (9 inches) that accommodates a finished opening in the packaging of 150mm (5.9 inches) left/right(L/R) and 177.8mm (7 inches) S/I. The 2 outer coils L/R dimension is a bit narrower at 203mm (8 inches) to give a little boost in SNR. The opening is large enough to accommodate interventional procedures such as needle placement for cryoablation, laser ablation and biopsy applications. A unique feature of the coil is that it is encased in a waterproof polyethylene material with a low profile thickness (< 13mm) for complete access to the opening. To keep the profile low, most of the components are located in a remote gateway. Additionally, the cable is designed to quick disconnect allowing for replacement of the coil and not the hardware. Finally, the coil is designed to be usable in both the Siemens and GE MR platforms.

Results: The iCoil works well across both platforms. We utilized the iCoil mostly on the Siemens Espree MRI platform due to more open configuration of the bore and in-room monitor setup. Sterilization was performed in the specially designed chamber using MetriCide OPA plus solution. The imaging was not quite as good as an 8-channel coil, but the open, low-profile design more than made up for the slight decrease in imaging quality. Even in situations where the coil did not have to be sterile the waterproof design made clean up easier if prep solution or blood were spilled on the coil. We have utilized the iCoil in at least 30 different procedures from liver, prostate and extremity procedures with good functionality and image quality in each situation.

Conclusion: The iCoil works well for interventional MRI procedures and facilitates better sterility during the procedure with larger opening for needle placement.

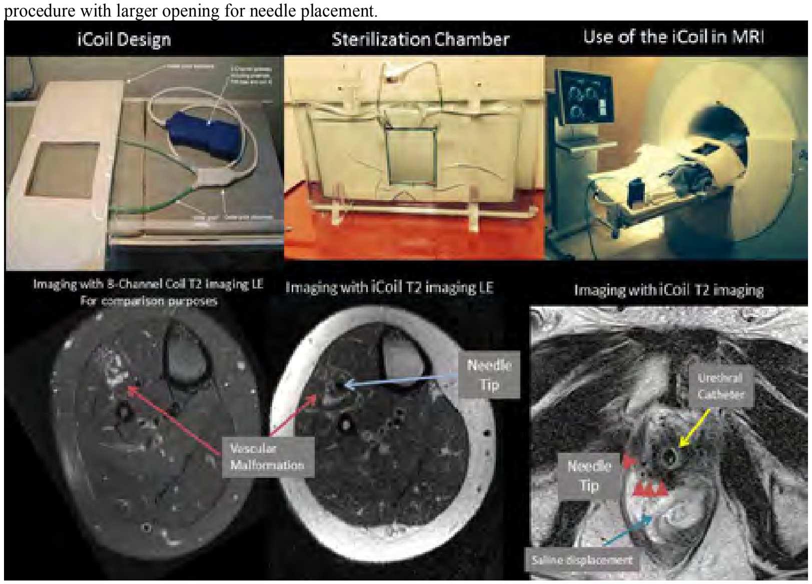

Simultaneous contact-free monitoring of the cardiac and respiratory cylce in real-time during MRI using an optical tracking system

Falk Lüsebrink[1], Oliver Speck[1]
[1] Biomedical Magnetic Resonance, Otto-von-Guericke University, Magdeburg, Germany

Purpose: This contact-free measurement constitutes a novel approach to monitor the cardiac and respiratory cycle simultaneously in real-time during magnetic resonance imaging (MRI). Switching of the gradients and the magnetohydrodynamic effect due to the static magnetic field disturbs electrocardiographic measurements, while optical based methods are not. The purpose of this work was to evaluate the practicability of this approach to measure physiological parameters.

Material and Methods: A mock MR scan of the head was conducted of eight subjects for approximately ten to fifteen minutes. They were placed in a 3 T MR system (Magnetom Skyra, Siemens, Erlangen, Germany) and their heads were fixated with a cushion inside a 32-channel head coil (Head 32, Siemens, Erlangen, Germany). An MR compatible camera system (MR 384i, Metria Innovation, Milwaukee, WI, USA) was used to measure head movements. The camera was placed in the center of the bore facing directly downwards on the subject's head. A moiré phase tracking marker was attached to their nasal bridge (Fig. 1). Physiological parameters were extracted from the subjects' head motion in real-time.

Figure 1: Subject with moiré phase tracking marker attached to his nasal bridge.

Results: The assessment of detected heart beats has been performed by calculating the sensitivity (*Se*) and the positive predictive value (*+P*):

$$Se = \frac{TP}{TP + FN} = 99.6\%$$

$$+P = \frac{TP}{TP + FP} = 99.5\%$$

where TP is the number of true positives, FN the number of false negatives and FP the number of false positives of all subjects. Processing time per camera frame is less than 0.4 ms.

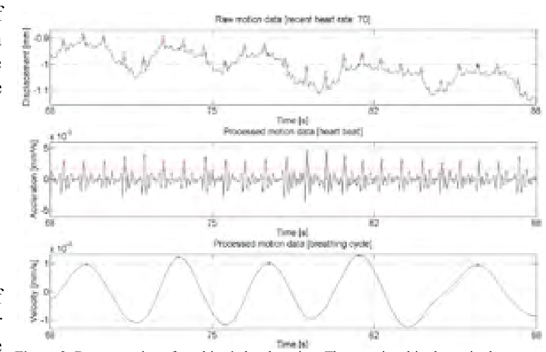

Figure 2: Demonstration of a subject's head motion. The raw signal is shown in the upper, the processed signal for the heart beat detection in the middle and the processed signal for the respiration in the bottom graph. Red circles represent detected heart beats and blue stars detected respiration cycles. The red dashed line indicates a threshold based on the median of the detection heart beats.

Conclusion: The detection of cardiac and respiratory signals is possible simultaneously and reliably in real-time using this innovative method (Fig. 2). It enables contact-free monitoring of vital signs and the application for real-time triggering to acquire data which is insensitive to physiological motion seems possible.

Acknowledgements: This work is supported by the German Ministry of Education and Research (BMBF) under grant number '03FO16101A' and the Land of Saxony-Anhalt under grant number 'I 60' within the Forschungscampus *STIMULATE*.

A 40 channel Wireless Torso-Pelvic Array Coil for Parallel MR Imaging Interventional Applications at 3.0 T

Seunghoon, Ha[1],Szymon Rzeszowski[1], Haoqin Zhu[1], Labros Petropoulos[1]
[1]*Research and Development, IMRIS Inc., Minneapolis, USA*

Introduction: Multichannel arrays with a large number of channels are the preferred RF coil technology for abdominal imaging applications, owing to their ability to uniformly cover large imaging regions with improvement is SNR, and are optimum for utilizing parallel imaging. However, the presence of all large number of channels with their associated electronic and cabling including cable traps increases significantly the weight that the coil structure exerts on a frail patient, which can be on the excess of 20lbs (10kg) or more while restricts patient accessibility which is needed for interventional applications.. As a result, massive coil arrays and their associated cabling can be used for diagnostic imaging applications but their significant weight and space restrictions impede or prohibit the applications for utilizing MR for interventional or surgical procedures.

In order to address this problem, an ultralight multichannel wireless torso array coil without cabling that is ideal for interventional MR application on the abdomen/pelvic region. Specifically, a 40 channel novel wireless-cableless combo torso-pelvic coil technology is presented. The proposed design incorporates an 8 channel ultralight wireless anterior torso-pelvic array coil with a 32 channel cableless posterior phased array coil. The total weight of the wireless coils is less than 8 ounces (200grams) which is 90% lighter than a traditional cabled coil of the same size, while the posterior coil is cableless and it embedded into the diagnostic table. As the results indicate below, the 40 channel wireless-cableless combo design, compares favorably to a cabled traditional phased array design with the similar number of channels in terms of coverage (FOV), image quality, and parallel imaging on a 3.0 T MRI. The advantages of the proposed design include the significant weight reduction of the entire combined structure, the elimination of RF heating issues caused by cables and cable baluns, and the increase of available usable space inside the bore of the magnet. Furthermore, because of the absence of preamps and interconnecting cables, the wireless coils have large openings on the top and the side parts of the coil and are intentionally optimized for interventional and intraoperative procedures, as well as multi-modal imaging such as Radiation Therapy, X-ray, CT, or PET combining with MRI [3].

Fig.1: *40 Ch. Wireless combo array*

Methods: Figure 1 illustrates the 40 channel phased array wireless coil consisting of 8 elements covering on the anterior part, while 32 elements are nested on the table. The anterior wireless coil design consists of 4 rows with 2 elements per row, while the cableless posterior coil consists of 8 rows of 4 elements each. Since the wireless coil requires no matching, the performance of the coil depends on the sensitivity of each element which is directly correlated to the unloaded Q of the coil. For each element of the anterior wireless coil the unloaded Q_u was measured to be greater than 180 measured at 3.0T. Each of the 32 elements of the posterior coil is tuned to 123.2 MHz, matched to 50 Ω and isolated from each other via pre-amp decoupling. The wireless array coil elements were also tuned to 123.2 MHz with passively detuned circuits. All elements incorporate an RF fuse for patient protection. Mutual coupling between adjacent elements is resolved by a combination of geometric and capacitive decoupling techniques [4]. The isolations were measured below -15 dB from next neighbor coil elements. The ratio of unloaded and loaded quality Q factor (Q_u/Q_L) for the each element of the coil array is 4.8. The coils are placed on a vest style holder with side straps that enable side access for interventional applications.

Results: Using a body coil phantom doped with a NaCl and CuSo4 solution, the 40 channel wireless-cableless combo phased array coil was tested for its imaging performance on a Siemens Magnetom Skyra 3.0 T. Table 1 depicts a comparison between the 40 channel wireless-cableless array coil, a 50 channel OEM cabled body array coil and a 32 channel OEM cabled coil. Our proposed coil design is superior in SNR by10% but lack in uniformity -10% when compared to the OEM body array equipped with 10 more coil elements. As table 1 indicates, the 40 channel wireless-cableless combo array coil outperforms the 32channel cabled OEM coil in uniformity by 10% and SNR by 56%. After passing all the required safety tests, the wireless array coil was further evaluated using volunteer imaging including parallel imaging with IPAT factors up to 3 or (2x2 isometric). Fig. 2 displays volunteer images of the torso areas using the 40 channel wireless-cableless combo array using sequences suitable for body array imaging with or without breathhold. Furthermore, figures 3 and 4 show a comparison between the 40 channel coil with a 50 channel OEM Body matrix coil. Using a set of sequences targeting torso, spine and pelvic areas of the volunteer, the results indicate that the image quality, uniformity and SNR of the 40 channel wireless-cableless combo array are equal or better than the traditional cabled 50channel OEM Body array coil.

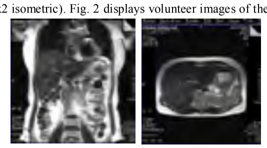

Fig. 2 *T2 torso image using the 40 ch. wireless coil: Image on Left T2 Haste Coronal IPAT3 no breath-hold. Image on right T2 Haste Axial IPAT 2 no breath-hold*

Conclusion: An ultralight 40 channel wireless-cableless combo phased array torso/abdomen coil has been presented. The absence of cables, electronics and cable traps for the coil resulted in reduction of the weight of the coil by as much as 90% when compared to a cabled phased array coil with the same number of channels. In addition, the proposed design has 56% better SNR and 10 % better uniformity when compared with the 32 channel OEM matrix coil. Volunteer imaging with IPAT up to 3 or (2x2 isometric) on the torso, pelvic and spine area reinforces the proof that the proposed design is better in diagnostic image quality when compared to a cabled OEM coil. The elimination of cables and active components leads the proposed design to improve patient access, coil quality and reliability. Additional benefits include ultralight weight, lower cost, superior access for interventional and surgical applications (such as spine interventions, liver ablations, etc.), and compatibility with multiple imaging modalities and systems.

Fig. 3: *Comparison between a 40ch Wireless Combo array(left) with a 50 ch OEM Body coil(right): Seq: T2 Haste Coronal IPAT 3*

Reference:

1. Hardy CJ, Giaquinto RO, Piel JE, Rohling KW, Marinelli L, Blezek DJ, Fiveland EW, Darrow RD, Foo TK. "128-channel body MRI with a flexible high-density receiver-coil array." J Magn Reson Imaging. 2008 Nov;28(5):1219-25

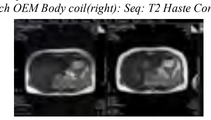

Fig. 4: *Comparison between a 40ch Wireless Combo array(left) with a 50 ch. OEM Body coil(right): Seq: T2 Haste Axial IPAT 2*

Coil Configuration	Signal / SD Noise	SNR	% difference	Uniformity(signal mean High/signal mean Low)
40 channel Wireless-Cableless COMBO coil	1778.0/2.2	808.2	156%	2451.3/1027.5=59%
32 ch OEM Spine Coil +18 channel OEM anterior Body coil	1537.6/2.1	732.2	141%	2442.0/1194.8=65.7%
32 channel OEM posterior Spine coil	1345.9/2.6	517.7	100% (base)	2475.5/801 =49% (base)

Table 1. Performance of RF coils employed on MR phantom study.

RTHawk: A Development and Control System for Real-Time Interventional MRI

R. Reeve Ingle[1], Bob S. Hu[1], Kenneth O. Johnson[1], Michelle M. Nystrom[1], William R. Overall[1], Galen D. Reed[1], Juan M. Santos[1]
[1]*HeartVista, Inc., Menlo Park, California, United States*

Purpose Magnetic resonance imaging (MRI) is a powerful tool used to assist many different interventional applications. RTHawk, which is an open, flexible research environment that was designed to minimize latency and increase interactivity of real-time imaging, allows developers to build and customize advanced MR applications. This MRI platform can be especially significant in applications such as electrophysiological (EP) interventions, high-intensity focused ultrasound (HIFU) ablation, and convection-enhanced drug delivery (CED), enabling real-time device guidance, feedback monitoring, and device control.

Methods and Applications The RTHawk real-time platform enables the development of customized pulse sequences, image reconstruction pipelines, and visualization tools. Pulse sequences are designed in SpinBench, a GUI-based design tool (Fig. 1). Sequences can be tested throughout the design process using a fully featured interactive Bloch simulator. The image reconstruction architecture uses a pipeline topology to provide an adjustable environment expressed in JavaScript. RTHawk includes an extensive library of building blocks to create complex sequences and reconstructions. Custom blocks can be easily integrated into the libraries.

Figure 1. Pulse sequence design in SpinBench. A 2D slice-selective excitation and 16-interleave spiral readout are designed. The slice profile and off-resonance response are simulated using the integrated Bloch simulator.

The RTHawk platform enables on-the-fly switching between different sequences. Multi-threading is automated for high-performance processing. The dynamic nature of the platform allows sequences and reconstructions to interact, and to integrate a variety of external inputs including HIFU information, real-time updating of scan planes to track catheter positions, etc. Post-processing steps can be further integrated directly into the reconstruction.

Unique interfaces for each application are built with Qt. GUI elements can be connected to the control and reconstruction pipeline for custom interactions with immediate feedback. Interventional devices can be readily integrated with RTHawk for real-time feedback and control. RTHawk has been successfully used at research institutions for a variety of applications including catheter tracking, MR-guided HIFU, EP ablation, and CED (Fig. 2).

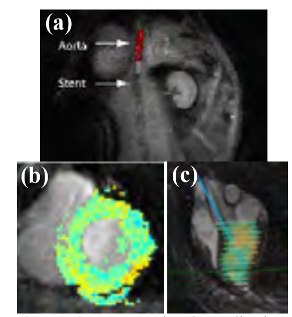

Figure 2. Interventional applications using RTHawk. **(a)** Catheter tracking. **(b)** Real-time temperature mapping for HIFU (V. Rieke, UCSF). **(c)** EP ablation (G. Wright, Sunnybrook, Toronto).

Conclusions Real-time MRI is a powerful tool that can complement and guide interventions, but the demanding technological requirements can delay or preclude its integration with many interventional applications. RTHawk is an open platform that can empower researchers and device manufacturers to customize the MRI integration, enabling low-latency real-time imaging in many interventional applications.

Advances in Tracking Multiple Markers within a MR scanner

D Brujic[1], F Galassi[2], M Ristic[1]
[1] Imperial College London, London, United Kingdom
[2] Radcliffe Department of Medicine, The University of Oxford, Oxford, United Kingdom

Purpose A novel method that significantly accelerates the localisation of multiple markers embedded within an interventional tool is presented. This improvement is achieved using only three one-dimensional projections and a novel solution to the `peak-to-marker' correspondence problem. Faster localisation enables higher tracking sampling rate that in turn improves the interventionist's eye-hand coordination and leaves more time for image updating. The method may be used for tracking wireless as well as wired markers that use a single receiver channel.

Materials and Methods Recently, a solution based on three 1D projections has been suggested [1], but it imposes severe constraints on the tool movement and on the configuration and number of markers. The key issue in any method that uses 1D projections is to remove fictitious points generated in the process of marker reconstruction. Standard methods to remove surplus points use additional projections but their scanning time is prohibitive. Instead, the solution proposed here uses a known geometrical arrangement of the markers embedded within a device. The essence of the solution is the search for the pre-defined path that passes through all the markers. Only known distances between the markers along the path are used for the search. The algorithm is implemented as a recursive linear search.

Results The method was validated using Monte Carlo simulations and by experiments performed in a 3T MR scanner. The method was used in a preclinical evaluation of MRI guided prostate biopsy Fig 1. The evaluation involved miniature RF markers (3x3x8mm), a customized GRE sequence, robot, phantom and an MR-compatible moving platform [2]. Acquisition time was 15 milliseconds, which represents a time saving of 400% compared to other methods. The computational time to localise 5 markers was around 1ms. The maximum error when using up to 5 markers was within the 0.5mm. Dynamic tracking tests proved the reliability of the method when the markers move at a speed anticipated in interventional procedures.

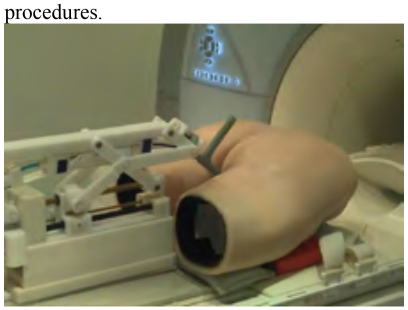

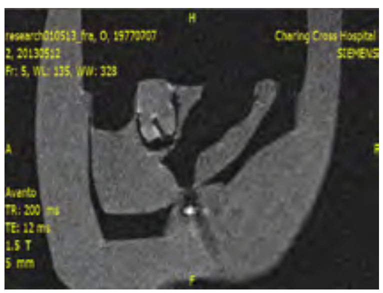

Fig. 1 a) System setup: robot, probe and phantom; b) MR scan after firing showing a hit

Conclusion Due to its speed, generality and robustness the method may be incorporated in many interventional MRI guided procedures such as navigation and motion compensation. Importantly, the method does not impose restrictions on the interventional tool movement.

References

1. Ooi M, Aksoy M, Maclaren J, Watkins R, Bammer R. Prospective motion correction using inductively coupled wireless RF coils. MRM 2013;70; 639-647
2. Galassi F, Brujic D, Rea M, Lambert M, Desouza N, Ristic M. Fast and accurate localization of multiple RF markers for tracking in MRI-guided interventions. Magn Reson Mater Phy May 2014

Miniaturizing floating traps for suppression of induced RF currents on linear conductors

Gregory H. Griffin[1,2], Kevan J.T. Anderson[1], Graham A. Wright[1,2]
[1]*Imaging Research, Sunnybrook Research Institute, Toronto, Canada* [2]*Department of Medical Biophysics, University of Toronto, Toronto, Canada*

Purpose: At present, conductive devices inside patients undergoing MRI present a significant safety risk in the form of unwanted heating around said devices. Many beneficial MRI exams and interventions are currently contraindicated due to the presence of a conductive device. Work in the past has created specialized interventional devices, to allow for specific procedures to be carried out safely under certain stringent conditions [1,2]. In general though, MRI-based interventional procedures involve a catheter with several conductors running along the length. To effectively suppress currents flowing on conductors inside the patient, traps should be distributed along the length inside the patient. This work proposes using a miniaturized version of Seeber's floating trap concept, to suppress current on any conductor passing through the lumen of the trap [3]. In future, the authors envision embedding several miniaturized floating traps into a catheter wall, thus suppressing RF current formation on any conductor (including guidewires, as well as transmission lines to coils at the tip) running down the catheter lumen. This work aims to demonstrate that a distribution of miniature traps can theoretically suppress dangerous currents to a safe level, and experimentally verify the functionality of miniature traps.

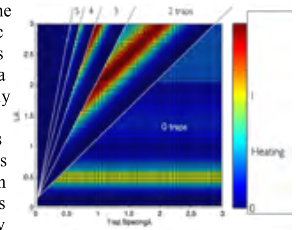

Figure 1: Simulated heating of various conductor lengths (vertical axis) and trap densities (horizontal axis). Both axes are scaled to wavelength.

Methods: Using knowledge of trap geometry, the theoretically induced impedance on a wire passing through a floating trap was calculated from the inductance and resistance of the trap. As the trap is miniaturized, the ratio of trap inductance to resistance inside the trap goes down, and theoretically induced impedance is significantly reduced. It was calculated that a miniature copper trap with 9F (3mm) outer diameter, 1mm lumen and 2cm in length can induce at most 42 Ω of impedance if perfectly tuned. A simulation was then carried out in MATLAB, to calculate the relative heating of an unmodified conductor and several other conductors with various miniature trap distributions along their length. A conservative induced trap impedance of 35 Ω was used in simulation. Relative heating is the 1g-averaged SAR in a cube around the conductor tip, under application of a unit RF electric field tangent to the wire. Several conductors of various lengths with different trap densities were investigated, beginning with 0 traps and working up to a catheter made entirely of traps. Each SAR value was normalized to the maximum SAR produced with 0 traps in place. Following this simulation, two sizes of miniature trap were built; both 1.4 cm long, trap 1 with 20mm/6mm outer diameter and lumen, and trap 2 with 3mm/1mm. The induced impedance of these traps was then measured using a network analyzer. To date, the change in induced current pattern on a wire due to a single trap has also been measured experimentally in a phantom and compared with a commercial Method of Moments simulation (FEKO, E&MSS, South Africa) [5].

Results: The measured induced impedance of traps 1 and 2 were 252 Ω and 38 Ω respectively, as compared to the calculated ideal values of 283 Ω and 42 Ω. Figure 1 shows results of the MATLAB simulation of trap density vs. conductor length; the important result here is the dark blue region on the left of the image. This indicates that for any conductor length, traps inducing 35 Ω, spaced at most λ/4 apart can reduce heating to less than 10% of the maximum heating achieved with an unmodified wire. The induced current with a single trap in place was reduced as predicted by FEKO, within the error of the current measurement.

Conclusion: This work has shown that the impedance induced by floating traps and the effects of miniaturization can be accurately modeled based on geometry. Further it was shown with bench-top and phantom experiments that these properties are realizable in a fabricated catheter-sized trap. In simulation it was shown that several catheter-sized traps distributed along a catheter inside the body could effectively suppress heating to a safe level. More experimentation is required and ongoing to further experimentally verify the current suppression abilities of several traps inside a dielectric body.

References: [1] Weiss et al. MRM 2005 [2] Ladd & Quick, MRM 2000 [3] Seeber et al. Concepts in MR 2004 [4] ASTM F2181-11a [5] Griffin et al. MRM 2014

MR Monitoring of Thermochemical Ablation Injections

Florian Maier[1], Christopher J. MacLellan[1], David Fuentes[1], Erik N. K. Cressman[2], Ken-Pin Hwang[1,3], Joshua P. Yung[1], John D. Hazle[1], and R. Jason Stafford[1]

[1]Department of Imaging Physics, The University of Texas MD Anderson Cancer Center, Houston, TX, United States
[2]Deptment of Interventional Radiology, The University of Texas MD Anderson Cancer Center, Houston, TX, United States
[3]Global Applied Science Laboratory, GE Healthcare Technologies, Waukesha, WI, United States

Purpose. Thermochemical ablation (TCA) provides a novel concept in minimally invasive ablative procedures in which two reactive solutions [1], such as an acid and a base, release heat as they react prior to entering the tissue as a hot salt solution. Thermal damage results in surrounding tissue via the released thermal energy. Recently, evaluation studies of TCA were performed using thermal probes to monitor temperature changes during the treatment. However, this allows evaluating temperature at a few positions only. In this work, use of a improved multi-parametric MR pulse sequence [2,3] for online monitoring of TCA treatments is investigated to provide more detailed insight for effective delivery to advance the understanding of this technology towards clinical translation.

Material and Methods. The pulse sequence was implemented on 3 T MRI (Discovery MR750, GE Healthcare, Waukesha, WI). A basic 2D gradient echo sequence (2DFAST) was modified. Variable flip angles for dynamic T1 mapping were attained by modifying the pulse amplitude after the acquisition of each temporal phase. A readout echo train ($n \leq 16$) was added to the sequence with positive read-out polarity and a flyback pulse to minimize artifacts. The sequence allows for shifted echo trains with each temporal phase to attain higher temporal resolution of the T2* decay when combined. The following pulse sequence parameters were used: $\alpha_1 = 10°$, $\alpha_2 = 25°$, $TE_1 = 2.0$ s, inter-echo spacing = 1.0 ms, TR = 44 ms, flip angles = 1025, echo shifts = 2, bandwidth = 1116 Hz/px, matrix = 128×128, field of view = 256×256 mm^2, acquisition time = 6.0 s (full dataset 24 s). Multiple flip angle measurements were performed during two TCAs in *ex vivo* canine and bovine liver. The exothermic reaction of acetic acid (3 ml, 10 M) and sodium hydroxide (3 ml, 10 M) was employed. Auto-regressive moving average (ARMA) processing [4] was performed to estimate PRF, T2*, and signal amplitudes of each chemical species. Based on the signal of each flip angle excitation T1 was estimated.

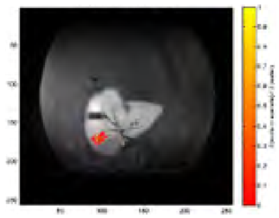
Fig. 1 Real-time monitoring of TCA ablation. Magnitude images of canine liver overlayed with normalized sodium acetate signal (colored) after injection.

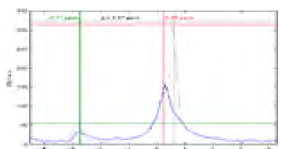
Fig. 2 Real-time spectra of a pixel inside the ablation region after injection. Fourier transform (FT) of the signal (solid lines, blue), FT of the extrapolated signal at TE = 0 (dotted lines, blue), and FT of the signal of each species at TE = 0 (dotted lines, gray). Peak positions of water (red) and sodium acetate (green) and the shift (black).

Results. Fig. 1 shows sodium acetate maps based on the ARMA results (cf. Fig. 2). The measured offsets between the peaks (2.89 - 2.97 ppm) matched the expectations. The variable flip angle T1 estimation (Fig. 3) overestimated T1 slightly (compared to IR data). MR temperature imaging (MRTI) was in good agreement with the thermal probe measurement (Fig. 4) after injection was finished.

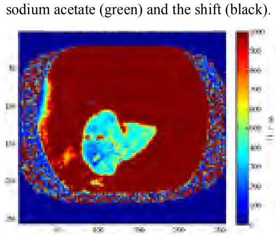
Fig. 3 Real-time T1 map after injection.

Conclusion. During MR temperature imaging, high resolution PRF can be obtained for each species at each time point from ARMA processing of the echo train [4]. By using echo-shifting, higher spectral bandwidth data can be accumulated over multiple time points to unwrap peaks. T2* could be used for long term temperature and drift correction and combined with similar information from T1 mapping. Additionally, the T2* and T1 maps can be analyzed to assess tissue damage [3-6].

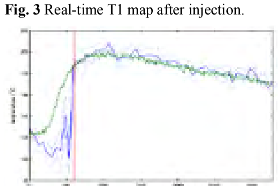
Fig. 4 Absolute temperature of thermal probe (green) and MRTI temperature difference (blue) during a TCA injection.

References. [1] Cressman ENK, et al. Int J Hyperthermia 26(4), 2010. [2] Maier F, et al. Proc ISMRM, 2014. [3] Taylor BA, et al. NMR Biomed. 24(10), 2011. [4] Taylor BA, et al. Med Phys. 35(2), 2008. [5] Todd N, et al. Proc ISMRM, 2013. [6] Todd N, et al. Magn Reson Med. 69(1), 2013.

Wireless hybrid passive and active tracking for automatic image plane alignment

M. Neumann[1], E. Breton[1], L. Cuvillon[1], L. Pan[2], E. Rothgang[2], A. Hengerer[2], M. de Mathelin[1]
[1]ICube, Strasbourg University, CNRS, IHU Strasbourg, Strasbourg, France
[2]Center for Applied Medical Imaging, Siemens Corporate Research, Baltimore, MD, USA

Purpose

Automatic image plane alignment increases heavily the time efficiency of percutaneous interventions under MRI guidance. Existing active [1,2] and passive [3,4] tracking approaches rely respectively on additional electrical hardware or on direct detection in the MR images. In this work a hybrid tracking approach for automatic image plane alignment combining detection in MR images (passive) and in images from an RGB-D sensor (active) is presented. The tracking performance is evaluated using an MR compatible testbed.

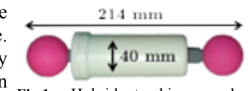

Fig.1: Hybrid tracking marker prototype consisting in a passive MRI marker surrounded by 2 colored balls.

Material and methods

All imaging experiments are performed in a 1.5T system (Siemens Aera) using an interactive, real-time, multi-slice TrueFISP sequence (Beat_IRTTT [5], Siemens Corporate Research & Technology). The hybrid tracking approach is implemented within a custom software interface on an external PC that is connected via Ethernet to the MRI console PC. The hybrid tracking marker consists in a cylindrical MR contrast-agent filled marker used for detection within MR images, equipped with 2 colored balls at its distal ends for detection within RGB-D images (Fig.1). Two orthogonal MR image planes are alternately acquired and automatically aligned to the detected marker positions. For this purpose, the detected poses of the marker from MR images and RGB-D sensor images are combined (Fig.2) using an information filter, implemented to combine data with different acquisition frequencies. In case of failed probe detection (line-of-sight obstruction / probe outside MR image plane) in one modality, the probe can still be tracked in the complementary modality. In order to translate the detected marker position from the RGB-D sensor to the MRI frame of reference, an online registration approach is implemented allowing to determine the rigid transformation between MRI and RGB-D sensor frames in the beginning of the intervention. The precision quality of the developed approach is evaluated using an MR compatible testbed on which the tracking marker can be mounted (Fig.3): the position sensor provides a ground-truth marker pose within the MRI scanner frame.

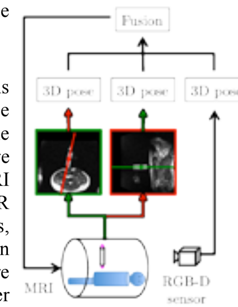

Fig.2: Hybrid workflow: pseudo axial (green) and sagittal (red) MR scan planes are alternately acquired. RGB-D sensor based and MR image based detection results are fused and scan planes are accordingly aligned to the tracking target.

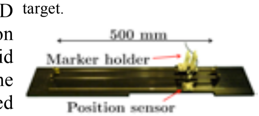

Fig.3: MR compatible testbed

Results

With a mean translation speed of 15.1 mm/s, the root mean square error between detected hybrid marker position and the ground-truth was 5.7 mm, which is on the order of the pixel size and the image slice thickness. Combination of both tracking sensors allows for robust tracking.

Conclusions

The hybrid workflow combines the tracking performance of a passive approach based on MR images with the high frequency measurements of an active approach using an RGB-D sensor. Their combination allows for flexible and reliable tracking without heavy instrumentation, and can be easily introduced into the clinical workflow. Such plastic low cost probe prototype can be chemically sterilized or made single use.

References: [1] Qing et al., ISMRM 2010; [2] Viard et al., EMBC 2007; [3] DeOliveira et al., ISMRM 2008; [4] Maier et al., ISMRM 2011; [5] Pan et al., ISMRM 2011.

A Comparative Method to Evaluate the Performance of different Resonant MR Marker Designs

E. Pannicke, M. Kaiser, G. Rose, R. Vick
Institute for Medical Engineering, Otto-von-Guericke University Magdeburg, Germany

Purpose: Resonant MR markers tuned to the Larmor frequency can be used for instrument visualization. Two methods are generally used to prove the performance of the MR marker. One method is to obtain an MR image using a low flip angle sequence [1]. Thereby, a comparison with already implemented designs is only of limited value since the signal intensity is highly dependent on several parameters, e.g. used MR sequence, protocols and image post-processing. Secondly, electrical parameters can be determined by measuring the scattering parameters through inductive coupling to a vector network analyzer [2]. However, experience has shown that the resonance frequency and quality factor of an MR marker is relative to its electrical environment. Thus, we demonstrate a method for measuring the amplification of the B_1 field caused by the resonant MR marker.

Material and Methods: Two different resonance MR marker designs were compared: a homogeneous Swiss Roll ([3], Design A) and a heterogeneous resonator, consisting of one dedicated inductance and capacitance (Design B). The MR markers were tested within a $CuSO_4$ solution inside a 3T MR scanner (MAGNETOM Skyra, Siemens AG Healthcare Sector, Germany) using a TSE sequence ($TE/TR = 14\,ms/\,4000\,ms$, matrix 512×357, slice 2 mm, FOV 180 mm×124 mm). The transmitter (TX) voltage was increased from $0V$ to the scanners reference voltage in $5V$ steps for the purpose of determining a B_1 field map according to [4]. The MR images were reconstructed offline in order to obtain a non-clipped range of signal intensities. The B_1 field amplification A was determined by fitting the signal intensities vs. the transmitter output voltages to the function given in [4].

Results: The obtained amplification factors are shown in Fig. 1(a) and (b). Both designs have significant differences in the amplitude and shape of the amplification. Whereas the pattern of design B is heterogeneous with areas of field amplification ($A > 1$) and damping ($A < 1$), the pattern of design A consists only of hyperintense areas. The profile of design A shows enhanced signal intensity only inside the Swiss Roll.

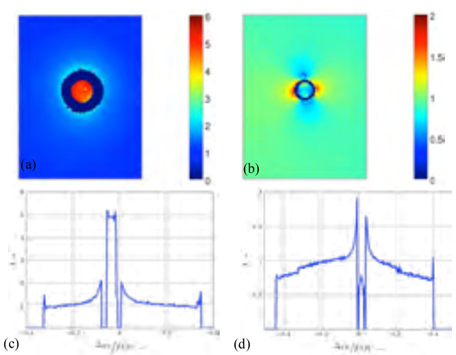

Fig. 1 B_1 amplification map of marker A (a) and B (b) as well as profile through the center of the MR markers A (c) and B (d), respectively

Conclusion: A different way to estimate the performance of a resonance marker in a realistic setup inside the MR-scanner was suggested. This approach enables a qualitative and quantitative comparison of different MR marker designs.

References: [1] Ellersiek, et al., Sensors and Actuators B: Chemical 02/2010; 144(2):432–436.; [2] Nopper R, et al., IEEE Trans. Instrum. Meas 2010; 59(9):2450–7.; [3] Kaiser, et al., 21st ISMRM 2013; 1836.; [4] Alecci M, et al., MRM 2001; 46(2):379–85.

Acknowledgment: This work is supported by the German Ministry of Education and Research (BMBF) under grant number '03FO16102A' and the Land of Saxony-Anhalt under grant number 'I 60' within the Forschungscampus *STIMULATE*.

Feasibility Study of a Single-Layered Resonant MR Marker Fabricated by Thin Film Technology

M. Kaiser[1], E. Pannicke[1], M. Deckert[2], B. Schmidt[2], R.Vick[1], G. Rose[1]
[1]Institute for Medical Engineering, [2]Institute for Micro- and Sensor Systems,
Otto-von-Guericke University Magdeburg, Germany

Purpose: Resonant MR markers used for instrument visualization improve the hand-eye-coordination during interventional procedures. However, most studies are focused on wire-winding coils tuned with the help of SMD capacitors [1,2]. Such fabrication technologies are not applicable in terms of clinical use. Thus, the feasibility of a single-layered resonant marker fabricated by thin film technique was evaluated.

Material and Methods: The MEMS-based fabrication process, described in [3], involved seven process steps starting with (1) spin coating and curing of PI-2611, a polyimide precursor (HD MicroSystems, New Jersey, USA), resulting in thin films of 2.6 μm in thickness. Subsequent to (2) plasma surface treatment improving metal adhesion, (3) a 1 μm thick layer of copper is deposited by a sputtering process. Further processing steps comprise (4) photolithography, (5) wet chemical etching and (6) a final coating/curing of PI-2611 for electrical insulation and biocompatible marker sealing. Finally, (7) a dry etching process allowed for separation of the resonant structures and delamination. The highly flexible foil (Fig. 1) was wrapped around a carrier element (7 mm in diameter), whereas the single loops (L) and electrode surfaces (C) were aligned on top of each other. Electrical parameters, such as resonant frequency f_{res} and quality factor Q, were measured according to [4] within different media (air, $CuSO_4$ solution, 0.9% $NaCl$ solution). The MR marker was tested inside a 3T MR scanner (MAGNETOM Skyra, Siemens AG Healthcare Sector, Germany) using a TSE sequence ($TE/TR = 14\,ms/\,4000\,ms$, trix 512×357, slice 2 mm, FOV 180 mm×124 mm) with varying transmitter (TX) voltages. The amplification A was determined according to [5].

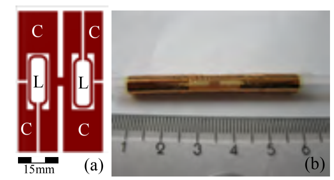

Fig. 1 (a) design of MR marker, (b) MR marker on carrier element

Results: The measured resonant frequencies and quality factors depend on surrounding media (Fig. 2). They range from 116.3 to 120.5 MHz and 14 to 15.8, respectively. The amplification A of the B_1 field in proximity of the MR marker is shown in Fig. 3. The MR marker generated an asymmetric profile with hyperintense ($A > 1$) and hypointense ($A < 1$) areas. Signal voids inside the structure occurred due to electromagnetic shielding of the metallic electrode surfaces.

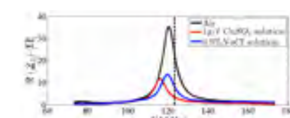
Fig. 2 Real part of measured input impedance $\underline{Z}_1(f)$ within different media

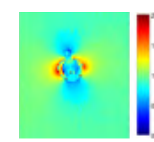
Fig. 3 Amplification A of the B_1 field in the proximity of the MR marker

Conclusion: The feasibility of single-layered MR markers fabricated by thin film technique is demonstrated. Due to the broad bandwidth, the influence of the surrounding tissue on the resonant frequency is reduced. Further studies have to be conducted regarding miniaturization of the proposed design.

References: [1] Busse H, et al., JMRI 2007; 26(4):1087–96.; [2] El-Tahir A, et al., 20th ISMRM 2012; 2947.; [3] Deckert, M, et al., 11. Magdeburger Maschinenbau-Tage, 2013, ISBN: 978-3-940961-90-7; [4] Nopper R, et al., IEEE Trans. Instrum. Meas 2010; 59(9):2450–7.; [5] Alecci M, et al., MRM 2001; 46(2):379–85.

Acknowledgment: This work is supported by the German Ministry of Education and Research (BMBF) under grant number '03FO16102A' and the Land of Saxony-Anhalt under grant number 'I 60' within the Forschungscampus *STIMULATE*.

Improved RF Transmit Coil and Methods for MRI

J. Thomas Vaughan and Jinfeng Tian
University of Minnesota, Minneapolis, MN, USA

Objective: To design an RF body coil and method for improving B1 uniformity and lowering local SAR without compromising transmit efficiency.

Background: MRI guided interventions often require extended fields of view (FOV). Strong RF gradients and consequential local SAR intensities commonplace with conventional, circularly polarized birdcage body coils in most clinical scanners limit both the success and safety of the MRI procedure, especially at 3T. Introduction of RF field conducting or modifying biomedical devices further exacerbate these problems. New transmit technologies and methods are needed.

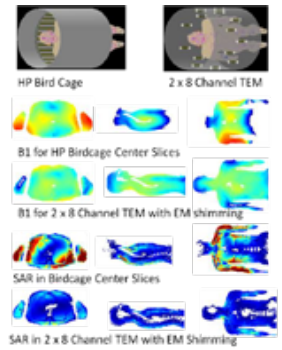

Fig 1. Calculated B1 and SAR for birdcage and multi-channel TEM coil.

Methods: A dozen new body coils including TEM and loop arrays were designed, simulated and compared to a conventional, high-pass (HP), circularly polarized body coil representative of those in most commercial MRI systems.[1] RF(B1 and E) field shimming was applied with the multi-channel coils. For all coils, B1 fields and SAR were calculated (REMCOM XFDTD) in the Duke human male model and normalized to global average SAR. Two of the 45cm long x 60 cm diameter, heart-centered body coils simulated are shown in Figure 1.

Results: In general the body coils composed of arrays of independently driven elements (multi-channel) applying per-element adjustment of transmit signal phase and magnitude (B1 and E-field shimming) improved on the uniformity of the B1 excitation and SAR fields. Not all of these coils maintained the transmit efficiency of the bird-cage reference however. A body coil comprised of two, interleaved z-axis rings of eight (2x8) elements, each adjusted independently in phase and magnitude (B1 shimming) was found to be one of the better solutions considering transmit efficiency, B1 uniformity, SAR minimization, and practicalities of implementation. B1 and SAR results of the 2x8 channel TEM coil are referenced to the birdcage coil in Figure 1.

Conclusions: Simulations predict that new 2 x 8 element and similar TEM body coils and EM shimming methods combine to significantly improve B1 field uniformity and to limit local SAR intensities, without compromising on transmit efficiency. RF field control in phase, magnitude, time and space facilitated by such 3D distributed , multi-channel transmit coils can also be used to optimize uniformity, SNR, contrast and SAR conditions over regions of interest for tracking or localizing MRI guided interventions.

Acknowledgements: NIH-NIBIB-R01 EB006835, NIH-NIBIB-P41-RR008079

References: Vaughan JT, "TEM Body Coils for MRI" in Handbook of RF Coils, Vaughan and Griffiths ed., John Wiley and Sons, (2012).

Numerical and Experimental Test Configuration for Evaluating MRI Induced RF Heating of Interventional Devices

Lucano E[1], Mendoza G[1], Lloyd T[2], Iacono MI, Wedan S[2], Kainz W[1], Angelone LM[1].

1. U.S. Food and Drug Administration, Center for Devices and Radiological Health, Office of Science and Engineering Laboratories. 2. Imricor Medical Systems

Purpose Computational modeling is often used to evaluate radiofrequency (RF) induced heating in patients with medical devices undergoing magnetic resonance imaging (MRI). As part of the evaluation, electromagnetic simulations are used to calculate the electromagnetic (EM) field generated by the RF coil used during MRI. Accurate modeling of both the magnetic and electric fields is particularly important for evaluating medical devices that are partially implanted or have external components in contact with the body. We present initial validation results for a test configuration consisting of an RF birdcage coil loaded with an ellipsoidal phantom intended for evaluating interactions between RF coils and partially implanted interventional devices.

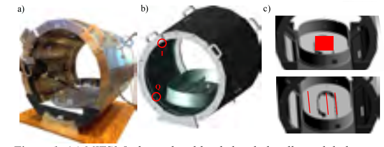

***Figure 1**: (a) MITS1.5 physical coil loaded with the ellipsoidal phantom and the ER3DV6 electric field probe (3). (b) computational model. (c) Position inside the ellipsoidal phantom of the selected area and three lines at a saline depth of 54 mm.*

Methods A commercially available high-pass birdcage body coil (MITS1.5, Zurich Med Tech, Zurich, Switzerland) was used for the measurements (1). The coil is composed of 16 rectangular strips ("rungs") laid out with cylindrical symmetry (diameter = 740 mm). The rungs were connected at each end by 32 distributed capacitances (Fig. 1a) (2). The coil was shielded by a metallic enclosure and was driven at two ports (*I* and *Q* in Fig.1a) in quadrature mode. The nominal resonant frequency of the unloaded physical coil was f_r=63.5 MHz ± 1 MHz. EM field data collection was performed using a robotic measurement system (DASY 5NEO, (3)). The net input power was set to obtain a magnetic field magnitude of 1 A/m at the isocenter of the coil. The computational model was implemented with the commercially available xFDTD software (Remcom Inc., State College, PA), which has been extensively used for EM simulations (4). The computational birdcage coil model was geometrically equivalent to the physical coil (Fig. 1b). Both the coil and the shield were modeled as perfect electric conductors (PEC). In the numerical model, the 16 distibuited capacitors, located in each of the two the rings of the coil, were modeled as PEC rectangular slabs with lumped elements composed of a 460 Ω resistor and 64 pF capacitor in parallel. To drive the coil, the two (*I* and *Q*) ports were placed in the gaps of one of the two rings 90° apart, as in the physical coil. Both ports were fed by voltage sources with a series resistance of 50 Ω. In both the physical and numerical coils, the ellipsoidal phantom consisted of a plexiglass container (6 mm thick, 750 mm long and 400 mm wide) with a plexiglass device support and a port. The device support and port allow for evaluation of a partially inserted catheter (Fig. 1a). The physical phantom was filled to a depth of 90 mm with a 2.5 gr/L NaCl saline solution with a conductivity of 0.47 S/m. The conductivity was verified with a commonly used conductivity meter (YSI model 30, YSI Incorporated, Yellow Springs, Ohio 45387 USA). In the numerical simulation, the dielectric constant 3.2 was used for the plexiglass. A conductivity of 0.47 S/m and dielectric constant of 80 were used for the saline solution. The frequency response and the EM analysis were performed using broadband and resonant sinusoidal excitations, respectively. Figure 1c shows the rectangular area and three lines selected for the electric field evaluation inside the phantom at a saline depth of 54 mm.

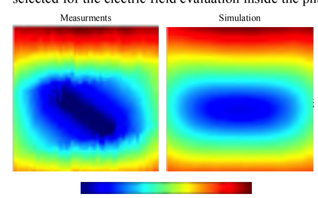

***Fig 2:** Measured and simulated map of electric field magnitude. Data normalized to obtain a magnetic field of 1 A/m at the isocenter of the coil*

Results For the physical coil, the resonant frequency was 63.5 MHz with S_{11} equal to -19dB for the *Q* and -16dB for the *I* port. The numerical model had a resonant frequency of 62.6 MHz with S_{11} equal to –8.8 dB for the *Q* and -9.0 dB for the *I* port. The total net input power required to generate a magnetic field magnitude of 1 A/m at the isocenter was 374 W for the physical coil and 345 W for the numerical model. When comparing the net input power between I and Q port, there was a 17% difference for the measurements and a 20% difference for the simulations. Figure 2 shows the measured and simulated electric field map. Within the area evaluated, the percentage error between measurments and simulation was less than 30%.

Discussion and Conclusions. Because of the asymmetric loading of the cylindrical phantom with respect to the source positions (Fig 1b), both the numerical and physical coil showed an asymmetric behavior of the two ports. The model was able to closely replicate the total net input power required by the coil and the imbalance between the two sources. A variation of less than 30% in the electric field was observed between the physical and numerical coil with the exception of the central asymmetry in the measurements. Because of the homogeneity of the electric field magnitude along device support, the ellipsoidal phantom could be used for measurements of RF-induced heating along leads with controlled exposure conditions. Further evaluation is underway to determine the source of the discrepancies in the electric field asymmetry between simulated and measured results.

References
(1) Neufeld E. et al., Phys Med Biol; 54:4151–4169., 09.
(2) Lucano et al., ISMRM (2014), 4903.
(3) SPEAG, Zurich, Switzerland
(4) Collins et al. MRM 65:1470–1482 (2011)

Gradient-induced Voltages on 12-lead ECG Traces during High-Duty-Cycle MRI sequences and a Theoretically-Based Method for Their Removal.

Shelley HL Zhang[1], Zion TH Tse[2], Charles L Dumoulin[3], Ronald Watkins[4], Wei Wang[1], Jay Ward[5], Raymond Y Kwong[6], William G Stevenson[6] , Ehud J Schmidt[1]. [1] Radiology & [6]Cardiology , Brigham & Women's Hospital, Boston, MA, [2] Engineering, Univ. of Georgia, Athens, GA, [3]Radiology, Cincinnati Children's Hospital Medical Center, Cincinnati, OH, [4]Radiology, Stanford Univ., Stanford, CA, [5]Mirtle Inc., Andover, MA.

Purpose: 12-lead ECG traces are the standard for physiologically monitoring patients with ischemic histories. Reliable intra-cardiac ECG traces (EGMs) are required for electro-anatomic mapping (EAM) of electrical circuits in the heart during electrophysiology procedures. Both 12-lead ECGs and EGMs are perturbed by MRI, excluding interventions in severely ill patients. We developed methods to remove Magnetohydrodynamic (MHD) artifacts from both 12-lead ECGs and EGMs [1, 2]. We also developed MRI-compatible 12-lead ECG and EAM systems, which acquired clean ECG/EGM traces during low-duty-cycle MRI sequences (TR>20 msec). The current study measures the magnitude and spectrum of gradient-induced voltage in high-duty-cycle MRI sequences and attempts to remove this noise by evaluating its dependence on MRI gradients.

Materials & Methods: A modification of the hardware used in [1] enabled measuring gradient-induced voltages over 0-24 kHz and within +/-10V, together with the MRI gradient waveforms. 12-lead ECGs were measured in 10 volunteers at 3T. A 19-parameter equation for induced voltages on each ECG electrode $V_k(t)$was derived, expanding previous work [3,4]. $V_k(t) = p_{1k}\frac{\partial G_x}{\partial t} + p_{2k}\frac{\partial G_y}{\partial t} + p_{3k}\frac{\partial G_z}{\partial x} + p_{4k}G_x(t) + p_{5k}G_y(t) + p_{6k}G_z(t) + p_{7k}\frac{\partial G_x}{\partial t}G_x + p_{8k}G_x^2 + p_{9k}\frac{\partial G_y}{\partial t}G_y + p_{10k}G_y^2 + p_{11k}\frac{\partial G_z}{\partial t}G_z + p_{12k}G_z^2 + p_{13k}\frac{\partial G_x}{\partial t}G_z + p_{14k}G_x\frac{\partial G_z}{\partial t} + p_{15k}G_xG_z + p_{16k}\frac{\partial G_y}{\partial t}G_z + p_{17k}G_y\frac{\partial G_z}{\partial t} + p_{18k}G_yG_z + C_k$, where $G_x,\ G_y,\ G_z$ are the three MRI gradients, $\frac{\partial G_x}{\partial t}, \frac{\partial G_y}{\partial t}, \frac{\partial G_z}{\partial t}$ are their time derivatives and $p_{1k} \dots p_{18k}$, and C_k are constants. This equation allows estimating induced voltages even in electrodes which are farthest (>20 cm) from magnet iso-center. Least-squares regression of this equation to ECGs measured during 3-4 second training 2D SSFP, 2D GRE and 3D FSE sequences, after subtraction of a clean ECG R-R ("template"), provided the coefficients $p_{1k} \dots p_{18k}$ and C_k. The equation was then used to remove noise from ECGs in real-time during 30-200 second multi-slice scans of these sequences.

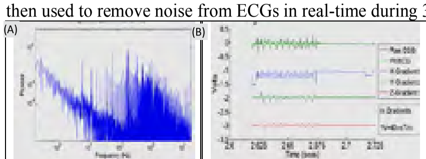

Fig.1: Gradient-induced voltage recorded at Left Leg during transverse 3D FSE. (A) Induced voltage spectrum ranges over 0-24 KHz, peaking at 1 KHz. (B) Enlarged view of induced voltage versus recorded gradient waveforms. ~0.5 Volt induced voltage (top green trace) is >100 times the real ECG voltage (5 mV). 19-parameter fit (top black trace) fits >95% of induced voltage.

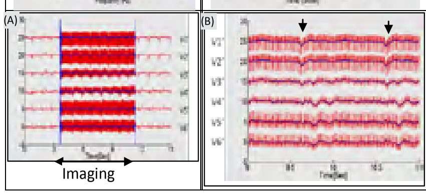

Fig.2: Gradient-induced voltage recorded in 6 precordial leads (V1-V6) during transverse 2D GRE. (A) Regions of ECG obtained when MRI is not pulsing, used for the ECG template, surround imaging region (black line) which has strong induced voltages (Red traces). Blue traces show ECGs cleaned of induced voltages using 19-parameter equation. (B) Enlarged view shows quality of removal of induced voltages, with QRS complexes clearly identified (arrows).

Results: Figures 1 & 2 show the broad frequency spectrum and large magnitude of the induced voltages. The success of the 19-parameter equation in fitting this noise and restoring a clean ECG is demonstrated. The fit coefficients vary, as predicted, with electrode position, sequence, sequence parameters and slice orientation. Residual artifacts remain at the beginning and end of each imaging interval, a result of strong "ring-down" signals observed at these times. We hope to remove some of these events with hardware switching [1, 2].

Conclusion: The success of a novel approach in removing 12-lead ECG gradient-induced voltage during high-duty-cycle MRI sequences was demonstrated, allowing accurate physiological monitoring during intervention.

References [1] Tse, MRM '13, [2] Schmidt, MRM '14. [3] Bowtell, MRM '00, [4] Bernstein, MRM '89.

Acknowledgements: NIH 1 R03-EB013873-01A1 & U41-RR019703, AHA 10SDG261039.

RF safety in MRI: gauging body-average SAR and local heating of interventional coils

M. Arcan Ertürk[a,b], Abdel-Monem El Sharkawy[b], Paul A. Bottomley[b]
[a] University of Minnesota Medical School, Minneapolis, MN; and
[b] Russell H. Morgan Dept. of Radiology, Johns Hopkins University, Baltimore, MD, USA

Purpose: Monitoring RF exposure is critical to MRI safety. Commercial MRI scanners do not reliably estimate RF specific absorption rates (SAR), and may improperly restrict MRI scanning[1]. Scanner SAR cannot be used for gauging exposure when testing interventional leads and devices used in MRI[1,2]. Accurate scanner-independent RF dosimetry of both body-average and local SAR are thus essential for ensuring regulatory compliance and MRI safety, but are presently non-existent. We built a dosimeter and transducer to measure body-average SAR in 3T scanners, and tested it in Philips, GE and Siemens scanners, and in humans[1,2]. To measure local heating (∝local SAR) for interventional MRI coils, we used RF radiometry[3,4] based on Planck's radiation Law. The temperature was measured in the sensitive region of a 3T loopless antenna based on the RF noise recorded without MRI.

Fig 1. (a) 3T MRI whole-body SAR transducer. (b) Power calibration curves for 3 GE, 3 Philips, & (c) 2 Siemens scanners.

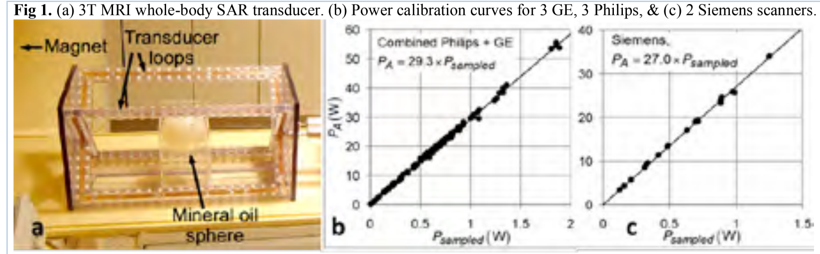

Methods. For body SAR, an RF transducer comprising 2 orthogonal loops as a body load, and a spherical MRI phantom to set the MRI flip-angle (Fig. 1a), was placed in the scanner and connected to a high dynamic range RF power meter. Transducer power was calibrated vs actual power deposited. Whole-body absorbed power was measured in 26 subjects vs body weight and body mass index (BMI).

Fig 2. 3T loopless antenna radiometer tracks local temp. to ±0.24°C. Antenna is most sensitive to heating at junction (inset: MR thermometry).

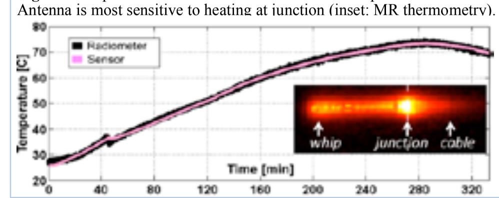

To measure local heating, we built a radiometer receiver to measure the RF noise from a 3T MRI loopless antenna. It was calibrated vs temperature in a gel phantom. Local heating (ΔT) using the antenna for RF excitation was measured by radiometry, and by fiber-optic thermal sensors and MRI thermometry for comparison.

Results. A single linear calibration curve sufficed for whole body dosimetry on 3 Philips, 3 GE (Fig. 1b), and 2 Siemens (Fig. 1c) 3T scanners within ~3% accuracy. Whole-body power varied approx. linearly with patient weight and BMI. The loopless antenna radiometer linearly tracked temperature to within ±0.3°C (Fig. 2). Radiometric, computed, and MRI thermometric measures of peak ΔT agreed. The radiometer measured peak 1g-averaged ΔT in a tissue (RF) equivalent phantom within ±0.4°C.

Discussion: Our 3T whole-body RF dosimeter accurately measures RF exposure independent of the scanner. Active internal MRI detectors serving as RF radiometers can 'self-monitor' local temperature free of MRI or the complications of added thermal transducers. Together, these technologies could allow monitoring of both body-average and local RF exposure for regulatory compliance and safety testing of interventional devices and leads.

Supported by NIH grant R01 EB007829.

References: (1) El-Sharkawy AM et al. Med. Phys. 2012; 39:2334-41. (2) Qian D et al. Med Phys 2013; 40: 122303. (3) El-Sharkawy AM et al. IEEE Trans Circ Sys 2006; 53: 2396-2405. (4) Erturk MA et al. Proc ISMRM 2014: 22; 2349.

Understanding RF Safety for MRI

J. Thomas Vaughan, Jinfeng Tian, Devashish Shrivastava
University of Minnesota, Minneapolis, MN, USA

Objective: To better understand the RF fields effecting success and safety of MRI

Background: Radiofrequency safety is one of the most important and least understood aspects of MRI. RF safety issues are further complicated by the introduction of biomedical devices and MRI guided interventions. The first step to improving success and safety of iMRI is a better understanding of RF field propagation, loss and consequential heating in the human anatomy.

Methods, Results and Discussion:

B1: Referring to Figure 1, a uniform magnetic flux density, (T) excite field over an ROI is the primary objective of a body coil. As can be seen, destructive interference patterns of the short Larmor wavelength traveling waves in the body lead to a nonuniform excite field over the whole body.
E: Accompanying the B1 field, the E field, (V/m^2) is similarly non-uniform and propagating through the entire body.
SAR: The power loss density, (W/kg) is half the dot product of displacement current losses to the tissue dielectric and conduction current losses to the tissue conductor integrated over the full body. This SAR is also highly non-uniform, with highest local values trending toward the body periphery closest to the body coil elements.
dT/dt: An increase in heating over time, (C/s) results from the SAR in tissue, and follows a similar distribution misleading some into believing that SAR is predictive of thermal contours.
T: Temperature, (C) is the appropriate metric for predicting and determining safety in the MRI exam. Absolute temperature magnitude (not SAR and not dT) is the cause of burns, pain, and systemic thermal stress (heat stroke). Contrary to regulatory guidelines (1) and therefore industry and clinical practice, SAR alone predicts neither the magnitude nor the location of true thermal hot spots or systemic stress. SAR must be equated to temperature through an accurate bioheat equation (2) to determine the safety of an RF transmit system and protocol, especially when RF conductive interventional devices are introduced.

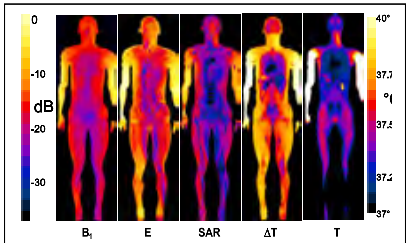

Figure 1. RF fields, SAR, and temperature calculated for the Duke male model inside a 45cm long, heart centered, circularly polarized body coil within a 3T magnet.

Conclusion: By tracking temperature rather than SAR, safety will be improved. These topics will be covered in comprehensive detail at our upcoming ISMRM Safety Workshop (3)

Acknowledgements: NIH-NIBIB-2R0-EB007327, NIH-NIBIB-P41-RR008079

References: 1.) Criteria for Significant Risk Investigations of Magnetic Resonance Diagnostic Devices: Guidance for Industry and Food and Drug Administration Staff (June 20, 2014)
2.) Shrivastava D, Vaughan JT. "A generic bioheat transfer thermal model for a perfused tissue." J Biomech Eng 2009 Jul;131(7):074506. PMCID: PMC2737815
3.) ISMRM Workshop on Safety in MRI:Guidelines, Rationale&Challenges 5-7 September,2014

Device Powering using InductivelyCoupled Coils with Transmit MR Excitation

Madhav Venkateswaran[1], Daniel Van der Weide[1], Krishna Kurpad[2]
[1]Electrical and Computer Engineering, [2]Radiology, University of Wisconsin-Madison.

<u>*Purpose*</u>: To investigate feasibility of using inductively-coupled coils to harvest RF energy transmitted during MR excitation for integration into wireless endoscopic capsules (1) for robotic actuation and wireless trigger release of drugs with MRI guidance.

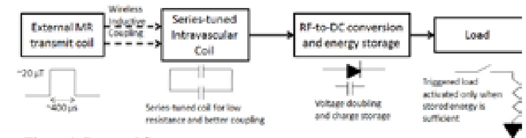

Figure 1: Proposed Setup.

<u>*Material and Methods*</u>: Eq (1) gives the induced EMF in a loop that is incident with a sinusoidal magnetic field excitation.

$$V_{ind,pk} = \omega NA\left(\overrightarrow{B_{RF}}.\vec{n}\right) \quad ...(1)$$

Figure 2: Circuit Simulation Model.

For a 1.5T scanner (f = 63.86 MHz), we assume a single hard pulse of magnitude 20µT and duration 400µs and a 3-turn series-tuned 5cm x 2mm rectangular loop placed parallel to B_0 (Fig 1). For a quadrature excited field, only one component is perpendicular to the loop and contributes to the EMF and so $B_{RF} = 10\sqrt{2}$ µT. The inductively-coupled coil is assumed to be series-tuned (low impedance) to maximize the induced current with the voltage doubling circuit placed across the series tuning capacitor. The model for the voltage doubling circuit is shown in Fig 2. The sample loading impedance at coil terminals and also the effect of quality factor reduction due to loading by the voltage doubling circuit across the series-tuning capacitor is modeled by R1 and has to be determined using measurements under loaded conditions (25Ω considered here was estimated to be reasonable based on bench measurements). At the start of the RF pulse, the series diode results in a near-open circuit and so will not load the series-tuned coil (sample loading effects will however be present), accelerating charge build-up. As the voltage builds and the diodes get forward biased, the circuit loading will be present in addition to the sample loading. However, as the capacitors C1 and C2 used (50nF each) are quite large at the MR frequency, the series tuning will not be affected. The main effect is a further reduction in coil quality factor (Q).

Inductive	Calculation	Simulation
Voltage (V)	1.7	-
Current (mA)	68	70.4
RF Power at input of Vdblr (mW)	115.6	123.87
Steady State DC Power at R2 (mW)	-	3
RF to DC efficiency	-	2.4%

Table 1: Results Summary.

To verify induced EMF calculations, we performed a coupled full-wave and circuit simulation using COMSOL Multiphysics using a simplified model that modeled the external transmit excitation from an idealized birdcage coil with the inductively-coupled coil at the centre (2). The loading impedance R1 and tuning capacitors were modeled using lumped elements.The voltage doubling circuit was modeled in Agilent ADS.

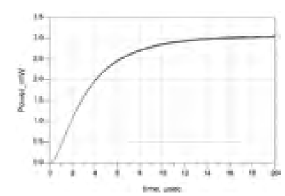

Figure 3: Continuous Output Power Delivered to 50Ω load.

<u>*Results*</u>: Table I summarizes the main results. The rectified power available at the output of the voltage doubling circuit delivered to a 50Ω load as a function of time is shown in Fig 3. The simulation estimates that the output power stabilizes to a value of about 3 mW after about 14µs into the transmit pulse. This may possibly be used to move a capsule or miniaturized robot with a very low power actuator. For use as a switch to trigger release of drugs, an appropriate switching diode at the output terminal can be designed to conduct only when charge accumulation reaches a specific design value.

<u>*References*</u>: (1) G. Kosa et al. *ICRA* 2008. (2) M. Venkateswaran et al. #4317, *ISMRM*, 2013.

Electro/magneto/thermal Acoustic ultrasound generation in iMRI Devices

G. Scott, M. Etezadi-Amoli, H. Nan, M. Aliroteh, A. Arbabian, P. Stang, J. Pauly
Electrical Engineering, Stanford University, CA, United States

Purpose: Interventional devices can be visualized actively when integrated as micro-transceive elements within a transmit/receive array system that localizes RF power deposition for device safety. EP catheters, which have exposed tips and long insulated shafts, act as insulated dipole antennas when driven by a toroid exciter [1]. Liver ablation devices have short insulated shafts and can be driven as monopole antennas [2]. In both cases (Fig. 1), it is the RF current flow to the tip that allows for B1 generation and visualization near the tip. However, these same RF currents should also be capable of generating ultrasound (US) signals by thermal, electric and magnetic interactions. We demonstrate the generation of US signals at classic ablation frequencies or by modulated 64 MHz and discuss possible applications for added device safety monitoring or tracking.
Methods: A variety of device models were employed: Leveen probe, EP-style exposed tip, and bipolar coax tip (Fig 2a-c). For RF ablation tests in 0.5-1MHz, a ground pad provided a return path and up to 100W RF power (typical of ablation) was transmitted to the Leveen or EP probe immersed in saline. We used frequency modulated continuous wave (FMCW), and stepped frequency CW (SFCW) [3,4] covering output signal bandwidths of 250-400kHz, sufficient for 5 mm range resolution. Thermo-acoustic signals were detected at double the input RF frequency, and electroacoustic signals from metal-electrolyte interface interactions occur at the fundamental. With a magnetic field present, Lorentz forces generate a magneto-acoustic signal. For 64 MHz, we injected power into the bipolar coax tip, and amplitude modulated at ~1 MHz with FMCW, SFCW or pulses (Fig 2d). This generates a heat function oscillating in the ultrasound band around 1 MHz. Signal transmission and detection were programmed with a Medusa control system [5], and an Olympus V303 detected the US.
Results: Fig. 2e shows the generated thermo-acoustic (red) and electroacoustic (blue) resulting from a single 10ms long FM chirp, using device (a) at depth of 7 cm. Magneto-acoustic US [3] will be present in a magnetic field. Fig 2f shows a thermo-acoustic signal from 1 MHz AM modulated 64 MHz in device (c) using pulse trains and achieving >1000 SNR with 100W drive. These should be detectable at 100mW levels.
Conclusions: Device structures suitable for iMRI visualization can also generate thermo-electromagnetic ultrasound. This opens interesting options for additional therapy monitoring or tracking with iMRI.

References:
[1] M. Etezadi-Amoli, Proc. 22th ISMRM, 3704, 2014. [2] M. Etezadi-Amoli, Proc. 22th ISMRM, 3711, 2014. [3] M. Aliroteh, Elec. Lett, 50,790,2014. [4] H. Nan Appl Phys Lett 104, 224104, 2014. [5] P. Stang, IEEE TMI, 31:370- 379, 2012. NIH Grant support: R01EB008108, P01CA159992, DARPA MEDS program.

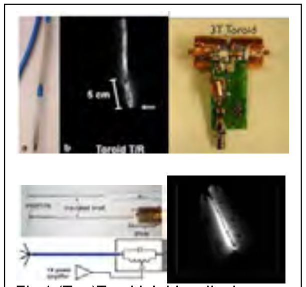

Fig.1 (Top)Toroidal drive dipole visualization and (bot) monopole drive with Leveen RF ablation probe visualization at 3T in pig cadaver.

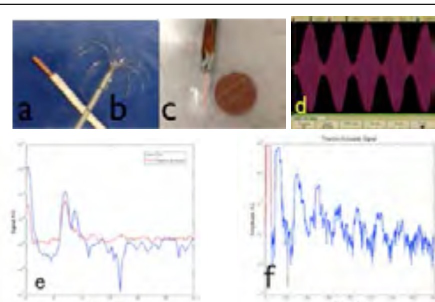

Fig 2: a) EP model, b) Leveen c) bipolar electrodes. d) 1 MHz amplitude modulated 64 MHz. e) 1 MHz Thermo-acoustic (red) and electro-acoustic (blue). f) 64 MHz thermo-acoustic US.

List of Speakers, Poster Presenters, Moderators and Faculty Members

Agar, Nathalie
Department of Radiology
Brigham and Women's Hospital
Harvard Medical School
75 Francis Street
Boston, MA 02115, USA
nagar@rics.bwh.harvard.edu

Blanco Sequeiros, Roberto
Department of Radiology
University of Turku
Kiinamyllynkatu 4-8
20520 Turku, Finland
roberto.blanco@oulu.fi

Bock, Sascha
Department of Diagnostic and Interventional Radiology
University Hospital Giessen
Neuen Bäue 11
35390 Giessen, Germany
bock-sascha@web.de

Bomers, Joyce G. R.
Department of Radiology
Radboud University Nijmegen
P.O. Box 9101, internal postal code 766
Nijmegen 6500 HB, Netherlands
joyce.bomers@radboudumc.nl

Bottomley, Paul
Department of Radiology and Radiological Science
Johns Hopkins School of Medicine
600 North Wolfe Street
Baltimore MD 21287, USA
bottoml@mri.jhu.edu

Brujic, Djordje
Department of Mechanical Engineering
Imperial College London
Exhibition Road
London SW7 2AZ, UK
d.brujic@imperial.ac.uk

Burrow, Bobbie
Department of Radiology and Imaging Sciences
Emory University Hospital
1364 Clifton Road, NE Suite D112
Atlanta, GA 30322, USA
bobbie.burrow@emoryhealthcare.org

Busse, Harald
Department of Diagnostic and Interventional Radiology
Leipzig University Hospital
Liebigstr. 20
04103 Leipzig, Germany
harald.busse@medizin.uni-leipzig.de

Chubb, Henry
Division of Imaging Sciences and Biomedical Engineering
King's College London
216 Brixton Road
London SW9 6AP, UK
henry.chubb@kcl.ac.uk

Chung, Peter
Princess Margaret Cancer Centre
University of Toronto
610 University Ave
Toronto, M5G 2M9, ON, Canada
ellen.hoffman@rmp.uhn.on.ca

Dadakova, Tetiana
Department of Diagnostic Radiology
University Medical Center Freiburg
Breisacher Str. 60a
79110 Freiburg, Germany
tetiana.dadakova@uniklinik-freiburg.de

Düring, Klaus
MaRVis Medical GmbH
Vahrenwalder Str. 269A
30179 Hannover, Germany
k.duering@marvistech.com

Eibofner, Frank
Diagnostic and Interventional
Radiology
University of Tübingen
Hoppe-Seyler-Straße 3
72076 Tübingen, Germany
frank.eibofner@med.uni-tuebingen.de

Erturk, Arcan
Department of Radiology and
Radiological Science
Johns Hopkins School of Medicine
600 North Wolfe Street
Baltimore, MD 21287, USA
arcanerturk@gmail.com

Fallah-Rad, Mehran
IMRIS Inc.
5101 Shady Oak
Minnetonka, MN 55343, USA
mfallahrad@gmail.com

Farahani, Keyvan
Division of Cancer Treatment
and Diagnosis
National Cancer Institute
9609 Medical Center Drive
Bethesda, MD 20892, USA
farahani@nih.gov

Fischbach, Frank
Department of Radiology and
Nuclear Medicine
Otto-von-Guericke-University
Leipziger Str. 44
39120 Magdeburg, Germany
frank.fischbach@med.ovgu.de

Fritz, Jan
Department of Radiology and
Radiological Science
Johns Hopkins School of Medicine
600 North Wolfe Street
Baltimore, MD 21287, USA
jfritz4@jhmi.edu

Fütterer, Jurgen
Department of Radiology
Radboud University Nijmegen
P.O. Box 9101, internal postal code 766
Nijmegen 6500 HB, Netherlands
j.futterer@rad.umcn.nl

Gangi, Afshin
Department of Diagnostic and
Interventional Radiology
University Hospital of Strasbourg
1 place de l'hôpital - BP 426
67091 Strasbourg, France
gangi@rad6.u-strasbg.fr

Garnon, Julien
Department of Diagnostic and Interventio-
nal Radiology
University Hospital of Strasbourg
1 place de l'hôpital - BP 426
67091 Strasbourg, France
juliangarno@gmail.com

Gedroyc, Wladyslaw M.
St Mary's Hospital
Imperial College London
Praed Street
London W2 1NY, UK
w.gedroyc@imperial.ac.uk

Golby, Alexandra
Department of Neurosurgery
Brigham and Women's Hospital
Harvard Medical School
75 Francis Street
Boston, MA 02115, USA
agolby@bwh.harvard.edu

Griffin, Greg
Imaging Research
Sunnybrook Research Institute
S612 2075 Bayview Ave
Toronto, M4N 3M5, ON, Canada
greg.griffin@sri.utoronto.ca

Gross, Robert
Department of Neurosurgery
Emory University Hospital
1365 Clifton Road, NE Suite 6200
Atlanta, GA 30322, USA
rgross@emory.edu

Gutberlet, Matthias
Department of Diagnostic and
Interventional Radiology
Heart center – University Leipzig
Strümpellstr, 39
04289 Leipzig, Germany
matthias.gutberlet@herzzentrum-leipzig.de

Güttler, Felix
Department of Radiology
University Hospital Jena
Erlanger Allee 101
07747 Jena, Germany
felix.guettler@med.uni-jena.de

Ha, Seunghoon
IMRIS Inc.
5101 Shady Oak
Minnetonka, MN 55343, USA
sha@imris.com

Hägele, Julian
Clinic for Radiology and Nuclear Medicine
University Hospital Lübeck
Ratzeburger Allee 160
23538 Lübeck, Germany
haegele@uni-luebeck.de

Halperin, Henry
Department of Radiology and Radiological
Science
Johns Hopkins School of Medicine
600 North Wolfe Street
Baltimore, MD 21287, USA
hhalper@jhmi.edu

Hegde, Shashank
Department of Radiology and Radiological
Science
Johns Hopkins School of Medicine
600 North Wolfe Street
Baltimore, MD 21287, USA
shashank.s.hegde@gmail.com

Hetts, Steven
Department of Radiology and Biomedical
Imaging
University of California
505 Parnassus Avenue, L-352
San Francisco, CA 94143, USA
steven.hetts@ucsf.edu

Hoogenboom, Martijn
Department of Radiology and Nuclear
Medicine
Radboud University Medical Center
Geert Grooteplein-Zuid 10
Nijmegen 6500HB, Netherlands
martijn.hoogenboom@radboudumc.nl

Ingle, Reeve
HeartVista, Inc.
998 Hamilton Ave.
Menlo Park, CA 94025, USA
ringle@heartvista.com

Jayender, Jagadeesan
Department of Radiology
Brigham and Women's Hospital
Harvard Medical School
75 Francis Street
Boston, MA 02115, USA
jayender@bwh.harvard.edu

Janowski, Miroslaw
Division of MR Research
Department of Radiology and Radiologi-
cal Science
Johns Hopkins School of Medicine
733 N. Broadway street, Room 649
Baltimore, MD 21205, USA
neuroibis@gmail.com

Jolesz, Ferenc A.
Department of Radiology
Brigham and Women's Hospital
Harvard Medical School
75 Francis Street
Boston, MA 02115, USA
jolesz@bwh.harvard.edu

Kaegebein, Urte
Department of Biomedical Magnetic Resonance
Otto-von-Guericke University
Sandtorstr. 23
39106 Magdeburg, Germany
urte.kaegebein@ovgu.de

Kahn, Thomas
Department of Diagnostic and Interventional Radiology
Leipzig University Hospital
Liebigstr. 20
04103 Leipzig, Germany
thomas.kahn@medizin.uni-leipzig.de

Kaiser, Mandy
Institute for Medical Engineering
Otto-von-Guericke University
Universitätsplatz 2
39106 Magdeburg, Germany
mandy.kaiser@ovgu.de

Karakitsios, Ioannis
Institute for Medical Science and Technology
University of Dundee
1 Wurzburg Loan
Dundee, DD2 1FD, UK
i.karakitsios@dundee.ac.uk

Kerimaa, Pekka
Department of Radiology
Oulu University Hospital
Kiinanmyllynkatu 4-8
Turku 20521, Finland
pekka.kerimaa@ppshp.fi

Kholmovski, Eugene
UCAIR
University of Utah
729 Arapeen Drive
Salt Lake City, UT 84108, USA
ekhoumov@ucair.med.utah.edu

Knuttel, Floor
Department of Radiology
University Medical Center Utrecht
Heidelberglaan 100
Utrecht 3584 CX, Netherlands
f.m.knuttel@umcutrecht.nl

Kraitchman, Dara L.
Department of Radiology and Radiological Science
Johns Hopkins University
600 N. Wolf Street
Baltimore, MD 21287, USA
dkratc1@jhmi.edu

Kranjc, Matej
Faculty of Electrical Engineering
University of Ljubljana
Tržaška cesta 25
SI-1000 Ljubljana, Slovenia
Matej.Kranjc@fe.uni-lj.si

Krombach, Gabriele A.
Department of Radiology
University Hospitals Giessen
Klinikstr. 23
35392 Giessen, Germany
gabriele.krombach@radiol.med.uni-giessen.de

Kuhl, Christine
Department of Diagnostic and Interventional Radiology
University Aachen
Pauwelsstr. 30
52074 Aachen, Germany
ckuhl@ukaachen.de

Kuo, Ihyuan
EpiSonica Corporation
35 Keyan Road
Zhunan, 35053 Taiwan
ihyuank@episonica.com

Laniado, Michael
Department of Radiology
University Hospital Dresden
Fetscherstr. 74
01307 Dresden, Germany
michael.laniado@uniklinikum-dresden.de

Lewin, Jonathan S.
Department of Radiology and Radiological Science
Johns Hopkins School of Medicine
600 North Wolfe Street
Baltimore, MD 21287, USA
jlewin2@jhmi.edu

Lewis, Christina
Department of Radiology
Mayo Clinic
200 First Street
Rochester, MN 55905, USA
Lewis.Christina@mayo.edu

Lillaney, Prasheel
Department of Radiology and Biomedical Imaging
University of California
185 Berry St Suite 350
San Francisco, CA 94107, USA
plillane@gmail.com

Lockwood, Joshua
Physical Sciences
Sunnybrook Research Institute
S612 2075 Bayview Ave
Toronto, M4N 3M5, ON, Canada
0jtl1@queensu.ca

Losey, Aaron
Department of Radiology and Biomedical Imaging
University of California
505 Parnassus Avenue, L-352
San Francisco, CA 94143, USA
aaron.losey@ucsf.edu

Lotz, Joachim
Department of Diagnostic and Interventional Radiology
University Medical Center
Robert-Koch-Strasse 40
37099 Göttingen, Germany
joachim.lotz@med.uni-goettingen.de

Lucano, Elena
Center for Devices and Radiological Health
U.S. Food and Drug Administration
400 Gateway Blvd
Burnsville, MN 55337, USA
elena.lucano88@gmail.com

Lüsebrink, Falk
Department of Biomedical Magnetic Resonance
Otto-von-Guericke University
Sandtorstr. 23
39106 Magdeburg, Germany
falk.luesebrink@ovgu.de

Maenhout, Metha
Department of Radiation Oncology
University Medical Centre Utrecht
Heidelberglaan 100
Utrecht 3584CX, Netherlands
m.maenhout@umcutrecht.nl

Maier, Florian
Department of Imaging Physics
University of Texas
1515 Holcombe Blvd
Houston, TX 77030, USA
science@fmaier.eu

Matsumoto, Tatsuhiko
Graduate School of System Informatics
Kobe University
1-1 Rokkodai-cho
Nada-ku, Kobe 657-8501, Japan
137x024x@stu.kobe-u.ac.jp

Matsuoka, Yuichiro
Center for Information and Neural Networks
National Institute of Information and Communications Technology
1-4 Yamadaoka, Suita City
Osaka, 565-0871, Japan
yuichir34@gmail.com

McDannold, Nathan
Department of Radiology
Brigham and Women's Hospital
Harvard Medical School
75 Francis Street
Boston, MA 02115, USA
njm@bwh.harvard.edu

Ménard, Cynthia
Department of Radiation Oncology
Princess Margaret Hospital
610 University Avenue
Toronto, M5G 2M9, ON, Canada
cynthia.menard@rmp.uhn.on.ca

Moche, Michael
Department of Diagnostic and Interventional Radiology
Leipzig University Hospital
Liebigstr. 20
04103 Leipzig, Germany
michael.moche@medizin.uni-leipzig.de

Monfaredi, Reza
Children's National Medical Center
111 Michigan Avenue
Washington, DC 20010, USA
RMonfare@childrensnational.org

Moonen, Chrit
Image Sciences Institute
University Medical Center Utrecht
Heidelberglaan 100
Utrecht 3584 CX, Netherlands
C.Moonen@umcutrecht.nl

Morelli, John
Department of Radiology and Radiological Science
Johns Hopkins School of Medicine
600 North Wolfe Street
Baltimore, MD 21287, USA
dr.john.morelli@gmail.com

Morita, Shuhei
Graduate School of Engineering
Tokai University
4-1-1 Kitakaname Hiratsuka
Kanagawa, 259-1292, Japan
3bdrm013@mail.tokai-u.jp

Neumann, Markus
ICube
University Hospital of Strasbourg
1 place de l'hôpital - BP 426
67091 Strasbourg, France
m.neumann@unistra.fr

Nicholson, Andrew
Department of Radiology and Imaging Science
University of California
287 Christopher Dr
San Francisco, CA 94131, USA
andrewdavidnicholson@gmail.com

Nimsky, Christopher
Department of Neurosurgery
University Hospital Marburg
Baldingerstrasse
35033 Marburg, Germany
nimsky@med.uni-marburg.de

Nour, Sherif
Department of Radiology and Imaging Sciences
Emory University Hospital
1364 Clifton Rd NE
Atlanta, GA 30322, USA
sherif.nour@emoryhealthcare.org

Oto, Aytekin
Department of Radiology
University of Chicago
5841 South Maryland Avenue MC 2026
Chicago, IL 60637, USA
aoto@radiology.bsd.uchicago.edu

Overduin, Christiaan
Department of Radiology
Radboud University Nijmegen
P.O. Box 9101, internal postal code 766
Nijmegen 6500 HB, Netherlands
c.overduin@rad.umcn.nl

Pannicke, Enrico
Institute for Medical Engineering
Otto-von-Guericke University
Universitätsplatz 2
39106 Magdeburg, Germany
enrico.pannicke@ovgu.de

Pavlina, John
Department of Diagnostic Radiology
University Medical Center Freiburg
Breisacher Str. 60a
79110 Freiburg, Germany
john.pavlina@uniklinik-freiburg.de

Pearl, Monica
Department of Radiology and Radiological Science
Johns Hopkins School of Medicine
600 North Wolfe Street
Baltimore, MD 21287, USA
msmit135@jhmi.edu

Petrușca, Lorena
Department of Radiology
University Hospitals of Geneva
Rue Gabrielle-Perret-Gentil 4
1211 Genève 14, Switzerland
lorena.petrusca@unige.ch

Powell, Tracy
Department of Radiology and Imaging Sciences
Emory University Hospital
1364 Clifton Road, NE Suite D112
Atlanta, GA 30322, USA
tracy.powell@emoryhealthcare.or

Razavi, Reza
Division of Imaging Sciences
King's College London
4th Floor, Lambeth Wing
St Thomas' Hospital
London SE1 7EH, UK
reza.razavi@kcl.ac.uk

Reiser, Maximilian
Institute for Clinical Radiology
Ludwig-Maximilians-University Hospital
Marchioninistr. 15
81377 München, Germany
maximilian.reiser@med.uni-muenchen.de

Rempp, Hansjörg
Diagnostic and Interventional Radiology
University of Tübingen
Hoppe-Seyler-Str. 3
72076 Tübingen, Germany
Hansjoerg.Rempp@med.uni-tuebingen.de

Rödel, Stefan
Department of Radiology
Hospital Dresden-Friedrichstadt
Friedrichstr. 41
01067 Dresden, Germany
drstroedel@aol.com

Rosenberg, Christian
Department of Diagnostic Radiology and Neuroradiology
University Hospital Greifswald
Ferdinand-Sauerbruch-Str.
17475 Greifswald, Germany
rosenberg@uni-greifswald.de

Schaudinn, Alexander
Department of Diagnostic and
Interventional Radiology
Leipzig University Hospital
Liebigstr. 20
04103 Leipzig, Germany
alexander.schaudinn@medizin.uni-leipzig.de

Schmidt, Ehud
Department of Radiology
Brigham and Women's Hospital
Harvard Medical School
75 Francis Street
Boston, MA 02115, USA
eschmidt3@partners.org

Scott, Greig
Electrical Engineering
Stanford University
Packard 222 350 Serra Mall
Stanford, CA 94305, USA
greig@mrsrl.stanford.edu

Seevinck, Peter R.
Imaging Division
University Medical Center Utrecht
Heidelberglaan 100
Utrecht 3584CX, Netherlands
p.seevinck@umcutrecht.nl

Shiina, Atsushi
Graduate School of Engineering
Tokai University
453-5 Minamiyana, Hadano
Kanagawa, 257-0003, Japan
4bdrm011@mail.tokai-u.jp

Taslakian, Bedros
Department of Diagnostic Radiology
American University of Beirut
Riad El-Solh PO Box: 11-0236
Beirut 1107 2020, Lebanon
btaslakian@gmail.com

Tavallaei, Mohammad
Robarts Research Institute
Western University
1151 Richmond St. N.
London, ON N6A 5B7, Canada
atavall@robarts.ca

Tempany, Clare
Department of Radiology
Brigham and Women's Hospital
Harvard Medical School
75 Francis Street
Boston, MA 02115, USA
ctempany@bwh.harvard.edu

Tewes, Susanne
Institute for Diagnostic and
Interventional Radiology
Hannover Medical School
Carl-Neuberg Str. 1
30625 Hannover, Germany
Tewes.Susanne@mh-hannover.de

Thompson, Scott
Department of Radiology
Mayo Clinic
200 First Street
Rochester, MN 55905, USA
thompson.scott@mayo.edu

Thorne, Bradford
Department of Radiology and
Biomedical Imaging
University of California
185 Berry St Suite 350
San Francisco, CA 94107, USA
bradford.thorne@gmail.com

van Breugel, Marjolein
Department of Radiology
University Medical Center Utrecht
Heidelberglaan 100
Utrecht 3508GA, Netherlands
j.m.m.vanbreugel@umcutrecht.nl

Vanney, Guy
IMRIS Inc.
5101 Shady Oak
Minnetonka, MN 55343, USA
Gvanney@imris.com

Vaughan, J. Thomas
Diagnostic Radiology
University of Minnesota
2021 Sixth Street S.E.
Minneapolis, MN 55455, USA
vaugh020@umn.edu

Venkateswaran, Madhav
Electrical and Computer Engineering
University of Wisconsin-Madison
1111 Highland Ave
Madison, WI 53705, USA
mvenkateswar@wisc.edu

Wacker, Frank
Diagnostic and Interventional Radiology
Hannover Medical School
Carl-Neuberg Str. 1
30625 Hannover, Germany
wacker.frank@mh-hannover.de

Wang, Peng
Medical Physics
University of Wisconsin-Madison
530 N Eau Claire Ave Apt 208
Madison, WI 53705, USA
pwang6@wisc.edu

Weiss, Clifford
Department of Radiology and
Radiological Science
The Johns Hopkins Hospital
600 N. Wolfe Street
Baltimore, MD 21287, USA
cweiss@jhmi.edu

White, Mariah
Department of Radiology
Mayo Clinic
200 First Street
Rochester, MN 55905, USA
White.Mariah@mayo.edu

Willie, Jon
Department of Neurosurgery
Emory University Hospital
1365-B Clifton Road NE, Suite B6200
Atlanta, GA 30322, USA
jon.t.willie@emory.edu

Woodrum, David
Department of Radiology
Mayo Clinic
200 First Street
Rochester, MN 55905, USA
woodrum.david@mayo.edu

Wybranski, Christian
Department of Radiology and
Nuclear Medicine
Otto-von-Guericke University
Leipziger Str. 44
39120 Magdeburg, Germany
christian.wybranski@med.ovgu.de

Xu, Di
Biomedical Engineering
Department of Radiology and
Radiological Science
Johns Hopkins School of Medicine
4000 Linkwood RD
Baltimore, MD 21210, USA
xu.di.bme@gmail.com

Yasin, Rashid
Mechanical Engineering
University of California
300 UCLA Medical Plaza Suite B119
Los Angeles, CA 90095, USA
rmyasin@gmail.com

Zhang, Shelley
Department of Radiology
Brigham and Women's Hospital
Harvard Medical School
75 Francis Street
Boston, MA 02115, USA
shelleyzhang@gmail.com

Zhang, Shuo
Biomedizinische NMR Forschungs GmbH
Max Planck Institute for Biophysical
Chemistry
Am Fassberg 11
37077 Göttingen, Germany
szhang@gwdg.de

Author Index

A

B

C

D

E

G

H

I

T

U

V

W

X

Y

Z